Cranfield
University

Adam R. Round

Ultra-structural Analysis

Of

Breast Tissue

Cranfield Postgraduate Medical School

Thesis submitted for the award of Ph.D.

Cranfield University

Postgraduate Medical School

Department of Materials and Medical Sciences

Thesis submitted for the award of Ph.D.

2006

Adam R. Round

Ultra-structural Analysis of Breast Tissue

Supervised by Dr K. D. Rogers and Dr C.J. Hall

Presented on the 20th of July 2006

1 Abstract

Previous research has shown that diagnostic information could be obtained from small angle X-ray scattering from breast tissues. The observed differences were attributed to two possible causes, the production of a new type of collagen around tumours and the action of matrix metalloproteinases degrading the collagen around tumours. Using both synchrotron radiation and conventional X-ray sources data was collected to investigate these hypotheses. 225 X-ray scattering profiles were collected from breast tissue samples from 82 individual patients using synchrotron radiation. The differences between normal, malignant and benign tissues were investigated and structural differences in the collagen were determined. The effects of metalloproteinase action on collagen were also investigated and computer modelling was used to simulate the diffraction profiles from collagen with structural alterations. The structural differences in diseased tissues were attributed to a difference in the structure of collagen which was observed as a reduction in peak intensity and increased axial D spacing (0.3 nm increase in D period) compared to normal tissues. The differences between malignant and benign disease were attributed to metalloproteinase action degrading the collagen around tumours. Automatic classification was applied using principal component analysis to tissue samples from up to 6 cm away from the tumour site, approximately 90 % of the tissue samples at 6 cm were classified as cancer using the X-ray scattering profile but which were diagnosed as normal by standard histopathological methods. The results of this research have shown that X-ray scattering profiles contain diagnostic information relating to the structure of collagen. The changes associated with disease may be observed at up to 6 cm from the tumour site and that these differences in the X-ray scattering profile may be measured using a conventional X-ray source.

2 Dedication

To my mother and father, thank you for all your help, support and encouragement throughout the years.

Without you I would not be the man I am today.

3 Acknowledgements

Many thanks to:

My family for their support throughout my career and my father Dr R. Round for proof reading this thesis.

My supervisors Dr K.D. Rogers and Dr C.J. Hall for their advice, expertise and instruction.

Dr S.J. Wilkinson for his advice, computing experience, help with experimentation and for the picture of the SRS.

All the people who helped perform the experiments Dr R. Lewis, Dr K. Siu and all the members of the Monash University research group. Dr S. Pearson and Mr G. Falzon from the University of New England, Armadale, Australia. Dr E. Schultke and her colleagues from the University of Saskatchewan.

The staff at Daresbury Laboratories for the facilities that allowed this research to be undertaken, Notably Dr G. Grossman and Dr T. Geraki, managers of station 2.1 and Mr M. Wardell for the technical drawings of the new sample holder.

The Nottingham City Hospital tissue bank for supplying the breast tissue samples used in this study and pathology department for the sectioning and staining of the breast tissue samples.

Dr S. Pinder and Dr E. Provenzano from Addenbrooke`s Hospital for the histopathological analysis of the breast tissue.

Cranfield University and the synchrotron radiation department of Daresbury Laboratories for the funding and opportunity to pursue this research.

Dr T. Wess from Cardiff University for his expertise in small angle X-ray scattering and the computer simulation of collagen micro-fibrillar shear.

Dr C. Kennedy from Cardiff University, Dr M. Tobin from Daresbury laboratories and Dr N. Stone from Cranfield post graduate medical school for their help with principal component analysis.

Mr H. Suhonen for making available his programme for X-ray scattering simulation and Mr M. Ibison from Liverpool University for processing the simulations.

Miss H Myers for the picture of her breast.

Miss L Williams for her drawing of a breast.

Dr Kalju Kahn for the pictures of the collagen molecules.

IOP Publishing, Dr R. Lewis and Mr P. Pionetta for permission to reproduce graphs.

4 Table of Contents

1 Abstract I
2 Dedication II
3 Acknowledgements III
4 Table of Contents IV
5 Table of Figures V
6 Outline of Thesis VII
7 Introduction 1
7.1 The breast 1
7.2 Breast cancer 4
7.3 Collagen structure 10
7.4 X-ray production 17
7.5 The interaction of X-rays with matter 25
7.6 X-ray scattering 29
7.7 Interpretation of X-ray diffraction data 34
7.8 Experimental effects on the X-ray scattering pattern of collagen 41
7.9 X-ray scattering for disease diagnosis 48
7.10 Models which may explain the differences in the X- ray scattering patterns 51
7.11 Automated analysis techniques 58
7.12 Possibilities for other tissue systems 61
7.13 Aims of this Thesis 62
8 Materials and methods 64
8.1 Experimental procedures 64
8.2 X-ray scattering data processing 75
8.3 Data analysis 85
9 Contribution to Knowledge 94
10 Results 96
10.1 Summary 96
10.2 Parameters which may affect X-ray scattering from collagen 96
10.3 Synchrotron radiation investigation of breast tissue 119
10.4 Conventional X-ray source investigation of breast tissue 151
10.5 Investigation into diagnostic effects at distance 157
10.6 Degradation of tissue 163
10.7 Computer Simulation of X-ray Scattering 179
11 Discussion 182
11.1 Summary 182
11.2 Parameters affecting X-ray scattering from collagen 182
11.3 Experimental errors in breast tissue diagnosis data collections 189
11.4 Errors in breast tissue diagnosis data analysis 195
11.5 Diagnostic X-ray scattering 199
11.6 Sensitivity and specificity of SAXS as a diagnostic test 207
11.7 Effect at distance 209
11.8 Degradation of tissues 210
11.9 Computer simulation 213
11.10 Cause of structural differences in diseased tissues 214
12 Conclusion 217
12.1 Structural differences between tissue types 217
12.2 Proposed cause of structural differences 218
12.3 Diagnosis using a conventional X-ray source 219
12.4 Automated diagnosis 219
13 Further Work 220
13.1 Absolute calibration 220
13.2 New sample holder 221
13.3 Micro-focused investigation of individual points in tissue 221
13.4 Optimisation of a conventional X-ray source to maximise diagnostic information 221
13.5 Automated diagnosis 222
13.6 Double blind study 222
13.7 Use of alternate techniques to investigate collagen structure 223
14 References 224
14.1 Web Based References 230
Appendix I 233
Appendix II 237

5 Table of Figures

Figure 7.1 The human female breast 1
Figure 7.2 Structures of the breast. 2
Figure 7.3 Representation of collagen repeating base unit G-X-Y 11
Figure 7.4 Representation of collagen molecules 13
Figure 7.5 Arrangement of the five tropocollagen molecules in the repeating unit of a micro fibril 13
Figure 7.6 Arrangement of collagen molecules in a micro fibril 14
Figure 7.7 Gap and overlap regions in micro fibrils 15
Figure 7.8 Small Angle X-ray scatter pattern of rat tail tendon (type I collagen) 16
Figure 7.9 Daresbury Laboratory synchrotron radiation source and experimental hall buildings 19
Figure 7.10 Comparison of X-ray sources 24
Figure 7.11 Diagram showing scattered wave propagates in all directions 27
Figure 7.12 Plot of observed intensity of scattered X-rays with increasing distance 28
Figure 7.13 Plot of observed X-ray intensity with angular position 28
Figure 7.14 Representation of a simple scattering system 29
Figure 7.15 A simple scattering system 33
Figure 7.16 The autocorrelation/Patterson function of the simple scattering system 33
Figure 7.17 X- ray scattering pattern from rat tail tendon meridian and equatorial directions 35
Figure 7.18 Variation in preferred orientation of rat tail tendon 36
Figure 7.19 Percentage scatter observed after attenuation from water at 10keV 42
Figure 8.1 Silver behenate calibration for X-ray scattering 68
Figure 8.2 Basic illustration of capillary tube mounting 70
Figure 8.3 Capillary tube holder 71
Figure 8.4 Brass sample holder 72
Figure 8.5 Tensile test rig sample mounting 73
Figure 8.6 Region of interest highlighting the diffraction peaks from rat tail tendon 78
Figure 8.7 Calibrated rat tail tendon with annotation rings corresponding to 67 nm D spacing 79
Figure 8.8 Radial region of interest applied to diffraction peaks of rat tail tendon. 81
Figure 8.9 Intensity versus Q spacing for raw data showing offset due to background noise 82
Figure 8.10 Porod plot showing gradient to be subtracted form the raw data. 82
Figure 8.11 Intensity versus Q spacing for raw data showing reduced offset after subtraction 83
Figure 8.12 Porod plot showing plateau indicating the subtraction was correct 83
Figure 8.13 SAXSess X-ray scattering image showing annotation for integration 84
Figure 8.14 Output of PAN fit to show fitting model 89
Figure 10.1 X-ray scattering data from hydrated rat tail tendon 97
Figure 10.2 X-ray scattering from hydrated rat tail tendon with applied force 98
Figure 10.3 Effect of force on S of 1st order axial peak from hydrated rat tail tendon 99
Figure 10.4 X-ray scattering image of hydrated chicken tendon under 22.45 N load 101
Figure 10.5 X-ray scattering from chicken tendon with varying applied force 102
Figure 10.6 Change in 1st order axial peak intensity against applied force 104
Figure 10.7 Change in S position of 1st order peak against applied force 105
Figure 10.8 Change in S position of 3rd order axial peak against time and force 105
Figure 10.9 Change in 1st order peak width with increasing force 107
Figure 10.10 X-ray scattering image of hydrated chicken dermis with 0 N and 4 N applied force 110
Figure 10.11 X-ray scattering from chicken dermis with varying applied force 111
Figure 10.12 Change in S position of 1st order peak against applied force for chicken dermis 113
Figure 10.13 X-ray scattering images from dehydrating rat tail tendon at 0, 9 and 24 minutes 114
Figure 10.14 X-ray scattering intensity form a sample of rat tail tendon during dehydration 116
Figure 10.15 Effect of dehydration on S spacing of the 1st order axial peak of rat tail tendon. 117
Figure 10.16 Typical X-ray scattering images of fibrous normal breast tissue 121
Figure 10.17 Typical X-ray scattering images of malignant breast tissue 122
Figure 10.18 Typical X-ray scattering images of highly fatty breast tissue 123
Figure 10.19 Plot of 3rd order Bragg peak spacing against area for all diagnostic data 128
Figure 10.20 Plot of 3rd order Bragg peak spacing against area using data from a single experiment 130
Figure 10.21 Bragg peak position versus area of samples with >80% tumour (by data collection) 131
Figure 10.22 Plot of spacing versus 3rd order Bragg peak area (possible diagnostic areas annotated) 132
Figure 10.23 S spacing position against peak area for 2nd order Bessel peak 134
Figure 10.24 Radius of gyration against relative intensity ratio 135
Figure 10.25 Relative intensity ratio versus the % fat content of the samples 136
Figure 10.26 Relative intensity ratio versus the % fibrous content of the samples 136
Figure 10.27 The principle components which describe the variance in the data set 143
Figure 10.28 Coefficients showing agreement with principle components F1 and F2 144

Figure 10.29 F1 and F2 from 0 to 1.6nm^{-1} 145
Figure 10.30 Separation of tissue types using linear discriminate analysis 147
Figure 10.31 Significant loadings against S spacing 149
Figure 10.32 SAXSess X-ray scattering images of both normal and cancer samples 152
Figure 10.33 S against typical intensity plots for tumour and normal tissue 153
Figure 10.34 Results of PCA using Pirouette in the range S= 0.017nm^{-1} to 0.037 nm^{-1}. 154
Figure 10.35 loadings 2 and 3 plotted against S 156
Figure 10.36 Plot of the L2 score for each sample against the distance from the tumour site 158
Figure 10.37 Area of the 3rd order Bragg peaks for samples increasing in distance from tumour site 160
Figure 10.38 Relative intensity ratio of samples at increasing distance from tumour site 161
Figure 10.39 Degradation of rat tail tendon by matrix metalloproteinase 164
Figure 10.40 Degradation of pork dermis by matrix metalloproteinase 165
Figure 10.41 Axial peak area of breast tissue control and degradation series 166
Figure 10.42 Change in Peak area of rat tail tendon by MMP and associated control 167
Figure 10.43 Area of Bessel and axial Bragg peaks for MMP and control series of pork tissue 168
Figure 10.44 Change in S spacing of 3rd order axial peak for breast 169
Figure 10.45 Change in 3rd order axial S position of the of pork dermis 170
Figure 10.46 Change in 3rd order axial S position of rat tail tendon 171
Figure 10.47 Change in 3rd order peak width of breast tissue collagen with MMP action 172
Figure 10.48 Change in Rg of rat tail tendon in the presence of MMP 173
Figure 10.49 Change in Rg of pork dermis in the presence of MMP 173
Figure 10.50 Average intensity change near beam stop, rat tail tendon in the presence of MMP 174
Figure 10.51 Average intensity change near beam stop, pork dermis in presence of MMP 175
Figure 10.52 Change in average intensity between 3rd and 5th axial peaks of rat tail tendon 176
Figure 10.53 Change in average intensity between 3rd and 5th order axial peaks of pork dermis 176
Figure 10.54 Variation in collagen D spacing with increasing temperature 177
Figure 10.55 Variation in area of collagen 3rd order axial peak with increasing temperature 178
Figure 10.56 Calculated spacing versus intensity for increasing shear between micro fibril units 180
Figure 10.57 Calculated spacing versus intensity for increasing standard deviation of the D period 181
Figure I.1 New sample holder fully assembled 233
Figure I.2 Sample holder base unit designed by Dr S. Wilkinson 233
Figure I.3 Sample securing discs, sample holder disc (top) and sample clamp disc (bottom) 234
Figure I.4 Sample holder disc 235
Figure I.5 Sample clamp disc 236

6 Outline of Thesis

The scope of this thesis can be simplified to two major aims, firstly to use small angle X-ray scattering to further understand the previously observed differences in the collagen of malignant tissues and to determine the likely biological mechanism causing the differences. Secondly to demonstrate the possibility of using small angle X-ray scattering to provide an automated diagnostic tool for use in a clinical setting to aid diagnosis.

To allow readers with little or no experience of small angle X-ray scattering or breast cancer to better understand the subject matter of this thesis the introduction begins with the basic structure of the female human breast, a summary of breast cancer and the structure of collagen. After which a brief explanation of synchrotron radiation and the production of X-rays from conventional sources is included, before describing small angle X-ray scattering and the methods that were used for determining structural information from small angle X-ray scattering data. The literature regarding the differences in the collagen of diseased tissues and the proposed mechanisms responsible is then reviewed.

Full details of the experimental procedures including sample preparation, mounting and the parameters of the radiation source used were included so as to enable duplication of this work in future if required. Data processing and analysis procedures were detailed fully as well.

Owing to the large amount of data collected the raw data is not presented in its entirety, only a representative sample of raw scattering images are presented followed by the fully processed data showing trends and differences which are discussed and

upon which the conclusions of this thesis are based. Finally suggestions for further work required to produce a viable automated diagnostic tool and to further examine the changes in the collagen using other techniques are presented.

The conclusions of this thesis further support the observations of diagnostic differences observed in the scattering pattern of tissue samples. The differences observed in the small angle X-ray scattering were interpreted and related to structural differences in the collagen. It is suggested that a combination of the proposed biological remodelling mechanisms account for the structural differences in collagen from normal, benign and malignant tissues. The suggested cause of observed differences between normal and diseased tissues is the presence of a new type of collagen surrounding the diseased area. The difference between malignant and benign disease is the action of matrix metalloproteinase which degrades the surrounding collagen which allows metastasis.

7 Introduction

7.1 The breast

The term breast in general usage, refers to the superior ventral surface of the body extending from the neck to the abdomen. As a medical term and in the context of this thesis, breast refers to the milk producing organs located on the female chest (Figure 7.1).

Figure 7.1 The human female breast

Picture reproduced with permission of photographer and model (Miss H. Myers)

7.1.1 Breast tissue constitution

The tissue of the human female breast consists of a combination of four components, lobules (otherwise known as glands), milk ducts, adipose tissue and connective tissue. The lobules are arranged in groups termed lobes. The number of lobes varies between individuals but is approximately fifteen to twenty for most women. They are arranged in a radial pattern centred on the nipple (See Figure 7.2), with a larger concentration of lobes in the top outer most area of the breast. Milk is produced by glands in the lobules and flows through a branching network of ducts which converge into a number of larger connecting ducts called lactiferous sinus, from which the milk flows to the nipple.

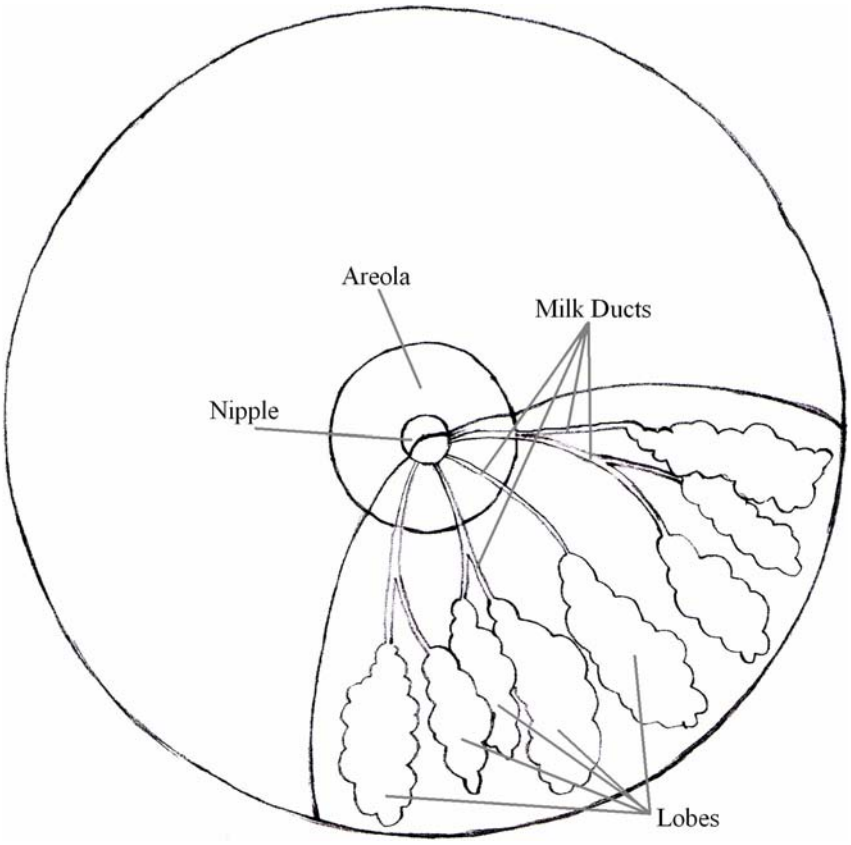

Figure 7.2 Structures of the breast.

Picture reproduced with permission of artist (Miss L. Williams).

The lobes are supported by surrounding adipose tissue (fat) and connective tissue consisting of ligaments (made of collagen) and a fibrous matrix (predominantly made of collagen).

7.1.2 Changes with age

The proportions of fat and collagen in the breast change with age. Young women have a high proportion of collagen in the breast so the breast is dense and firm. A study to assess the accuracy of screening mammography stated that 61% of women aged between 40 to 44 had radiographically dense breasts compared to only 27% of women between the ages of 70 to 79 (Carney, 2003). As age increases connective tissue is replaced by fat. With increased fat the density of the breast is lower, but as there is reduced collagen there is less support so the breast is not as firm.

At menopause the lobules shrink due to the decrease in oestrogen and the concentration of blood vessels and blood flow decreases as there is lower vascular demand (Shah, 2001). The average amount of water in breast tissue reduces post menopause reflecting the difference between high water content of epithelial connective-tissue compartments in pre-menopausal tissue and the low water-content adipose which dominates postmenopausal breast tissue (Shah, 2001).

7.1.3 Changes during the menstrual cycle

Ovarian hormone fluctuations during the menstrual cycle have been related to physiological changes within the breast. Many women report swelling and increased sensitivity of the breasts (possibly to the point of pain) prior to menstruation. The observations of swelling and sensitivity correspond with published results which reported an increase in blood flow of 50 % and a 28 % increase in the amount of water present in the tissues of the breast during the luteal phase (Shah, 2001). The luteal phase is a portion of the menstrual cycle that begins with the formation of the corpus luteum (which occurs shortly after ovulation) and ends with the start of the menstrual flow and lasts approximately 14 days (Steadman, 2000). The luteal phase is also the point at which progesterone levels are at their highest and the point when the

rate of cell division in the breast is greatest (More.com, Hormones and Breast Cancer). Marked changes during the menstrual cycle have been observed in the basement membrane, sub-basement membrane zone and delimiting layer of fibroblasts surrounding the ductules. Basement membrane markers such as laminin, heparan sulphate proteoglycan, and type IV and V collagens are reported to be greatly reduced during the mid-cycle period (days 8 to 22), while collagen types I, III, VI and VII remained unchanged (Ferguson, 1992).

7.2 Breast cancer

7.2.1 Summary

Cancer covers a wide range of cellular growth abnormalities resulting in variation in prognosis and treatment. The first step towards effective treatment is accurate diagnosis. The major factors to be determined being tumour type (ductal or lobular etc.) and the nature of the tumour (benign or malignant). After which the stage and grade is determined which is based on the aggressiveness (*in situ* or invasive) and the presence of metastasis. There is a range of screening tests to aid the diagnosis of cancer, but to determine the nature of the primary lesion, tissue samples from the tumor itself are required. The tissue is stained to highlight the stroma and cellular structures, before analysis by a trained pathologist who uses features such as the size of the cell nuclei, cell distribution and the appearance of the stroma to determine the nature of the tissue.

7.2.2 What is "Cancer"

The definition of cancer from Steadman's medical dictionary 27th edition (Steadman, 2000) is:

"General term frequently used to indicate any of various types of malignant neoplasms, most of which invade surrounding tissues, may metastasize to several sites, and are likely to recur after attempted removal and to cause death of the patient unless adequately treated; especially, any such carcinoma or sarcoma, but, in ordinary usage, especially the former."

A neoplasm being an abnormal tissue that grows by cellular proliferation more rapidly than normal, shows partial or complete lack of structural organization and functional coordination with the normal tissue, and usually forms a distinct mass of tissue which may be either benign or malignant (Steadman, 2000).

7.2.3 Incidence and mortality

Monitoring of the effectiveness of diagnosis and treatment of any disease requires compiling statistics including the number of new cases diagnosed and the mortality rate associated with the disease.

The number of people diagnosed each year is termed the incidence, for breast cancer incidence was, in 2001: 34,347 (National Statistics, series MB1 no.32), in 2002: 34,319 (National Statistics, series MB1 no.33) and in 2003 around 36,500 (National Statistics, breast cancer incidence 2003) in England. Worldwide more then 1.2 million people will be diagnosed with breast cancer in 2005, which makes breast cancer one of the most common forms of cancer and highlights the need for improved diagnosis and treatments to help save the lives of those diagnosed.

The mortality rate for breast cancer in England was 10,800 in 1999 (National Statistics, breast cancer incidence 1999). The mortality and incidence rates are not directly related as the patients diagnosed in any one year will not be the same patients

who died in that year. The deaths resulting from the disease will have been diagnosed a number of years earlier and so mortality and incidence rates reflect the effectivness of the diagnosis and treatment of any disease.

7.2.4 Malignant or benign

Benign lesions are those presenting no danger to life or well being. In relation to cancer benign describes tumours which do not invade surrounding tissues and do not metastasise. The use of the word benign is not truly apt as although benign tumours pose a low threat, if left untreated they will continue to grow and can reach a size where there is a risk to health.

In contrast malignant lesions are threatening to life, virulent, destructive or harmful and in a clinical sense, a course which progresses rapidly to death. In relation to cancer, malignant describes tumours with uncontrolled growth and a tendency to metastasise.

7.2.5 Tumour type

Tumors are classified in a hierarchy according to the type of tissue they originate from, then by the location and or the behavior of the tumor cells (See Table 7.2.1 for general types from different tissues and Table 7.2.2 for breast cancer).

Name	Tissue type
Fibromas	Fibrous connective tissue
Melanomas	melanin cells (pigment cells in the skin)
Carcinomas	Any epithelial tissue such as are found in skin, bronchi and stomach
Adenocarcinomas	Any epithelial glandular tissue such as are found in the prostate and colon
Sarcomas	Connective tissue such as muscle, cartilage, lymph nodes and bone
Lymphomas / leukemia	White blood cells

Table 7.2.1 Tumour classifications based on tissue type of primary tumour

Type	Description
Ductal Carcinoma	Carcinoma originating in the milk ducts, or forming duct like structures
Lobular Carcinoma	Carcinoma originating in the lobes (glands) of the breast
Medullary Carcinoma	Invasive breast carcinoma that forms a distinct boundary between tumour tissue and normal tissue
Mucinous carcinoma	Rare carcinoma formed of mucus-producing cancer cells
Inflammatory breast cancer	Inflamed breasts (red and warm) with dimples and/or thick ridges. It is caused by cancer cells blocking lymph vessels or channels in the skin over the breast.
Paget's disease of the nipple	Carcinoma originating in the milk ducts and spreads to the skin of the nipple and areola
Phylloides tumor	Very rare originating in the connective tissues of the breast

Table 7.2.2 types of breast cancer and their descriptions

The two most common forms of breast cancer (ductal carcinoma and lobular carcinoma), are further subdivided using the terms infiltrating and *in situ* to give infiltrating ductal carcinoma (IDC), ductal carcinoma *in situ* (DCIS), infiltrating lobular carcinoma (ILC) and lobular carcinoma *in situ* (LCIS). *In situ* refers to tumours which have not spread from the original site, conversely infiltrating refers to tumours which have invaded adjacent tissues.

7.2.6 Breast cancer stages

Breast cancer can be divided into stages depending on the extent of disease proliferation (See Table 7.2.3). The stage assigned to a cancer will be used when making clinical management decisions. The stage of a cancer is determined using a range of tests which include mammograms, X-rays of other areas of the body and biopsies of breast tissue and lymph nodes. Stages 1, 2 and 3 are also called primary breast cancer as they indicate that the disease has not metastasised and stage 4 can sometimes be called secondary breast cancer as it indicates the tumour has metastisised. In addition to the stages the term "locally advanced breast cancer" is used to describe a tumor with a margin that has advanced into the muscle or skin of the chest and which may have spread to the sentinel lymph node in the arm pit only.

The margin of a tumour is the border formed between the mass of cancerous cells and the cells of the surrounding normal tissues. Locally advanced breast cancer indicates the complication of the advancement of the margin into other tissues. As there is no metastatic spread, locally advanced breast cancers may be either stage 2 or 3 depending on size.

Stage	**Tumour Diameter**	**Lymph nodes in armpit affected**	**Metastasis**
1	2cm Max	No	No
2	2cm to 5cm Max	No	No
3	Over 5cm	Yes	No
4	Any	Possibly	Yes
Locally Advanced Breast Cancer *(Any or all of the indicators on the right) i.e. it can be applied to either stage 2 or3*	Over 5cm	Yes	No But the tumor margin has advanced into the muscle or skin of the chest

Table 7.2.3 Parameters used to determine the stage of breast tumours

7.2.7 Tumour grade

Current histopathological analysis techniques stain biopsy tissue taken from the site of an area suspected to be cancerous. Before staining the tissues are treated with formalin (10% formaldehyde solution) to prevent degradation of the tissue, embedded in paraffin wax to allow sectioning to give multiple slices through each piece of tissue to be investigated. The stains used highlight connective tissues and the nuclei of cells allowing pathologists using visualise structures in the tissues with optical microscopy. The presence of abnormal cells and disrupted stroma indicates disease within the sample but cancer covers a spectrum from benign through into malignant up to and including highly aggressive fast growing tumours. The Scarff-Bloom-Richardson

system (Kufe, 2003) is used to classify the degree of malignancy of diseased tissues and uses three features to determine the grade of a cancer:

1. Tubule formation (percentage of cancer composed of tubular structures)
2. Nuclear pleomorphism (change in cell size and uniformity)
3. The frequency of cell mitosis (rate of cell division)

Each feature is scored (from 1 to 3) based on how abnormal the feature is (1 being mostly normal and 3 being highly abnormal) (See Table 7.2.4).

Tubule Formation (% of Carcinoma Composed of Tubular Structures)	**Nuclear Pleomorphism (Change in Cells)**	**Mitosis Count (Cell Division)**	**Score**
> 75%	Small, uniform cells	Up to 7	1
10-75%	Moderate increase in size and variation	8 to 14	2
less than 10%	Marked increase in size and variation	15 or more	3

Table 7.2.4 Scarff-Bloom-Richardson grading features and associated scores (from Imaginis, histological grade)

The individual scores from the three features are added together to give an overall score which corresponds to one of the three cancer grades (See Table 7.2.5).

Score	**Grade**	**Description**
3,4,5	**I** *(lowest)*	Well-differentiated breast cells; cells generally appear normal and are not growing rapidly; cancer arranged in small tubules.
6,7	**II**	Moderately-differentiated breast cells; have characteristics between Grade I and Grade III tumours.
8,9	**III** *(highest)*	Poorly differentiated breast cells; Cells do not appear normal and tend to grow and spread more aggressively.

Table 7.2.5 Scarff-Bloom-Richardson overall scores, grades and descriptions (from Imaginis, histological grade)

7.3 Collagen structure

7.3.1 Summary

Collagen is the most abundant protein in the human body, found in skin, bone, cartilage and is the major component of connective tissues. There are over 19 different types of collagen, some of which form highly aligned fibrils found in tendons. Others form matrices with minimal preferential orientation found in the extra cellular matrix (ECM) of breast tissue.

The molecular structure of collagen and its hierarchical structure have been studied using a variety of techniques, including electron microscopy beginning in the 1950`s and more recently X-ray diffraction including the use of synchrotron radiation (reviewed by Bigi, 1991 and 1996). The structure and function of many different collagen types is known, from the base repeating unit of three amino acids up through the varying levels of structural hierarchy from single collagen molecule to triple helix, micro-fibril, fibril and fibre (Mayne, 1987; Orgel, 2001; Wess, 2005).

7.3.2 Base sequence of collagen

The fundamental building block found in all collagen molecules is the repeating unit of amino acids G-X-Y where G is glycine, X is often proline and Y is often hydroxyproline (see Figure 7.3). The separation between one glycine molecule and the next is 0.84 nm (Orgel, 2001), this spacing can be observed as maxima using wide angle X-ray scattering and is termed the d spacing.

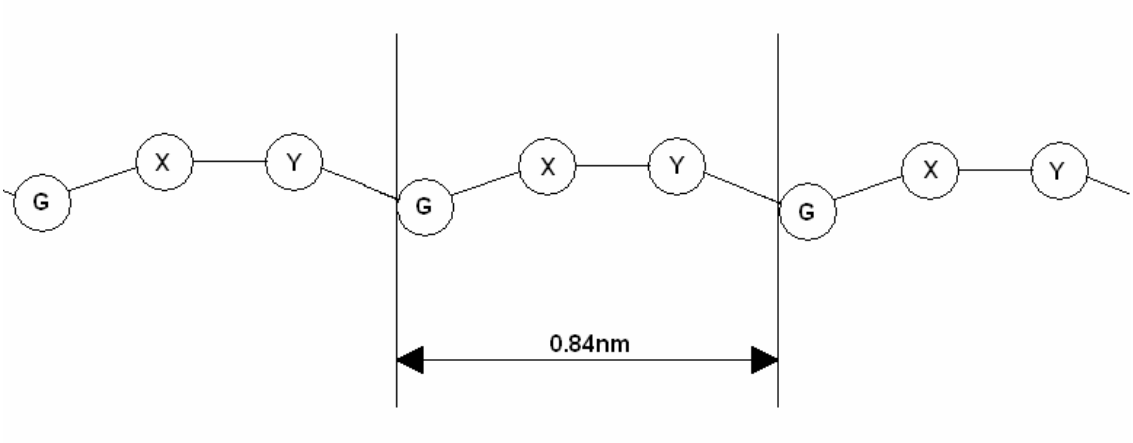

Figure 7.3 Representation of collagen repeating base unit G-X-Y

The substitution of other amino acids such as threonine instead of proline and hydroxyproline in the place of X and Y at some of the points along the length of the chain gives rise to structural differences.

7.3.3 Individual collagen molecule

The full molecular structure of contains over 1000 individual amino acids, coiled into a left handed helix (Orgel, 2001). The structural differences caused by amino acid substitution to the basic repeat pattern (G-X-Y) results in many subtly different forms of the collagen molecule denoted by (α1(I), α1(II),…..α2(I), α2(II),…..α3(I), α3(II),….etc).

7.3.4 Tropocollagen or Triple Helix

The different types of collagen are formed from different combinations of the individual collagen molecules (see Table 7.3.1 for five of the most commonly found types of collagen (compiled from Kuhn, 1987; Keilty, 1993; Seljee, 2005; Tryggvason, 1987)).

Type	Super molecular Structure	Tropocollagen Triple Helix Formed From	Distribution and comments
I	67 nm Banded fibrils	$[\alpha1(I)]_2\,\alpha2(I)$ or $[\alpha1(I)]_3$	Most tissues. About 90 % of all collagen, forming the largest and strongest well structured fibres. Found in skin, tendons, bones, ligaments, cornea, internal organs, filamental cartilage, placenta, arteries, dentines and liver.
II	Small 67 nm Banded fibrils	$[\alpha1(II)]_3$	Cartilage, cornea, vitreous humor, inter-vertebral disc. Discovered in chicken cartilage and gut. Now known from hyaline cartilage, invertebrate discs, the notochord and the adult vitreoul body
III	Small 67 nm Banded fibrils	$[\alpha1(III)]_3$	Soft tissues, with type I collagen. Reticular networks (stretchable connective tissues), (foetal) skin, blood vessels, internal organs, smooth muscles, lungs, arteries, uterus, liver and stroma.
IV	Non-fibrillar Network	$[\alpha1(IV)]_2\,\alpha2(IV)$ or $[\alpha3(IV)]_2\,\alpha4(IV)$ and other forms	Basement membranes. Structural aggregates of basement membranes. Underlying most epithelial cells and surrounding muscle, nerve, fat and smooth muscle cells. Distinctive amino acid composition and high contents of glycosylated hydroxylysines.
V	Small fibers	$[\alpha1(V)]_3$ or $\alpha1(V)\,\alpha2(V)\,\alpha3(V)$ and other forms	Minor amounts in most tissues with type I collagen, pre-cellular membranes, most interstitial tissues, placenta, skin and smooth muscle cells.

Table 7.3.1 Collagen Types I-V. Their triple helix components and their distribution in the Body

Three collagen molecules coil together (see Figure 7.4) to form a tropocollagen molecule, a right handed super helix which is approximately 290 nm long with a diameter of 1.15 nm (Orgel, 2001).

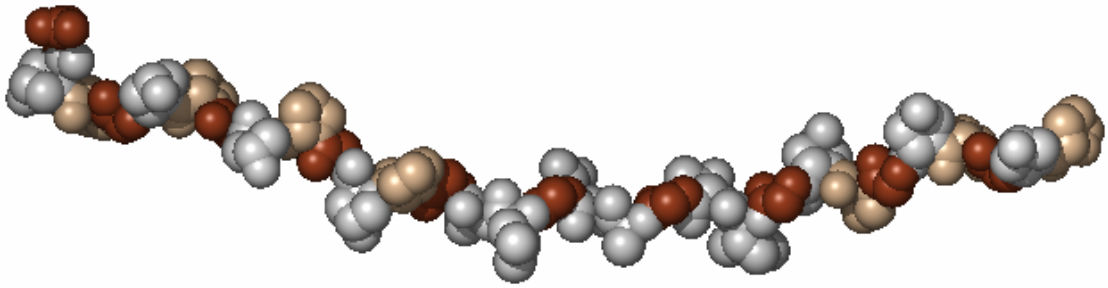

A

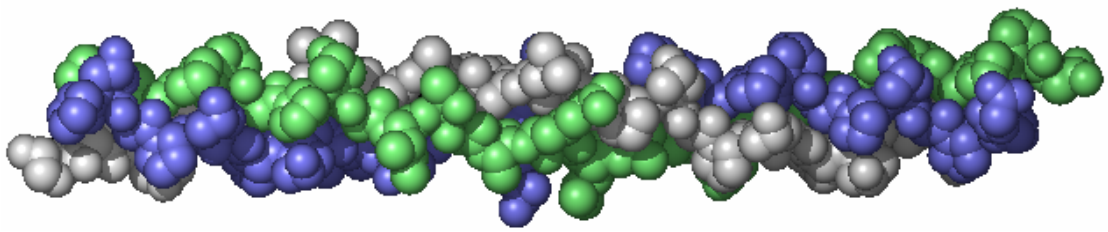

B

Figure 7.4 Representation of collagen molecules

A) Collagen polypeptide
B) Collagen triple helix (tropocollagen)

Reproduced with permission of Dr K. Kahn,
Department of Chemistry and Biochemistry, University of California, Santa Barbara

7.3.5 Collagen micro fibril

In the fibril forming collagens (types I, II, III, and V etc.) five tropocollagen molecules combine in a staggered spiral formation (see Figure 7.5) which forms the repeating unit of the micro-fibril level of the structural hierarchy of collagen.

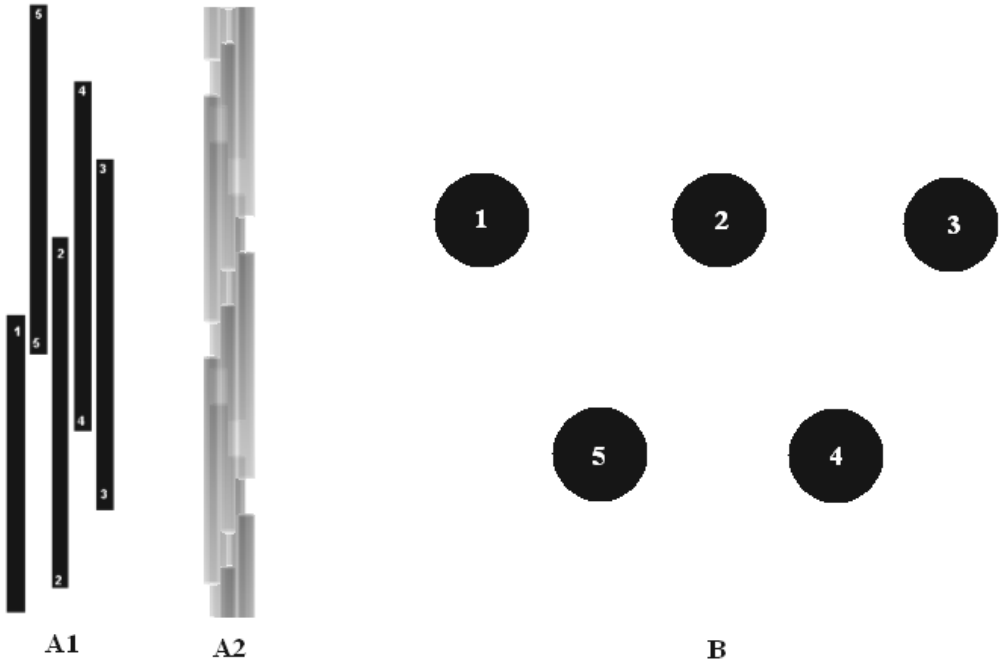

Figure 7.5 Arrangement of the five tropocollagen molecules in the repeating unit of a micro fibril

A) Axial arrangement (1 planer view, 2 showing spiral nature)
B) lateral arrangement

A micro fibril is formed from many repeating units (Figure 7.5 A) longitudinally aligned, where each individual tropocollagen molecule of the n^{th} unit in line with the corresponding tropocollagen molecule of the $n(+1)^{th}$, $n(+2)^{th}$, $n(+3)^{th}$,……etc. unit (Figure 7.6 A). Groups of micro fibrils are packed laterally in bundles in an approximately hexagonal close-packed formation (Figure 7.6 B).

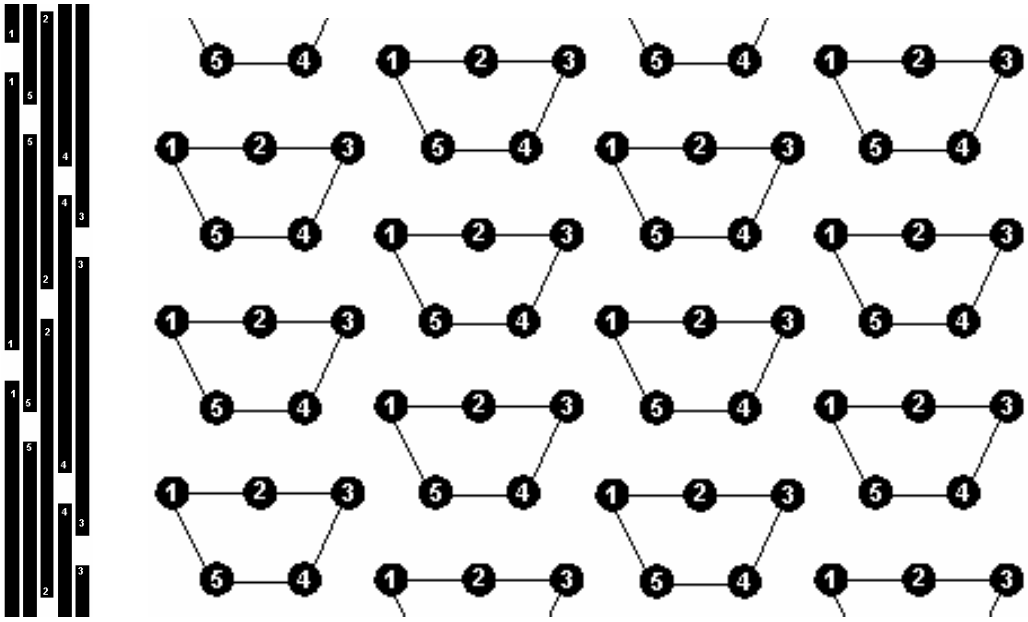

A B

Figure 7.6 Arrangement of collagen molecules in a micro fibril

(A. Axial arrangement, B. lateral arrangement)

Although the n^{th} unit is aligned longitudinally with the $n+1^{th}$ unit there is a gap separating each unit of approximately 36 nm for type I collagen (Orgel, 2001). When viewed in projection the gaps between adjacent micro fibrils will align, producing a reduction in the projected electron density where the gaps are present compared to where the collagen molecules overlap (see Figure 7.7).

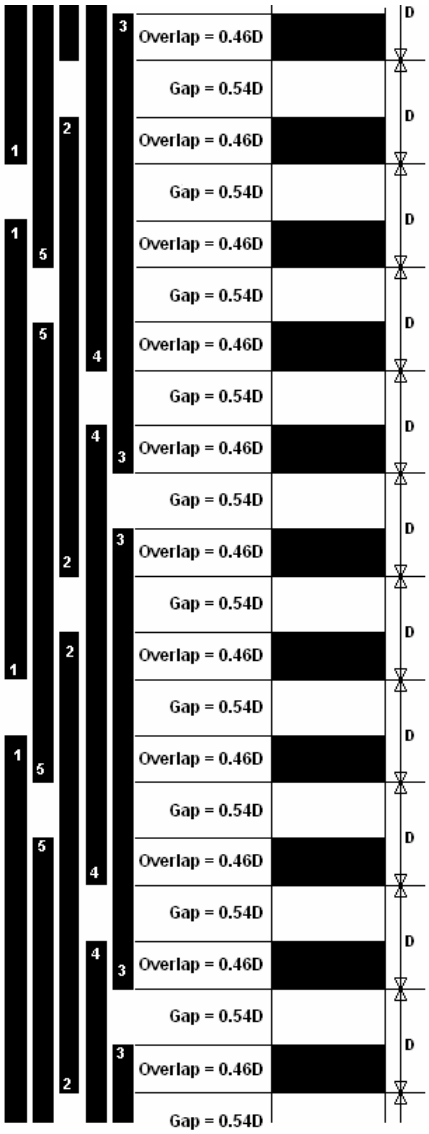

Figure 7.7 Gap and overlap regions in micro fibrils

The gap and overlap regions result in repeating differences in the projected electron density the spacing between the start of one region and the next is termed the D spacing.

The gap and overlap regions can be observed by both electron microscopy (as striations in the image) and small angle X-ray diffraction as maxima (see Figure 7.8). The maxima in the scatter pattern corresponds to the spacing between the start of one overlap or gap region and the next and is termed the D Spacing which is approximately 67 nm for type I collagen.

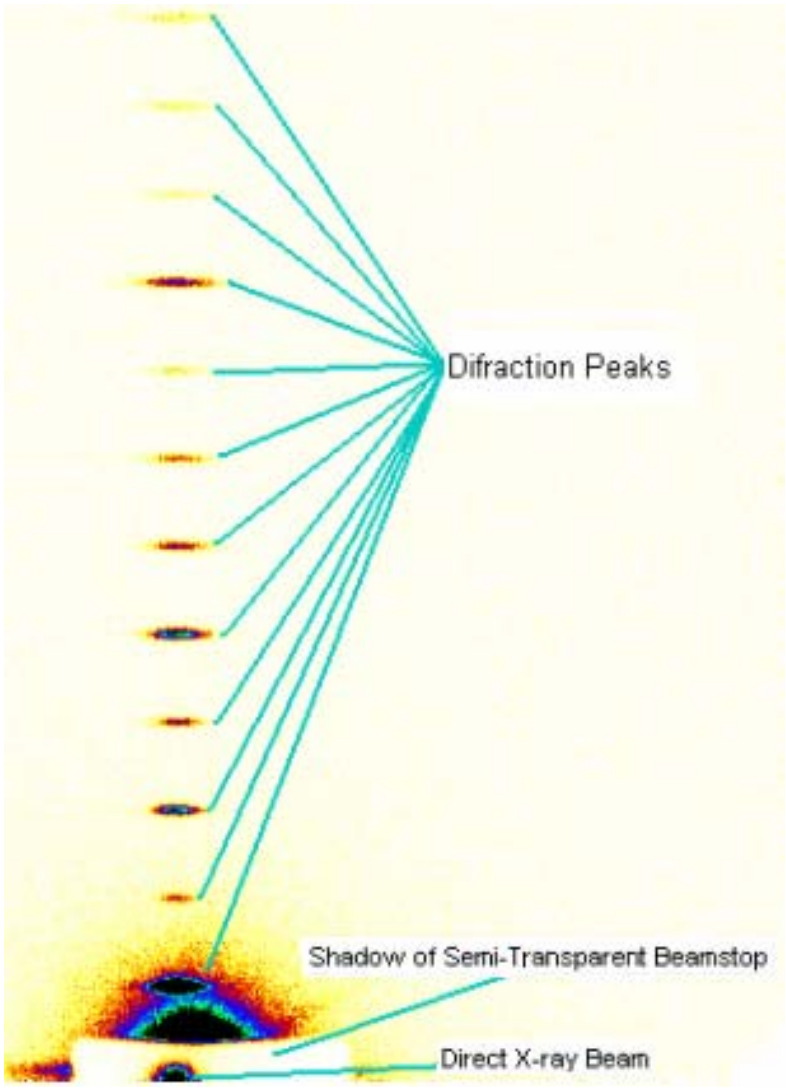

Figure 7.8 Small Angle X-ray scatter pattern of rat tail tendon (type I collagen)

7.3.6 Fibrils and fibres

Groups of micro fibrillar bundles combine to form fibrils. In tendon fibrils align to form fibres which are all aligned in one axis to provide structural supporting along that axis. However, in other connective tissues they form a fibre matrix with no preferential alignment providing structural support in multiple directions. The scattering pattern reflects this variation in alignment where the peaks appear as arcs with lengths that represent the variation in alignment of the fibrils in the sample and the maximum intensity of the arc shows increased alignment in that direction.

7.4 X-ray production

7.4.1 Overview

There are several methods of producing X-rays but only two are currently employed for use in scientific experimentation. The conventional method is using an X-ray tube, producing X-rays by acceleration of an electron beam at a metal target to cause excitation. An alternative method is to harness synchrotron radiation (radiation produced as electrons are deviated from their path by a magnetic field). Synchrotrons produce much greater intensities of X-rays but are large scale facilities with relatively limited access. Conventional X-ray tubes produce lower intensities of X-rays than a synchrotron, but can be implemented as a dedicated tool in a clinical environment. Examples of dedicated clinical X-ray equipment utilising X-ray tubes as the source are imaging systems for screening mammography as well as diagnosing broken bones, computed tomography for the visualisation of tumours and X-ray radiotherapy devices.

7.4.2 Synchrotron radiation

7.4.2.1 Summary

Synchrotrons are facilities dedicated to producing electromagnetic radiation for scientific research. The wavelength of the radiation produced ranges from infrared to hard X-rays. The radiation is extracted along evacuated tubes termed beam lines. The beam lines lead to experimental stations where the experimental equipment is housed. Different stations are optimised (selection of appropriate wavelength and intensity of the radiation) for specific types of experiments ranging from small and wide angle X-ray scattering to infrared spectroscopy or circular dichroism.

7.4.2.2 Brief history of synchrotron radiation

Synchrotron radiation is radiation emitted from charged particles spiralling around magnetic field lines (Thompson, 2001). Synchrotron radiation as a natural phenomenon is ancient. The light that we observe from the Crab nebula is produced by this process. The first observed production of synchrotron radiation from a man made source was in 1947 at General Electrics (G.E.) 70 MeV synchrotron (Thompson, 2001 and Lewis, 1997). The G.E. synchrotron was not fully shielded and the electron tube used was transparent, permitting a bright arc of light to be observed. Initially the experiments using synchrotron radiation were "parasitic" using the radiation produced by machines that were operated for other experiments. The first and second generation of synchrotron light sources were dedicated machines to harness the radiation produced by the "bending magnets" of an electron storage ring. The Daresbury Laboratory synchrotron radiation source (SRS) (Figure 7.9) was the first machine designed and dedicated to produce synchrotron radiation for research, the first experiments using the dedicated 2 GeV storage ring at the SRS began in 1981. Currently the major synchrotron facilities are third generation machines using not only bending magnet radiation but insertion devices, large magnets added into the straight sections between bending magnets to causes the electrons to deviate along a sinusoidal path and produce more intense radiation. There are more than 50 synchrotron facilities worldwide dedicated to producing and using synchrotron radiation for scientific research for many different fields from materials science and crystallography to environmental science and medical imaging.

Figure 7.9 Daresbury Laboratory synchrotron radiation source and experimental hall buildings
Picture reproduced with permission of photographer (Dr S. Wilkinson)

7.4.2.3 Basic design of a synchrotron

At the heart of all synchrotrons is an electron storage ring, a quasi-circular orbit of electrons travelling at relativistic speeds. The electron beam circulates in a high vacuum chamber to prevent losses due to collisions between electrons and other particles. The vacuum chamber is constructed from multiple straight sections, each connected with a bend where a bending magnet diverts the path of the electron beam so that it travels along the next straight section. The total angle of all the bends in the storage ring is set to be 2π radians (360°), ensuring that the output trajectory from the final bend returns the beam to the input trajectory of the first bend, allowing the electrons to travel around the ring in a closed orbit.

7.4.2.4 Synchrotron radiation from bending magnets

Bending the trajectory of the electrons requires a force (produced by bending magnets). Electromagnetic radiation is produced when an electric charge such as an electron is accelerated and its intensity is proportional to the magnitude of the acceleration.

7.4.2.5 Synchrotron radiation from insertion devices

Insertion devices (wigglers or undulators) are magnets, or more specifically an arrangement of magnetic dipoles placed on a straight section of the storage ring. The arrangement of the dipoles causes the path of the electron beam to be diverted in a sinusoidal path, the entry and exit trajectories of the electron beam have to be identical in order that the insertion device has no adverse effect on the electron orbit. As with the bending magnets the electrons are being accelerated and so produce synchrotron radiation. The advantage of the insertion device is that the number of poles, the period between poles and the magnetic field strength can be varied. The variations allow the insertion devices to be optimised to produce the maximum intensity of radiation at the wavelengths required, as well as being able to optimise the size of the fan of radiation produced.

7.4.3 Conventional X-ray radiation production

7.4.3.1 Summary

Since their discovery in 1895 X-rays have become vital for medical diagnostics and a valuable research tool for the scientific community. Conventional sources use the interaction of electrons with a target metal to release energy in the form of X-rays. The spectrum of the X-rays emitted is different depending on the elemental composition of the metal target.

7.4.3.2 Brief history of conventional X-ray radiation production

The discovery of X-rays is credited to Professor Wilhelm Conrad Roentgen in 1895. He called the emissions he observed X-rays because of their mysterious nature. The use of X-rays for scientific research was quickly adopted, X-ray diffraction quickly developed followed by X-ray spectroscopy leading to advances in material science. But no where is the use of X-rays more apparent than in the medical field. X-ray imaging has been a valuable diagnostic tool since 1900 (Imaginis.com, Milestones in medical diagnosis) when widespread implementation of imaging the chest using X-rays allowed early detection of tuberculosis. Since 1900 the imaging modalities available have been improved, modern clinicians still use X-ray attenuation images for diagnosing broken bones and breast cancer screening, but also have access to use computed tomography and contrast enhancement when required.

7.4.3.3 Basic design of a conventional X-ray tube

Electrons are accelerated from a cathode towards the target metal anode. The incident electron beam interacts with the electrons and the nuclear field of the target metal producing heat and X-rays. If the incident electrons of the beam interact with outer shell electrons of the metal target the kinetic energy of the incident electron is converted to infra red radiation (heat). Over 95% of the electron interactions will occur with outer shell electrons producing heat leaving less than 5% to produce X-rays. This means X-ray tubes are an inefficient way of converting electrical energy into X-rays.

The intensity of the X-ray beam is proportional to the kinetic energy and the current of the incident electron beam. Greater kinetic energy increases the intensity of the X-rays produced and is achieved by increasing the potential difference between the cathode and anode. Increasing the current results in more electrons in the beam,

therefore there will be a greater number of interactions, resulting in a greater intensity of X-rays being produced.

7.4.3.4 Characteristic radiation

Characteristic radiation is the result of an interaction of an incident electron with an electron from the inner shell of the target metal. It is termed characteristic as the energy spectrum of the radiation produced is characteristic of each element used as a target. The mechanism of X-ray production is when the interaction occurs, enough energy is transferred to the inner shell electron to eject it from its orbit ionising the metal atom. The ionised state for the metal is unstable and so one of the outer electrons will fill the space resulting in a corresponding release of electromagnetic radiation (fluorescence) in the form of an X-ray photon. The energy of the photon which is released is equal to the difference in energy between the shell the electron changed from and the shell it changed to, for instance the X-ray energy of copper kα radiation is 8.047 keV. The difference in the electron shell energy is identical for all the atoms of that metal, multiple interactions emitting X-rays with specific energy results in greatly increased X-ray intensity at the characteristic energies of the target metal. The electron biding energies are different for each metal and so the associated peaks of intensity in the X-ray spectrum are different for each metal.

7.4.3.5 Bremsstrahlung radiation

In a rare 0.5 % of interactions, an electron comes in close proximity to the nucleus of a target atom and experiences attractive forces due to the positive charge of the protons in the nucleus (Seibert, 2004). The attractive electrostatic forces of the nucleus cause the incident electron to deviate from its path and alter its kinetic energy. The difference in the kinetic energy pre and post interaction is released as X-rays and termed bremsstrahlung (a German word which translated means breaking radiation).

The bremsstrahlung is emitted as a continuous spectrum. The maximum energy of the bremsstrahlung is equal to the maximum energy of the incident electron (the electron was stopped by the interaction and all its kinetic energy was transferred to a single X-ray photon). The maximum intensity of the bremsstrahlung occurs at approximately one third of the maximum energy. The intensity of the bremsstrahlung decreases rapidly at lower energies and is almost 0 below 5 keV.

7.4.3.6 Spectrum from conventional X-ray sources

The observed spectrum for an X-ray tube is the combination of the mono-energetic spikes of the characteristic radiation superimposed over the bremsstrahlung. By altering the target material and adjusting the voltage and current of the electron beam the output can be optimised for use in dedicated equipment.

7.4.4 Comparison of synchrotron and conventional X-ray radiation

7.4.4.1 Intensity

The intensity of a radiation source is given in terms of its brightness, which defines the number of photons per unit area of the radiation source per unit solid angle of the radiation cone per unit spectral bandwidth. The lowest intensity of the sources of X-rays is bremsstrahlung with a flux of approximately $5x10^{10}$ photons s^{-1} mm^{-2} $mrad^{-2}$ 0.1%b.w.$^{-1}$ (Figure 7.10). A decade higher is the characteristic radiation of a conventional source with a flux of approximately $5x10^{11}$ photons s^{-1} mm^{-2} $mrad^{-2}$ 0.1%b.w.$^{-1}$. The bending magnets provide greater flux up to $10x10^{13}$ photons s^{-1} mm^{-2} $mrad^{-2}$ 0.1%b.w.$^{-1}$ and the wigglers have the greatest flux at over $10x10^{14}$ photons s^{-1} mm^{-2} $mrad^{-2}$ 0.1%b.w.$^{-1}$ depending on the design.

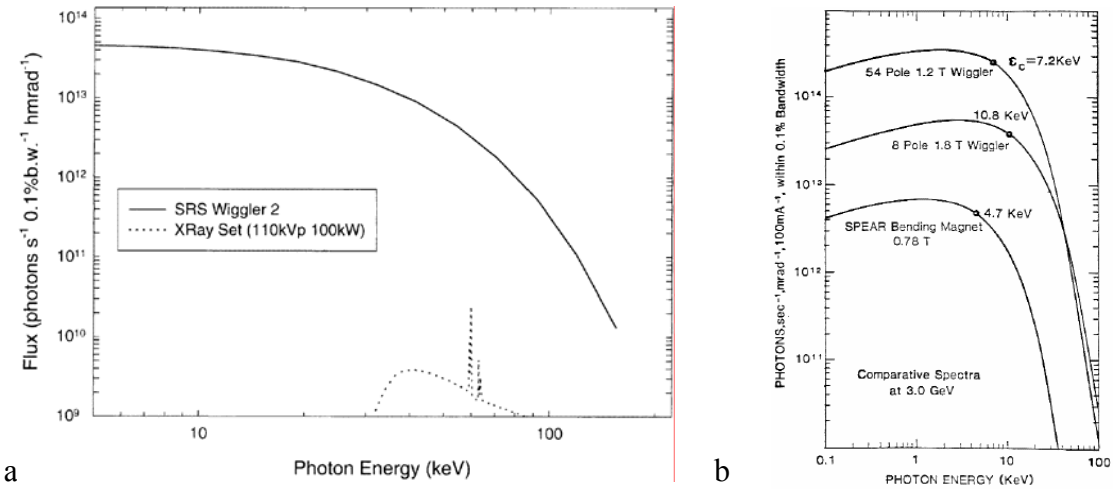

Figure 7.10 Comparison of X-ray sources

(a) Comparison of a wiggler and a conventional X-ray source (Lewis, 1997).

(Reproduced with permission of IOPP and author)

(b) Comparison of the different radiation sources at Stanford synchrotron radiation laboratory

(Reproduced with permission of the Stanford synchrotron radiation laboratory website author)

7.4.4.2 Energy

The energy range accessible by synchrotron radiation is broad band at high intensity, the bremsstrahlung of conventional sources is also broad band but at comparatively low intensity. The mono-energetic spikes of the characteristic radiation provide intensities between the bremsstrahlung and synchrotron radiation sources. However, different target metals are required to access different energies, with a finite set of energies available from appropriate metal elements.

7.4.4.3 Divergence

Due to the way synchrotron radiation sources produce radiation (naturally formed in beams) there is only minimal divergence in the vertical direction. The divergence in the vertical direction is dependant on the machine parameters and is quoted as:

$$\text{Vertical divergence} = 1/\gamma \qquad \textbf{Equation 7.1}$$

Where

γ = electron energy (in storage ring) MeV / electron rest energy (0.511 MeV)

Equation 7.2

Therefore for the synchrotron radiation source (SRS) at Daresbury Laboratories, which is a 2 GeV storage ring $\gamma = 3.91 \times 10^3$ and therefore the divergence in the vertical direction is 2.56×10^{-4} radians.

For synchrotron experiments the horizontal divergence is generally low and is dependant on the size of the magnets, the distance from the source and the size of slits used. However, with conventional sources the X-rays radiate spherically from the point of emission, resulting in a large divergence. The radiation is emitted isotropically hence the intensity will reduce rapidly with increasing distance.

7.5 The interaction of X-rays with matter

7.5.1 Overview

Not all X-ray photons passing through matter will interact, some proportion of the photons may pass through without interaction, depending on the attenuation properties of the matter. X-ray photons which do interact with matter are ether scattered or absorbed dependant on the nature of interaction.

7.5.2 Photon interactions with electrons

Consider X-ray photons passing through a sample of matter. Many of the X-ray photons will pass through the sample unaffected and some of the X-ray photons will interact with electrons within the sample. When an X-ray photon interacts with an electron some of the photon's energy may be transferred, the energy of the scattered photon is reduced and its wavelength is increased (called the Compton effect). The change in wavelength generally does not exceed more than a few percent of λ for the

wavelengths used in experiments and is proportional to the amount of energy which is transferred to the electron according to the relationship.

$$E=hc/\lambda$$

Equation 7.3

E is the energy of the X-ray photon.

c is the speed of light in a vacuum ($3x10^{8}$ m s^{-1}).

h is Planck's constant($6.6x10^{-34}$ J s).

λ is the wavelength of the X-ray photon.

X-rays scattered elastically with no change in wavelength are termed coherent. Coherent scattering from electrons preserves the phase of the X-rays. X-ray crystallography utilises the interference caused by coherently scattered X-rays from ordered arrangements of electrons to investigate structure. X-rays scattered with resultant changes in their wavelength are incoherent, interference does not occur. Compton scattering is ignored in angular dispersive scattering experiments.

7.5.3 Interaction as an electromagnetic wave

When observing interference effects X-rays should be considered as electromagnetic waves rather than particles.

Consider an electromagnetic wave, its plane of propagation (X) and the plane of oscillation of the electric vector (Y). An electron in the path of the wave, due to its electric charge, will oscillate in the plane of the electric vector (Y). As accelerating charges are the source of electromagnetic radiation, the oscillating electron acts as a source, emitting waves of the same frequency as the incident wave in all directions; thus the electron is considered to scatter the incident wave.

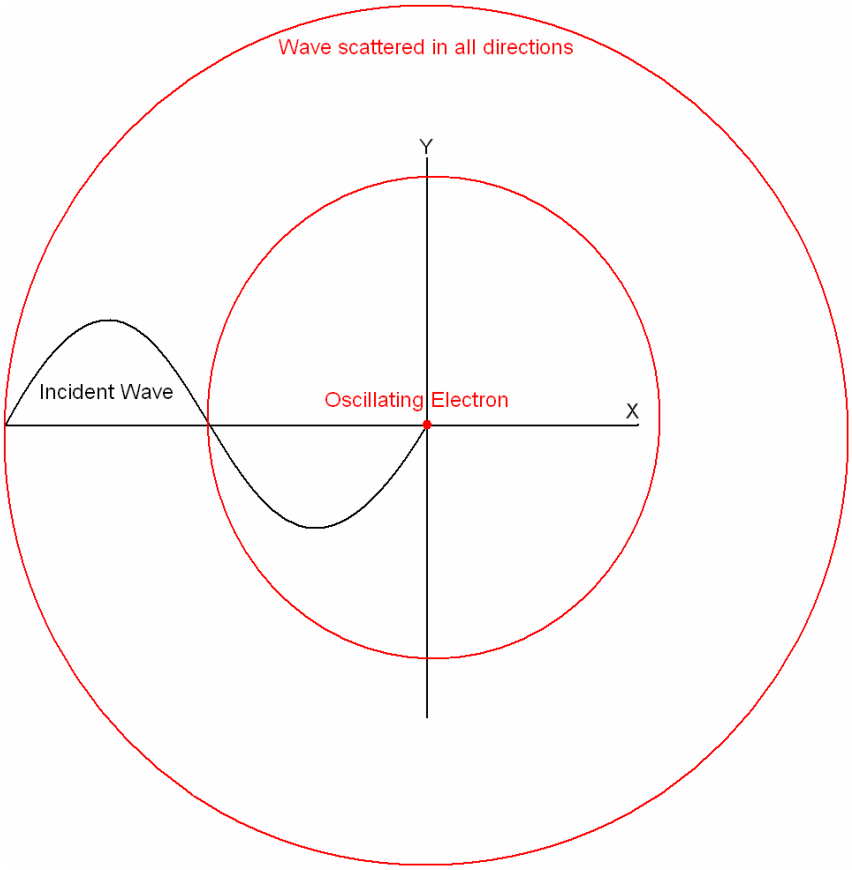

Figure 7.11 Diagram showing scattered wave propagates in all directions

The intensity of scatted X-rays at an arbitrary point can be calculated using the following formula.

$$I_s = I_o(\mu_o/4\pi)^2(e^4/m^2R^2)\sin^2\phi_Y$$

Equation 7.4

I_s = Observed Intensity

I_o = Incident Intensity

μ_o = Permeability of free space ($4\pi x10^{-7}$ N A^{-2})

e = Charge on an electron ($-1.6x10^{-19}$ C)

m = Mass of electron ($9.1x10^{-31}$ kg)

R = Distance to observation point

ϕ_Y = Angle in radians between observation point and oscillation axis (Y)

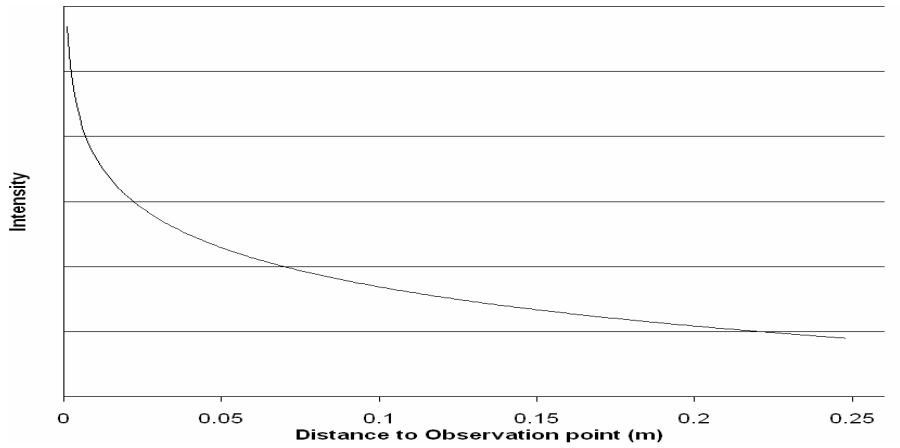

Figure 7.12 Plot of observed intensity of scattered X-rays with increasing distance

As the distance to an arbitrary observation point increases the observed intensity at this point reduces rapidly. The maximum intensity observed with angle is in the plane of propagation of the incident wave (x, equal to $n\pi/2$). The intensity decreases in a sinusoidal manner with angle to the minima perpendicular to the plane of propagation, which is the plane of oscillation of the electric vector (Y, equal to $n\pi$).

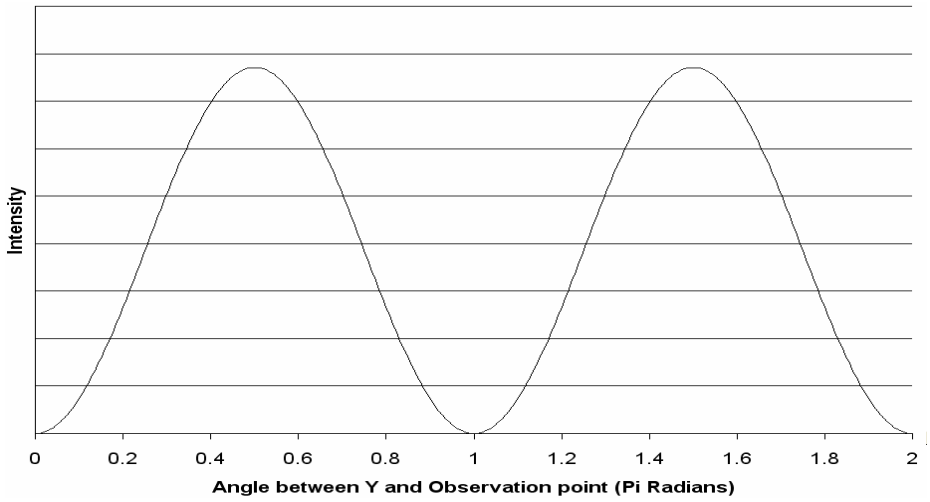

Figure 7.13 Plot of observed X-ray intensity with angular position

All electrons in the irradiated area will emit X-rays at the same wavelength of the interrogating beam and all in phase. If there is a repeating formation to the electrons interference will occur resulting in maxima and minima related to the wavelength of the X-rays and the distance between the repeating formations.

7.6 X-ray scattering

7.6.1 Overview

X-ray scattering from real systems on a molecular level, involves assemblies of many atoms interacting with the incident X-rays simultaneously. The oscillating electrons in the assemblies emit X-rays which are in phase when emitted. The distance the electrons are separated results in a difference in path length between each electron and any given point of observation. A difference in path length results in a phase difference between the emitted waves. Measuring the intensity over a range of observation points provides a modulation of intensity with position that relates to the wavelength of the X-rays and to the separation of the electrons. As the wavelength is known the observed intensity modulations can be used to determine the separation of the electrons, the basis of X-ray scattering measurements.

7.6.2 Phase difference

Consider two electrons separated by a vector $\underline{r}$, parallel X-rays incident on the electrons with vector $\underline{k}_i$, will be scattered by the same angle (see Figure 7.14). The scattered X-ray is defined by the vector $\underline{k}_f$.

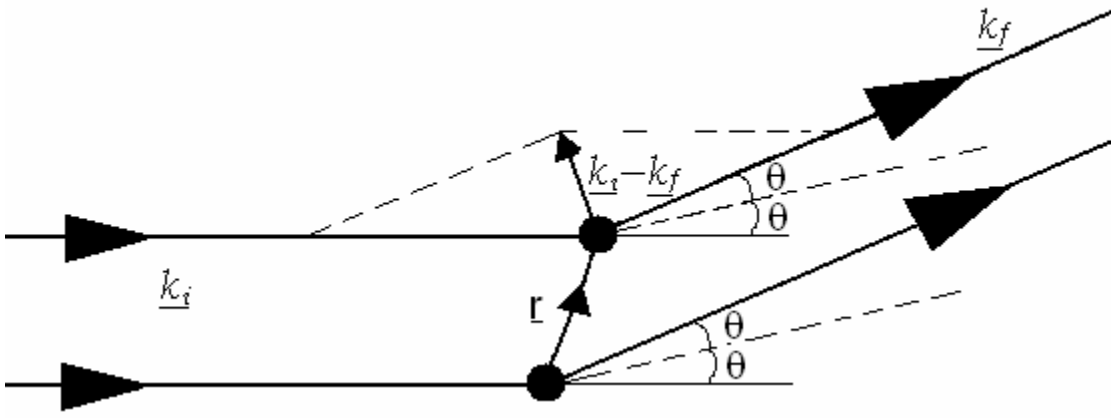

Figure 7.14 Representation of a simple scattering system

There will be a difference in the path lengths between waves scattered by each of the electrons separated by $\underline{r}$ and can be shown as (Hukins, 1981):

Path Length Difference = $\underline{r}.\underline{k}_i - \underline{r}.\underline{k}_f$ **Equation 7.5**

Path Length Difference = $\underline{r}.(\underline{k}_i - \underline{k}_f)$ **Equation 7.6**

To express a path length difference as a phase difference in radians:

Phase Difference = $(2\pi/\lambda)$ (Path Length Difference) **Equation 7.7**

Therefore:

Phase Difference = $(2\pi/\lambda)\ \underline{r}.(\underline{k}_i - \underline{k}_f)$ **Equation 7.8**

As the scattering vector $\underline{Q}$ is defined as:

$\underline{Q} = (2\pi/\lambda)\ (\underline{k}_i - \underline{k}_f)$ **Equation 7.9**

Thus the phase difference can be simplified to:

Phase Difference = $\underline{r}.\underline{Q}$ **Equation 7.10**

7.6.3 Intensity of scattered X-rays

If $\rho(\underline{r})$ is the electron density of a scattering volume the number of electrons in the volume element will be $\rho(\underline{r})\delta\underline{r}$. If the scattering volume is sufficiently small so that the scattered X-rays are all from the same position and hence will have the same phase. In this case the amplitude scattered A_s is (Hukins, 1981):

$$A_s = \rho(\underline{r})\delta\underline{r}\ A_0 P^{0.5}(\mu_o/4\pi)(e^2/mR)$$ **Equation 7.11**

A_0 = Amplitude of incident X-ray beam

P = Polarisation factor

R = Distance to observation point

Scattering from larger volumes where phase differences result in interference, may be represented by:

$$A_s = \rho(\underline{r})\delta\underline{r}\ A_0 P^{0.5}(\mu_o/4\pi)(e^2/mR)\ \exp(i\ \underline{r}.\underline{Q}) \qquad \textbf{Equation 7.12}$$

An X-ray scattered through an angle by a scattering body is then given by:

$$F(\underline{Q}) = A_0 P^{0.5}(\mu_o/4\pi)(e^2/mR)\int \rho(\underline{r})\ \exp(i\ \underline{r}.\underline{Q})\ d\underline{r} \qquad \textbf{Equation 7.13}$$

The limits of integration are over the entire volume of the scattering body.

This equation can be simplified by ignoring the effect of polarisation (as if P is sufficiently different from unity the data is generally corrected to remove its effect). μ_o, 4π, e and m are constants, A_0 and R are scaling factors so all may be ignored. Thus the simplified, normalised equation describing both the amplitude and phase of the scattered wave can be written:

$$F(\underline{Q}) = \int \rho(\underline{r})\ \exp(i\ \underline{r}.\underline{Q})\ d\underline{r} \qquad \textbf{Equation 7.14}$$

The amplitude of the scattered wave is the Fourier transform of the electron density (ρ) of the scattering body.

7.6.4 The phase problem

To determine the electron density (ρ) of the scattering body, it would appear that the inverse Fourier transform of F(Q) integrating over all space could be used (Hukins 1981):

$$\rho(\underline{r}) = \int F(\underline{Q}) \exp(i\, \underline{r}.\underline{Q})\, d\underline{Q} \qquad \textbf{Equation 7.15}$$

Unfortunately F(Q) is a complex number and only the amplitude and can be determined experimentally. Without the associated phase the direct mathematical solution to this problem is invalid. The reason for the loss of the phase information is the time period of the oscillation of the electric vector of the X-ray. Assuming the scattered X-rays have a wavelength 1.5×10^{-10} m the frequency will be approximately 2×10^{-18} s. In order to measure the phase to within a fifth of a cycle measurement times of around 4×10^{-19} s are required, which is beyond current detection capabilities.

7.6.5 What is observed in an X-ray scattering experiment

The intensity of scattered X-rays at particular angles is the observed variable. For a wave represented by the complex number F(Q) the observed intensity I(Q) is (Hukins 1981):

$$I(\underline{Q}) = F(\underline{Q})\, F^*(\underline{Q}) = \int P(\underline{r}) \exp(i\, \underline{r}.\underline{Q})\, d\underline{r} \qquad \textbf{Equation 7.16}$$

Where F* is the complex conjugate of F.

Therefore the observed intensity is the Fourier transform of the autocorrelation function P(r) of the electron density (ρ) of the scattering body.

The autocorrelation function describes the vectors (distance and direction) between all scattering objects in the scattering volume. All the vectors in the autocorrelation function are represented from the same origin and therefore can only describe the relative separations of the scattering objects not their positions (See Figure 7.15 and Figure 7.16). The inverse transform of F(Q) F*(Q) yields the autocorrelation function P(r) of the electron density (ρ) of the scattering body, also known as the Patterson function. The determination of simple structures can be aided using the Patterson function. For large structures the number of vectors produced makes the use of the Patterson function impractical and indefinite due to the likelihood of multiple solutions.

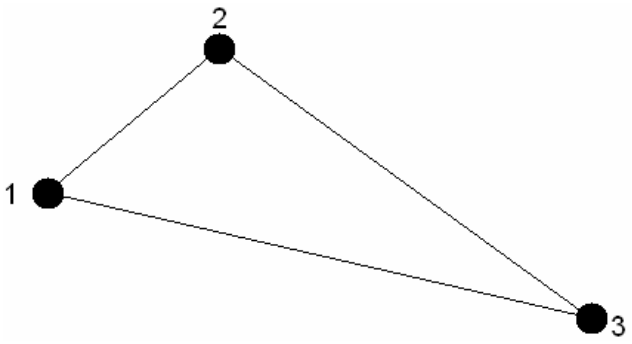

Figure 7.15 A simple scattering system

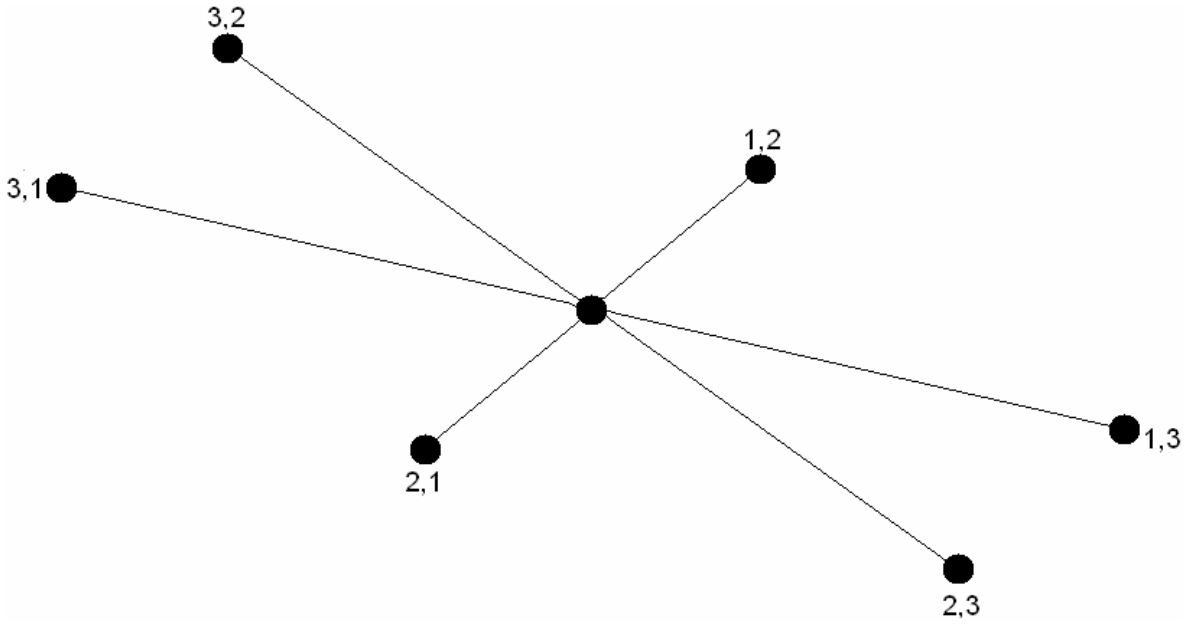

Figure 7.16 The autocorrelation/Patterson function of the simple scattering system

7.7 Interpretation of X-ray diffraction data

7.7.1 Overview

The electron density function of the scattering volume cannot be directly recovered from the diffraction pattern due to the phase problem (see Section 7.6.4). However, indirect methods have been developed in crystallography to solve structures. A model of the scattering system can be built from prior knowledge of the system using computer software. The results of the diffraction experiments can be compared to the Fourier transform of the model, the model can be refined in an iterative process until the comparison shows the model matches the experimental data adequately. In complex biological systems such as tissues, as there is usually not enough prior knowledge upon which to base a model. However, simple models of the major components may be used along with other techniques, to provide information about the size and shape of scattering objects, the spacing of ordered structures and orientation of the scattering structures within the system.

7.7.2 Orientation

X-ray scattering provides information regarding the spacing between ordered scattering objects and their orientation. For aligned collagen fibres the scattering axis is identified by the meridian (Bragg) peaks (See Figure 7.17) which relates to the gap overlap spacing of collagen. Equatorial (Bessel) peaks relate to the diameter of the collagen fibrils and their packing.

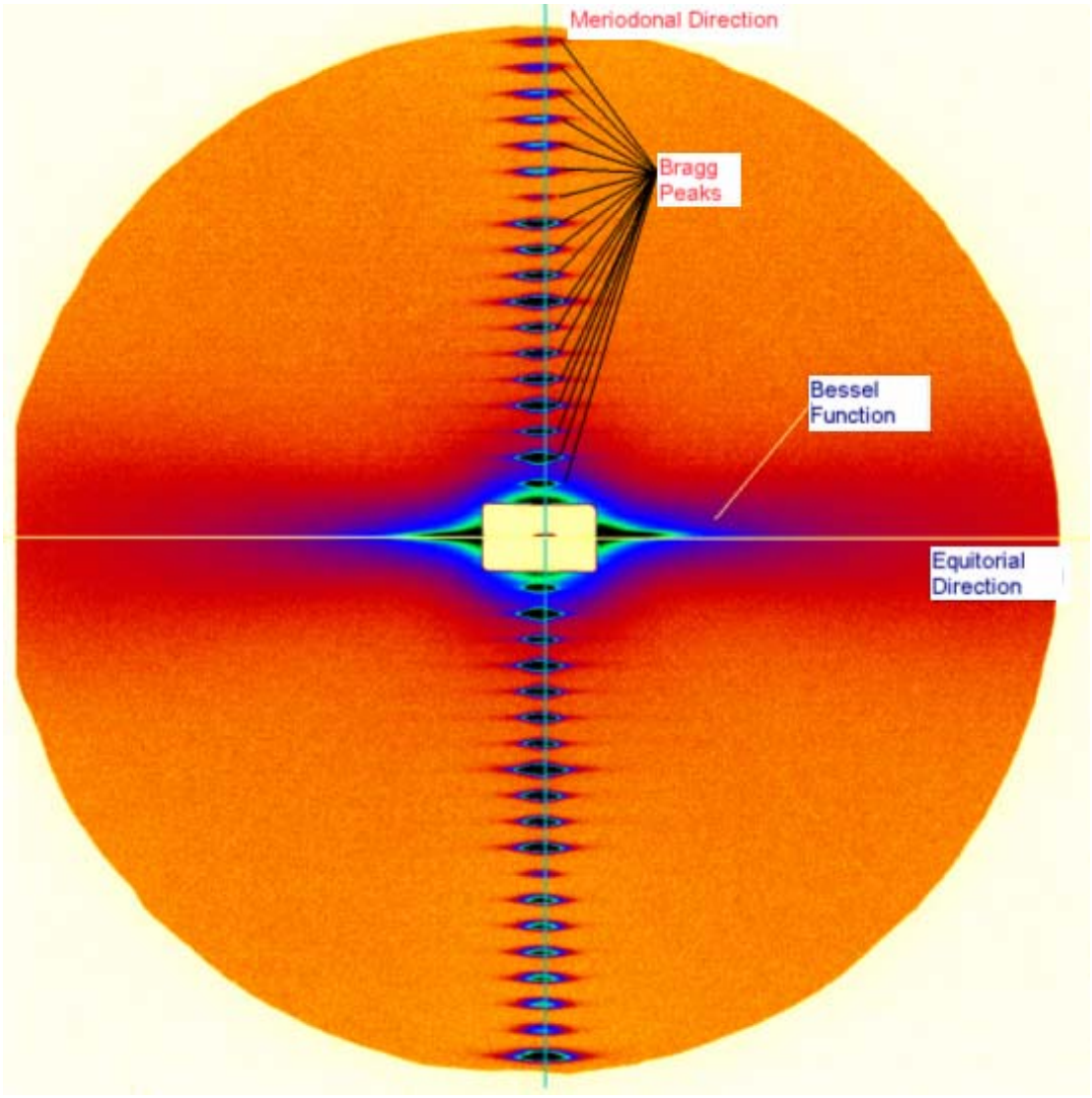

Figure 7.17 X- ray scattering pattern from rat tail tendon meridian and equatorial directions

The X-ray scattering pattern for a sample of rat tail tendon (type I collagen) with peaks showing the preferred orientation in the vertical direction.

If there is some variation of the orientation, peaks are observed at other positions in the scatter pattern relating to the vertical axis for each orientation in the sample. The observed pattern from a distribution of orientations appears as arcs along a line of equal spacing with a length proportional to the variation of the orientation. If there is no preferred orientation i.e. there are orientations in all directions, the peaks appear as rings on the detector (Figure 7.18). Changes in the preferred orientation perpendicular to the plane of the detector manifest as a reduction in peak intensity, but can be determined by altering the plane of the sample with respect to the detector.

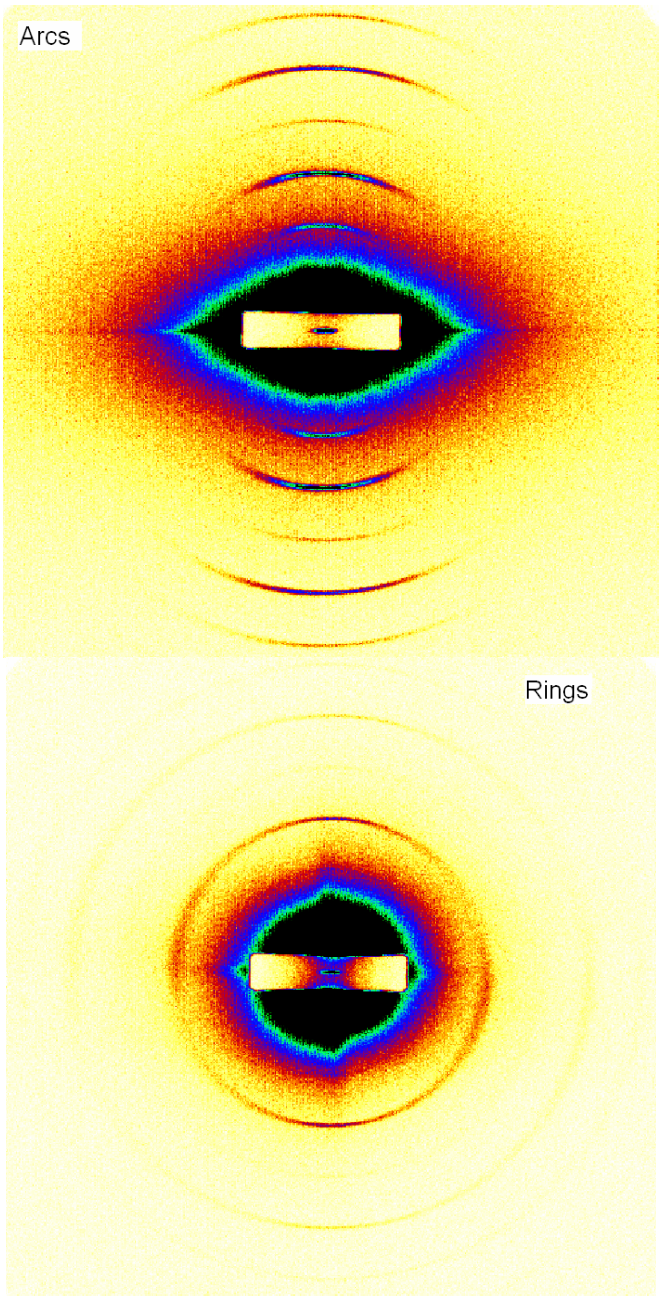

Figure 7.18 Variation in preferred orientation of rat tail tendon

7.7.3 Spacing information

7.7.3.1 Bragg's law

Bragg's law gives the condition for constructive interference of scattered radiation from an ordered structure, relating the wavelength of the incident X-ray beam to the angle of constructive interference for a given periodicity (Hukins, 1981 and Fernandez, 2004).

$$\lambda = 2D \sin\theta$$

Equation 7.17

Where:

λ = the wavelength of incident X-rays.

D = the periodicity of the order within the scattering structure.

θ = the angle between the incident and scattered X-ray beams.

Scattering data is generally presented by relating the observed intensity to the modulus of the scattering vector $\underline{Q}$:

$$\underline{Q} = \underline{k_i} - \underline{k_f}$$

Equation 7.18

For elastic scattering the modulus of both the incident vector (k_i) and the scattered vector (k_f) are equal:

$$\underline{k_i} = \underline{k_f} = 2\pi/\lambda$$

Equation 7.19

The directions of the vectors differ by the scatter angle 2θ, so the modulus of the scattering vector can be described as:

$$Q = (4\pi/\lambda) \sin\theta$$

Equation 7.20

Alternatively the data may be expressed using S:

$$S = Q/2\pi = 2 \sin\theta/\lambda$$

Equation 7.21

Diffraction maxima at observed values of Q or S can be related to the spacing between ordered scattering objects D using Bragg's law:

$$D = \lambda/2 \sin\theta = 2\pi/Q = 1/S$$

Equation 7.22

7.7.3.2 Bessel Functions

Scattering from cylindrical structures results in diffraction maxima related to their diameter, the distance between the cylinders and their degree of order. The maxima appear in the form of Bessel functions which oscillate as a sine wave damped with increasing S. The position of the first maxima is dependant on the order of the Bessel function and the diameter of the scattering objects. Layer lines which are a series of maxima offset from the equatorial axis of the diffraction pattern, may be observed for highly ordered systems. The maxima observed on the equator are the first order Bessel functions. The diameter of scattering objects that give rise to these maxima can be determined from the Bessel functions (Eikenberry, 1982). Assuming the subsidiary maxima after the innermost maximum arise solely from the fibril transform, then:

$$A = 5.14/\pi Q_1$$

Equation 7.23

$$A = 8.42/\pi Q_2$$

Equation 7.24

Where:

A = the diameter of the scattering object

Q_1 = the first subsidiary maxima

Q_2 = the second subsidiary maxima

7.7.4 Variation in Bragg spacing

As the position of the X-ray scattering maxima are related directly to the spacing, so the variation of the spacing within the scattering volume affects the shape of the maxima. For a small distribution of spacings the X-ray scattering peak would show a maximum at the average spacing and would reduce in intensity away from the maximum dependant on the distributions of the spacings. A biological sample such as collagen will have a normal distribution of axial spacings around the mean so the observed X-ray scattering peaks appear approximately Gaussian. As the distribution of spacings increases, so the width of the X-ray scattering peak increases and the peak height decreases, thus the ratio of peak height to peak width at half height of the maxima can be used to indicate the degree of the spacing variation.

7.7.5 Radius of gyration

The radius of gyration is a similar concept to the moment of inertia, but the electron density rather than the mass density is used as the weighting. The radius of gyration represents the second moment of the distribution of the size and shape about the mean.

One can write the equation to describe the beginning of the scattering curve where S is close to 0 (Feigin, 1987).

$$I_{(s)} = I(_0)\exp(-S^2R_g{}^2/3)$$

Equation 7.25

Taking the natural logarithm of Equation 7.25 gives

$$\ln I_{(s)} = \ln I(_0) - S^2R_g{}^2/3$$

Equation 7.26

Thus R_g^2 can be obtained from the slope of the linear part (at low S) of the ln $I_{(s)}$ versus S^2 plot (the Guinner plot) and therefore R_g can be determined.

An accurate value of R_g can be determined provided that all the scattering objects are identical and at low concentration so that there is no inter-particle interference or aggregation (monodisperse solutions). In the case of tissues this is not true and the value of R_g obtained provides an estimate of the average R_g for all of the scattering objects in the scattering volume with dimensions from a few nanometres to many tens of nanometres.

7.7.6 Porod's Law

The intensity of scattering $I_{(s)}$ at larger values of Q follows Porod's law (Porod, 1951):

$$I_{(s)} = 2\pi(\Delta\rho)^2 S_{(a)}/Q^4$$

Equation 7.27

$\Delta\rho$ = the difference in the electron density between the scattering objects and the surrounding medium (i.e. the contrast)

$S_{(a)}$ = the surface area of the scattering objects per unit mass

Using the Porod plot $I_{(s)}Q^4$ against Q^4, the theoretical observed intensity tends towards a constant. However, in practice the desired X-ray scattering profile is superimposed over flat background. The gradient at larger Q values in the Porod plot is numerically equal to the flat background, allowing it to be calculated and subtracted (see Section 8.2.1.5).

7.7.6.1 Dimensionality

The dimensions of a scattering object result in scaling differences to Porod's law. The dimensionality can be described such that a rod is 1 dimensional and a disk is 2 dimensional resulting in a power law decay of Q^{-1} and Q^{-2} respectively (Porod, 1951). Particularly relevant to the scattering observed from collagen is the result for polymer chains, locally rod like structures which are coiled over large distances giving Q^{-2} or $Q^{-5/3}$ (Porod, 1951).

7.7.7 Determination of power law exponent

The power law values are the gradient of linear sections on ln $I_{(s)}$ versus ln Q plots and appear at large values of Q in the SAXS regime. Power law decays begin and end with exponential regions that appear as knees in the data and there may be multiple power law decays visible. The exponential knees reflect the preferred size of the scattering objects by (Beaucage, Analysis Chapter 8):

$$r = 1/Q$$

Equation 7.28

7.8 Experimental effects on the X-ray scattering pattern of collagen

7.8.1 Amount of scattering material in sample

7.8.1.1 Sample cross section

The intensity of the observed scattering pattern is dependant upon to the intensity of the interrogating X-ray beam and the scattering volume of the sample. Therefore if the sample volume is reduced, for the same cross section of beam there will be less scatter.

7.8.1.2 Sample thickness

Increasing the sample thickness provides a greater scattering volume given the same cross section. However, increasing the volume will also increase attenuation. If the increase in attenuation is greater than the increase in scatter, the observed intensity will decrease. Using equation 7.11 (page 30) and the electron density of water (3.343×10^{23} g^{-1}) the intensity of scatter from varying thicknesses of water can be obtained. Equation 7.29 was used to calculate the percentage transmission through varying thicknesses of water. By combining the results of the scatter intensity and the transmission, the scatter after attenuation can be found for increasing thickness of samples (Figure 7.19). The maximum observed scatter for water at 10 keV is at approximately 2 mm. Maxima for other materials will depend on their mass attenuation coefficient, electron density and X-ray energy.

$$I = I_o \exp(-MAC\rho x)$$

Equation 7.29

ρ = absorber density (1.0 g/cm^3)

x = absorber thickness (cm)

MAC = mass attenuation coefficient (5.18 cm^2/g at 10 keV)

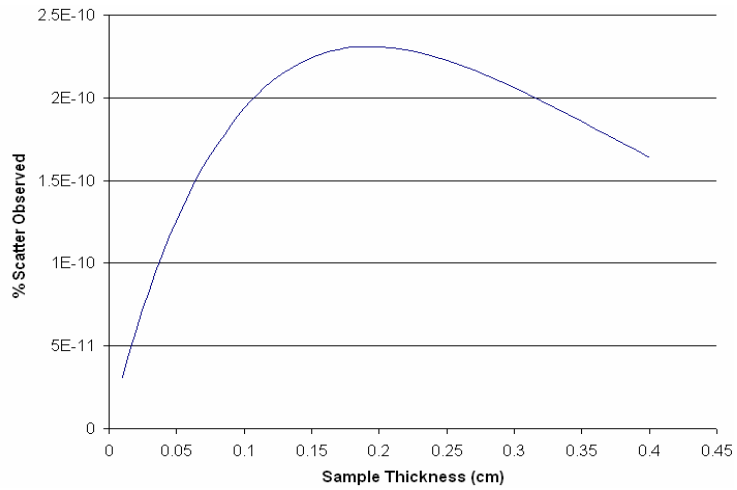

Figure 7.19 Percentage scatter observed after attenuation from water at 10keV

As sample thickness increases so does the percentage scatter. However, attenuation also increases reducing the observed intensity. The maximum scatter can be observed for water at 2mm for 10keV X-rays.

7.8.2 Dehydration

The bond of water to proteins is very important in determining the three dimensional structure. There is unbound water present around most proteins which acts as a lubricant between adjacent proteins. Water binds to the surface of the proteins and water is required for the hydrogen bonding in the internal bonds between amino acids. Dehydration initially causes a reduction in the unbound water around the proteins and as dehydration progresses water bound to the protein surface will be removed. Intramolecular hydrogen bonding makes a major contribution to protein structure, the presence of water causes the hydrogen bonds to lengthen making the protein more flexible (Fernandez, 2003). The removal of water results in the shortening of the hydrogen bonds. The shortening of the hydrogen bonds results in a contraction of the protein structure leading to increased stability, but also a reduction in the size of the proteins and increased stiffness of the protein structure. Contraction of the structure of collagen can be observed during dehydration using small angle X-ray scattering as a reduction of the D spacing from 67.2 to 64.7 nm upon air drying (Wess, 2000).

Dehydration is not a uniform process and as such there is increased variability in the D spacing of dehydrated collagen. Increased variability in the spacing is observed as a reduction in the degree of order and thus the number of diffraction maxima observed in the scattering pattern, 34 meridional peaks when dry compared with 140 meridional peaks from hydrated collagen (Wess, 2000).

Change in the hydrogen bond lengths caused by the loss of water during dehydration alters the electron density profile within the repeating axial unit cell of the fibril. The change in the electron density profile results in a change in the relative intensities of the diffraction peaks. In hydrated rat tail tendon the odd orders are predominantly

stronger than the even orders However, in dry rat tail tendon this relationship is altered and the even orders are predominantly stronger (Table 7.8.1).

	Hydrated		Dry	
Order	Spacing D(Å)	Intensity	Spacing D(Å)	Intensity
1	670	Very Strong	650	Very Strong
2	335		325	Strong
3	223	Strong	216.6	Strong
4	167.5		162.5	
5	134	Strong	130	
6	11.6		108	Strong
7	96		93	
8	84		81	Strong
9	74	Strong	72	Strong
10	67		65	
11	61		59	
12	56	Strong	54	Strong

Table 7.8.1 Spacing and intensity for hydrated and dry rat tail tendon

(Compiled from SRS Station 2.1 user information)

7.8.3 External Force

It is known that application of tension (Fratzl, 1997) affects the D spacing and peak intensity of collagen. The effects of tension on the fundamental molecular structure of collagen have been investigated wide angle X-ray scattering to determine the changes in the d spacing (Sasaki, 1996a). This work was continued (Sasaki, 1996b) by determining the contribution to the elongation of the sample by three differing mechanisms.

These mechanisms are:

1. Molecular elongation (strain).
2. Increase in gap region between longitudinally adjoining molecules along the fibre axis.
3. Relative slippage of laterally adjoining molecules along the fibre axis.

Their results showed that a strain of up to 4 % could be produced by the application of stresses up to 20 MPa. By comparing the changes in relative intensities of the 2nd and 3rd order peaks using SAXS between 0 % and 2 % strain they determined that 1.7 %

of the elongation was caused by strain and the other 0.3 % was caused by a combination of the other two modes. Further investigation attempted to clarify the relationship between molecular events that cause D spacing changes (the staggered overlap and gap regions in the fibrilar structural level in type I collagen) and applied force using SAXS (Sasaki, 1999). The results showed that the contribution from modes 2 and 3 were negligible at average stresses below 8 MPa. Average stresses above 10 MPa were required to cause a significant contribution by modes 2 and 3. Also at strains below the 8 MPa threshold no creep or time dependant properties were noted.

An investigation into the time dependant properties of collagen (Perslow, 1998) showed results for stresses of 0.01-0.05 MPa. No time dependant properties could be observed within this range, which agrees with other literature on the subject (Sasaki, 1999). This work was carried out on skin samples rather than tendon and showed an increase in scattered intensity after the application of the pre-strain and was attributed to the force causing some alignment of the network of collagen fibres in the samples.

7.8.4 Temperature

7.8.4.1 Experimental temperature

To quantify the thermal stability of the triple helix structure of a given collagen the term T_{melt} is used. At the temperature T_{melt} the viscosity is reduced to a level where changes in optical rotation properties can be observed. These changes are caused by the thermal movements which become larger than the cooperative interactions that stabilize the triple-helix of collagen (Seljee, 2005). The thermal stability of the collagen triple helix varies between types of collagen and is related to the amount of Hydroxyproline present (Privalov, 1982) (see Table 7.8.2).

Sample	Ratio of Proline to Hydroxyproline	T_{melt}	Body temperature
Cod skin	155/1000	16 °C	10-14 °C
Frog skin	174/1000	25 °C	Endothermic
Shark skin	191/1000	29 °C	24-28 °C
Calf skin	232/1000	39 °C	37 °C

Table 7.8.2 Thermal stability information for skin samples from different animals

At temperatures above T_{melt} the collagen helix converts to a random coil (Leikina, 2002**).** Random coil is a term given to polymer conformations where the monomer subunits are orientated randomly with the constraint of being bonded to adjacent units. A random coil is not one specific shape but is a statistical distribution of the shapes of all protein chains in a population of macromolecules. Leikina et al. (2002) also state in contrast to the existing consensus, that type 1 collagen from human lungs and rat tail tendon undoubtedly melt several degrees below body temperature and therefore the thermodynamically favored conformation at body temperature is a random coil. If it was possible to observe the structural difference between the random coil and helix formation using X-ray scattering, it might shown that there are temperature dependant differences between normal and diseased tissues.

7.8.4.2 Storage temperature

As with any biological sample there will be natural degradation by enzymes and bacteria following excision. This process can be slowed by reducing the temperature but even at the temperature of a typical domestic freezer (-15º to -20 ºC) there may still be significant degradation over time. To ensure degradation of the samples is kept to a minimum over time it is necessary to maintain cryogenic temperatures (-80 ºC).

7.8.4.3 Freezing effects

As water freezes it expands, due to the molecular alignment of the ice crystals as they form. The formation of large ice crystals will rupture cells and alter biological structures such as collagen. The size of ice crystals which form is dependant on how

quickly the sample is cooled. If the sample freezes quickly there is less time for the water molecules to align and so only smaller ice crystals can form. However, if the sample is cooled more slowly the water molecules have more time to align and can form larger crystals. As it is the aim to prevent external influences on the structures within the samples, it is beneficial to freeze the samples as quickly as possible i.e. "snap" freezing by complete immersion in liquid nitrogen (-195.8 °C, 77 K). Even using a fast rate of freezing it cannot be assumed the process does not alter the structures, therefore the number of times a sample is allowed to thaw and require refreezing should be kept to a minimum.

7.8.5 Formalin fixation

Fixation by formalin (10 % formaldehyde solution) is a method of preserving tissues, preventing degradation and disinfecting, it is the preferred standard for pathologists. Formaldehyde dehydrates the protoplasm of the cells in the tissue and any bacteria present, replacing the normal fluid in the cells with a gel-like rigid compound, due to coagulation properties of formaldehyde. For the purpose of tissue preservation this is ideal as the formaldehyde disinfects the tissue, provides a rigid gel maintaining cell contours and as the formaldehyde is still present the fixed samples are resistant to further bacteriological attack.

However, the properties that make formalin attractive for tissue preservation for pathologists, cause structural differences in the collagen. Fixation causes an absolute reduction in the D spacing of the collagen fibrils (Fullwood, 1993), though it has been claimed that the relative differences between tissue types were maintained (Fernandez, 2004).

7.9 X-ray scattering for disease diagnosis

A clear difference in scattering has been demonstrated between normal and malignant breast tissue samples using small angle X-ray scattering with synchrotron radiation (Rogers, 1999; Lewis, 2000; Fernandez, 2002, 2004 and 2005) and with conventional X-ray sources (Kidane, 1999; Lazarev, 2000; Poletti, 2002a; Ryan, 2005). Two mechanisms have been suggested to explain the structural differences. Firstly the collagen present around tumours is structurally different from the collagen of normal tissues. Chemically distinct collagen was identified near cancerous tissues which shared characteristics in common with that found in embryonic foetal tissues (Pucci-Minafra, 1993). Also the fibroblasts in cancerous tissues showed foetal like characteristics (Schor, 1988). Secondly an increase in levels of matrix metalloproteinase (MMP) has been observed in tumour tissues (Duffy, 2000) and it was suggested that MMP action could be a possible cause for the reduction in the order of the collagen. Peak intensities in the collagen diffraction peaks for malignant samples were consistently less than those for normal samples (Rogers, 1999; Lewis, 2000). The reduction in the intensity of the diffraction peaks observed in the tumour sample SAXS was attributed to a lower structural order of the collagen within the specimens. Histopathological investigation was used to verify that the scatter pattern changes were not simply due to a reduction in the amount of collagen present in the samples. Lewis et al. (2000) also provided evidence of the reduction of collagen peak intensity at up to 6 cm from the tumour and Fernandez et al. (2004) suggest the increase in surface area of scattering objects is caused by the pealing off of fibrils as the collagen degrades, supporting the hypothesis of MMP action but neither of these observations rule out the possibility of a different form of collagen being produced. Fernandez et al. (2002) supports the different collagen hypothesis by stating that the invasive tumour front is rich in loose newly formed fibrils. The results presented indicate that new formation of different collagen and MMP degradation could both be

occurring within malignant tissues (Rogers, 1999; Lewis, 2000; Fernandez, 2002 and 2004). No conclusions can be draw regarding the cause of the changes without further studies and corroborating evidence.

The results of SAXS from breast tissue suggest that characteristics of the molecular structure may be used as a marker of disease progression. Fernandez et al. (2002) analysed results from different tissues (both healthy and invaded areas of adipose and collagen, as well as necrotic areas) within the samples by using a very small (0.2 by 0.2 mm^2) X-ray beam and related the scatter to physical structures, providing both an insight to the structure of collagen in the invaded tissues and signatures of malignancy which could be used for diagnosis. Lewis et al. (2000) and Rogers et al. (1999) averaged the scatter pattern by oscillating the sample (at a speed of 2 mm per second) through the X-ray beam during the exposure, giving pseudo homogeneous scatter from the whole sample. Lewis et al. (2000) and Rogers et al. (1999) investigated the collagen Bragg peaks to find differences between normal and tumour tissue relating not only the peak intensity to disease state but also showed that an increase in the D spacing indicated the presence of benign disease. Fernandez et al. (2002) reported an increase of 0.3 nm in the D spacing of malignant tissues. However, Fernandez et al. (2002) did not have a normal comparison, the healthy tissue was at distance from the tumour, which although distant is still effected according to the results of Lewis et al. (2000). Fernandez et al. (2002) also found differences in the scattering of the "background" between collagen peaks, stating scattering is stronger from invaded regions indicating an increase in the specific surface area of the scattering objects. Using the scatter from a region where the Porod law applies, between the 5^{th} and 6^{th} collagen peaks, S= 0.08-0.09 nm^{-1} (Fernandez, 2004 and 2005), mapped areas of scatter intensity were compared to histopathological boundaries do indicate changes in tissue type discernable from SAXS.

A large amount of data has been collected using synchrotron radiation (Table 7.9.1). Although Fernandez et al. (2000), (2004) and (2005) have collected over 3000 scatter patterns from a range of pathologies and tissue types all the data comes from only 44 patients and contained no normal samples from disease free patients. The largest single study (Lewis, 2000) contains 43 patients which given the range of differing pathologies manifest in breast cancer is not a significant enough sampling to give accurate sensitivities and specificities for a diagnostic technique. However, all the studies showing differences between diseased and normal tissue are very encouraging and the synchrotron radiation studies have provided evidence for possible causes of the observations.

Author	Year	Patients	Samples	Scattering Images
Rogers	1999	6	12	
Lewis	2000	43	99	
Fernandez	2000	9		636
Fernandez	2004	7		571
Fernandez	2005	28		1893

Table 7.9.1 Number of patients, samples and scattering data collected from synchrotron studies

To enable small angle X-ray scattering of tissue to be used as a diagnostic tool in a clinical environment, the ability to collect data which provides reliable and reproducible markers of disease using conventional X-ray tube sources must be demonstrated. In the past energy dispersive methods have been employed to collect data using conventional X-ray sources (Speller, 1999; Kidane, 1999; Ryan, 2005). Although these studies provided information for scattering in different scatter vector ranges than is observed in the synchrotron studies and cannot be directly compared, distinct differences between tumour and normal tissue types were observed. Angular dispersed studies using conventional sources have provided data for breast tissue in comparable momentum transfer ranges to SAXS (Lazarev, 2000; Poletti, 2002a). Both groups reported differences between the scattering observed from normal and

diseased tissue. However, data was only collected from relatively few samples, 7 normal and 2 cancerous by Poletti et al. (2002a) and Lazarev et al. (2000) studied 4 samples, a normal and a cancerous sample from both the left and right breast of one patient.

To demonstrate SAXS as a viable, rapid diagnostic technique, further studies looking at a wide range of pathologies from a large number of patients is required. The studies need to assess the sensitivity and specificity using a laboratory based X-ray source and taking into account the heterogeneity in the amount of actual diseased tissue in any sample. Further work is also required to understand the cause of the X-ray scattering pattern changes and determine which if any differences observed are caused by new collagen production or MMP action.

7.10 Models which may explain the differences in the X- ray scattering patterns

7.10.1 Summary

The structural differences in the collagen of cancer invaded breast tissue may be caused by two responses known to be present in tissues surrounding tumours. The action of matrix metalloproteinases (MMP) degrading the collagens and/or the host response of increased production of anomalous matrix components (desmoplasia). It is conceivable that the excess connective tissues associated with desmoplasia have a different structure from normal as the matrix components have been expressed under different conditions to normal tissues. A unique form of collagen has been detected close to tumours called onco-foetal, laminin binding (OF/LB) collagen (Pucci-Minafra, 1993). The term OF/LB describes the locations in which this newly identified form of collagen is found (i.e. in oncological and foetal tissues) and the

tendency of this form of collagen to bind laminin. Although there have been claims that this new form of collagen has been detected using small angle X-ray scattering (James, 2002), the claims have yet to be substantiated. Although MMPs have been shown to be present at increased levels in cancerous breast tissues and that the MMPs are involved in cancer initiation, progression and metastasis by degradation of the collagens in the extra cellular matrix (ECM) (Duffy 2000), the specific effects of MMP on the scattering pattern of collagen is not fully understood.

7.10.2 Collagen around tumours is different to collagen in normal tissues

7.10.2.1 Known presence of distinct collagen around tumours

Collagen from samples of infiltrating ductal carcinoma of the human breast contained greater amounts of the collagen type I trimer compared to regular collagen types (Pucci-Minafra, 1986). Human breast and colon carcinoma both contained the new form of collagen with increased levels of type I trimer which was not found in normal adult tissues but that was found in embryonic foetal tissues (Pucci-Minafra, 1993). Due to the locations where this collagen is found and its affinity to bind laminin it was termed OF/LB collagen (onco-foetal, laminin binding collagen) and was suggested as a powerful marker for malignancy (Pucci-Minafra, 1993). The OF/LB tropocollagen molecule, though previously thought to be composed of three α_1(I) chains (Minafra, 1984; Pucci-Minafra, 1985; Luparello, 1986), was shown to be composed of three distinct chains, a unique acidic component which is structurally distinct from the α_1(I) chain and the other two chains that when adequately resolved appear as α_1(III) and α_1(I) (Pucci-Minafra, 1993). The association of OF/LB collagen with malignant tumours is further substantiated by the observed increase in expression of its constituent pro- α_1-chains of both type I and III procollagens in tissue surrounding malignant tumours (Kauppila, 1998).

OF/LB collagen has a longer axial periodicity than the normal form of type I collagen observed in breast tissues (Pucci-Minafra, 1986), which is a heterotrimer of two α_1(I) and one α_2(I) chains. The observations of the OF/LB collagen (Pucci-Minafra, 1993) were obtained by performing 2D electrophoresis, enzyme treatment and peptide mapping. Therefore although there is a suggested difference in the axial periodicity, Pucci-Minafra et al. (1986) and (1993) have presented no direct evidence that the differences between the collagen types is significant enough to be observed using small angle X-ray scattering. However, if there is a difference, observations using small angle X-ray scattering should provide evidence to support the hypothesis.

7.10.2.2 Observation of distinct collagen by X-ray scattering

Differences in the SAXS pattern of tissues from normal and cancerous breast tissue have been observed (Rogers, 1999; Lewis, 2000; Fernandez, 2002) and the presence OF/LB collagen cited as a possible cause. It has been claimed that foetal collagenous breast tissue had been located in association with breast carcinoma using synchrotron fibre diffraction (James, 2002).

Diffraction peaks which correspond to a spacing of 32.1 $\pm$ 0.5 nm were reported in tissues adjacent to cancer sites (James, 2002) and are identical to those found in primordial foetal tendon and skin (James, 1998). It was postulated (James, 2002) that the rings were associated with a degradation fragment 32.1 nm long resulting from the cleaving of type IV collagen by a metal dependant collagenase as identified in cell cultures from malignant tumours (Fessler, 1984). The 32.1 nm spacing identified in foetal collagen was indexed to the 11^{th} order of the 353 nm lattice and the length of the compact rod-like 7S collagen domain of type IV collagens (James, 1998). The 353 nm lattice was also reported to be present in the results from collagen adjacent to

breast tumours (James, 2002), but the 32.1 nm ring was not attributed to it in this case and there was no discussion to identify the most likely hypothesis.

The SAXS data presented in James 2002 caused contention with researchers in the field of SAXS from breast tissue. A number of issues regarding the experimental procedure and data analysis are summarised here in Table 7.10.1.

None of issues that were raised by Rogers et al. (2003) or Suortti et al. (2003) were adequately addressed in the reply from James (2003) and some were not addressed at all. Such as the fact that Rogers et al. (2003) state they do not believe the major conclusion of the work (that the findings show structural changes preceding breast cancer) was supported by any of the data presented. Without further publication the doubts raised by Suortti et al. (2003) and Rogers et al. (2003) remain unanswered leaving the claims of James unsubstantiated and therefore confirmation of the detection of OF/LB collagen using SAXS by James was not possible.

Comments from: Suortti, 2003 and Rogers, 2003	Reply James, 2003	Supporting evidence in the reply of James, 2003
The reported 32.1nm peak indexes to 4.2 nm and is therefore suggested to correspond to fat.	Maintained the initial indexing was correct, substantiated by the fact the 32.1nm ring was present in samples where there was no fat as determined by histopathology	Some data is provided in the reply though it does not adequately support the claims.
The presence of the 353 nm lattice is not supported by the data presented.	maintains that the 353 nm lattice is present and states that to be able to observe the lattice you need the highest quality samples and results	James states continued observation of the lattice in all 2D collagen tissues but does not present any evidence to support this or the previous claim.
Disease state of some of the tissue was determined by eye.	James' reply to this is that it is certainly possible to discern differences with a hypodermic needle but does not address the fact that the diagnosis of at least some of the samples was stated to be done by eye.	There is an associated change of texture that can be identified using a hypodermic needle, which may indicate disease. Texture is not a definite correlation and cannot be used to accurately confirm disease state, thus is not a valid alternative to histopathology.
Normal breast tissue data are absolutely identical to that previously presented as foetal tendon and skin tissue in James et al. (1998). If they are separate data they are either; free of noise or the noise is identical. There is no discernable difference in the intensity or position of the peaks between either plot and there is a possible printing error identical in the plots from both papers.	James states that the figures used are from different samples and does not account for the striking similarity of the plots.	No evidence is presented to explain why the two plots are so similar.
Erroneous citation of Lewis, 2000 supporting the variation in collagen fibril radius, when no mention of variation in fibril radius is mentioned in Lewis, 2000.	James offers no explanation as to the inclusion of the erroneous reference and does not correct the statement that Lewis et al. (2000) supports the results.	James states Eikenberry, 1982 discusses changes in Bessel function implies changes in radii.
Omission of key experimental and data processing methods that hinder any repetition i.e. X-ray wavelength, X-ray beam dimensions, the volume/mass of specimen, the method for determining the peak positions and intensities.	James states that the experiments were undertaken on different beam lines with different focusing, which if that is the case would also require an explanation of adequate normalization to remove these effects which was not included in the original paper (James, 2002) or the reply to the comments (James, 2003).	James does not give the omitted information in the reply but states it has been previously published, thought does not give a reference in the reply and it is not clear that any reference in the original paper cites the experimental procedure. The only possible reference to the experimental procedure is (James, 1993).

Table 7.10.1 Comments and responses regarding observation of OF/LB in breast cancer tissue using SAXS

7.10.3 Matrix metalloproteinases degrade collagen around tumours

7.10.3.1 Summary

The observation of activity of interstitial collagenase during metamorphosis in tadpoles having the ability to degrade rigid rods of collagen led to the discovery of many similar proteases that became known as Matrix metalloproteinases (MMPs) (Brinckerhoff, 2002). MMPs participate in many normal biological processes including organ morphogenesis, nerve growth, ovulation, bone remodelling, wound healing, angiogenesis, apoptosis, etc. and pathological processes including arthritis, cancer and cardiovascular disease among others (Nagase, 1999). There are a number of members of the matrix metalloproteinase family which act to degrade the basement membranes and interstitial tissues of the extracellular matrix. Small angle X-ray scattering can detect the fibrillar collagens which make up the interstitial tissues (types I, II and III) and therefore detect changes caused by degradation.

7.10.3.2 Mechanism of MMP action

MMPs cleave the tropocollagen (collagen triple helix, see Section 7.3.4) in two, yielding ¾ and ¼ length fragments of the original molecule (Gross, 1965). The cleaved fragments of the collagen were unstable at physiological temperatures and degraded to yet smaller fragments. As the degradation process progresses there will be a reduction in the amount of ordered collagen as more collagen is removed from the ordered structure. The degradation of collagen should be visible using small angle X-ray scattering as a reduction in the peak intensity of the scattering pattern, if no changes to the ordering of the collagen are occurring the spacing and peak widths should remain unaltered.

7.10.3.3 Association of MMP with breast cancer

The correlations between MMPs and cancer are well known. Characteristic and localized areas of collagen rarefaction and fragmentation observed in the stroma of ductal infiltrating carcinoma of the human breast was reproduced in vitro by human collagenase digestion on reconstituted fibrils (Pucci-Minafra, 1987). Increased MMP-2 expression has been associated with increased metastatic potential in a variety of systems (Thompson, 1994), as has type IV collagenase (Thompson, 1994; Monteagudo, 1990). Increased levels of MMP-2 (Thompson, 1994) and type IV collagenase (Monteagudo, 1990) were observed in invasive carcinomas but not in benign or normal tissues. Altering MMP activation via manipulation of gene expression (Montel, 2004) or MMP inhibitors (Heppner, 1996) demonstrates that MMP activity is required for tumour progression and metastasis in several model systems (for review see MacDougall, 1995).

Suggested mechanisms by which MMP contribute to tumour invasion and metastasis include promotion of angiogenesis, activation of stimulating growth factors or their receptors, and inactivation of inhibiting growth factors. However, it is generally assumed that the primary mechanism by which MMP promote tumour invasion and metastasis is by degradation of the ECM, including both basement membranes and interstitial connective tissue (Duffy, 2000). The changes to structure caused by the action of MMP may be visible using small angle X-ray scattering or other techniques and may account for the reduction in collagen structure around tumours as well as at distance from the tumour.

7.11 Automated analysis techniques

7.11.1 Summary

The implementation of an automated diagnostic system could be of great benefit in two areas:

1. To surgeons during excision procedures, allowing them to make more informed decisions on the location of the tumour margin and therefore how much tissue needs to be removed. More precise excisions would benefit patients as there would be no additional surgeries or excess tissue removed.

2. In the pathology lab to provide automated analysis of small angle X-ray scattering patterns which may be collected using a conventional source.

X-ray scattering data contains a lot of information about the structure of the sample that may not be directly related to the disease state. Using multivariate analysis methods the features most directly associated with disease state can be found and used to compare future samples against, giving an automated result for the disease state of the sample under examination.

7.11.2 Need for automated analysis

It is proposed that a diagnostic test which can inform a surgeon during the procedure whether the entire tumour has been removed would reduce the need for further surgery. Current practice requires visual judgment of the margin (which may be diffuse) by the surgeon and then confirmation by histopathology (see Section 7.2.7) using the excised tissue to confirm that all the tumour tissue was removed. The current analysis method providing histopathology results during surgery takes

approximately half an hour which is time consuming and means extended times under anaesthetic for the patient.

7.11.3 Proposal for a dedicated diagnostic tool

By utilising small angle X-ray scattering from tissue using a conventional source it may be possible to produce histopathology results in a matter of minutes. This is in contrast to approximately 36 hours for normal histopathology, as there is no need for tissue processing (i.e. formalin fixing, wax embedding, sectioning and staining). If the analysis could be applied to automatically determine the disease state it would provide a diagnostic tool which could be implemented at a surgical unit with no need for additional highly trained personnel. Additionally as the samples would not be treated in any way conventional histopathology could still be applied to confirm adequate tissue removal.

7.11.4 Automatic analysis using a multivariate approach

For a given point in the scatter pattern there are many physical properties of the tissue which combine to produce the intensity at that point. This means that each value is partially redundant in that it captures many aspects of the object in a single value. Multivariate analysis aims to identify correlations in the measurements of intensity which allow redundancy to be exposed and therefore allows parameterisation at a much reduced level, aiding classification. Typically in the principal component analysis only three numbers are derived, along with three static models, to accurately define any given scatter pattern. The accuracy to which it does this depends on the situation but is often greater than 95%.

To understand how this works, consider a number of data sets m, which are measurements of intensity against S (see Section 7.7.3.1). If there are n points in each set then a covariance matrix can be formed of dimensions n^2, where each element is the variance between one point X and another Y. The covariance is defined as:

$$\mathrm{cov}(X,Y) = \frac{\sum_{i=1}^{m}(X_i - \overline{X})(Y_i - \overline{Y})}{(m-1)}$$

In words the covariance is:

The product of the difference between the X and Y positions and the respective mean values, for each point, summed over all the data sets and normalised[*1].

If the covariance is positive this means that both points increase together. If the covariance is negative, when one increases the other decreases. When the covariance is zero then the two points are independent of each other. Since the covariance matrix is by definition square, eigenvectors can potentially be calculated for it. This process will generate n orthogonal eigenvectors and the associated matrix of n eigenvalues. Principal component analysis (PCA) uses these to assess which unit eigenvectors are the most important in describing the variance in the data. It turns out that the eigenvector with the highest eigenvalue is the most significant and it is called the principal component. Put another way, the principal component accounts for the maximum variance in the data. Furthermore, it is possible to ignore the eigenvectors with very small eigenvalues and still accurately describe the covariance matrix. Doing this can dramatically decrease the number of parameters used to describe the complete data and is the principal behind some lossy data compression methods. Given any set of eigenvectors, there is a simple piece of matrix maths to returns to the mean subtracted data, which can be compared to the original in order to quantify the

[*1] Note: the leading diagonal of the matrix is the variance for each point

significance of the eigenvectors in terms of the percentage variance in the data they represent.

Having got to this point, it is possible to plot the result of the reduction using axes defined by the most significant eigenvectors. In PCA these are usually referred to as the principal components or loadings. The associated significance values are often called the scores. Each of the m original data sets will produce a single point in this space. Most PCA programs will allow visualisation like this with three loadings, and provide the ability to manipulate the plot on a screen to hunt for groupings. The strength of this approach is that using the principal components guarantees an optimal display for capturing the variance in our data. If there is significant clustering discovered in the plot of scores in the loading space it is then possible to run single or multi-category classification procedures. The result of this will be a model which classifies the scores of the principle components or in our case with disease state. This will allow subsequent data to be classified automatically by reducing it using the same techniques and comparing the principle components scores to the model.

7.12 Possibilities for other tissue systems

The changes in breast tissue associated with disease are likely to be similar in other collagenous tissues. Therefore it is reasonable to assume that if changes can be observed in the SAXS pattern from breast tissue diagnostic changes may be observable in other organs with a high content of connective tissue such as lungs and colon. The presence of onco foetal, laminin binding (OF/LB) collagen in both breast and colon tumours (Pucci-Minafra, 1993) supports the idea that this technique may be applied to colon cancer.

It may also be possible to see the disruption to ordered systems by the progression of tumours in structures like the brain. Myelin which covers some neurons shows a high degree of order which can be seen as maxima in the SAXS pattern. In other organs it may not be possible to use SAXS for disease diagnosis. If no highly ordered structures are present in the tissue no observation of disruption can be observed with tumour invasion. However, it may be possible to observe an increase in amorphous scatter which corresponds to an increased number of scattering objects present in the tissue.

It is unlikely that this technique could be used in vivo for two reasons. Firstly the large X-ray dose which would be required. Secondly the fact that the small signal resulting from the tumour would be swamped by the signal from the large amounts of normal tissue surrounding it, though with techniques such as CT this may be overcome. However, after a suspicious mass is located using mammography, diagnosis using SAXS could be performed on a small sample of tissue excised from the suspect location as part of a biopsy.

7.13 Aims of this Thesis

The aims of this research are as follows:

- Provide further evidence of reported structural changes observed in collagen of breast tissue around tumours.

- Provide markers from small angle X-ray scattering data that can be used to distinguish normal, malignant and benign tissues.

- Determine the biological cause of the structural changes in collagen associated with malignant and benign disease i.e. whether the cause is matrix metalloproteinase action or the production of a new type of collagen.

- Determine if the structural changes in collagen caused by tumour progression can be observed at distances up to 6 cm from the tumour.

- Collect diagnostic data from a conventional source within a reasonable time (less than 30 minutes) to show that diagnostic measurements using small angle X-ray scattering could be obtained in a clinical setting.

- Provide automated determination of the disease state of tissue using multivariate analysis on data from small angle X-ray scattering.

- Use multivariate analysis to provide automated diagnosis using data from a conventional X-ray source to demonstrate the possibility of implementing a clinical system to provide automated diagnostic information.

8 Materials and methods

8.1 Experimental procedures

8.1.1 Sample handling

8.1.1.1 Preservation

The samples were subject to biological decay and thus precautions were taken to minimise structural changes to the samples. Medical samples are often preserved, sometimes termed fixed using formalin. Formalin is a solution of formaldehyde which causes cross links between the proteins thus preventing decay. As formalin fixing is known to remove water from tissues and thus affect the structure of the collagen in a similar way to dehydration (see Section 7.8.2), the fixing process for tissues used in this project was delayed until after the data collection procedure. To prevent decay during storage the samples were kept frozen at -80 °C thus reducing enzyme and bacteriological action to a minimum. X-ray scattering data could not be collected from frozen samples, therefore the samples had to be thawed out and then refrozen between each data collection process. Repeated freeze thaw cycles are not believed to have a severe effect on the scattering pattern, but effects on the cells have been reported from histopathological techniques. The samples were therefore frozen and thawed the minimum number of times possible. Once all the X-ray scattering data had been collected from the samples they were then fixed using formalin.

8.1.1.2 Sample preparation

The experiments undertaken required samples from many different types of tissue, all requiring preparation. Data was collected from human tissue samples, consisting of core cut biopsy tissue from breast samples, as well as biopsy samples of tumour from brain, lung, liver and colon. Fresh samples of rat tail tendon were used to calibrate the experiments and chicken leg tendon, chicken dermis and pork dermis were used for specific investigations.

8.1.1.2.1 Human tissue samples

All tumour samples were collected by surgeons during procedures to remove diseased tissue. The normal breast tissue samples were collected from (a) cosmetic reduction procedures (mammoplasty) where excess breast tissue is surgically removed (b) bilateral mastectomy procedures from the opposite breast to that in which the disease had been diagnosed, (c) the opposite quadrant of the diseased breast where the effect of the tumour was expected to be minimal due to the distance between the tumour site and the location the tissue was taken from.

All tissue samples were snap frozen in liquid nitrogen (-196 °C, 77K) and stored at -80 °C until use. Most of the breast specimens were core cut biopsy samples approximately 1 mm in diameter and varying in length. These required no further sectioning prior to the X-ray data collections. However, some specimens of breast tissue were excised and varied considerably in size (0.5 cm^3 to 10 cm^3) and thus required dissection to an appropriate size for X-ray data collection.

8.1.1.2.2 Rat tail tendon

The rat tail was stored at -5 °C and was allowed to defrost before preparation began. Using a scalpel an incision was made along the length of the tail at a depth adequate to penetrate the epidermis. The epidermis was carefully removed using forceps and then discarded. A section of approximately 2 cm was removed from the tip of the tail, proximal to the distal insertion. The exposed tendons were then pulled from the tail and placed in a 50 mMol solution of potassium phosphate buffer, pH 7.0, to prevent dehydration. Once all the exposed tendons were removed the tail was cut proximally to the next distal insertion and the newly exposed tendons were removed. This procedure continued until the remaining section of tail was less than 5 cm in length.

8.1.1.2.3 Chicken and pork dermis

An incision was made along the length of the chicken thigh at a depth adequate to penetrate the epidermis. The epidermis together with the layer of subcutaneous fat was separated from the flesh. The pork was purchased from a butcher with a square section of skin still covering the flesh. The epidermis was carefully separated from the meat preserving the subcutaneous fat. Once removed the dermis samples were stored in potassium phosphate buffer and kept refrigerated. Appropriately sized samples of dermis and or fat were prepared when required for the experiments.

8.1.1.2.4 Chicken leg tendon

The tendons of the chicken thigh were separated from the muscle preserving the greatest length possible during the initial collection. All samples collected were stored refrigerated in potassium phosphate buffer until required. Appropriately sized sections of the tendons were removed from the original lengths when they were required.

8.1.1.3 Post X-ray data collection sample handling

After all required experimental data was collected from the human tissue samples, the tissue specimens were fixed and stored in 10 % formalin solution. The fixed samples were then examined using the current standard histopathological techniques for cancer diagnosis (see Section 7.2.7). In brief the samples were sectioned and stained at the Nottingham City Hospital histopathology department. The stained sections were analysed by experienced pathologists (Dr S. Pinder and Dr E. Provenzano, Addenbrookes Hospital) who produced a detailed report.

8.1.2 Synchrotron radiation experiments

8.1.2.1 Summary

Synchrotron radiation (see Section 7.4.2) was used for many of the experiments detailed in this thesis as it was believed that the high intensity and therefore shorter data collection time would be preferable. Avoiding long exposure times was desirable as during data collection the samples were in a warm environment, were not fixed and so may have been subject to physiological decay. Minimising the length of time the samples were not at cryogenic temperatures before fixing increased the likelihood that the samples were still in good physiological condition for histopathological analysis. Histopathological analysis was required to determine the clinical diagnosis (see Section 7.2.5) of the tissue in order to allow comparison of the X-ray scattering data with the current standard technique. The synchrotron experiments detailed in this thesis were all undertaken on station 2.1 at the UK Synchrotron Radiation Source (SRS) at Daresbury laboratories.

8.1.2.2 Daresbury Laboratory SRS station 2.1 experimental parameters

Station 2.1 at the SRS utilises radiation from a bending magnet (see Section 7.4.2.4) and is a fixed energy station (beam energy 8 keV) i.e. the X-ray energy/wavelength cannot be altered. The beam dimensions can be altered as required from 0.6 mm vertical and 1 mm horizontal to approximately 5 mm vertical and 10 mm horizontal. The sample to detector distance can be varied between 1 m (approximate S range of 0.032 to 0.64 nm^{-1}) to a maximum of 8 m (approximate S range of 0.008 to 0.064 nm^{-1}). The detectors that were used to collect the X-ray scattering data for all the experiments on station 2.1 were 2 dimensional gas filled, wire, delay line detectors. To enable the data collected from each experiment to be accurately calibrated, an X-ray scattering pattern from a calibration standard (a sample with a known D spacing) was collected every time the distance between the sample stage and

detector was changed. The samples used to collect the reference were silver behenate (D=5.838 nm) for shorter sample to detector distances or hydrated rat tail tendon (D=67 nm) exposed horizontally and vertically for longer sample to detector distances. Reference samples for calibration were chosen based upon whether a minimum of 3 orders of diffraction could be seen and whether the orders were spaced far enough to allow them to be resolved separately (Figure 8.1).

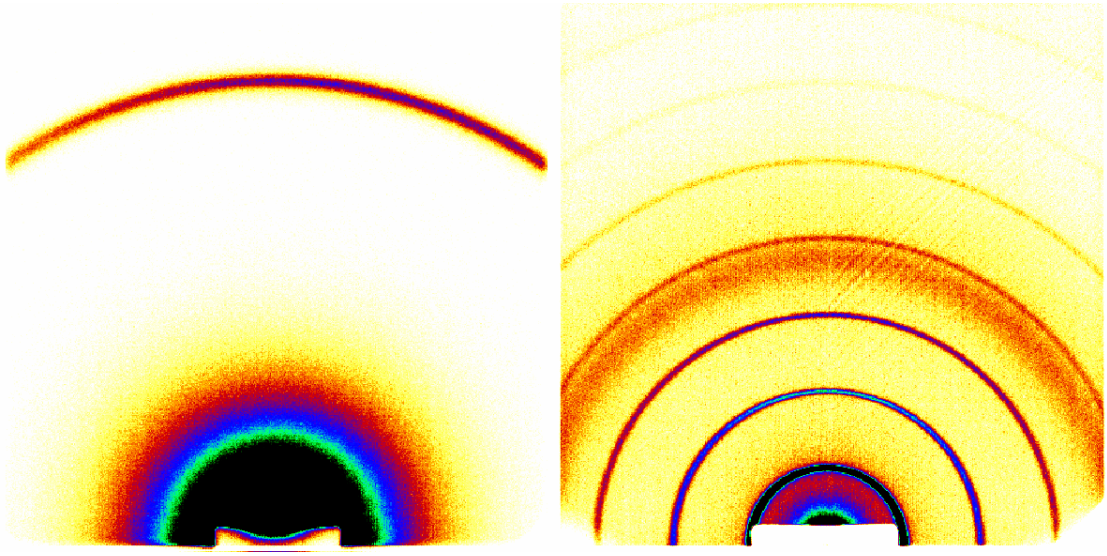

6.25 m **1 m**

Figure 8.1 Silver behenate calibration for X-ray scattering

With a sample to detector distance of 6.25 m only the 1st order peak of silver behenate was seen and so hydrated rat tail tendon was used to calibrate in this case. At 1 m, 6 orders of scattering peaks were observed from silver behenate thus silver behenate was used to calibrate experiments with short camera lengths

8.1.2.3 Data collection protocol

For each separate experiment there was variation in the beam line and experimental parameters (See Table 8.1.1 for a summary). The position of the sample can be altered using a remotely controlled motor system, allowing for adjustment to reposition the samples in the beam for alignment and to investigate different points in the samples. For the breast tissue data collections the samples were oscillated in the vertical direction, to collect the average X-ray scattering pattern from the tissue. To asses the homogeneity of samples data was also collected from a series of individual points along the length of a number of samples.

Experiment	Sample Holder	Camera length (m)	Exposure time (s)	Beam dimensions (mm^2)
Breast tissue data collection	Capillary tubes sealed with wax	6.25 and 1	300	1
Collagen degradation	Brass cell with mica windows	6.25	300	2
Temperature investigation	Brass cell with mica windows	6.25	300	2
Tension	Tensile testing rig with environment chamber	6.25	90	2
Dehydration	Tensile testing rig with environment chamber	6.25	90	2

Table 8.1.1 beam line and experimental parameters for each experiment

8.1.2.4 Sample holders

Two methods of securing the sample were utilised, each for different experiments. Glass capillary tubes were used for the standard data collections investigating the differences between normal and diseased tissue. Brass sample holders with ruby mica windows capable of sealing in liquid were used for raster scans and collagenase degradation experiments.

8.1.2.4.1 Glass capillary tubes

The glass capillary tubes (also known as Lindemann tubes) used in these experiments were manufactured by "Glas Technik", dimensions 1 mm diameter, length 80 mm and wall thickness 10 μm. The 1 mm diameter tubes were chosen to match the diameter of the breast tissue samples facilitating mounting. Before the sample can be mounted the sealed base of the tube must be removed. The top of the capillary tubes flare out to 2 mm, allowing the tube to be held inside a larger tube (1.5 mm diameter) resting on the flared edge. To insert the sample, it was held above the top of the capillary tube and using light suction provided by a rotary vacuum pump the sample was drawn down the capillary. To aid stiff collagenous samples into the tube thin fuse wire was used to push the sample. However, this causes the sample to be compressed in the tube, rather than stretched as it would be using vacuum alone. For samples which contain more fat

there was a danger of the sample being drawn through the tube and into the vacuum pump. To guard against this a filter was fitted inside the tube to the vacuum pump.

Once the sample was positioned roughly in the middle of the capillary tube the tube was sealed to prevent dehydration (see Figure 8.2). A small amount of phosphate buffer was added to the capillary tube and then the ends were dipped into molten wax to form a seal. The capillary effect was used to draw the wax into the capillary tube where it cooled and solidifying to make a watertight seal. The capillary tube was labelled and then stored in dry ice until the data collection.

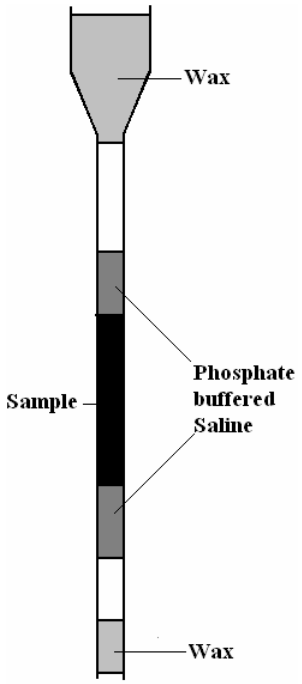

Figure 8.2 Illustration of capillary tube mounting

Sample was held in the middle of the tube surrounded by Phosphate buffered saline and the tube was sealed at both ends with wax.

During data collection the capillary tubes were placed in a specially designed holder (see Figure 8.3). Each capillary tube rested in one of five 1.5 mm holes in the top piece of the holder, its vertical position fixed by the point at which the capillary tube diameter increases. The bottom of the capillary tube was held in position by matching 1.5 mm holes in the bottom piece of the holder which ensured the capillary tube was parallel to the vertical axis of the sample stage motion control.

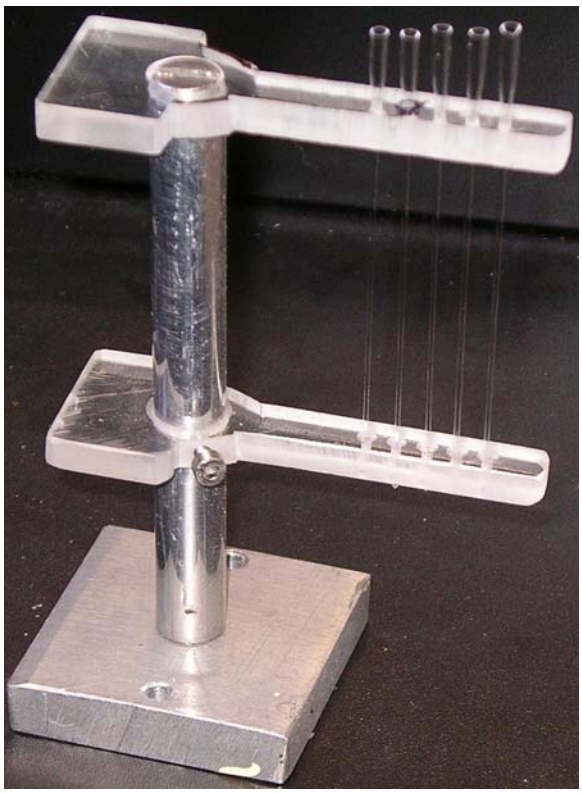

Figure 8.3 Capillary tube holder

Five capillary tubes containing samples were mounted in the holder simultaneously and were positioned in the beam for data collection individually using the sample stage motors.

8.1.2.4.2 Brass sample holders

Brass sample holders (otherwise known as “liquid cells”) were available for use during the experiments. The liquid cells have been used on the station for a number of years and the design has proved simple and versatile. This design of sample holder was selected for use in the degradation experiments as it allowed for sections of tissue (1 mm depth, 5 mm diameter) to be placed in a volume of liquid and for the temperature to be controlled.

The sample was mounted between two discs of ruby mica, separated by a polythene spacer (Figure 8.4). The spacer permitted a 1 mm separation between the mica discs and a diameter of 5 mm in which the sample was held. The samples were placed on the mica disc in a polythene spacer, phosphate buffer was added to prevent dehydration and the second mica sheet was placed on top. Surface tension of the

liquid held the mica sheets in place. The polythene spacer and tissue assembly was mounted in the main body of the brass holder and held in place using the threaded securing ring. The brass sample holder was secured in place on the motor controlled sample stage ready for data collection. The main body of the brass holder contained channels for circulating liquid from a temperature control unit. This was used to keep the sample at the desired temperature for the duration of experiment. For the MMP degradation experiments the temperature was maintained at 37 °C for the full 2 hours of the data collection for each sample. For the thermal degradation experiments temperatures of 5 °C, 20 °C, 37 °C and 60 °C were maintained for 20 minutes each.

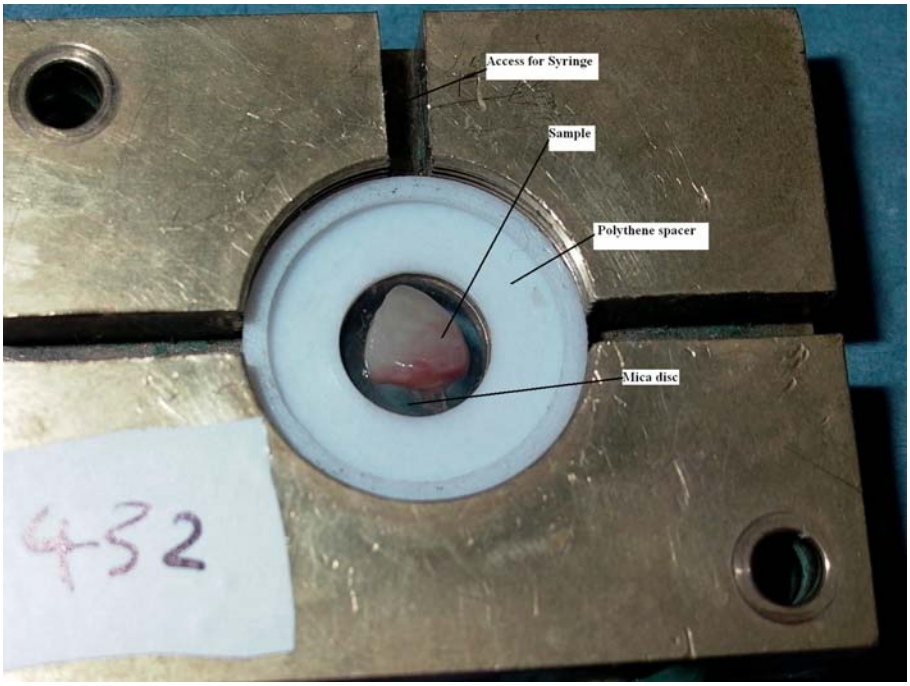

Figure 8.4 Brass sample holder

The tissue sample rests on the lower mica disc, in the hole of the spacer. A second disc is placed over the sample and the assembly secured with a threaded ring.

The brass sample holder had access for syringes to add the buffered MMP solution or the buffered control solution into the sample volume. The MMP or control solution was added into the sample holder after an initial exposure of the sample was taken, giving a reference for each series. A standard buffer solution was prepared, which was separated into two bottles, to which one the MMP was added and the other was left unaltered as the control.

8.1.2.4.3 Tensile testing rig

The tensile testing rig was designed and built by Dr C. Martin (Keele University). The force applied to the sample was controlled by two geared stepper motors that move the jaws of the sample mounting stage together or apart at the same rate. The sample was secured using brass clamps that grip the sample firmly. These clamps were then secured to the sample mounting stage using double pronged brass pins. The upper motor section was mounted on a hinge that rested on a strain gauge, so when the sample was under tension the force on the sample was calculated from the reading on the strain gauge. The strain gauge was calibrated using known weights and was accurate to one tenth of a Newton. The vertical position of the jaws was controlled externally using a computer, allowing for the force to be controlled during exposure. In order to keep the samples hydrated whilst in the test rig cotton wool wetted with the phosphate buffer was placed on the lower jaw around the tendon (Figure 8.5).

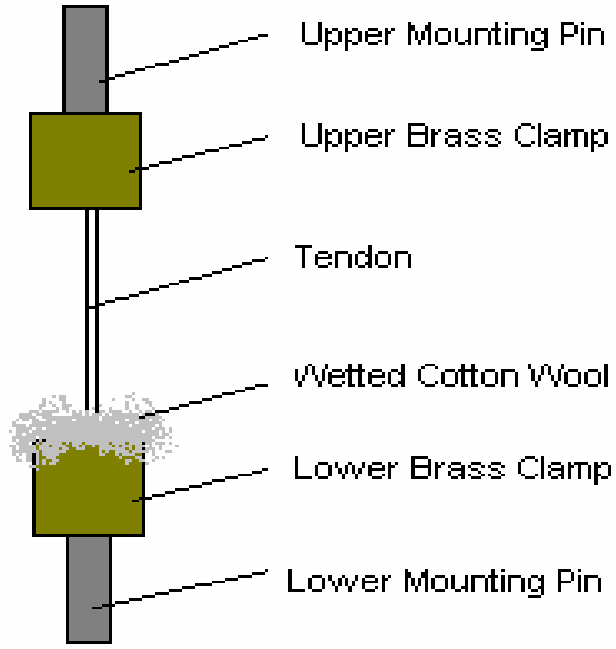

Figure 8.5 Tensile test rig sample mounting

8.1.3 Conventional X-ray tube experiments

8.1.3.1 Summary

To enable small angle X-ray scattering of tissue to be used as a diagnostic tool in a clinical environment, the ability to collect data which is reliable and reproducible must be demonstrated. To investigate the possibility of using a commercial X-ray source for collecting diagnostic scattering data, a collaboration with Professor Dr O. Glatter (University of Graz) using the SAXSess (Panalytical) was undertaken.

8.1.3.2 SAXSess experimental parameters

The SAXSess system is a laboratory based small angle diffractometer providing a monochromatic X-ray beam with a wavelength of 1.54 Å and a fixed camera length of 26.7 cm. The X-ray beam dimensions from this system were 20 mm horizontal and 0.25 mm vertical. Samples were exposed in a horizontal alignment with as much of the sample exposed to the beam as possibly. X-ray diffraction patterns were collected using an image plate detector of 6.5 cm by 5.5 cm with a 50 μm pixel size. The exposure time used for all the samples was 20 minutes.

8.1.3.3 Sample holder

The SAXSess system was evacuated to remove air from the X-ray path in order to minimise parasitic scattering and attenuation during data collection. Samples were held in a vacuum tight cylindrical holder approximately 10 cm in length and 1 cm diameter. The sample holder was constructed in two halves which separated to allow the sample to be placed between them and clamped together, making the seal. The internal dimensions to accommodate the sample were 2.5 cm in length by 1 mm height and 1 mm depth, the sample while in the holder was surrounded by phosphate buffered saline to prevent dehydration. The sample holder was fitted with X-ray transparent kapton windows to ensure minimal attenuation of the X-ray beam.

8.2 X-ray scattering data processing

8.2.1 Synchrotron radiation experiments

8.2.1.1 Removal of detector artefacts

There are two methods used to remove the detector artefacts. They can be suppressed by dividing the scatter image by the normalised detector response collected using an iron 55 radioactive source. Or by filtering the scattering image by removing high frequency components caused by the wire structure of the detector. PcDetpack is a software package developed for small angle X-ray scattering image analysis by Professor R. Lewis, which incorporates both of these correction methods.

Both methods require care to be taken in their implementation and ultimately all images treated were checked manually. The method of detector artefact removal used was different depending on the experiment. For the most recent experiments which were the breast tissue classification data, the temperature investigation and the degradation study the filter method was employed as data for these experiments was collected over a period of days. Errors with the detector response method caused by fluctuations over this period were apparent in the images. For the earlier experiments i.e. the dehydration and tension studies the data were collected during a period of between 10 to 12 hours and temperature effects were not apparent using the detector response method. For the earlier experiments the filtering method in PcDetpack was not fully tested. By the time the data for the more recent experiments was processed the testing of the PcDetpack filtering method was completed and so both methods were utilised and the most appropriate method for each experiment was used.

8.2.1.1.1 Detector response (iron 55 radioactive source) method

Using the detector flat field response collected using an iron 55 radioactive source requires that the conditions during the experimental data collection and the detector

response collection are exactly the same. The efficiency of the detector and the digital conversion of the detector output are both affected by fluctuations in temperature. Even though the temperature of the station is controlled, differences can occur resulting in artefacts persisting in the treated images.

First the detector response collected using an iron 55 radioactive source was normalised to the maximum pixel value, giving an image of the detector with all intensities scaled to be between 0 and 1. All the experimental exposures were divided by this normalised detector response. Thereby removing artefacts present in the data caused by the wire structure and consequent inefficiencies in the detector.

8.2.1.1.2 PcDetpack “remove wire structure” method

The PcDetpack “remove wire structure” filter uses the static structure in each image to remove the artefacts caused by the wire structure of the detector. High frequency filters isolate components in each individual scatter image caused by the wire structure of the detector. However, rapid changes in intensity such as the beam stop and sharp diffraction peaks may be incorrectly interpreted as part of the wire structure. Careful masking was therefore required to exclude structures which possessed high frequency components. Selection of the areas of the image to be excluded was performed by choosing a region of interest using the graphical user interface to exclude the beam stop, any flares of intensity in the image and any sharp diffraction peaks. Filters altering the pixel size and position were then used to fine tune the artefact removal. Varying values for the filters were tested and the combination of values which reduced the wire structure artefacts to a minimum without affecting the diffraction pattern were selected.

8.2.1.2 Calibration

The calibration procedure defines the centre of the scatter image and relates distances in pixels from the centre of diffraction to scatter angle. To calibrate the images PcDetpack was used to analyse the scattering from a sample with known D spacing (silver behenate or rat tail tendon). Accurate values for the centre of the scatter pattern and camera length were found by comparing initial approximations for the unknown parameters with those derived from the know parameters such as the beam energy, pixel size and the observed pixel positions of the peaks from a sample of known D spacing. The parameters for the centre of the scatter pattern, camera length beam energy and pixel size were then applied to all data collected for that experiment.

Regions of interest highlighting the observed peaks of the sample of known D spacing (See Figure 8.6) were analysed to find the maximum intensity and therefore the centre of each peak. Using the known orders of the visible peaks in the image the centre of diffraction and camera length were refined so that the expected positions of the peaks matched the observed positions. To accurately determine the centre of diffraction in both the vertical and horizontal directions this procedure was repeated for both vertical and horizontal exposures of hydrated rat tail tendon, or vertical and horizontal regions of interest for silver behenate.

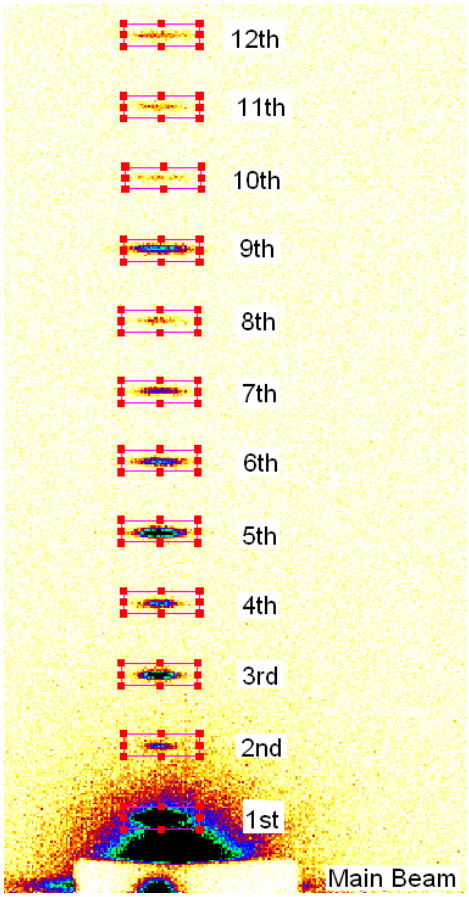

Figure 8.6 Region of interest highlighting the diffraction peaks from rat tail tendon

The accuracy of the calibration values were checked using Excel and where required further refined. The calculated centre of diffraction was further refined by calculating the camera length corresponding to each peak using the peak's observed distance from the calculated centre of diffraction and the theoretical diffraction angle. The diffraction angle of each peak was determined using Bragg's law (see Section 7.7.3.1). The solver function in Excel was used to vary the position of the centre of diffraction in order to minimise the standard deviation of the calculated camera lengths. The solution that gave the minimum standard deviation was the refined centre of diffraction in the vertical plane. Once the vertical plane was corrected the same procedure was used to refine the horizontal. If the calibration could not be refined to within the required limits of precision, the peak positions were re-calculated by fitting the peaks using the peak fitting procedure and using the more precise values in the Excel refinement procedure.

The centre of diffraction was determined in order to ensure that the calculated camera lengths from the position of each individual peak were identical to at least 5 decimal places. The calibration variables i.e. the centre of diffraction camera length etc. were then transferred to all the corresponding images. Annotation rings corresponding to the order of the D spacing for the sample were overlaid in order to visually check the calibration for every image to ensure any deviations of the peaks from the calibrated positions could be investigated (See Figure 8.7).

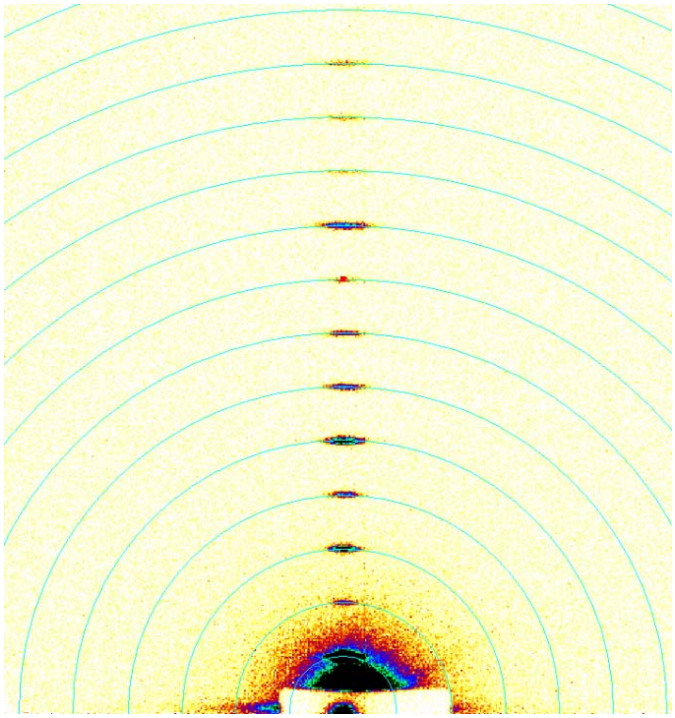

Figure 8.7 Calibrated rat tail tendon with annotation rings corresponding to 67 nm D spacing.

8.2.1.3 Normalisation

The intensity of scattering observed in the diffraction image is not only dependant on the scattering power of the sample but also upon the attenuation of X-rays by the sample. In the case of synchrotron experiments the intensity of the incident X-rays and therefore the observed scattering intensity is dependant on the current in the electron storage ring. To allow for direct comparisons of the intensity of scattered X-rays between different images the differences in the ring current and the attenuation for each sample were corrected for.

To correct the observed scattering intensity, the intensity of the direct X-ray beam after it has passed through the sample was recorded. This was done by calculating the integrated intensity of the beam in the scatter image observed through a semi transparent beam stop. A normalisation factor for each image was obtained by dividing 1 by the observed beam intensity of each image. The value of each pixel in each image was then multiplied by the associated normalisation factor. The normalisation factor for each image was recorded so the original intensity could be recovered for error calculation.

The observed intensity of the direct beam allows for normalisation of separate periods of data collections. However, there were still some observable differences between data collections. The differences in normalised intensity were caused by the use of different beam stops with different attenuation. There was no sample which was exposed in all the data collections therefore in order to normalise the intensity of scatter between data collections the values of amorphous scatter from all samples at a number of separate spacings were calculated. The values calculated near the beam stop showed large differences between samples and therefore could not be used for normalisation. The values of the amorphous scatter near the maximum values of S that was observed showed the minimum variation between samples. In the absence of absolute normalisation the average value of the amorphous scatter was used. The intensity of all images in an individual data set were adjusted by the same scaling factor, each data set had a different scaling factor which were adjusted so that the average amorphous scatter value for the chosen area in each data set was the same.

8.2.1.4 Radial sector integration

A sector region of interest was defined and applied to the image to radially integrate the X-ray scattering peaks (See Figure 8.8). The sector region of interest was then

applied to all the images from the experiment. The intensity at points of equal radius within the sector were then automatically integrated and exported to Excel where the data was then represented as spacing in nm^{-1} against intensity.

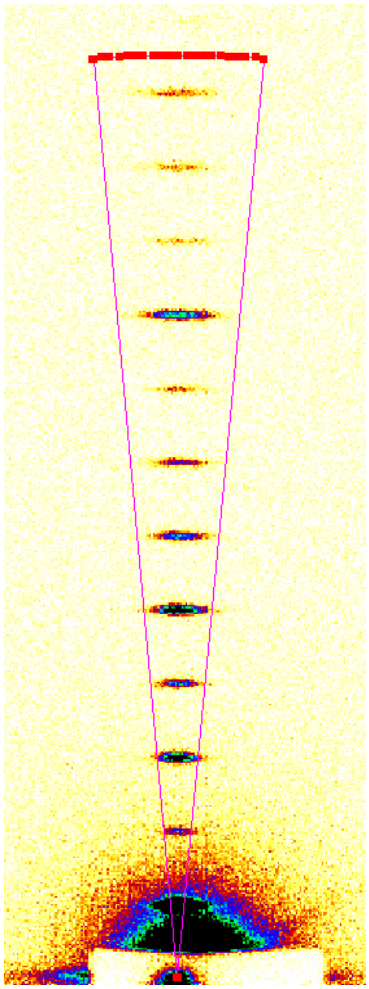

Figure 8.8 Radial region of interest applied to diffraction peaks of rat tail tendon.

8.2.1.5 Background offset subtraction

The observed scattering profile was superimposed over a background caused by the scattering of the X-rays by the air around the sample. The background was observed in all X-ray scattering data as an offset from zero (See Figure 8.9). The value for the offset was calculated using a Porod plot (see Section 7.7.6) and then subtracted from the original data. The data shown as an example for the background offset subtraction method (Figure 8.9, Figure 8.10, Figure 8.11 and Figure 8.12) was X-ray scattering data collected from normal tissue and the units of intensity were given as Normalised Photons per Pixel (NPP).

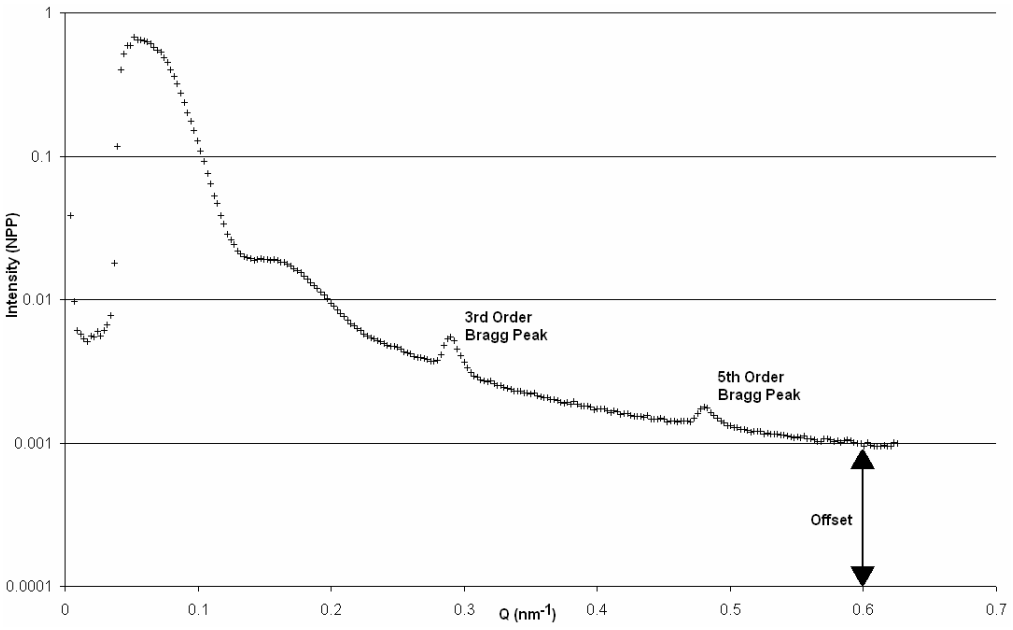

Figure 8.9 Intensity versus Q spacing for raw data showing offset due to background noise

The background offset was calculated directly for each X-ray scattering profile using Excel. The values for Q^4 versus IQ^4 were calculated from the original data then the gradient (see Figure 8.10) calculated using the LINEST (linear estimate) function. The calculated value of the gradient was then subtracted from the raw data to remove the background offset.

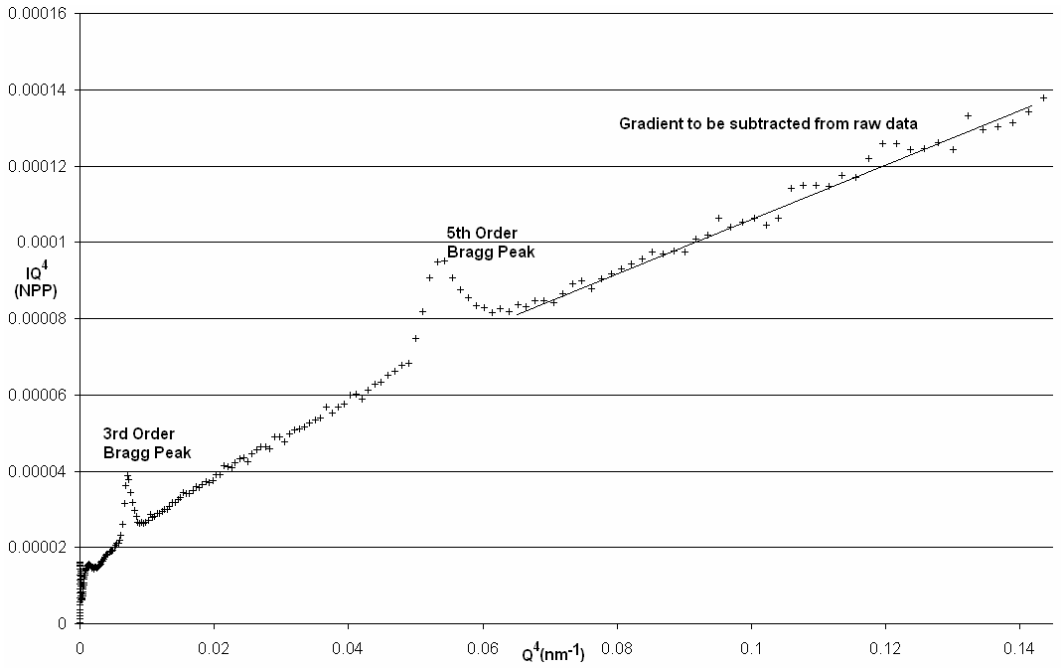

Figure 8.10 Porod plot showing gradient to be subtracted form the raw data.

After the calculated gradient was subtracted from the raw data the observed offset was reduced (See Figure 8.11). However, the offset will not be removed completely as the scattering intensity should not reach zero in this range nor should the intensity become negative.

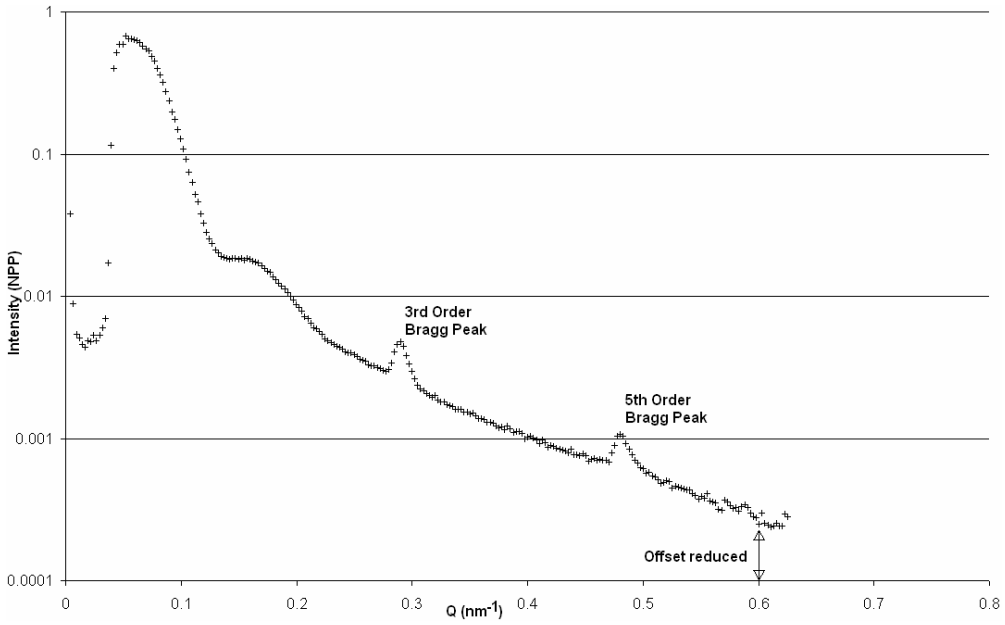

Figure 8.11 Intensity versus Q spacing for raw data showing reduced offset after subtraction

To verify the subtraction process, the subtracted data was viewed on a Porod plot and checked for the presence of a plateau (See Figure 8.12).

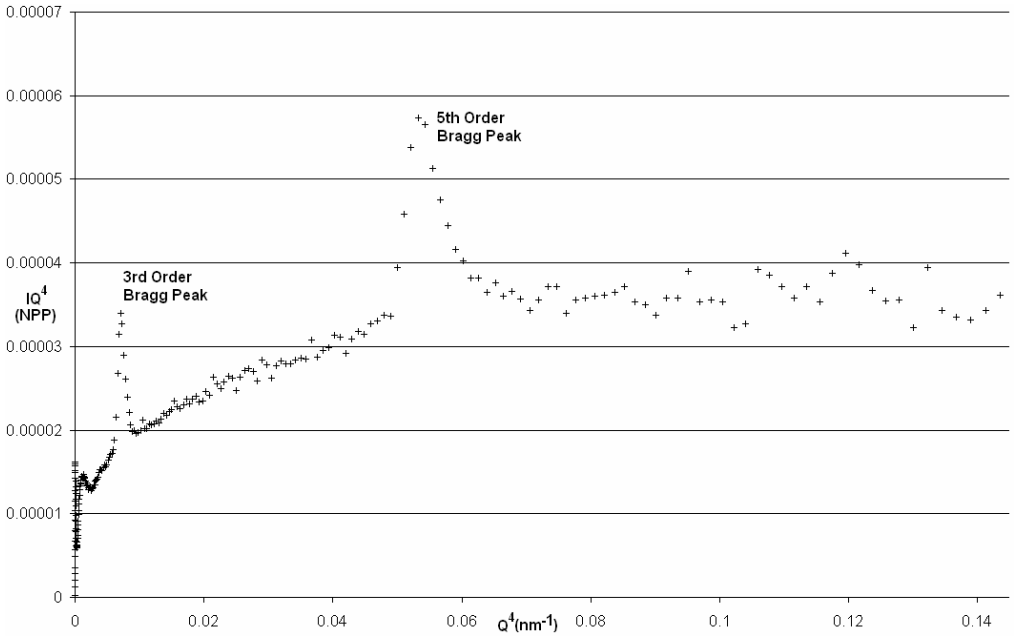

Figure 8.12 Porod plot showing plateau indicating the subtraction was correct

8.2.2 Conventional X-ray tube experiments

8.2.2.1 Integration to one dimensional plot

The 2-D X-ray scatter patterns were reduced to 1-D plots using proprietary SAXSquant software package (Anton Paar). A region of interest was applied to each 2D scatter image. The width of the region of interest was 1 cm and the length corresponded to the limits of the S space of interest (Figure 8.13). The data in the region of interest was integrated to produce a one-dimensional data set of intensity versus S.

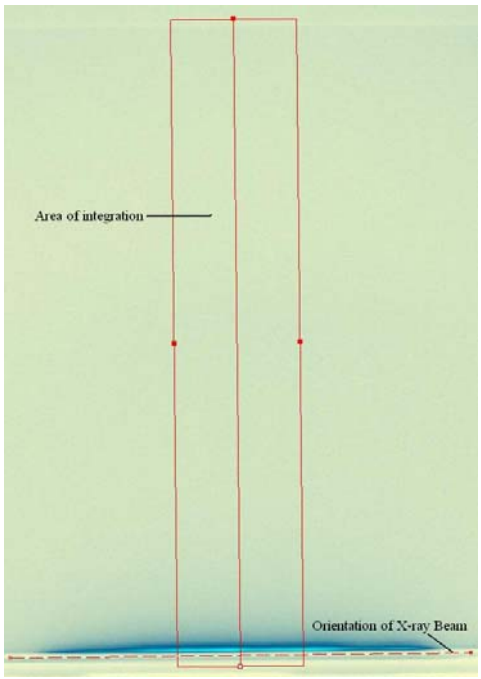

Figure 8.13 SAXSess X-ray scattering image showing annotation for integration

The dotted line is adjusted to match the orientation of the X-ray beam as the image plate may not be in the same position of exposure or reading. Once the position of the annotation was corrected the area inside the box can be integrated to produce the 1D scattering profiles.

8.2.2.2 Calibration

The sample to detector distance was not altered during the experiment, thus the same calibration parameters defining the range of S space observed were useable for all images. However, as the image plate was removed for each sample its vertical position may have changed. To correct for this to origin of S space was set to the position of the direct X-ray beam.

8.2.2.3 Normalisation

The intensity of the X-ray beam observed through the semi transparent beam stop was used to normalise the scatter data from individual samples. A background subtraction was used to remove any structure in the scatter associated with the holder. The background scatter pattern was collected using the sample holder filled with water.

8.3 Data analysis

8.3.1 Peak fitting

8.3.1.1 Summary

Two separate methods of peak fitting were implemented in the processing of data presented in this thesis. One method was used for the preliminary experiments investigating tension and dehydration and a second for the breast tissue and degradation studies. The first used two separate programs, one to fit the amorphous scatter in order for it to be subtracted to accurately fit the peaks using the other. The method of fitting the amorphous scatter was not ideal for subsequent interpretation as it was difficult to use a consistent function for all data when the amorphous scatter varied between samples. Data from the subsequent studies of breast tissue data and degradation were all processed using a fitting program designed for neutron scattering data. The second fitting method allowed fitting of the amorphous scatter scattering peaks simultaneously and was capable of semi automated fitting of multiple X-ray scattering profiles, making the second fitting method both simpler to use and more efficient.

8.3.1.2 Tension and dehydration experiments

The method used for the tension and dehydration experiments used two separate programs. The amorphous scatter was fitted using Table Curve 2D (Systat Software) and the peaks were fitted using Peakfit version 4 (Systat Software). Both Table Curve 2D and Peakfit used least squares minimisation to fit the data. Table Curve 2D fitted a library of equations automatically adjusting the variables, the results were then ranked to show the equation which best fitted the amorphous scatter.

X-ray scattering peaks, though theoretically Lorentzian in nature, are observed to be more Gaussian in practice due the convolution with the X-ray beam and to the normal distribution of spacing values about the mean (see Section 7.7.4). Therefore the Bragg peaks were fitted using a series of Gaussian approximations one for each of the peaks present in the data.

8.3.1.2.1 Processing method

The errors at each point in the X-ray scattering profile (assuming Poisson statistics) were calculated as the square root of the intensity using Excel. The S spacing, intensity and errors were read into table curve, the peaks and beam stop masked off leaving only the background between peaks as the region of interest.

The output of Table Curve 2D was an equation describing the background, which was entered into Excel along with all its variables where it is plotted over the graph of intensity versus S spacing (manually checking that it matched), ensuring the equation and variables were entered correctly. The fitted background was then numerically subtracted from the original intensity value to leave only the peaks.

Using Peakfit the areas between the peaks in the resulting subtracted profile were masked off leaving only the peaks as regions of interest to be fitted. This process was then repeated for all of the profiles in every data series to be fitted. The output from Peakfit was saved in Excel and then collated for interpretation.

8.3.1.2.2 Limitations

As the amorphous scatter was different for each of the different tissues the equation which gave the best fit was different. The aim of the tension and dehydration studies was to observe the changes in the axial peaks which could be achieved using the best fit to the amorphous scatter for accurate subtraction. However, the differences in fitting the amorphous scatter could have been problematic for fitting breast tissue where there was expected variation with disease. Also using two programs where each X-ray scattering profile had to be fitted separately would be time consuming for the large numbers of X-ray scattering profiles for the diagnostic tissue studies and degradation studies. Therefore alternate fitting methods were tested and implemented.

8.3.1.3 Diagnostic breast tissue data and degradation experiments

The peak fitting program selected to process the breast tissue data and the data from the degradation studies was “Peak Analysis” (PAN). PAN is part of the Data Analysis and Visualisation Environment (DAVE). PAN is a peak fitting program designed for use with neutron scattering data which is analogous to X-ray scattering. Using PAN allowed simultaneous fitting of multiple scattering profiles with both a decaying background and any number of peaks. The user defines a set of peaks as a model to fit the data and sets limits to constrain the model. The model is refined automatically within the constraints using a least squares minimisation. The resulting fitted model can then be saved to enable investigation of the peak parameters.

8.3.1.3.1 Data entry

Data was read into PAN using the grouped ASCII function; this allows multiple scatter plots to be fitted using the same model. To prepare the 1D data in the correct format the background subtracted data (see Section 8.2.1.5), stored as an excel spreadsheet containing intensity and S spacing information, was converted to a tab delimited text file format. Using an automated routine written using Interactive Data Language (IDL) (Research Systems inc.), the text file was converted into the correct format for PAN. The output of the IDL routine was a text file containing spacing information in S space, followed by the intensity information and the error at each point calculated using Poisson statistics (i.e. the error is the square root of the intensity) for each X-ray scattering profile in that group.

8.3.1.3.2 Fitting model

The Bragg peaks were fitted using Gaussian approximations (see Section 8.3.1.2). The Bessel functions which are theoretically a sine wave damped with increasing S (see Section 7.7.3.2) were fitted empirically using a series of Gaussian approximations.

The model used to fit all the experimental data (Figure 8.14) combined the Gaussian approximations for the Bragg and Bessel peaks with a quadratic equation defined by a user function with three variables p[0, 1, and 2], to describe the regions between the X-ray scattering peaks. The quadratic equation was defined as:

$$\mathbf{Y = ((x-p[0])^2-p[1])/(4p[2])}$$

Equation 8.1

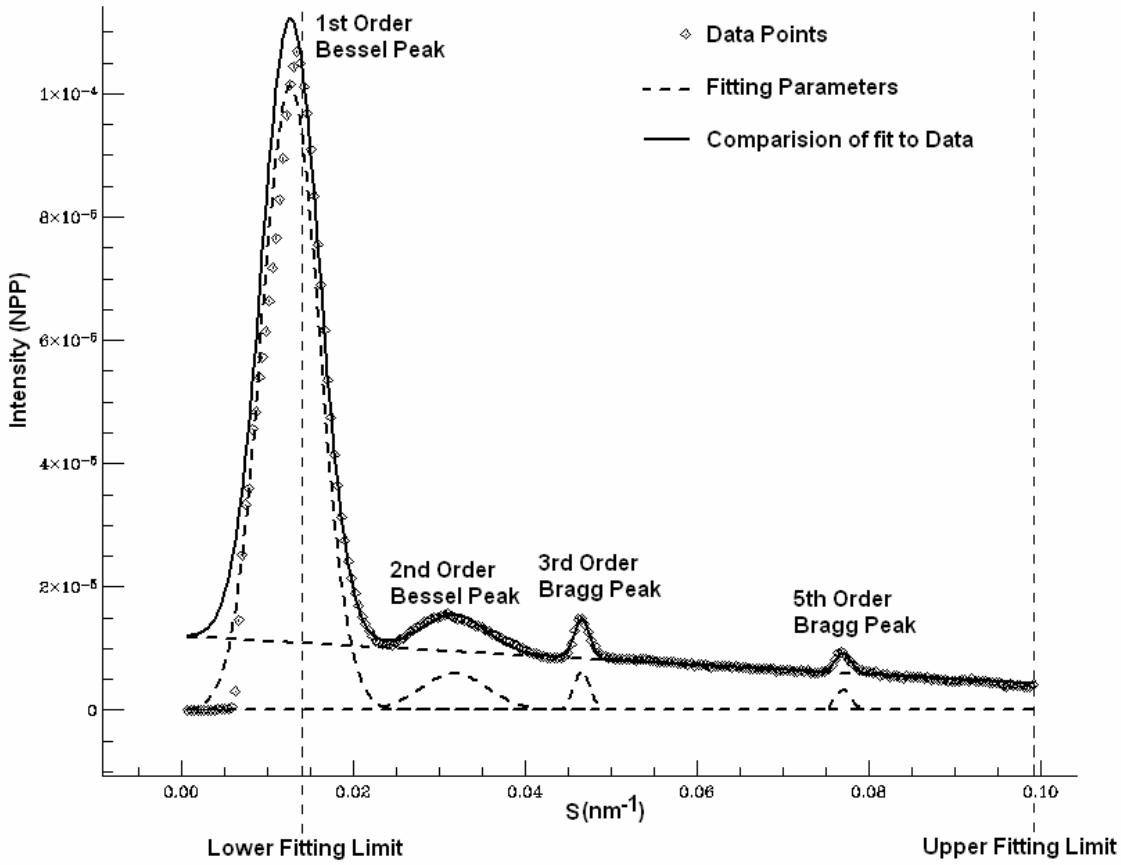

Figure 8.14 Output of PAN fit to show fitting model

8.3.1.3.3 Data output

PAN outputs the fits and the fitted parameters as text files. The output fits are used to calculate the R^2 values to give an indication as to the precision of the fit. The fitted parameters are read into Excel and formatted to enable plotting of different parameters to highlight trends and features of interest within the data.

8.3.2 Amorphous scatter

Parameters to analyse and interpret the amorphous scatter were calculated using Excel. The plot of ln I(s) against S^2 showed a linear section close to the beam stop. The linear estimate function (LINEST) was used to calculate the gradient of a portion of the linear region (S = 0.016 to 0.023 nm^{-1} approximately), which gave the value for Rg (see Section 7.7.5). The value of the power law exponent (see Section 7.7.7) was calculated using LINEST from a portion (S = 0.052 to 0.072 nm^{-1}) of the linear region

between the 3rd and 5th Bragg peaks on the ln I(s) against ln S plot. The portions of the linear regions used to calculate the values for Rg and the power law exponent were chosen so that the errors in the calibration of position would not cause the area to be outside the linear regions in any of the data.

The linear regions used to calculate the relative intensity ratio (RIR) were chosen as the intensity near the beam stop appeared higher in normal tissues than in malignant tissues (Round, 2005). Conversely between the 3rd and 5th Bragg peaks the intensity of amorphous scatter was higher in malignant tissues than normal tissues (Fernandez, 2002). The errors in the intensity normalisation caused by the variation in the attenuation of the beam stop reduced the confidence of directly comparing the intensity of amorphous scatter between two regions. Using a ratio of two points in the X-ray scattering profile eliminated the sensitivity to errors as any offset in intensity would be present in both regions and thus would not affect the result. The average intensity in the linear regions S = 0.007 to 0.012 nm^{-1} near the beam stop and S = 0.052 to 0.72 nm^{-1} between the 3rd and 5th axial peaks, were calculated in Excel. The value for the RIR for each sample was then obtained by dividing the average intensity near the beam stop by the average intensity between the 3rd and 5th axial peaks.

8.3.3 Multivariate analysis

8.3.3.1 Synchrotron X-ray scattering

Multivariate analysis was performed on X-ray scattering data collected using both 1 m and 6.25 m cameras. The X-ray scattering data was prepared in tab delimited text file format, the first column contained the spacing information and subsequent columns were the intensity of X-ray scatter at the corresponding spacing points for each sample.

8.3.3.1.1 1 metre analysis

Principal component analysis (PCA) was performed on data collected with a 1 m camera with the help of Dr C. Kennedy (Cardiff University). The principle components and associated scores were calculated and analysed to determine if differences between the tissue types could be observed and the region of the X-ray scattering data which showed the greatest difference between tissue types.

8.3.3.1.2 6.25 metre analysis

Analysis of the breast tissue data collected using a 6.25 m camera was performed under the supervision of Dr N. Stone (Cranfield post graduate medical school, Gloucester) using Matlab (Mathworks). The data consisted of multiple data collections acquired over 2 years, each data collection was saved as a separate file as although the spacing information was over similar ranges the actual spacing points were not identical. In order to analyse the data from all data sets simultaneously the data points had to be identical, to achieve this all data was fitted with a spline function and sampled at like points along the full range of X-ray scattering observed. The average scattering profile was then calculated and subtracted from each individual profile allowing the variations from the average to be analysed.

Principal component analysis was performed on samples with verified histopathological diagnosis. Only data from cancer samples containing over 80 % tumour tissue by volume was used as a basis to create a model using linear discriminant analysis which uses linear combination of the loadings and scores to maximise separation of the tissue groups. A number of pre-processing steps were tested (intensity normalisation, Log and multiplying by S^2 to scale the intensity) to determine which gave the best model. The validity of the models were tested using the leave one out (cross validation) method, which will show a dramatic reduction in

the accuracy of classification if the model is based on random variations rather than systematic differences between tissue types. Cross validation sequentially omits a single sample during the building of the model and then classifies the omitted sample to the model. The accuracy of the classification was checked using the known diagnosis from the histopathology.

The output of the PCA included the principle components (loadings) and associated scores. The output of the model gave the F values and the performance values for the model. The F values were a measure of the significance of each loading to the model and the critical F value (F crit) was the value of F above which the loading was significant in building the model. The performance values were the percentage of correctly classified samples, both individual for each tissue type and overall all tissue types. Separate performance values were obtained for both the model and its cross validation. The performance values were used to assess the different pre-processing methods. The average 'scores' and significant principal components (F value greater than F crit) from the best model, were then used to interpret the observed differences with regard to structural changes in the samples associated with disease. Data from samples of tissue taken at up to 6 cm away from the site of the tumour were compared to the model and a classification assigned in order to assess the effect at distance previously reported (Lewis, 2000).

8.3.3.2 Conventional X-ray tube scattering

The multivariate analysis software used with the data collected using the SAXSess system was “Pirouette” (Infometrix). The one dimensional scattering profiles were loaded into pirouette in a spreadsheet relating the spacing and the scattering intensity associated with that spacing for all the samples.

Six ordered principal components were calculated as were the 'scores' for each data set (see Section 7.11.4). The 'scores' and principal components were used to determine if there was any separation between the data collected from normal and diseased tissue and to interpret the observed differences with regard to structural changes in the samples.

9 Contribution to Knowledge

This section is included as a brief summary of the major areas where this thesis is a contribution to scientific knowledge.

- Corroboration of the previously reported 0.3 nm increase in D spacing of malignant collagen compared to collagen from normal tissue (Fernandez, 2002).

- Corroboration of reduction in axial peak intensity in cancer invaded regions of collagenous breast tissue (Lewis, 2000 and Fernandez, 2002).

- Supported previous research that changes to collagen are not localised and that changes to collagen are visible using X-ray scattering. Furthermore it is proposed that these changes can be used to classify samples taken at distance from diseased areas as cancer but which are identified normal by histopathology.

- First to propose biological mechanism of production of OF/LB collagen and MMP action to explain the structural differences between normal malignant and benign tissues observed using X-ray scattering.

- Showed that MMP action alone cannot be responsible for all changes between normal and diseased tissues observed using X-ray scattering.

- Proposed presence of OF/LB to be responsible for reduction of peak intensity increase in D spacing and increase in average size of scattering objects in fibroadenomas.

- Proposed the presence of OF/LB in both fibroadenoma and malignant tissues. The OF/LB collagen near malignant samples being further remodelled by the action of MMP. MMP action further reduces axial peak intensity and the average size of scattering objects and is responsible for the increase of surface area of scattering objects with length scale of a few tens of nanometres. The degradation of the surrounding collagen by MMP action allows the cancer cells to metastasise hence the malignant phenotype.

- First publication of automated diagnosis using PCA, on data collected using angular dispersive small angle X-ray scattering from a conventional X-ray source.

- X-ray scattering using a conventional source can also detect changes at distance from tumour and that with further study a dedicated clinical tool may be developed.

10 Results

10.1 Summary

The results presented in this section were the product of a number of separate experiments. Firstly the results of the investigations to ascertain the extent experimental parameters will affect the X-ray scattering pattern of collagen were presented. Secondly the data from X-ray scattering from breast tissue from both synchrotron and conventional X-ray sources were presented, followed by the investigations to determine the possible causes for the structural changes attributed to disease. This data included results from degraded collagen and computer simulation of X-ray scattering profiles from a model collagen system.

X-ray scattering intensity was presented in Normalised Photons per Pixel (NPP) following the normalisation of the intensity of the observed direct X-ray beam to 1 (see Section 8.2.1.3). Position of scattering features was presented using S (see Equation 7.21 in Section 7.7.3).

10.2 Parameters which may affect X-ray scattering from collagen

The sample mounting procedure for the collection of data from breast tissue samples requires suction to draw the sample into the capillary tubes and therefore the application of force (see Section 8.1.2.4.1). In order to determine the extent of the changes to the scattering pattern of collagen which could be caused by this mounting procedure, a series of experiments relating the change in force applied to a sample of collagen and the X-ray scattering pattern observed were undertaken.

10.2.1 Hydrated rat tail tendon with applied force

Twelve Bragg peaks corresponding to the 1st to the 12th order reflections of the 67 nm spacing of the collagen were present in all the images in the series. The degree of preferential alignment increases with the application of force (Figure 10.1) which was observed as a decrease in the width of the arc of the diffraction peaks (see Section 7.7.2), also the direction of preferential alignment changed as force was applied. The application of force pulls the tendon in line with the direction of the force, aligning fibrils and therefore increasing the degree of preferential alignment. The change in direction of preferential alignment indicated that the sample was not aligned in the direction of loading when mounted.

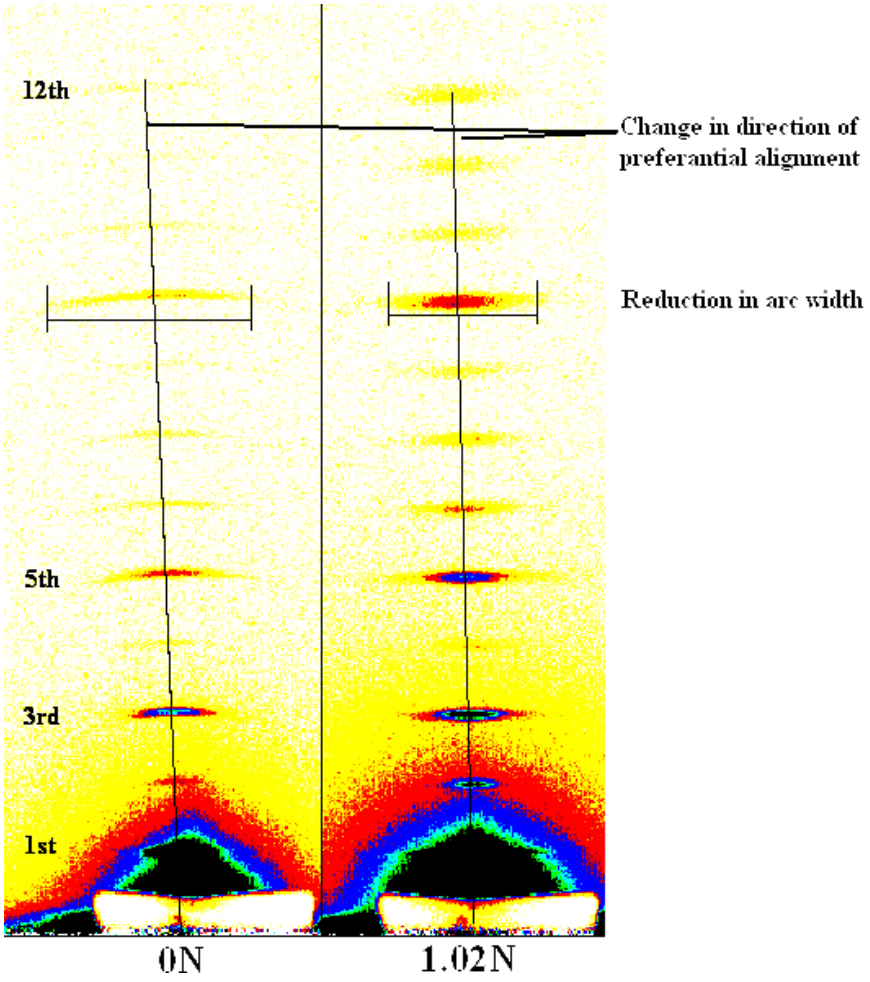

Figure 10.1 X-ray scattering data from hydrated rat tail tendon

With the application of load the direction of preferential alignment changed to reflect the direction of the applied load. The reduction in the width of the arcs of the peaks also indicated an increase in the degree of preferential alignment.

From the 1 dimensional (1D) plot (Figure 10.2) the X-ray scattering profile with no external loading has lower peak intensity for all visible orders compared to the two X-ray scattering profiles with applied load. Only three sets of data (0 N, 0.48 N and 1.02 N) were available for hydrated rat tail tendon as the sample snapped during the application of the next progressive load.

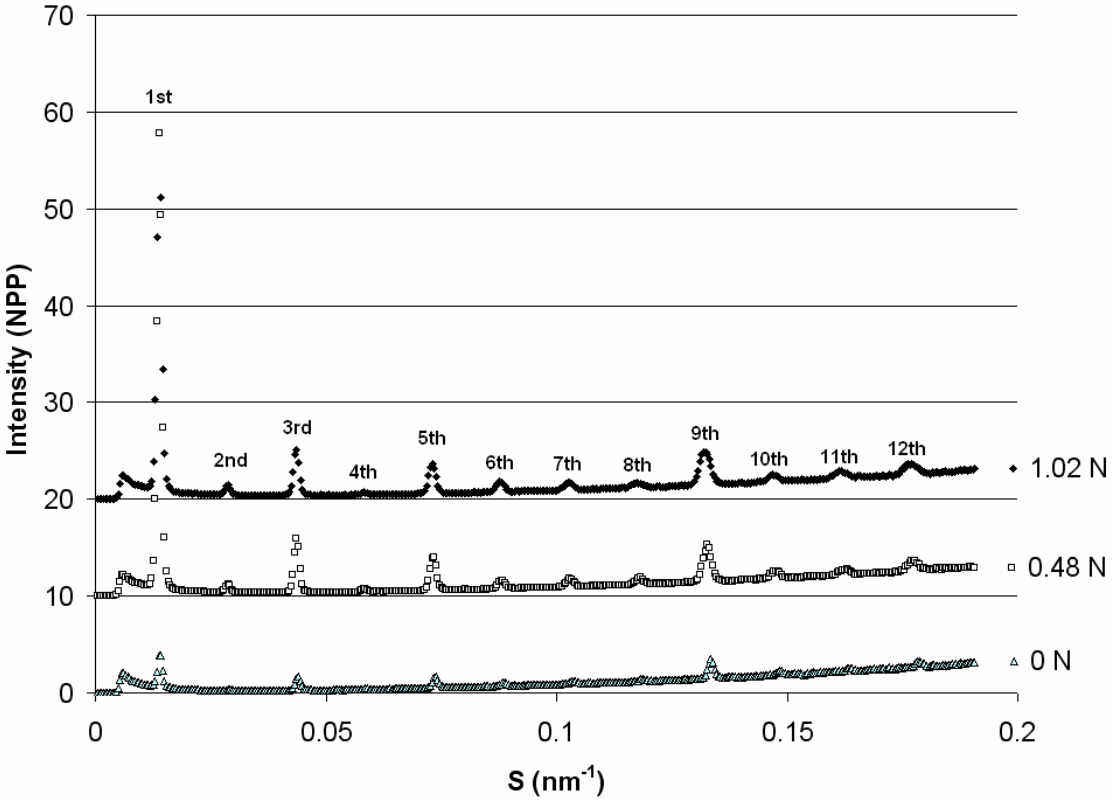

Figure 10.2 X-ray scattering from hydrated rat tail tendon with applied force

The intensity values were scaled by multiplying them by S^2 and the profiles were offset to allow improved visualisation of the changes with force. Twelve orders of the axial collagen peaks were visible, application of 0.48 N resulted in a large increase in peak intensity and a change in peak position to smaller S spacing. Further addition of force to 1.02 N resulted in a greater reduction of S spacing the peak positions though no further peak intensity changes were visible.

The peak parameters calculated by fitting the X-ray scattering profile (see Section 8.3.1) were summarised (Table 10.2.1). The application of force (0.48 N) causes an increase in the peak intensity of all the orders visible. The first order peak shows the greatest difference with the load, being a factor of 7 larger after the application of force compared to no loading which suggested an increase in the degree of order of

the collagen with increased force. Increasing the force from 0.48 N to 1.02 N did not appear to increase the peak intensity greatly. The peak intensities were different between the data for 0.48 N and 1.02 N observed as an increase the intensity of the even order peaks, while the odd orders (1, 3, 5, 7 and 9) exhibited lower intensities at 1.02 N than at 0.48 N. A change in the intensity ratios of the odd and even order peaks indicated changes to the electron density of the sample associated with dehydration. Though the effects of dehydration were limited they were not removed completely (see Section 11.2.2.4 and Section 11.2.2.5). The widths of the all the peaks except the 1st showed in increase of peak width with the application of force, though the errors associated with this change are large (Table 10.2.1). An increase of the peak width suggested that there is a small increase in the distribution of spacing around the average. The graph of applied load against S spacing (Figure 10.3) showed a decrease in spacing with increasing force.

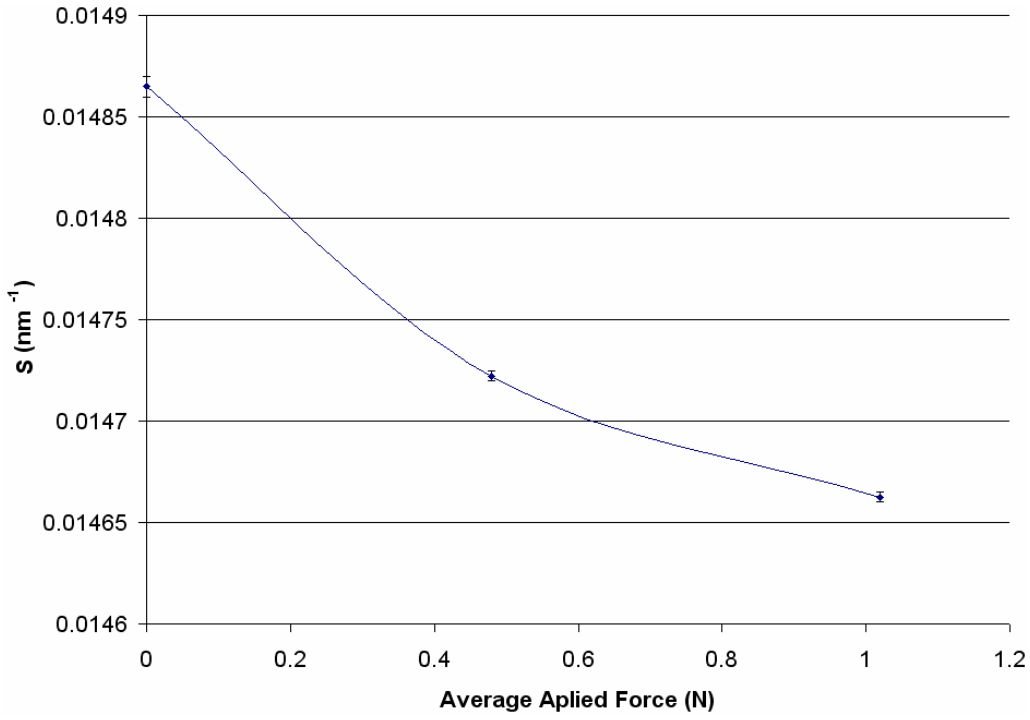

Figure 10.3 Effect of force on S of 1st order axial peak from hydrated rat tail tendon

A decrease in S position is observed with increasing applied force error bars shown are the calculated standard error from the peak fitting process

The decrease in S position of the peaks with increasing force was observed in all visible orders in the scattering profile (Table 10.2.1) indicating an increase in the D spacing of collagen related to the application of force.

Force (N)	0.48		1.02	
Peak Order	Value	Std Error	Value	Std Error
	Peak Intensity (NPP)			
1	2.24E+05	1.01E+03	1.90E+05	8.88E+02
2	9.29E+02	9.99E+02	1.17E+03	8.51E+02
3	2.19E+03	9.33E+02	1.75E+03	8.00E+02
4	6.83E+01	9.31E+02	3.71E+01	7.60E+02
5	4.54E+02	8.65E+02	3.63E+02	7.24E+02
6	7.11E+01	8.09E+02	8.78E+01	6.63E+02
7	4.85E+01	8.02E+02	3.98E+01	6.44E+02
8	3.43E+01	7.83E+02	2.06E+01	6.00E+02
9	1.03E+02	7.44E+02	9.58E+01	5.88E+02
10	1.65E+01	7.10E+02	1.39E+01	6.01E+02
11	8.60E+00	6.87E+02	1.37E+01	5.42E+02
12	1.59E+01	6.93E+02	1.53E+01	5.47E+02
	Peak S Position (nm^{-1})			
1	-0.00013	2.4E-06	-0.00018	2.48E-06
2	-0.00021	0.000549	-0.00037	0.000409
3	-0.00028	0.000215	-0.00044	0.000229
4	-0.00033	0.006325	-0.00055	0.008756
5	-0.00044	0.001025	-0.00072	0.001104
6	-0.00051	0.006175	-0.00086	0.005127
7	-0.0007	0.009268	-0.00106	0.010116
8	-0.00051	0.01557	-0.00111	0.022436
9	-0.0008	0.003763	-0.00138	0.003853
10	-0.00093	0.023173	-0.00154	0.024022
11	-0.001	0.041106	-0.00193	0.033424
12	-0.00108	0.027144	-0.00183	0.026985
	Peak Width (nm^{-1})			
1	-4.17E-05	1.51E-05	-2.18E-05	1.56E-05
2	1.28E-04	3.45E-03	3.55E-04	2.57E-03
3	1.70E-04	1.35E-03	3.73E-04	1.44E-03
4	7.87E-04	3.97E-02	1.40E-03	5.50E-02
5	4.49E-04	6.44E-03	9.31E-04	7.00E-03
6	9.02E-04	3.88E-02	1.67E-03	3.22E-02
7	7.17E-04	5.84E-02	1.76E-03	6.45E-02
8	7.93E-04	9.81E-02	2.60E-03	1.46E-01
9	1.68E-03	2.37E-02	3.13E-03	2.45E-02
10	2.20E-03	1.50E-01	2.94E-03	1.63E-01
11	3.22E-03	2.68E-01	5.16E-03	2.28E-01
12	3.12E-03	1.89E-01	4.94E-03	1.92E-01

Table 10.2.1 Change in peak parameters with applied force

The observed parameters listed were calculated using the 0 N as the initial value and represent the change from the initial values with applied force. The errors shown were the calculated standard errors of the fitting. The application of force causes an increase in the peak intensity of all orders, but increasing the force from 0.48 N to 1.02 N increased only the intensity in the even order peaks the odd orders (1, 3, 5, 7 and 9) exhibit lower intensities at 1.02 N than at 0.48 N. The position in S position of all the peaks reduces indicating an increase in the D spacing of the collagen, though the higher orders exhibit greater errors than the than spacing changes due to the increased error associated with fitting of lower intensity peaks. The width of the first order peak showed a small reduction while all other orders showed a small increase in width However, the change in peak widths were accompanied by relatively large errors.

10.2.2 Hydrated chicken tendon with applied force

Hydrated rat tail tendon samples snapped after the application of loads over 1.0 N and precise control of the tensile testing rig at low loads (<1 N) proved difficult. To allow investigation of a range of forces on collagen without the sample breaking, data was collected from a thick piece of tendon excised from a chicken leg.

The preferential alignment of the collagen was not vertical in the 2D images but was at an angle offset from vertical (Figure 10.4). This was expected as it was noted that the tendon was placed in the beam at a slight angle during the data collection.

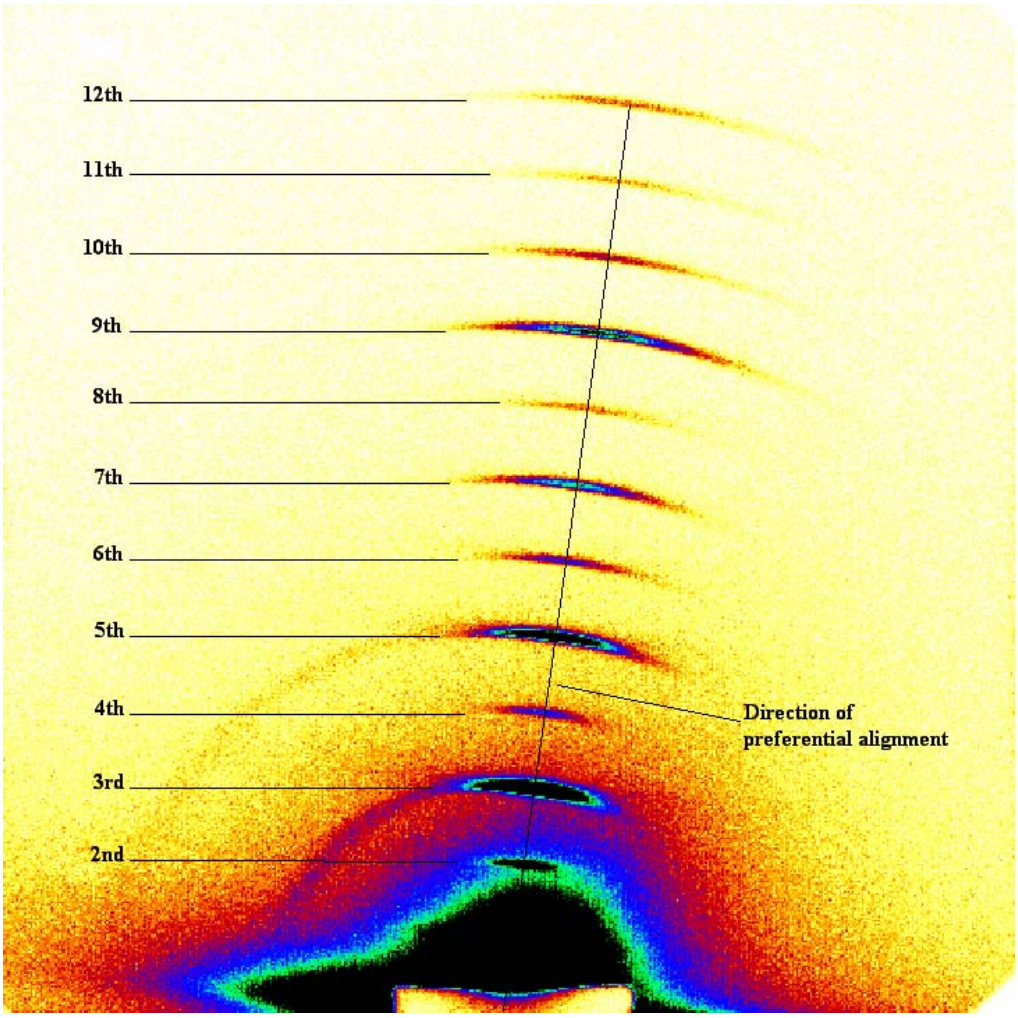

Figure 10.4 X-ray scattering image of hydrated chicken tendon under 22.45 N load

Twelve orders of diffraction were visible in the image though the 1st order was obscured in this image by the background intensity near the beam stop. The direction of preferential alignment is not vertical in this series However, it was noted that the sample was not mounted vertically during the experiment.

Twelve orders of diffraction were visible in all of the X-ray images (Figure 10.4) and X-ray scattering profiles in the series (Figure 10.5). The peak intensity observed in the X-ray scattering profiles increases with load up to approximately 13 N (Figure 10.5 and Figure 10.6) and then remains constant throughout the rest of the series at approximately 9 times the peak intensity with no force (Table 10.2.2). Peak position did not appear to be noticeably affected by the application of force by visual inspection of the X-ray scattering profile However, an increase in peak width with load was visible in the higher orders.

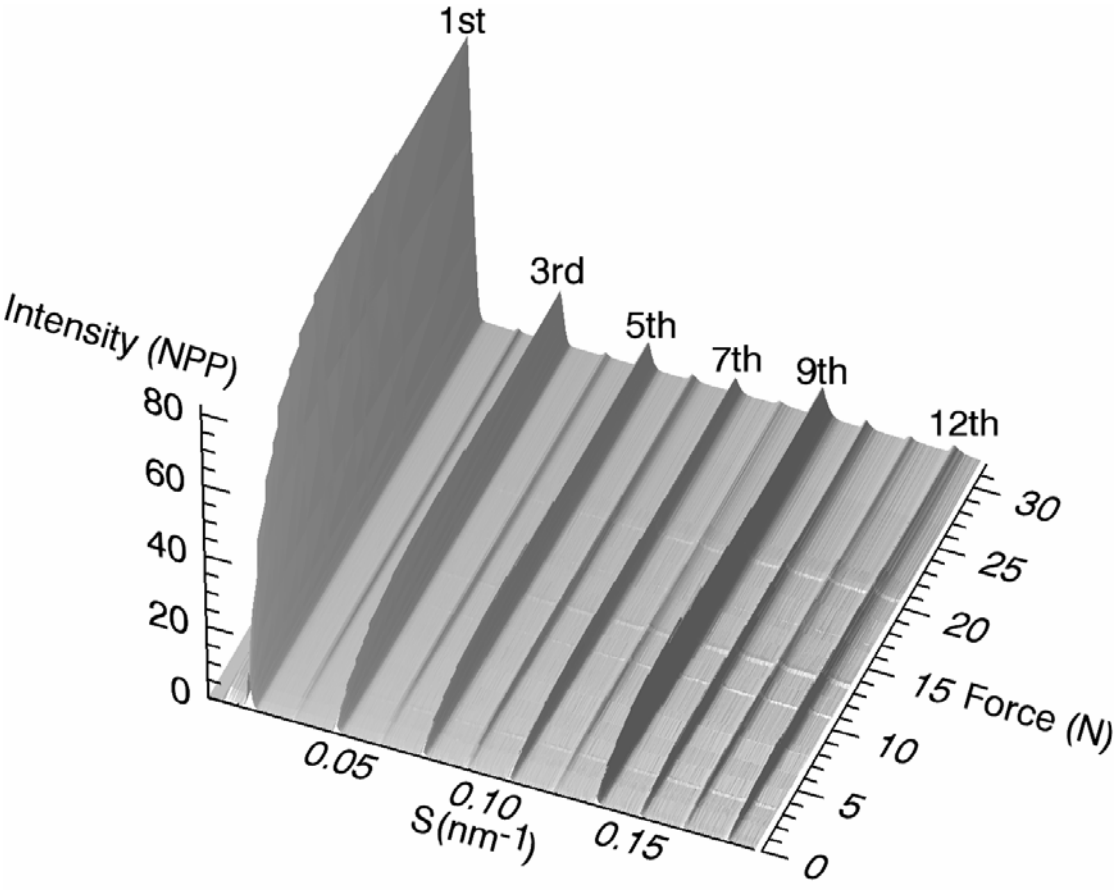

Figure 10.5 X-ray scattering from chicken tendon with varying applied force

An increase in force caused an increase in observed intensity up to approximately 13 N, above which the intensity appeared constant.

The peak intensity, position and width were quantified using peak fitting methods (see Section 8.3.1) the fitted parameters and associated standard errors were summarised in Table 10.2.2, Table 10.2.3 and Table 10.2.4 respectively.

	Peak 1 (NPP)		Peak 2 (NPP)		Peak 3 (NPP)		Peak 4 (NPP)		Peak 5 (NPP)	
Average Force (N)	Intensity	Std Error	Intensity	Std Error	Intensity	Std Error	Intensity	Std Error	Intensity	Std Error
0	4.882E+04	6.972E+02	1.217E+02	6.836E+02	9.674E+02	6.663E+02	3.318E+01	7.305E+02	2.240E+02	6.647E+02
0.29	7.480E+04	1.267E+03	1.882E+02	1.217E+03	1.458E+03	1.208E+03	4.351E+01	1.238E+03	3.294E+02	1.206E+03
0.745	1.144E+05	2.079E+03	2.889E+02	2.052E+03	2.145E+03	1.991E+03	6.953E+01	2.241E+03	4.861E+02	1.971E+03
1.685	1.981E+05	2.582E+03	5.177E+02	2.483E+03	3.701E+03	2.461E+03	1.168E+02	2.452E+03	8.234E+02	2.439E+03
1.865	1.932E+05	2.520E+03	4.951E+02	2.437E+03	3.530E+03	2.396E+03	1.206E+02	2.470E+03	7.931E+02	2.371E+03
2.355	1.869E+05	2.361E+03	4.812E+02	2.261E+03	3.418E+03	2.248E+03	1.075E+02	2.344E+03	7.678E+02	2.215E+03
3.03	2.609E+05	2.786E+03	6.754E+02	2.714E+03	4.918E+03	2.660E+03	1.699E+02	2.699E+03	1.087E+03	2.598E+03
3.245	2.565E+05	3.168E+03	6.854E+02	3.157E+03	4.848E+03	3.041E+03	1.664E+02	3.155E+03	1.072E+03	2.961E+03
3.76	2.563E+05	2.079E+03	6.779E+02	1.969E+03	4.785E+03	1.946E+03	1.725E+02	2.042E+03	1.054E+03	1.893E+03
4.105	2.963E+05	3.254E+03	7.922E+02	3.157E+03	5.711E+03	3.114E+03	2.139E+02	3.188E+03	1.249E+03	3.030E+03
4.605	2.935E+05	3.199E+03	7.839E+02	3.133E+03	5.612E+03	3.033E+03	2.028E+02	3.075E+03	1.240E+03	2.974E+03
4.945	3.383E+05	3.474E+03	9.611E+02	3.399E+03	6.634E+03	3.312E+03	2.614E+02	3.328E+03	1.433E+03	3.222E+03
5.13	3.350E+05	3.404E+03	9.392E+02	3.317E+03	6.583E+03	3.251E+03	2.560E+02	3.307E+03	1.422E+03	3.158E+03
5.39	3.157E+05	3.373E+03	8.846E+02	3.292E+03	6.152E+03	3.218E+03	2.367E+02	3.280E+03	1.357E+03	3.161E+03
6.005	3.283E+05	3.163E+03	9.221E+02	3.024E+03	6.387E+03	3.006E+03	2.377E+02	3.022E+03	1.409E+03	2.940E+03
6.58	3.656E+05	3.347E+03	1.048E+03	3.230E+03	7.210E+03	3.146E+03	2.949E+02	3.215E+03	1.539E+03	3.039E+03
6.84	3.639E+05	3.377E+03	1.040E+03	3.283E+03	7.201E+03	3.186E+03	2.913E+02	3.315E+03	1.536E+03	3.070E+03
7.505	3.652E+05	3.176E+03	1.033E+03	3.088E+03	7.239E+03	3.002E+03	2.908E+02	3.047E+03	1.558E+03	2.910E+03
8.12	3.915E+05	3.498E+03	1.178E+03	3.392E+03	7.816E+03	3.267E+03	3.331E+02	3.333E+03	1.635E+03	3.161E+03
8.34	3.905E+05	3.583E+03	1.168E+03	3.510E+03	7.780E+03	3.381E+03	3.262E+02	3.379E+03	1.637E+03	3.243E+03
8.63	3.905E+05	2.551E+03	1.156E+03	2.472E+03	7.755E+03	2.365E+03	3.163E+02	2.351E+03	1.634E+03	2.268E+03
9.455	3.860E+05	3.786E+03	1.136E+03	3.797E+03	7.743E+03	3.571E+03	3.127E+02	3.531E+03	1.644E+03	3.434E+03
10.27	4.105E+05	3.790E+03	1.253E+03	3.829E+03	8.147E+03	3.525E+03	3.533E+02	3.464E+03	1.648E+03	3.359E+03
10.435	4.100E+05	3.714E+03	1.250E+03	3.627E+03	8.129E+03	3.459E+03	3.468E+02	3.405E+03	1.659E+03	3.338E+03
10.775	4.084E+05	3.974E+03	1.255E+03	4.011E+03	8.174E+03	3.727E+03	3.500E+02	3.658E+03	1.666E+03	3.522E+03
11.08	4.081E+05	3.999E+03	1.229E+03	3.925E+03	8.161E+03	3.751E+03	3.513E+02	3.726E+03	1.676E+03	3.562E+03
12.09	4.066E+05	3.384E+03	1.238E+03	3.294E+03	8.178E+03	3.172E+03	3.435E+02	3.145E+03	1.692E+03	3.023E+03
13.115	4.170E+05	3.523E+03	1.310E+03	3.397E+03	8.108E+03	3.222E+03	3.582E+02	3.138E+03	1.574E+03	3.001E+03
13.435	4.184E+05	3.623E+03	1.290E+03	3.543E+03	8.234E+03	3.347E+03	3.541E+02	3.226E+03	1.592E+03	3.095E+03
13.785	4.183E+05	3.687E+03	1.301E+03	3.619E+03	8.249E+03	3.412E+03	3.583E+02	3.342E+03	1.614E+03	3.179E+03
14.895	4.184E+05	3.431E+03	1.293E+03	3.287E+03	8.301E+03	3.174E+03	3.573E+02	3.076E+03	1.651E+03	2.992E+03
16.08	4.133E+05	3.558E+03	1.289E+03	3.434E+03	7.785E+03	3.182E+03	3.487E+02	3.125E+03	1.436E+03	2.923E+03
16.365	4.149E+05	3.689E+03	1.272E+03	3.539E+03	7.892E+03	3.354E+03	3.453E+02	3.204E+03	1.485E+03	3.075E+03
16.695	4.171E+05	3.306E+03	1.308E+03	3.149E+03	7.965E+03	2.978E+03	3.548E+02	2.887E+03	1.516E+03	2.766E+03
17.2	4.188E+05	3.638E+03	1.297E+03	3.504E+03	8.044E+03	3.298E+03	3.560E+02	3.211E+03	1.521E+03	3.050E+03
18.51	4.201E+05	3.714E+03	1.289E+03	3.602E+03	8.140E+03	3.389E+03	3.626E+02	3.288E+03	1.562E+03	3.152E+03
20.1	4.096E+05	2.728E+03	1.267E+03	2.587E+03	7.486E+03	2.390E+03	3.339E+02	2.309E+03	1.368E+03	2.190E+03
20.415	4.109E+05	3.348E+03	1.274E+03	3.154E+03	7.586E+03	2.959E+03	3.385E+02	2.863E+03	1.389E+03	2.710E+03
20.89	4.130E+05	3.215E+03	1.285E+03	3.082E+03	7.652E+03	2.857E+03	3.413E+02	2.746E+03	1.412E+03	2.618E+03
21.865	4.148E+05	3.353E+03	1.286E+03	3.207E+03	7.766E+03	2.991E+03	3.500E+02	2.873E+03	1.449E+03	2.749E+03
26.665	4.101E+05	2.985E+03	1.314E+03	2.833E+03	7.434E+03	2.602E+03	3.358E+02	2.505E+03	1.342E+03	2.379E+03
31.94	4.089E+05	3.030E+03	1.284E+03	2.893E+03	7.376E+03	2.637E+03	3.223E+02	2.525E+03	1.330E+03	2.408E+03

Table 10.2.2 Fitted peak intensity (NPP) against force (N) and associated standard errors

The application of force up to 13 N caused in increase in the intensities of the axial peaks an average of 9 times the observed intensity with no force. Force above 13 N did not further increase the observed intensities.

The increase in peak intensity up to 13 N was clearly observed in the plot of the 1st order peak intensity against applied force (Figure 10.6). The increase in intensity was attributed to an increase in the alignment and ordering of the sample as the fibres are pulled into line with the direction of the applied force.

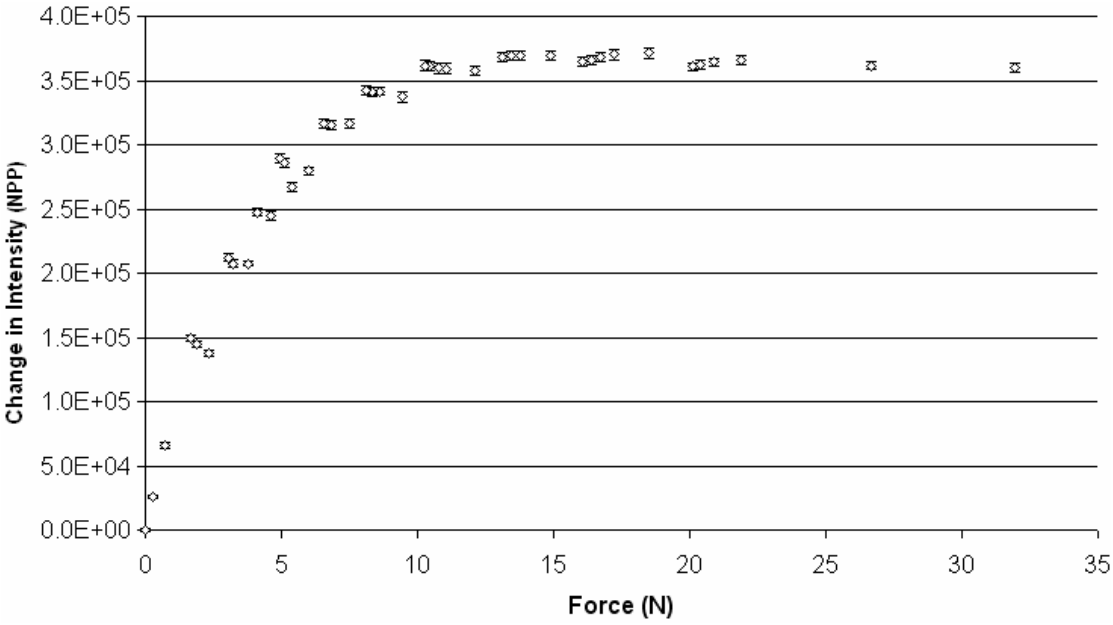

Figure 10.6 Change in 1st order axial peak intensity against applied force

The change in intensity is measured as the difference at each point from the intensity observed with no applied force. The errors shown are the standard errors calculated in the fitting process. The increase in peak intensity with force was observed up to approximately 13 N above which the peak intensity remains constant.

The changes to the peak positions occur below 13 N, above this value the 1st order shows little change (Figure 10.7), while the higher orders show a small increase in spacing (Table 10.2.3). However, this increase is not force dependant but time dependant (Figure 10.8) and was attributed to a result of dehydration (see Section 11.2.3.2). The change in peak position observed as a result of the application of forces above 13 N corresponds to a change to the D spacing of the collagen of 1.3 nm. The region with the greatest rate of change was below 5 N which corresponds to approximately 0.5 nm/N, between 5 N to 10 N the rate of change falls to 0.007 nm/N beyond which the rate of change reduces to negligible levels.

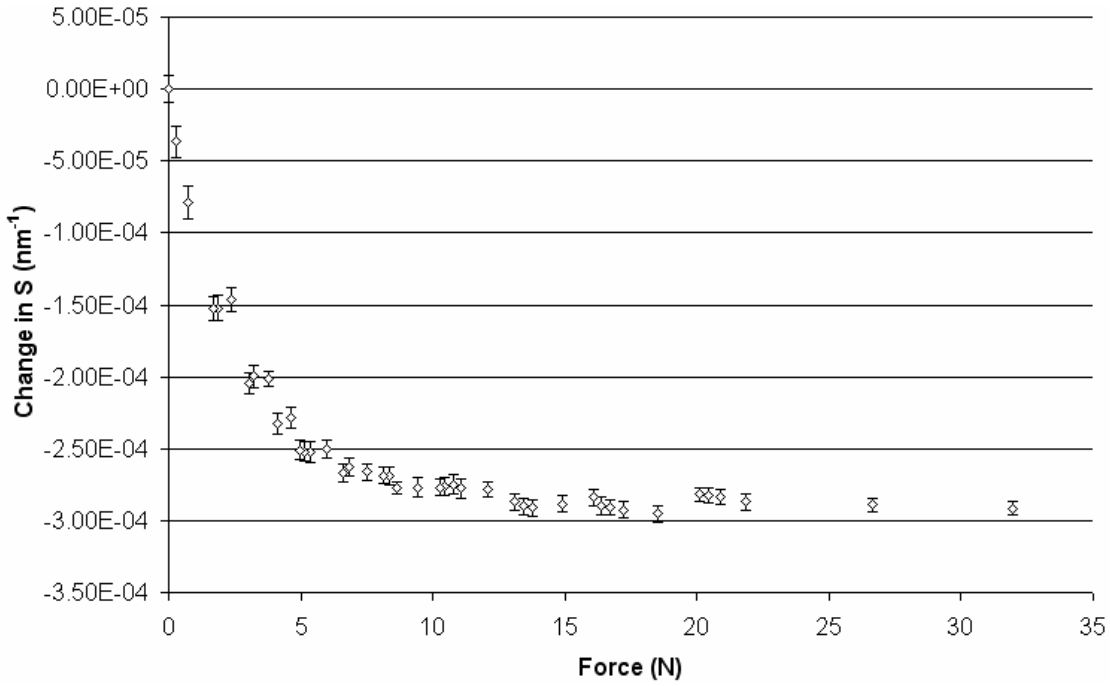

Figure 10.7 Change in S position of 1st order peak against applied force

The change in peak position is measured as the difference at each point from the peak position observed with no applied force. The errors shown are the standard errors calculated in the fitting process. The peak position reduces most dramatically at low force (<5 N), between 5 N and 10 N the rate of change with force was reduced and above 13 N increased force does not result an observable change in peak position.

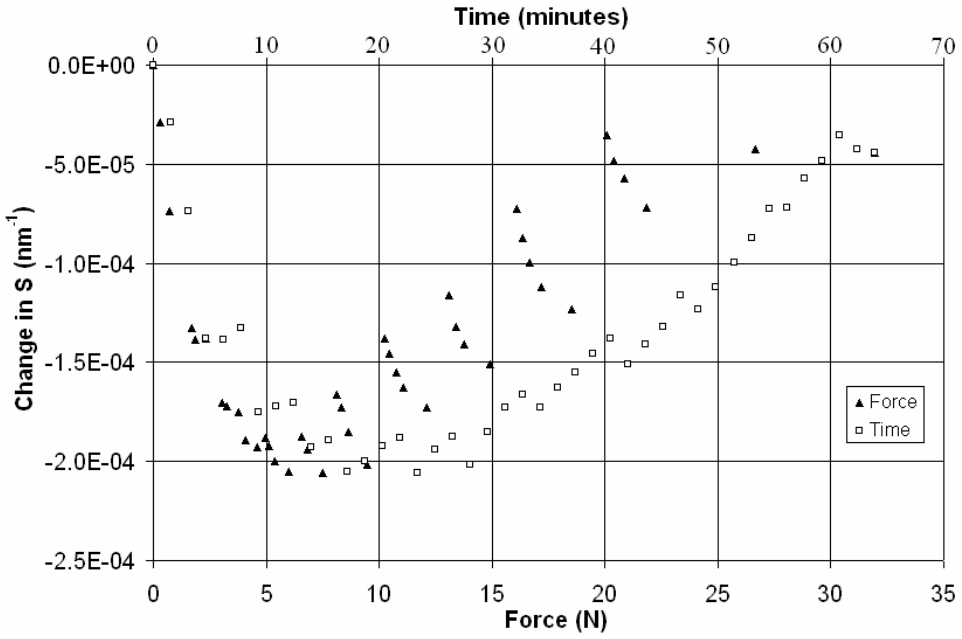

Figure 10.8 Change in S position of 3rd order axial peak against time and force

Below 5 N the change in D spacing is dependant on force. Above 5 N the effect of force is minimal. The time (dehydration) dependant effect occurs between 10 and 20 minutes showing a nearly linear relationship between the change in S spacing and time. The application of force did affect the spacing shown by the periodic reductions which correspond to the time when an increase in force was applied. However, this change was minimal when compared to the change caused by dehydration.

	Peak 1 S (nm^{-1})		Peak 2 S (nm^{-1})		Peak 3 S (nm^{-1})		Peak 4 S (nm^{-1})		Peak 5 S (nm^{-1})	
Average Force (N)	Position	Std Error	Position	Std Error	Position	Std Error	Position	Std Error	Position	Std Error
0	1.493E-02	9.437E-06	2.985E-02	3.897E-03	4.478E-02	4.944E-04	5.970E-02	1.318E-02	7.463E-02	2.192E-03
0.29	1.489E-02	1.112E-05	2.979E-02	4.609E-03	4.475E-02	5.971E-04	5.970E-02	1.989E-02	7.458E-02	2.659E-03
0.745	1.485E-02	1.192E-05	2.981E-02	4.868E-03	4.470E-02	6.642E-04	5.959E-02	1.942E-02	7.455E-02	2.967E-03
1.685	1.477E-02	8.546E-06	2.973E-02	3.403E-03	4.464E-02	4.783E-04	5.956E-02	1.530E-02	7.450E-02	2.181E-03
1.865	1.477E-02	8.548E-06	2.970E-02	3.449E-03	4.464E-02	4.902E-04	5.953E-02	1.395E-02	7.449E-02	2.209E-03
2.355	1.478E-02	8.296E-06	2.972E-02	3.382E-03	4.464E-02	4.764E-04	5.953E-02	1.533E-02	7.448E-02	2.153E-03
3.03	1.472E-02	7.050E-06	2.966E-02	2.808E-03	4.461E-02	3.918E-04	5.952E-02	1.123E-02	7.448E-02	1.813E-03
3.245	1.473E-02	8.134E-06	2.966E-02	3.197E-03	4.460E-02	4.505E-04	5.953E-02	1.324E-02	7.447E-02	2.095E-03
3.76	1.472E-02	5.210E-06	2.968E-02	2.050E-03	4.460E-02	2.916E-04	5.951E-02	7.675E-03	7.447E-02	1.352E-03
4.105	1.469E-02	7.236E-06	2.963E-02	2.806E-03	4.459E-02	3.925E-04	5.952E-02	1.027E-02	7.447E-02	1.844E-03
4.605	1.470E-02	7.152E-06	2.964E-02	2.744E-03	4.458E-02	3.920E-04	5.951E-02	1.075E-02	7.446E-02	1.809E-03
4.945	1.467E-02	6.773E-06	2.962E-02	2.450E-03	4.459E-02	3.624E-04	5.953E-02	9.155E-03	7.449E-02	1.725E-03
5.13	1.467E-02	6.715E-06	2.963E-02	2.472E-03	4.458E-02	3.577E-04	5.953E-02	9.047E-03	7.448E-02	1.705E-03
5.39	1.467E-02	7.056E-06	2.961E-02	2.597E-03	4.458E-02	3.796E-04	5.951E-02	9.821E-03	7.447E-02	1.755E-03
6.005	1.468E-02	6.304E-06	2.962E-02	2.328E-03	4.457E-02	3.404E-04	5.953E-02	9.202E-03	7.445E-02	1.570E-03
6.58	1.466E-02	6.001E-06	2.960E-02	2.178E-03	4.459E-02	3.206E-04	5.956E-02	7.814E-03	7.451E-02	1.555E-03
6.84	1.466E-02	6.090E-06	2.961E-02	2.184E-03	4.458E-02	3.232E-04	5.955E-02	8.106E-03	7.450E-02	1.573E-03
7.505	1.466E-02	5.724E-06	2.960E-02	2.077E-03	4.457E-02	3.028E-04	5.953E-02	7.427E-03	7.448E-02	1.451E-03
8.12	1.466E-02	5.882E-06	2.962E-02	2.021E-03	4.461E-02	3.124E-04	5.960E-02	7.370E-03	7.456E-02	1.554E-03
8.34	1.466E-02	6.065E-06	2.962E-02	2.078E-03	4.460E-02	3.224E-04	5.960E-02	7.738E-03	7.454E-02	1.597E-03
8.63	1.465E-02	4.243E-06	2.962E-02	1.449E-03	4.459E-02	2.250E-04	5.958E-02	5.586E-03	7.453E-02	1.113E-03
9.455	1.465E-02	6.460E-06	2.960E-02	2.287E-03	4.457E-02	3.384E-04	5.956E-02	8.470E-03	7.450E-02	1.657E-03
10.27	1.465E-02	6.139E-06	2.963E-02	2.117E-03	4.464E-02	3.323E-04	5.966E-02	7.902E-03	7.461E-02	1.740E-03
10.435	1.465E-02	6.015E-06	2.963E-02	2.030E-03	4.463E-02	3.255E-04	5.967E-02	7.847E-03	7.459E-02	1.686E-03
10.775	1.465E-02	6.482E-06	2.962E-02	2.226E-03	4.462E-02	3.452E-04	5.965E-02	8.259E-03	7.458E-02	1.793E-03
11.08	1.465E-02	6.518E-06	2.962E-02	2.232E-03	4.461E-02	3.476E-04	5.963E-02	8.199E-03	7.456E-02	1.783E-03
12.09	1.465E-02	5.510E-06	2.960E-02	1.857E-03	4.460E-02	2.918E-04	5.959E-02	7.074E-03	7.455E-02	1.480E-03
13.115	1.464E-02	5.651E-06	2.965E-02	1.880E-03	4.466E-02	3.178E-04	5.973E-02	7.391E-03	7.464E-02	1.757E-03
13.435	1.464E-02	5.777E-06	2.963E-02	1.939E-03	4.464E-02	3.181E-04	5.971E-02	7.729E-03	7.463E-02	1.774E-03
13.785	1.463E-02	5.893E-06	2.963E-02	1.941E-03	4.464E-02	3.229E-04	5.968E-02	7.646E-03	7.461E-02	1.773E-03
14.895	1.464E-02	5.470E-06	2.963E-02	1.848E-03	4.463E-02	2.980E-04	5.967E-02	7.153E-03	7.459E-02	1.589E-03
16.08	1.464E-02	5.812E-06	2.967E-02	1.943E-03	4.470E-02	3.448E-04	5.979E-02	7.934E-03	7.471E-02	2.035E-03
16.365	1.464E-02	6.008E-06	2.966E-02	2.043E-03	4.469E-02	3.517E-04	5.977E-02	8.406E-03	7.469E-02	2.021E-03
16.695	1.463E-02	5.314E-06	2.965E-02	1.778E-03	4.468E-02	3.084E-04	5.975E-02	7.170E-03	7.467E-02	1.746E-03
17.2	1.463E-02	5.838E-06	2.964E-02	1.959E-03	4.466E-02	3.353E-04	5.974E-02	7.804E-03	7.466E-02	1.918E-03
18.51	1.463E-02	5.941E-06	2.964E-02	2.034E-03	4.465E-02	3.360E-04	5.972E-02	7.850E-03	7.464E-02	1.887E-03
20.1	1.464E-02	4.517E-06	2.969E-02	1.537E-03	4.474E-02	2.816E-04	5.982E-02	6.622E-03	7.475E-02	1.681E-03
20.415	1.464E-02	5.528E-06	2.969E-02	1.894E-03	4.473E-02	3.394E-04	5.982E-02	7.947E-03	7.474E-02	2.021E-03
20.89	1.464E-02	5.286E-06	2.969E-02	1.775E-03	4.472E-02	3.216E-04	5.982E-02	7.590E-03	7.473E-02	1.899E-03
21.865	1.464E-02	5.469E-06	2.967E-02	1.845E-03	4.470E-02	3.275E-04	5.979E-02	7.581E-03	7.471E-02	1.916E-03
26.665	1.464E-02	4.945E-06	2.969E-02	1.626E-03	4.473E-02	3.124E-04	5.983E-02	7.196E-03	7.474E-02	1.895E-03
31.94	1.463E-02	5.056E-06	2.968E-02	1.686E-03	4.473E-02	3.220E-04	5.982E-02	7.718E-03	7.475E-02	1.958E-03

Table 10.2.3 Fitted peak S positions (nm^{-1}) against force (N) and associated standard errors

The 1st order peak shows a reduction in S position of the peak up to 13 N beyond which the position remained constant. The higher order peaks all show an initial reduction in the peak S position with force However, the effects of force were obscured by the increase in S position caused by dehydration However, large associated standard errors of higher orders result in only the 1st order being adequate for quantitative analysis.

The confidence in the peak positions of the higher (4th and 5th) orders was low as the fitting error was large. The peak intensities of the higher order peaks were relatively low due to short data collection times (90 seconds). The date collection time was kept short in order to collect a reasonable range of data before the effects of dehydration would be observable.

The application of minimal force <5 N caused a reduction in the width of the axial peaks, which suggested that the variance in axial spacing was reduced (Figure 10.9 and Table 10.2.4). At higher forces >10 N there was an increase in the width of the axial peaks which suggests at higher force the variation in the axial peak spacing increases. An increase in peak spacing distribution could be caused by the force not being evenly distributed or by dehydration which would not be even through out the sample. The data at high force >10 N was collected upwards of 20 minutes from when the experiment started so dehydration was likely to have occurred (see Section 11.1).

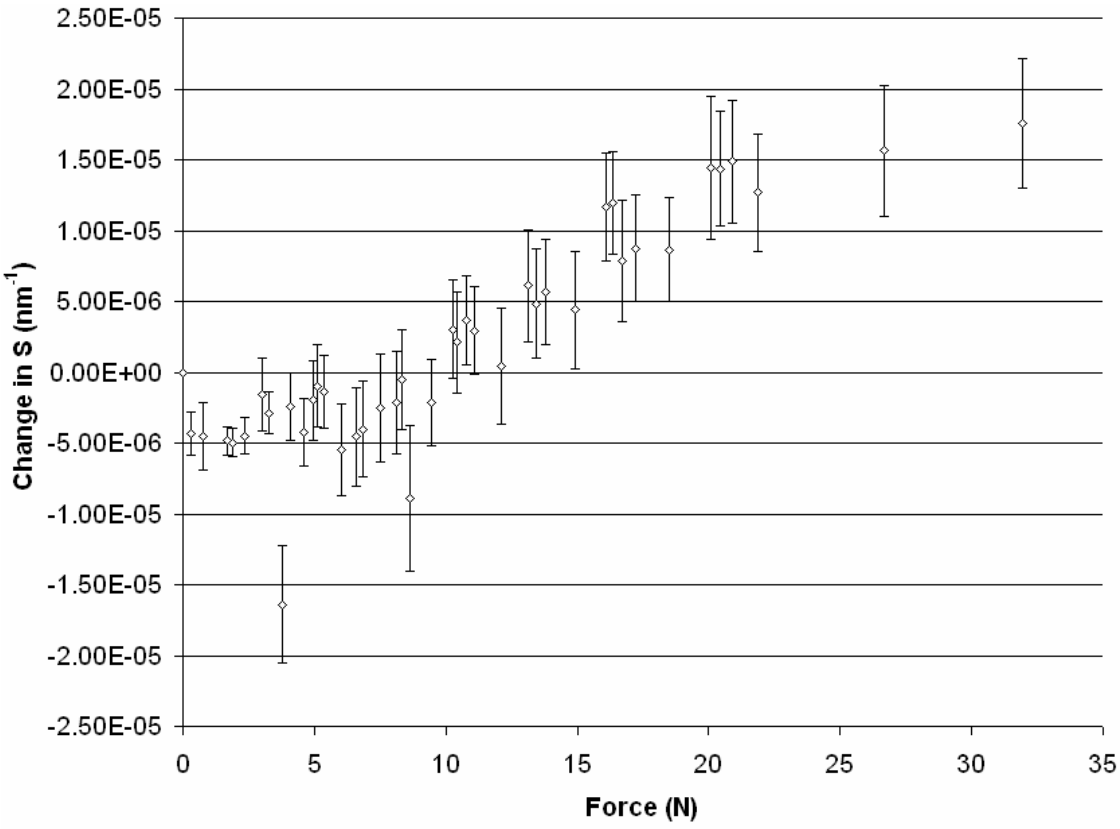

Figure 10.9 Change in 1st order peak width with increasing force

The application of low force (<2 N) caused a reduction in peak width beyond which peak width increased. The reduction in peak width stayed constant until the force was over 10 N where the peak width increased.

	Peak 1 S (nm^{-1})		Peak 2 S (nm^{-1})		Peak 3 S (nm^{-1})		Peak 4 S (nm^{-1})		Peak 5 S (nm^{-1})	
Average Force (N)	Width	Std Error	Width	Std Error	Width	Std Error	Width	Std Error	Width	Std Error
0	5.733E-04	9.618E-06	6.015E-04	4.032E-03	6.220E-04	4.962E-04	5.190E-04	1.329E-02	6.408E-04	2.297E-03
0.29	5.689E-04	1.116E-05	6.181E-04	4.647E-03	6.237E-04	5.971E-04	6.061E-04	2.059E-02	6.298E-04	2.686E-03
0.745	5.688E-04	1.198E-05	5.942E-04	5.047E-03	6.199E-04	6.679E-04	5.179E-04	2.149E-02	6.348E-04	3.000E-03
1.685	5.684E-04	8.617E-06	6.153E-04	3.434E-03	6.230E-04	4.783E-04	6.321E-04	1.549E-02	6.387E-04	2.208E-03
1.865	5.683E-04	8.619E-06	6.075E-04	3.480E-03	6.255E-04	4.902E-04	5.906E-04	1.404E-02	6.404E-04	2.219E-03
2.355	5.688E-04	8.298E-06	6.243E-04	3.419E-03	6.272E-04	4.764E-04	6.070E-04	1.672E-02	6.465E-04	2.155E-03
3.03	5.717E-04	7.053E-06	6.058E-04	2.835E-03	6.274E-04	3.920E-04	6.128E-04	1.135E-02	6.573E-04	1.813E-03
3.245	5.704E-04	8.135E-06	5.966E-04	3.416E-03	6.227E-04	4.555E-04	6.035E-04	1.439E-02	6.575E-04	2.122E-03
3.76	5.568E-04	5.482E-06	6.129E-04	2.111E-03	6.218E-04	2.952E-04	5.616E-04	7.706E-03	6.523E-04	1.353E-03
4.105	5.708E-04	7.241E-06	6.105E-04	2.842E-03	6.236E-04	3.931E-04	5.972E-04	1.035E-02	6.584E-04	1.846E-03
4.605	5.690E-04	7.251E-06	5.960E-04	2.804E-03	6.284E-04	3.923E-04	6.147E-04	1.086E-02	6.532E-04	1.810E-03
4.945	5.713E-04	6.778E-06	6.006E-04	2.479E-03	6.289E-04	3.630E-04	6.231E-04	9.175E-03	6.642E-04	1.727E-03
5.13	5.723E-04	6.720E-06	6.071E-04	2.504E-03	6.275E-04	3.580E-04	6.067E-04	9.060E-03	6.650E-04	1.706E-03
5.39	5.719E-04	7.056E-06	6.050E-04	2.631E-03	6.286E-04	3.796E-04	6.154E-04	1.012E-02	6.531E-04	1.764E-03
6.005	5.678E-04	6.419E-06	6.149E-04	2.330E-03	6.271E-04	3.452E-04	6.286E-04	9.544E-03	6.520E-04	1.577E-03
6.58	5.687E-04	6.120E-06	6.139E-04	2.241E-03	6.363E-04	3.206E-04	6.223E-04	8.103E-03	6.823E-04	1.557E-03
6.84	5.692E-04	6.209E-06	5.998E-04	2.212E-03	6.327E-04	3.235E-04	6.160E-04	8.880E-03	6.815E-04	1.574E-03
7.505	5.708E-04	5.828E-06	6.024E-04	2.106E-03	6.322E-04	3.028E-04	6.138E-04	7.430E-03	6.729E-04	1.451E-03
8.12	5.711E-04	6.004E-06	6.097E-04	2.076E-03	6.474E-04	3.127E-04	6.387E-04	7.727E-03	6.971E-04	1.577E-03
8.34	5.727E-04	6.084E-06	5.997E-04	2.103E-03	6.427E-04	3.232E-04	6.480E-04	7.850E-03	6.981E-04	1.599E-03
8.63	5.643E-04	4.454E-06	5.876E-04	1.462E-03	6.392E-04	2.254E-04	6.522E-04	5.677E-03	6.946E-04	1.114E-03
9.455	5.711E-04	6.585E-06	5.891E-04	2.480E-03	6.355E-04	3.389E-04	6.497E-04	8.478E-03	6.872E-04	1.661E-03
10.27	5.763E-04	6.160E-06	5.938E-04	2.315E-03	6.653E-04	3.328E-04	6.998E-04	8.133E-03	7.409E-04	1.778E-03
10.435	5.754E-04	6.036E-06	6.064E-04	2.055E-03	6.625E-04	3.259E-04	6.939E-04	8.060E-03	7.277E-04	1.755E-03
10.775	5.769E-04	6.489E-06	5.970E-04	2.437E-03	6.558E-04	3.457E-04	6.852E-04	8.361E-03	7.351E-04	1.797E-03
11.08	5.762E-04	6.526E-06	6.067E-04	2.289E-03	6.551E-04	3.480E-04	6.709E-04	8.363E-03	7.266E-04	1.787E-03
12.09	5.736E-04	5.527E-06	6.046E-04	1.859E-03	6.516E-04	2.918E-04	6.706E-04	7.221E-03	7.178E-04	1.483E-03
13.115	5.794E-04	5.651E-06	6.288E-04	1.910E-03	6.927E-04	3.179E-04	7.310E-04	7.403E-03	7.981E-04	1.757E-03
13.435	5.781E-04	5.797E-06	6.129E-04	1.994E-03	6.783E-04	3.201E-04	7.361E-04	7.885E-03	7.906E-04	1.775E-03
13.785	5.789E-04	5.893E-06	6.052E-04	1.966E-03	6.760E-04	3.229E-04	7.108E-04	7.758E-03	7.801E-04	1.779E-03
14.895	5.777E-04	5.470E-06	6.299E-04	1.850E-03	6.750E-04	2.980E-04	7.200E-04	7.180E-03	7.594E-04	1.590E-03
16.08	5.849E-04	5.821E-06	6.330E-04	1.973E-03	7.304E-04	3.448E-04	7.685E-04	8.135E-03	8.660E-04	2.037E-03
16.365	5.852E-04	6.008E-06	6.360E-04	2.044E-03	7.178E-04	3.601E-04	7.856E-04	8.592E-03	8.468E-04	2.040E-03
16.695	5.811E-04	5.334E-06	6.401E-04	1.784E-03	7.145E-04	3.084E-04	7.642E-04	7.234E-03	8.290E-04	1.751E-03
17.2	5.820E-04	5.838E-06	6.283E-04	1.964E-03	7.081E-04	3.353E-04	7.500E-04	7.859E-03	8.282E-04	1.919E-03
18.51	5.819E-04	5.941E-06	6.322E-04	2.109E-03	6.990E-04	3.361E-04	7.508E-04	7.998E-03	8.104E-04	1.896E-03
20.1	5.877E-04	4.537E-06	6.517E-04	1.537E-03	7.639E-04	2.816E-04	8.300E-04	6.790E-03	9.094E-04	1.681E-03
20.415	5.876E-04	5.528E-06	6.623E-04	1.894E-03	7.539E-04	3.406E-04	8.148E-04	8.145E-03	8.972E-04	2.023E-03
20.89	5.881E-04	5.286E-06	6.409E-04	1.779E-03	7.464E-04	3.227E-04	8.181E-04	7.784E-03	8.872E-04	1.901E-03
21.865	5.859E-04	5.469E-06	6.409E-04	1.847E-03	7.365E-04	3.275E-04	8.005E-04	7.617E-03	8.755E-04	1.931E-03
26.665	5.889E-04	4.968E-06	6.536E-04	1.633E-03	7.729E-04	3.125E-04	8.361E-04	7.227E-03	9.258E-04	1.898E-03
31.94	5.908E-04	5.056E-06	6.481E-04	1.686E-03	7.799E-04	3.220E-04	8.538E-04	7.766E-03	9.369E-04	1.962E-03

Table 10.2.4 Fitted peak widths (nm^{-1}) against force (N) and associated standard errors

The peak widths showed an initial decrease with the application of force low force (<2N) further increases in force do not alter the peak widths until over 10N where peak width increases.

10.2.3 Hydrated chicken dermis with applied force

The investigations using rat tail and chicken tendon showed the effects of force on collagen fibres. However, this was not directly applicable to tissues such as breast due to the collagen in these tissues not being preferentially aligned as they are in tendon. Breast tissues are a mixture of other components which my cause differences in the effect with force. To determine the effects of force on a sample more physiologically comparable to breast tissue the effects on hydrated chicken dermis were investigated, thus enabling more confidant interpretation to aid the data collections for X-ray scattering of breast tissue.

Axial peaks up to the 10th order were present in the X-ray scattering images (Figure 10.10) and the X-ray scattering profiles (Figure 10.11). The odd axial orders from chicken dermis have a greater intensity than the even orders which are barely visible. The data collected from all samples in the tension study were normalised using the same method and so the intensity of the axial peaks from the different samples could be compared. The axial peaks from chicken dermis were weak compared with those of the tendon, the 1st order maximum for the chicken dermis was approximately 4 NPP compared to approximately 60 NPP for rat tail tendon and 80 NPP for chicken tendon. Lower peak intensity for tissues was expected as the tendon was almost pure collagen with the highest degree of ordering and preferential alignment. Whereas the collagen in the dermis was not only less ordered but exhibited only minimal preferential alignment and contained fat and cellular material which will attenuate the signal but not contribute to the ordered axial scattering.

There is a region of increased intensity in the arcs visible in the 0 N exposure of the X-ray scattering images (Figure 10.10), which corresponds to the direction force was applied. This preferential alignment could have been naturally present in the dermis but it was thought unlikely for natural alignment to coincidentally line up with the direction in which the force was applied. The preferred orientation in the 0 N data was thought to be caused by the application of force during mounting. The application of load increases the overall peak intensity and increases the maximum intensity in the direction of the applied force which suggested an increase in the preferential alignment. However, the arcs were present throughout the series which suggested that although the fibres were pulled in the direction of the force, the near 360° range of collagen fibril orientation present naturally in the dermis prevents a large increase in preferential alignment and was the reason for the persistence of collagen in directions other than the preferred orientation throughout the series.

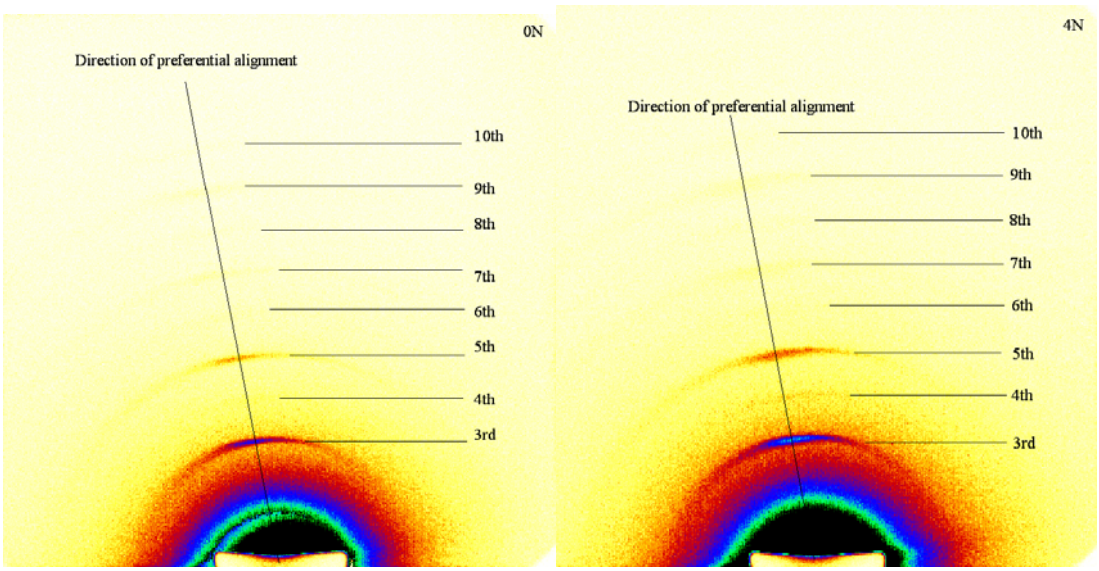

Figure 10.10 X-ray scattering image of hydrated chicken dermis with 0 N and 4 N applied force

Only 10 orders of the axial peak spacing can be observed the peaks were less intense than the tendon and appeared as rings showing minimal preferential alignment before the application of load.

The intensity versus S plot (Figure 10.11) showed that the even order peaks though weak are present, the intensity ratios of strong to weak peaks were as expected for hydrated collagen (see Section 7.8.2) and thus the low intensity of the even peaks was attributed to the reduced intensity compared to the tendon rather than a change to the degree of ordering. The application of force up to approximately 3 N resulted in an increase in intensity of the first order peak beyond which the peak intensity reduced.

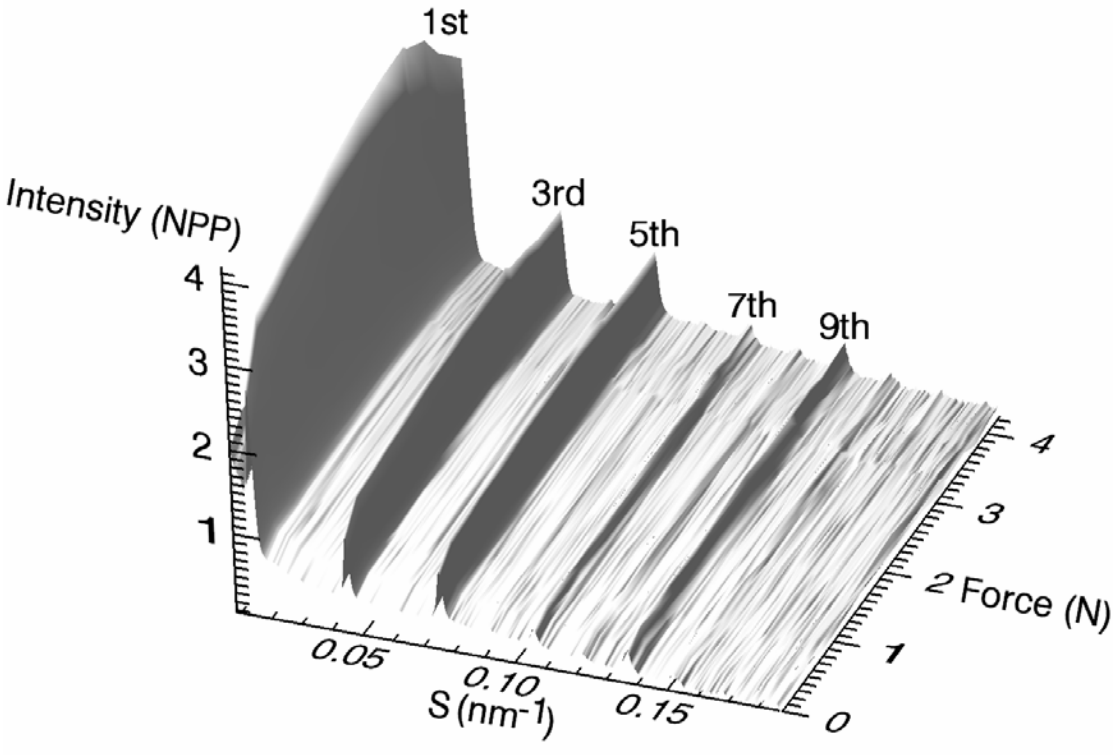

Figure 10.11 X-ray scattering from chicken dermis with varying applied force

Odd orders up to the 9th have greater intensity than the even orders which are present but very weak. Application of force caused an increase in observed intensity up to approximately 3 N beyond which peak intensity reduces.

A measurable shift to lower S with increased force was observed in the higher intensity 1st order peak (Figure 10.12), the shift was less clear in the weaker intensity peaks as it was within the standard error of the fitting (Table 10.2.5).

Minimal (within errors) change was observed in peak width until forces above 2 N were applied (Table 10.2.5). However, as the time of exposure at this time data above 2 N was collected was over 10 minutes after the experiment started the cause of the increase in peak width could be dehydration (see Section 11.1).

	Peak 1 Intensity (NPP)		Peak 3 Intensity (NPP)		Peak 5 Intensity (NPP)	
Average Force (N)	Value	Std Error	Value	Std Error	Value	Std Error
0	7.010E+03	2.116E+02	3.451E+02	1.958E+02	9.733E+01	1.766E+02
0.245	9.286E+03	1.518E+02	4.444E+02	1.409E+02	1.152E+02	1.257E+02
0.61	9.566E+03	1.748E+02	4.567E+02	1.577E+02	1.162E+02	1.406E+02
0.84	1.018E+04	6.735E+01	4.732E+02	6.173E+01	1.187E+02	5.360E+01
1.335	1.060E+04	7.444E+01	4.971E+02	6.743E+01	1.244E+02	5.871E+01
1.705	1.121E+04	1.691E+02	5.074E+02	1.522E+02	1.266E+02	1.352E+02
2.325	1.168E+04	1.797E+02	5.316E+02	1.599E+02	1.309E+02	1.384E+02
2.75	1.195E+04	1.713E+02	5.372E+02	1.513E+02	1.307E+02	1.298E+02
3.185	1.222E+04	1.827E+02	5.367E+02	1.614E+02	1.286E+02	1.368E+02
3.275	1.199E+04	6.678E+01	5.125E+02	5.912E+01	1.252E+02	5.042E+01
3.6	1.138E+04	5.602E+01	4.983E+02	4.957E+01	1.215E+02	4.336E+01
3.82	1.005E+04	1.918E+02	4.668E+02	1.695E+02	1.235E+02	1.556E+02
4.26	8.680E+03	9.154E+01	4.627E+02	8.333E+01	1.254E+02	7.307E+01
	Peak 1 S (nm^{-1})		Peak 3 S (nm^{-1})		Peak 5 S (nm^{-1})	
	Position	Std Error	Position	Std Error	Position	Std Error
0	1.519E-02	2.464E-05	4.556E-02	5.410E-04	7.593E-02	2.127E-03
0.245	1.516E-02	1.361E-05	4.558E-02	3.064E-04	7.596E-02	1.324E-03
0.61	1.517E-02	1.463E-05	4.556E-02	3.397E-04	7.598E-02	1.499E-03
0.84	1.515E-02	5.496E-06	4.553E-02	1.290E-04	7.593E-02	5.921E-04
1.335	1.513E-02	5.722E-06	4.549E-02	1.354E-04	7.587E-02	6.193E-04
1.705	1.511E-02	1.252E-05	4.547E-02	3.097E-04	7.583E-02	1.496E-03
2.325	1.508E-02	1.277E-05	4.541E-02	3.166E-04	7.577E-02	1.482E-03
2.75	1.504E-02	1.206E-05	4.538E-02	3.037E-04	7.572E-02	1.459E-03
3.185	1.501E-02	1.285E-05	4.533E-02	3.311E-04	7.565E-02	1.633E-03
3.275	1.497E-02	4.946E-06	4.529E-02	1.307E-04	7.558E-02	6.353E-04
3.6	1.494E-02	4.428E-06	4.527E-02	1.144E-04	7.556E-02	5.831E-04
3.82	1.494E-02	1.696E-05	4.530E-02	4.129E-04	7.560E-02	1.991E-03
4.26	1.501E-02	9.003E-06	4.539E-02	1.855E-04	7.570E-02	7.818E-04
	Width	Std Error	Width	Std Error	Width	Std Error
0	4.441E-03	1.548E-04	5.189E-03	3.399E-03	6.380E-03	1.339E-02
0.245	4.528E-03	8.549E-05	5.258E-03	1.925E-03	6.606E-03	8.323E-03
0.61	4.356E-03	9.192E-05	5.353E-03	2.135E-03	6.741E-03	9.432E-03
0.84	4.522E-03	3.453E-05	5.383E-03	8.108E-04	7.138E-03	3.721E-03
1.335	4.434E-03	3.596E-05	5.440E-03	8.605E-04	7.142E-03	3.904E-03
1.705	4.517E-03	7.867E-05	5.629E-03	1.977E-03	7.432E-03	1.023E-02
2.325	4.517E-03	8.029E-05	5.734E-03	2.006E-03	7.631E-03	9.358E-03
2.75	4.575E-03	7.579E-05	5.867E-03	1.909E-03	8.008E-03	9.246E-03
3.185	4.676E-03	8.083E-05	5.989E-03	2.080E-03	8.362E-03	1.030E-02
3.275	4.830E-03	3.108E-05	6.162E-03	8.210E-04	8.587E-03	4.086E-03
3.6	4.895E-03	2.782E-05	6.257E-03	7.199E-04	8.617E-03	4.005E-03
3.82	4.837E-03	1.069E-04	6.190E-03	2.597E-03	7.960E-03	1.418E-02
4.26	4.645E-03	5.657E-05	5.605E-03	1.166E-03	7.302E-03	4.927E-03

Table 10.2.5 Peak intensity, position and width for chicken dermis with varied applied force

The errors were the standard errors calculated during the fitting process. The application of force causes an increase in peak intensity up to 3 N above which intensity reduces. Peak position remains constant (within errors) for the first order peak until forces above 1 N were applied at which point position of the peak reduces linearly, the same trend is evident in the 3rd and 5th order peak. However, the low peak intensity results in the standard errors being large. Peak width remains constant until forces over 2 N were applied when peak width increases though the cause of this may be dehydration.

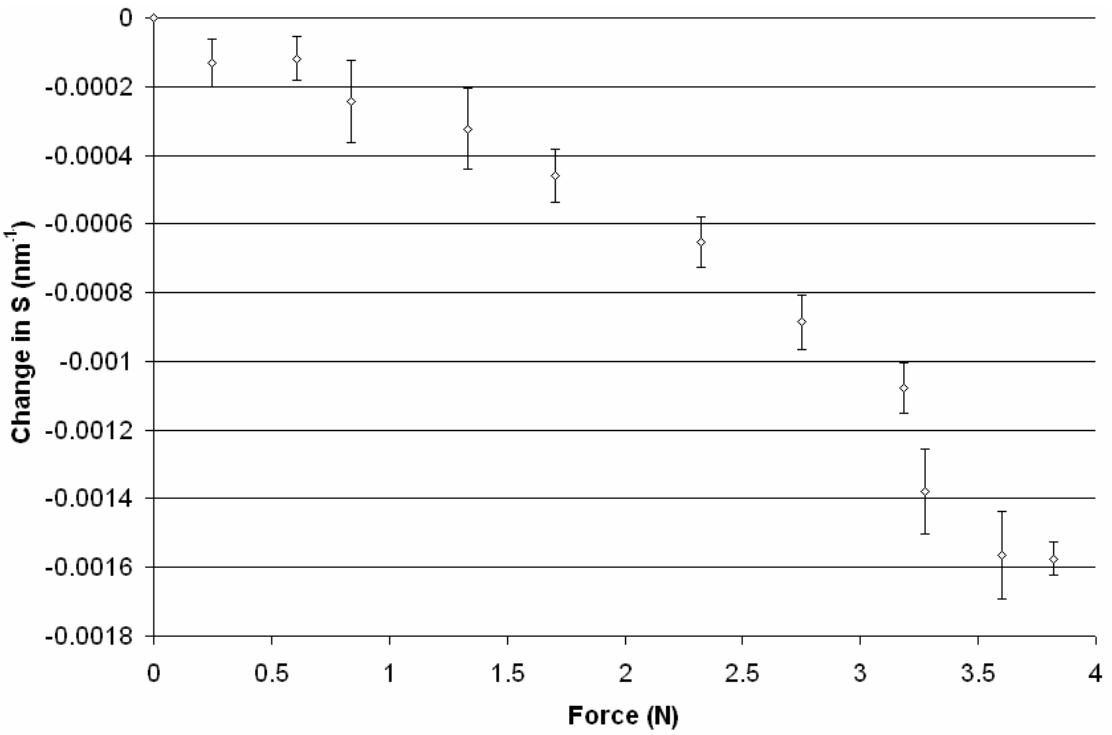

Figure 10.12 Change in S position of 1st order peak against applied force for chicken dermis

Minimal change in S spacing with force below 1 N, force above 1 N caused a linear decrease in S spacing. Errors shown are the standard errors calculated during the peak fitting process.

10.2.4 Dehydration of collagen in an open sample environment

The tension experiments were kept in a hydrated environment However, dehydration could not be prevented completely. The effects of dehydration on the X-ray scattering pattern of collagen were known (see Section 7.8.2) and as one of the effects of dehydration is to cause a reduction in the D spacing the effects observed due to tension may have been confounded. To assess at what time scales the effects of dehydration would begin to affect the results of the tension experiments a sample of rat tail tendon was placed in the tensile testing rig under the same conditions as the tension experiments.

Twelve orders of diffraction peaks are present in all images in the series and the thirteenth order peak became apparent in the 6th image (after 9 minutes) the intensity of the 13th peak increased throughout subsequent exposures (Figure 10.13). A shift in

the ratio of intensities occurs during the dehydration. The odd orders decrease in intensity while the even orders increase in intensity. This suggests structural changes within the fibril structure of the collagen. A shift in peak position towards higher S can be seen beginning after approximately 10 minutes and continuing until the end of the data collection, suggesting a reduction in the D spacing of the sample.

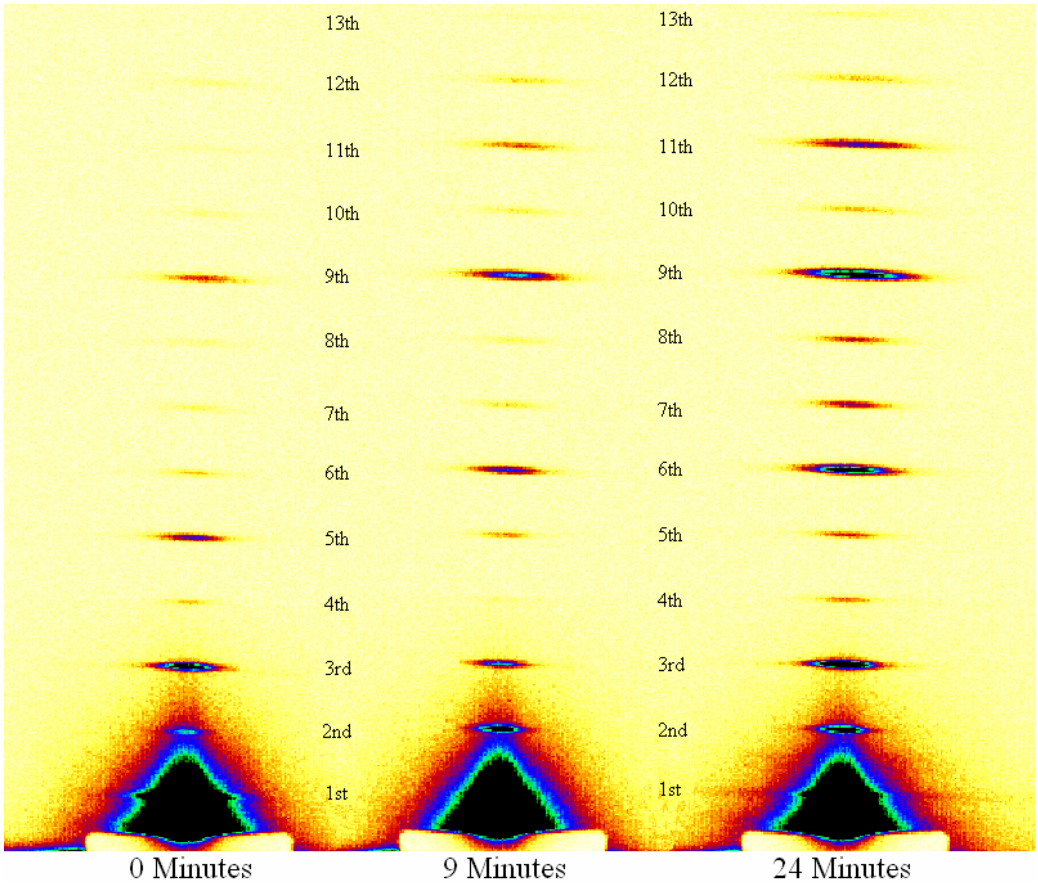

Figure 10.13 X-ray scattering images from dehydrating rat tail tendon at 0, 9 and 24 minutes

The 13th axial order of collagen becomes visible in the image taken after 9 minutes of dehydration and the intensity of the 13th order peak increases as the data collection continues. The 1st order appears less intense at 9 minutes than at the start but increases again by the 24 minutes. The 5th order appears to decrease in intensity while all the other orders appear to increase as dehydration occurs.

The 1D plot (Figure 10.14) shows the changes in intensity more clearly than the X-ray images and the table of peak intensities (Table 10.2.6). All the other peaks increase in intensity with the exception of the 1st, 3rd and 5th order reflections which decrease until after 10 minutes when the 1st, 3rd and 5th order intensity increases. The 13th order peak becomes visible after 9 minutes increasing in intensity and width throughout the subsequent exposures.

	Intensity (NPP)									
Time (Minutes)	Peak 1	Peak 2	Peak 3	Peak 4	Peak 5	Peak 6	Peak 7	Peak 8	Peak 9	Peak 10
0	1.528E+05	6.373E+02	2.326E+03	8.915E+01	4.798E+02	9.914E+01	5.927E+01	3.701E+01	1.747E+02	2.917E+01
1.5	1.484E+05	7.412E+02	2.301E+03	8.049E+01	4.863E+02	1.026E+02	5.420E+01	3.424E+01	1.949E+02	3.570E+01
3	1.385E+05	7.851E+02	2.236E+03	7.451E+01	4.842E+02	1.181E+02	6.352E+01	3.392E+01	2.217E+02	3.181E+01
4.5	1.209E+05	9.223E+02	2.128E+03	6.111E+01	4.522E+02	1.420E+02	6.481E+01	3.531E+01	2.515E+02	4.164E+01
6	9.534E+04	1.143E+03	1.859E+03	5.535E+01	4.259E+02	1.676E+02	6.481E+01	2.747E+01	2.961E+02	4.234E+01
7.5	6.129E+04	1.396E+03	1.499E+03	4.584E+01	3.519E+02	2.169E+02	6.740E+01	2.549E+01	3.362E+02	4.778E+01
9	2.249E+04	1.841E+03	1.018E+03	3.549E+01	2.515E+02	3.199E+02	6.771E+01	3.130E+01	4.077E+02	4.780E+01
10.5	6.513E+03	2.152E+03	8.931E+02	2.538E+01	1.437E+02	4.916E+02	7.261E+01	5.071E+01	5.488E+02	5.610E+01
12	1.761E+04	2.300E+03	1.408E+03	3.405E+01	9.799E+01	7.568E+02	9.990E+01	7.627E+01	7.294E+02	6.104E+01
13.5	3.244E+04	2.315E+03	2.118E+03	6.302E+01	1.056E+02	9.887E+02	1.344E+02	1.045E+02	9.243E+02	7.386E+01
15	4.227E+04	2.418E+03	2.702E+03	9.650E+01	1.300E+02	1.173E+03	1.741E+02	1.247E+02	1.071E+03	7.836E+01
16.5	4.794E+04	2.403E+03	3.043E+03	1.067E+02	1.537E+02	1.284E+03	1.837E+02	1.392E+02	1.144E+03	8.058E+01
18	5.204E+04	2.516E+03	3.331E+03	1.356E+02	1.680E+02	1.375E+03	2.048E+02	1.543E+02	1.212E+03	8.706E+01
19.5	5.569E+04	2.526E+03	3.618E+03	1.415E+02	1.774E+02	1.471E+03	2.334E+02	1.666E+02	1.290E+03	8.475E+01
21	5.883E+04	2.571E+03	3.860E+03	1.553E+02	2.072E+02	1.546E+03	2.481E+02	1.793E+02	1.367E+03	9.420E+01
22.5	6.150E+04	2.601E+03	4.073E+03	1.708E+02	2.242E+02	1.602E+03	2.700E+02	1.947E+02	1.409E+03	8.967E+01
24	6.423E+04	2.611E+03	4.217E+03	1.746E+02	2.460E+02	1.639E+03	2.799E+02	1.959E+02	1.442E+03	9.623E+01
	Intensity Std Error (NPP)									
0	8.133E+02	8.061E+02	7.924E+02	8.412E+02	7.531E+02	7.452E+02	8.286E+02	7.008E+02	6.927E+02	7.193E+02
1.5	9.107E+02	9.340E+02	8.901E+02	9.614E+02	8.526E+02	8.709E+02	8.195E+02	7.325E+02	7.799E+02	8.646E+02
3	8.950E+02	8.962E+02	8.690E+02	9.196E+02	8.470E+02	8.293E+02	7.993E+02	7.200E+02	7.787E+02	8.113E+02
4.5	5.844E+02	5.851E+02	5.682E+02	6.526E+02	5.367E+02	5.267E+02	5.092E+02	5.346E+02	5.025E+02	4.971E+02
6	4.280E+02	4.302E+02	4.138E+02	4.692E+02	3.978E+02	3.939E+02	3.622E+02	3.479E+02	3.699E+02	3.833E+02
7.5	3.677E+02	3.672E+02	3.542E+02	4.278E+02	3.436E+02	3.348E+02	3.225E+02	3.657E+02	3.185E+02	3.212E+02
9	1.934E+02	1.911E+02	1.841E+02	2.458E+02	1.768E+02	1.753E+02	1.660E+02	1.658E+02	1.637E+02	1.673E+02
10.5	5.440E+01	5.226E+01	5.061E+01	6.138E+01	4.890E+01	4.691E+01	4.468E+01	4.814E+01	4.504E+01	4.669E+01
12	1.084E+02	1.070E+02	1.046E+02	1.107E+02	1.006E+02	9.662E+01	9.342E+01	9.510E+01	9.219E+01	9.178E+01
13.5	1.695E+02	1.673E+02	1.624E+02	1.743E+02	1.546E+02	1.520E+02	1.460E+02	1.476E+02	1.453E+02	1.447E+02
15	2.098E+02	2.082E+02	2.024E+02	2.115E+02	1.906E+02	1.878E+02	1.904E+02	1.813E+02	1.799E+02	1.867E+02
16.5	2.325E+02	2.276E+02	2.230E+02	2.321E+02	2.155E+02	2.084E+02	2.029E+02	2.029E+02	1.986E+02	1.967E+02
18	1.699E+02	1.657E+02	1.610E+02	1.693E+02	1.526E+02	1.506E+02	1.466E+02	1.453E+02	1.428E+02	1.438E+02
19.5	3.032E+02	3.010E+02	2.925E+02	2.969E+02	2.813E+02	2.738E+02	2.655E+02	2.647E+02	2.588E+02	2.556E+02
21	2.946E+02	2.952E+02	2.817E+02	2.936E+02	2.696E+02	2.644E+02	2.575E+02	2.554E+02	2.511E+02	2.531E+02
22.5	3.297E+02	3.247E+02	3.173E+02	3.225E+02	3.042E+02	2.965E+02	2.981E+02	2.877E+02	2.809E+02	2.745E+02
24	3.826E+02	3.801E+02	3.698E+02	3.668E+02	3.532E+02	3.451E+02	3.373E+02	3.361E+02	3.280E+02	3.347E+02

Table 10.2.6 Peak intensities and associated standard errors for rat tail tendon during dehydration

The intensity and associated standard error values presented were calculated using peak fitting methods. Peak intensity changes slowly for the first 7.5 minutes (the 1st, 3rd and 5th order peaks decreasing all other peaks increasing) after 7.5 minutes the rate of change increases. The 1st, 3rd and 5th order drop to a minimum at approximately 10 to 12 minutes and then increase in intensity as dehydration continues.

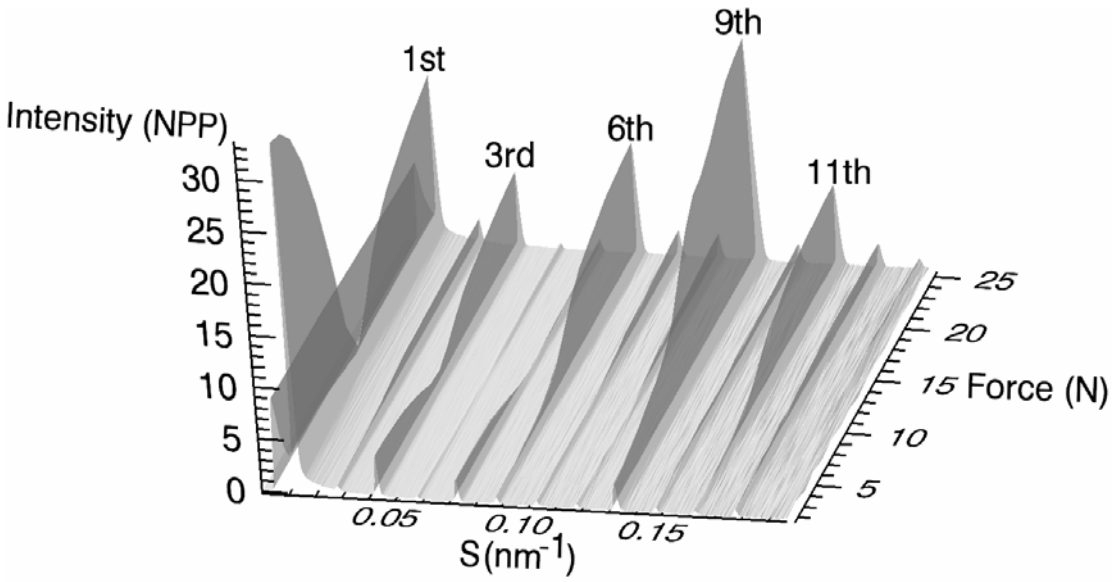

Figure 10.14 X-ray scattering intensity form a sample of rat tail tendon during dehydration

The intensity profile remained unchanged for approximately the first 5 minutes of data collection. The intensity of the 1st order peak reduces starting at approximately 5 minutes followed shortly after by the 3rd and 5th order peaks. The 1st, 3rd and 5th order peaks reduced to a minimum at around 10 minutes after which time their intensity increased. The 3rd order peak intensity increased above the intensity observed at the start of the data collection. All other peaks including the 13th order increased in intensity after 10 minutes of data collection. Shifts in peak position to lower S spacing were observed after 10 minutes of dehydration.

The shift of the peak positions to higher S can be seen as the sample becomes more dehydrated (Figure 10.15 and Table 10.2.7). The increase in S corresponds to a decrease in D spacing of 0.5 nm after 24 minutes. As the expected change in D spacing of dehydrated collagen is 3 nm (see Section 7.8.2), the sample of rat tail tendon was considered not to be fully dehydrated by the end of the data collection. Enough of a change was demonstrated to affect the results of the tension experiments.

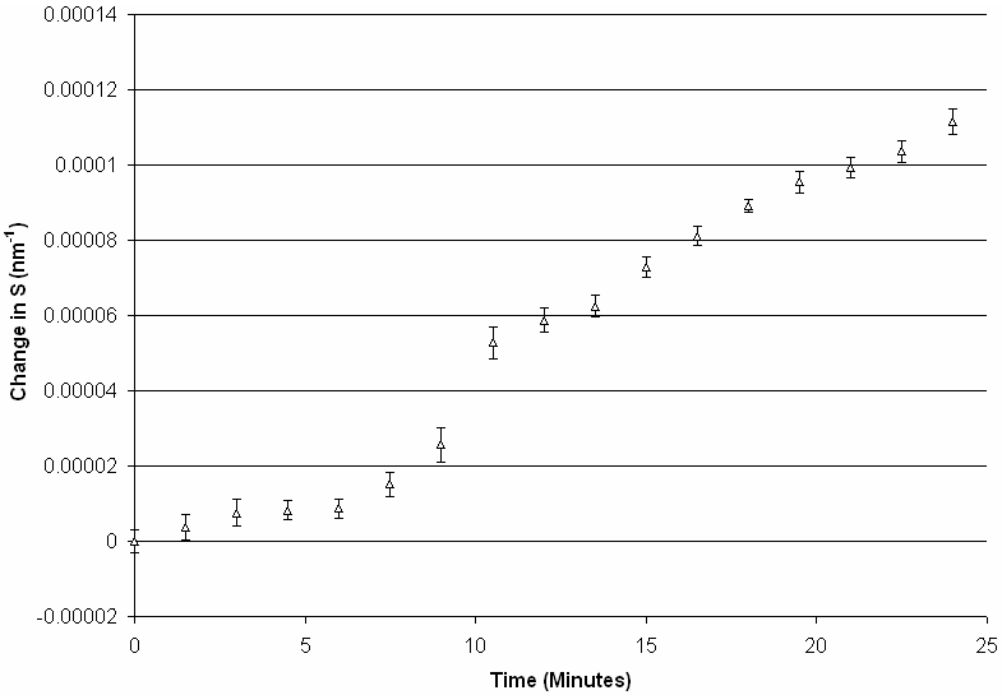

Figure 10.15 Effect of dehydration on S spacing of the 1st order axial peak of rat tail tendon.

The peak position increased slowly up to 6 minutes after which the rate of change increased. There was an increased change in the Spacing at approximately 10 minutes. However, this time corresponds to the lowest peak intensity and therefore the highest error and was therefore thought to be erroneous.

	Position S (nm^{-1})									
Time (Minutes)	Peak 1	Peak 2	Peak 3	Peak 4	Peak 5	Peak 6	Peak 7	Peak 8	Peak 9	Peak 10
0	1.493E-02	2.985E-02	4.478E-02	5.970E-02	7.463E-02	8.955E-02	1.045E-01	1.194E-01	1.343E-01	1.493E-01
1.5	1.493E-02	2.982E-02	4.478E-02	5.967E-02	7.463E-02	8.955E-02	1.045E-01	1.194E-01	1.343E-01	1.492E-01
3	1.493E-02	2.986E-02	4.477E-02	5.967E-02	7.460E-02	8.953E-02	1.045E-01	1.194E-01	1.343E-01	1.492E-01
4.5	1.493E-02	2.984E-02	4.477E-02	5.963E-02	7.459E-02	8.953E-02	1.044E-01	1.193E-01	1.343E-01	1.492E-01
6	1.493E-02	2.985E-02	4.476E-02	5.976E-02	7.459E-02	8.950E-02	1.044E-01	1.193E-01	1.343E-01	1.491E-01
7.5	1.494E-02	2.985E-02	4.477E-02	5.961E-02	7.459E-02	8.954E-02	1.044E-01	1.193E-01	1.343E-01	1.492E-01
9	1.495E-02	2.986E-02	4.478E-02	5.971E-02	7.461E-02	8.955E-02	1.045E-01	1.193E-01	1.343E-01	1.492E-01
10.5	1.498E-02	2.989E-02	4.482E-02	5.948E-02	7.466E-02	8.962E-02	1.046E-01	1.194E-01	1.344E-01	1.493E-01
12	1.498E-02	2.991E-02	4.484E-02	5.980E-02	7.479E-02	8.968E-02	1.047E-01	1.195E-01	1.345E-01	1.495E-01
13.5	1.499E-02	2.995E-02	4.488E-02	5.981E-02	7.486E-02	8.975E-02	1.047E-01	1.196E-01	1.346E-01	1.495E-01
15	1.500E-02	2.997E-02	4.490E-02	5.991E-02	7.486E-02	8.980E-02	1.047E-01	1.196E-01	1.347E-01	1.496E-01
16.5	1.501E-02	2.997E-02	4.493E-02	5.992E-02	7.490E-02	8.983E-02	1.048E-01	1.196E-01	1.347E-01	1.497E-01
18	1.501E-02	2.999E-02	4.493E-02	5.994E-02	7.491E-02	8.985E-02	1.049E-01	1.197E-01	1.348E-01	1.497E-01
19.5	1.502E-02	3.000E-02	4.495E-02	5.996E-02	7.493E-02	8.988E-02	1.049E-01	1.197E-01	1.348E-01	1.498E-01
21	1.502E-02	3.001E-02	4.497E-02	6.001E-02	7.494E-02	8.991E-02	1.049E-01	1.198E-01	1.348E-01	1.498E-01
22.5	1.503E-02	3.002E-02	4.498E-02	6.000E-02	7.496E-02	8.993E-02	1.049E-01	1.198E-01	1.349E-01	1.499E-01
24	1.504E-02	3.002E-02	4.498E-02	6.004E-02	7.496E-02	8.995E-02	1.050E-01	1.198E-01	1.349E-01	1.499E-01
	Position Std Error S (nm^{-1})									
0	1.851E-05	4.466E-03	1.243E-03	3.235E-02	6.339E-03	3.103E-02	6.028E-02	9.076E-02	1.896E-02	1.116E-01
1.5	2.140E-05	4.180E-03	1.422E-03	3.851E-02	6.961E-03	3.733E-02	7.397E-02	1.197E-01	1.899E-02	1.096E-01
3	2.240E-05	3.961E-03	1.428E-03	4.056E-02	6.882E-03	2.857E-02	5.573E-02	1.184E-01	1.614E-02	1.319E-01
4.5	1.660E-05	2.170E-03	9.659E-04	4.325E-02	4.813E-03	1.562E-02	3.660E-02	6.412E-02	9.275E-03	5.684E-02
6	1.545E-05	1.281E-03	8.163E-04	2.509E-02	3.705E-03	9.821E-03	2.697E-02	6.722E-02	5.728E-03	3.930E-02
7.5	2.036E-05	8.947E-04	8.632E-04	2.352E-02	3.818E-03	6.420E-03	2.173E-02	7.021E-02	4.295E-03	2.995E-02
9	2.836E-05	3.518E-04	6.578E-04	1.473E-02	2.773E-03	2.259E-03	1.189E-02	2.482E-02	1.847E-03	1.546E-02
10.5	2.676E-05	8.300E-05	2.057E-04	6.462E-03	1.353E-03	4.084E-04	2.866E-03	5.720E-03	3.761E-04	3.588E-03
12	2.051E-05	1.591E-04	2.657E-04	1.057E-02	4.142E-03	5.352E-04	4.196E-03	5.464E-03	5.820E-04	7.047E-03
13.5	1.761E-05	2.493E-04	2.806E-04	8.926E-03	5.916E-03	6.418E-04	4.942E-03	6.523E-03	7.183E-04	9.512E-03
15	1.673E-05	2.934E-04	2.703E-04	7.311E-03	5.990E-03	6.700E-04	4.618E-03	6.542E-03	7.664E-04	1.058E-02
16.5	1.633E-05	3.313E-04	2.670E-04	7.515E-03	5.472E-03	6.769E-04	4.861E-03	6.564E-03	7.972E-04	1.144E-02
18	1.094E-05	2.263E-04	1.759E-04	4.164E-03	3.709E-03	4.555E-04	3.146E-03	4.206E-03	5.446E-04	7.537E-03
19.5	1.846E-05	4.097E-04	2.944E-04	7.414E-03	6.287E-03	7.733E-04	5.026E-03	7.064E-03	9.331E-04	1.437E-02
21	1.690E-05	3.884E-04	2.680E-04	6.655E-03	5.219E-03	7.129E-04	4.576E-03	6.445E-03	8.484E-04	1.249E-02
22.5	1.807E-05	4.338E-04	2.835E-04	6.660E-03	5.433E-03	7.719E-04	4.688E-03	6.543E-03	9.256E-04	1.504E-02
24	2.031E-05	5.028E-04	3.200E-04	7.789E-03	5.743E-03	8.819E-04	5.287E-03	7.579E-03	1.055E-03	1.580E-02

Table 10.2.7 Axial peak positions and associated standard errors of rat tail tendon during dehydration

The peak position increased slowly before 6 minutes and rapidly thereafter. The change in peak position can be observed in all peaks. However, the errors on the higher peaks are large due to the low intensity of the higher order peaks.

The width of the axial peaks did not alter during the dehydration series (Table 10.2.8). The changes observed were negligible compared to the associated standard errors (see Section 11.2.2.3).

	Width S (nm^{-1})									
Time (Minutes)	Peak 1	Peak 2	Peak 3	Peak 4	Peak 5	Peak 6	Peak 7	Peak 8	Peak 9	Peak 10
0	3.018E-03	3.060E-03	3.160E-03	2.943E-03	3.498E-03	3.577E-03	3.586E-03	4.165E-03	4.144E-03	3.927E-03
1.5	3.022E-03	2.877E-03	3.189E-03	2.790E-03	3.439E-03	3.654E-03	3.998E-03	4.817E-03	4.110E-03	3.627E-03
3	3.005E-03	3.010E-03	3.181E-03	2.850E-03	3.419E-03	3.530E-03	3.841E-03	4.820E-03	3.986E-03	4.003E-03
4.5	2.979E-03	2.966E-03	3.133E-03	2.707E-03	3.512E-03	3.646E-03	4.029E-03	3.675E-03	4.023E-03	4.132E-03
6	2.985E-03	2.950E-03	3.175E-03	2.561E-03	3.436E-03	3.628E-03	4.190E-03	4.607E-03	3.972E-03	3.766E-03
7.5	2.941E-03	2.947E-03	3.163E-03	2.209E-03	3.390E-03	3.604E-03	3.930E-03	3.891E-03	3.932E-03	3.863E-03
9	2.857E-03	2.939E-03	3.152E-03	2.001E-03	3.417E-03	3.582E-03	4.187E-03	4.036E-03	3.982E-03	3.831E-03
10.5	2.778E-03	2.964E-03	3.144E-03	2.263E-03	3.452E-03	3.710E-03	4.036E-03	3.947E-03	3.970E-03	3.742E-03
12	2.886E-03	2.964E-03	3.097E-03	2.824E-03	3.482E-03	3.630E-03	3.887E-03	3.805E-03	3.988E-03	4.066E-03
13.5	2.923E-03	2.989E-03	3.170E-03	2.803E-03	3.502E-03	3.614E-03	3.944E-03	3.979E-03	3.958E-03	4.157E-03
15	2.923E-03	2.951E-03	3.125E-03	2.892E-03	3.543E-03	3.625E-03	3.663E-03	3.898E-03	3.951E-03	3.856E-03
16.5	2.919E-03	3.029E-03	3.155E-03	3.003E-03	3.380E-03	3.612E-03	3.812E-03	3.897E-03	3.977E-03	4.061E-03
18	2.908E-03	2.976E-03	3.151E-03	2.891E-03	3.543E-03	3.602E-03	3.809E-03	3.869E-03	4.001E-03	3.954E-03
19.5	2.937E-03	2.977E-03	3.152E-03	3.060E-03	3.439E-03	3.599E-03	3.826E-03	3.852E-03	4.030E-03	4.127E-03
21	2.926E-03	2.934E-03	3.181E-03	3.048E-03	3.475E-03	3.609E-03	3.824E-03	3.924E-03	4.001E-03	4.038E-03
22.5	2.918E-03	3.009E-03	3.152E-03	3.056E-03	3.472E-03	3.613E-03	3.672E-03	3.835E-03	4.019E-03	4.260E-03
24	2.952E-03	2.990E-03	3.160E-03	3.212E-03	3.465E-03	3.627E-03	3.800E-03	3.827E-03	4.018E-03	3.942E-03
	Width Std Error S (nm^{-1})									
0	6.000E+00	4.484E-03	1.244E-03	3.512E-02	6.343E-03	3.112E-02	8.536E-02	9.575E-02	1.905E-02	1.164E-01
1.5	2.151E-05	4.208E-03	1.449E-03	4.062E-02	6.964E-03	4.410E-02	8.287E-02	1.269E-01	1.901E-02	1.242E-01
3	2.250E-05	4.008E-03	1.428E-03	4.081E-02	7.138E-03	2.912E-02	5.788E-02	1.269E-01	1.634E-02	1.509E-01
4.5	1.675E-05	2.184E-03	9.659E-04	4.987E-02	4.817E-03	1.562E-02	3.872E-02	6.848E-02	9.352E-03	5.780E-02
6	1.560E-05	1.290E-03	8.166E-04	2.667E-02	3.705E-03	1.044E-02	2.749E-02	7.032E-02	5.729E-03	4.056E-02
7.5	2.043E-05	8.969E-04	8.636E-04	2.406E-02	3.877E-03	6.626E-03	2.288E-02	1.071E-01	4.338E-03	3.019E-02
9	2.838E-05	3.550E-04	6.578E-04	1.692E-02	2.775E-03	2.381E-03	1.360E-02	2.652E-02	1.848E-03	1.558E-02
10.5	2.775E-05	8.380E-05	2.058E-04	7.273E-03	1.413E-03	4.187E-04	2.873E-03	6.599E-03	3.767E-04	3.677E-03
12	2.052E-05	1.593E-04	2.656E-04	1.095E-02	4.423E-03	5.352E-04	4.204E-03	5.612E-03	5.825E-04	7.180E-03
13.5	1.777E-05	2.496E-04	2.806E-04	9.211E-03	5.935E-03	6.418E-04	5.001E-03	6.953E-03	7.184E-04	1.022E-02
15	1.689E-05	2.933E-04	2.706E-04	7.465E-03	6.055E-03	6.700E-04	4.931E-03	6.571E-03	7.666E-04	1.154E-02
16.5	1.649E-05	3.312E-04	2.670E-04	7.913E-03	5.472E-03	6.769E-04	4.862E-03	6.829E-03	7.972E-04	1.148E-02
18	1.146E-05	2.264E-04	1.759E-04	4.275E-03	3.774E-03	4.555E-04	3.158E-03	4.207E-03	5.446E-04	7.551E-03
19.5	1.849E-05	4.095E-04	2.943E-04	7.416E-03	6.379E-03	7.733E-04	5.027E-03	7.067E-03	9.341E-04	1.438E-02
21	1.709E-05	3.971E-04	2.680E-04	7.130E-03	5.226E-03	7.129E-04	4.612E-03	6.606E-03	8.484E-04	1.303E-02
22.5	1.807E-05	4.339E-04	2.835E-04	6.680E-03	5.553E-03	7.728E-04	4.919E-03	6.550E-03	9.257E-04	1.536E-02
24	2.030E-05	5.026E-04	3.200E-04	7.794E-03	5.749E-03	8.819E-04	5.295E-03	7.590E-03	1.056E-03	1.642E-02

Table 10.2.8 axial peak width and associated standard errors of rat tail tendon during dehydration

Minimal change to the axial peak widths was observed as even the minimum error of the 1st order peak was three times larger than the maximum change in width of the 1st order peak.

10.3 Synchrotron radiation investigation of breast tissue

10.3.1 Summary

The small angle X-ray scattering data from breast tissue using synchrotron radiation was collected at station 2.1 at Daresbury Laboratories Synchrotron Radiation Source (SRS) (see Section 8.1.2.2). The samples were mounted in capillary tubes in order to give some preferential alignment (see Section 8.1.2.4.1) and to limit dehydration which could affect the results. The X-ray scattering pattern from each sample was collected using a 2D X-ray detector (see Section 8.1.2.2). The resulting images were then processed (see Section 8.2.1) and analysed. Differences in the 2D images were apparent between normal samples and samples containing mainly malignant tissue. Quantitative analysis was performed on the 1D X-ray scattering profile obtained from a sector integration of the 2D image. Principal component analysis was also performed using the 1D X-ray scattering profiles in order to build a model which could be used for automated diagnosis.

10.3.2 Two dimensional X-ray scattering images

X-ray scattering images presented here (Figure 10.16, Figure 10.17 and Figure 10.18) were all visualised using the same palette setting to allow comparison. Differences between samples containing predominantly one type of tissue either normal fibrous tissue (Figure 10.16), malignant tissue containing mainly tumour and tumour stroma (Figure 10.17) and normal highly fatty tissue (Figure 10.18) could be seen in the X-ray scattering images. Differences between samples with varying amounts of tissue constituents were not clear with direct observation of the X-ray scattering images only and required further analysis methods to visualise the differences (see Section 10.3.3).

X-ray scattering images from fibrous normal tissues (Figure 10.16) showed strong peaks which correspond to the axial spacing of collagen with both odd and even order visible up to and including the 6^{th} order peak. The highly fatty normal tissues (Figure 10.18) also show in some cases scattering peaks associated with collagen, the intensity of which was proportional to the amount of fibrous tissues in the sample. In both cases of normal tissue the amorphous scatter was low compared to the images from malignant tissues (Figure 10.17) which shows a large amorphous scatter component and weak peaks associated with collagen even thought the tumour tissues are fibrous.

The X-ray scattering images indicate that a low intensity in the collagen peaks either indicates the possible presence of disease or a lack of collagen in the tissues. The amorphous scatter of normal tissues both fibrous and fatty was lower then the amorphous scatter of malignant tissues. Therefore using both the intensity of the collagen peaks and amorphous scatter upon which to base a diagnosis would appear to have potential as a reliable indicator for the presence of disease in a sample.

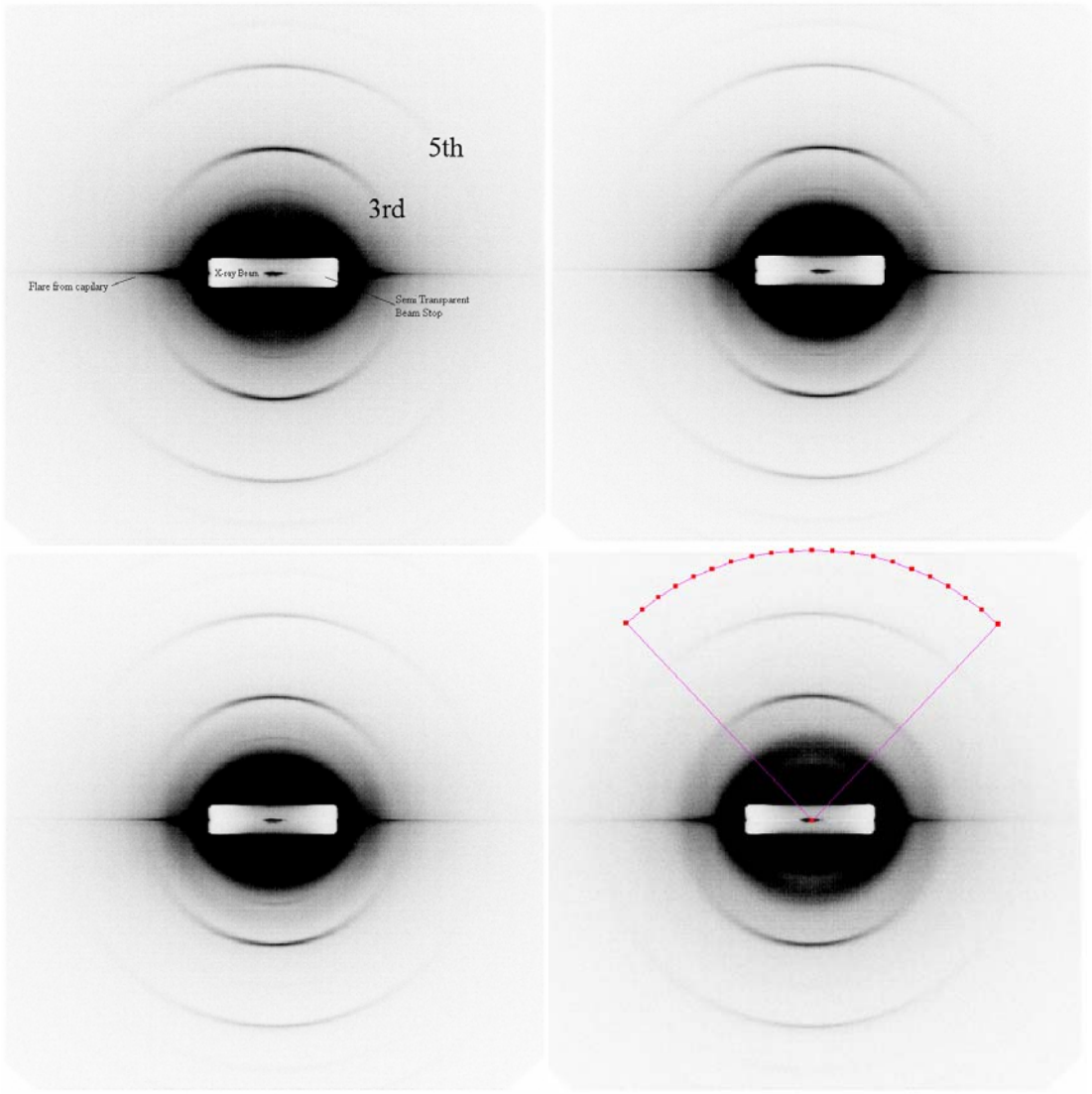

Figure 10.16 Typical X-ray scattering images of <u>fibrous normal</u> breast tissue

The X-ray scattering from normal tissues with >80 % fibrous component showed the 1st (hidden by the background with the chosen pallet), 3rd and 5th axial orders of collagen which are strong while the 2nd, 4th and 6th orders are present but weak. There was an almost 360° orientation in the axial peaks that has preferential alignment in the vertical direction due to the sample being held in the capillary. The X-ray beam can be seen through the semi transparent beam stop which was used for normalisation of the attenuation and X-ray beam decay. The bottom right image shows the sector area used for the integration to produce the 1D scattering profiles.

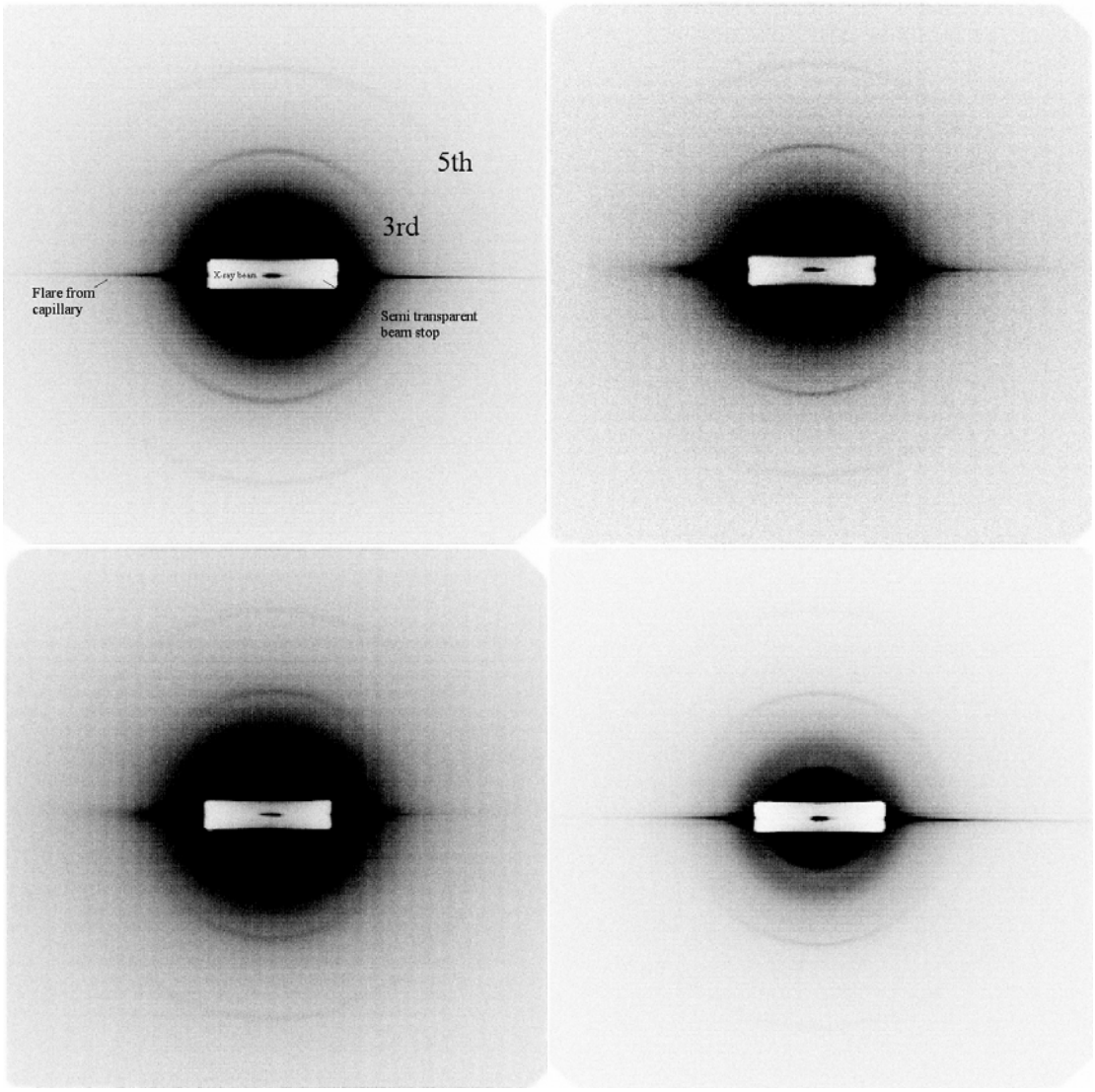

Figure 10.17 Typical X-ray scattering images of <u>malignant</u> breast tissue

The X-ray scattering from malignant tissues with >80 % tumour tissue by volume presented here showed the 1st (hidden by the background with the chosen pallet), 3rd and 5th axial orders of collagen which are present but weak. The even orders were not visible above the high background intensity. The low intensity prevents the visualisation of the 360° orientation. However, the preferential alignment in the vertical direction due to the sample being held in the capillary was observed.

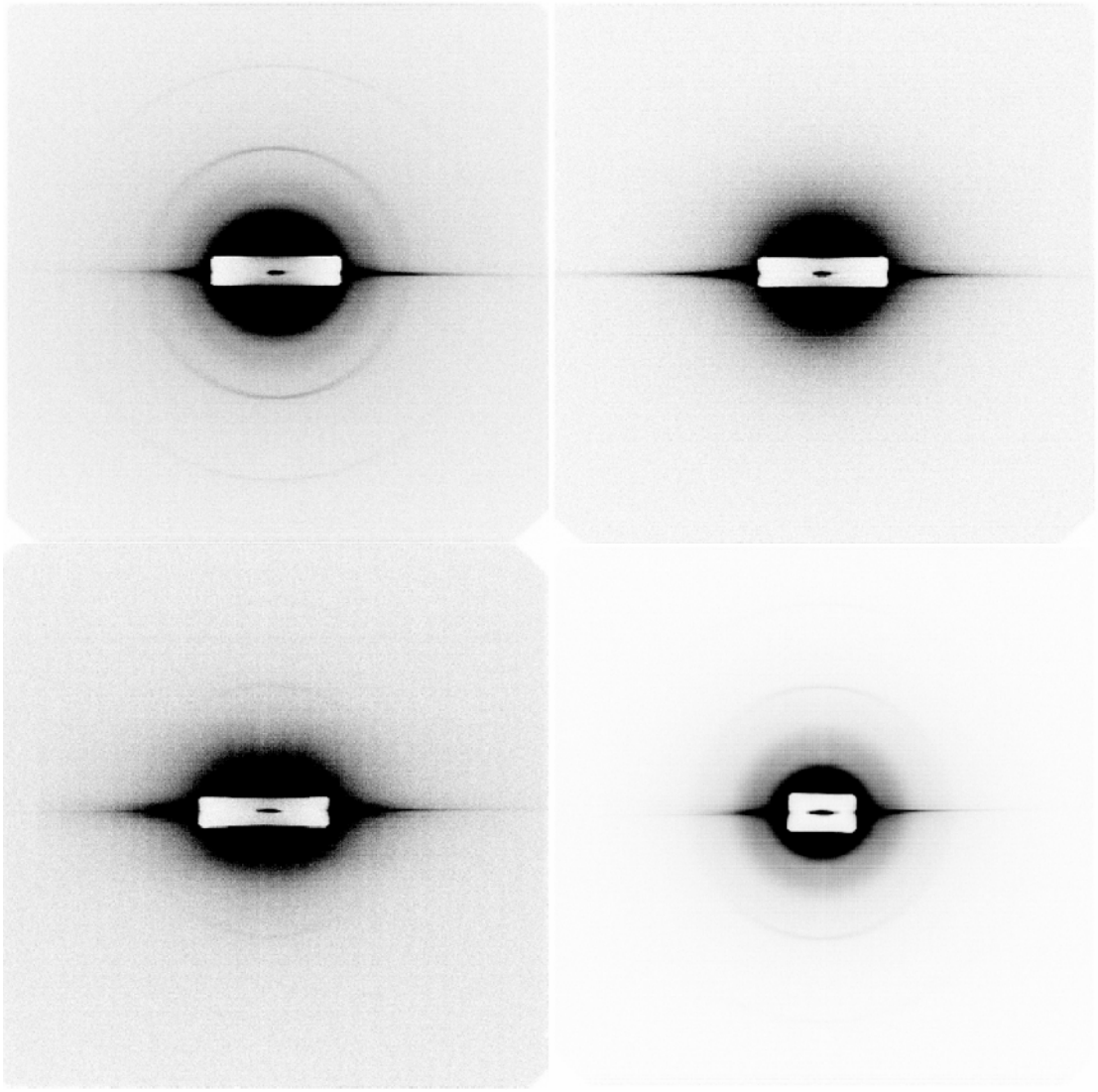

Figure 10.18 Typical X-ray scattering images of highly fatty breast tissue

The X-ray scattering images from tissues with >80 % fat by volume presented here showed the 1st (hidden by the background with the chosen pallet), 3rd and 5th axial orders of collagen which were present but weak in two of the images (left, top and bottom). The 1st and 3rd order only were visible in one image (right bottom) which contained 90 % fat by volume and no scattering associated with ordered collagen was present in the final image (top right) which contained over 99 % fat by volume. The even orders were not visible in any of the images due to their low intensity. The intensity of amorphous scatter in the X-ray scattering images from fat was relatively low compared to those of normal and malignant tissues. The three images which have scattering from collagen show 360° orientation with minimal preferential alignment in the vertical direction.

10.3.3 Quantitative analysis of one dimensional data

10.3.3.1 Parameters used and their significance

Differences in the small angle X-ray scattering from different tissue were previously described using both axial peak parameters (Lewis, 2000) and amorphous scatter (Fernandez, 2002). For our data the peak positions and peak areas were obtained using fitting methods (see Section 8.3.1). The gradient of the linear regions of the background were calculated (see Section 7.7.5 and Section 7.7.7), which produced the values for the radius of gyration (Rg) (S = 0.016 to 0.023 nm^{-1} aprox) and power law exponent (S = 0.052 to 0.072 nm^{-1} aprox). It should be noted that the values of Rg and the power law exponent represent the average value from all scattering objects in the tissue samples which may also be influenced by interference as the scattering systems are not monodisperse. The intensity of the X-ray scattering profiles was displayed in units of normalised photons per pixel (NPP) as the normalisation process used for the breast tissue normalised the intensity of the direct beam (observed through the semi transparent beam stop) to 1. The relative intensity ratio (RIR) was calculated by dividing the average intensity of the linear region next to the beam stop (S = 0.007 to 0.012 nm^{-1} aprox) by the average intensity of the linear region between the 3^{rd} and 5^{th} axial orders of collagen (S = 0.052 to 0.072 nm^{-1} aprox). The resulting values for each tissue type (normal, cancer and fibroadenoma assessed by histopathology) were compared using a two tailed student t test (assuming unequal variance) to determine which parameters showed significant difference between tissue types.

The precision of the fitting was checked independently by calculating the coefficient of determination (R^2) for each scattering profile and the calculated fit from the fitting software (DAVE, PAN). R^2 is calculated using an automated program written by Dr K. Siu and uses the original input data and the fitted output to calculate the coefficient of determination for the data between the selected spacing limits for fitting.

The calculated values of R^2 show that the fitting process produced parameters which described the observed scattering profile to within an average of 0.2% of the original data (Table 10.3.1). The lowest R^2 value obtained shows that the worst fit produced was within 2.2% of the original data. The R^2 calculation only checks the intensity value at each point and compares it with the original data therefore it was possible to have a high R^2 value from a non physical model. Non physical models were fitted in some cases where the scattering profile was noisy or if some of the Bragg peaks are not visible. PAN did not recognise the absence of a peak and altered the variables of Gaussian approximation of an absent Bragg peak to provide a more precise description of the amorphous scatter. It is for this reason that each fitted profile was checked manually to ensure the fitted parameters conform to a physical model comprising of a decaying background with Bessel and Bragg peaks (see Section 8.3.1.3.2) at appropriate spacing and any deviations from expected parameters were checked.

	Minimum	Average	Standard deviation
R^2	0.978383	0.998305	0.00221

Table 10.3.1 Results from coefficient of determination on all fitted data

The average of the coefficient of determination shows that the fitted peaks describe the data to within 0.2% of the original data on average and the worst fit shown by the minimum is fitted to within 2.2% of the original data.

The critical t values for the Student t test were for a 95 % confidence (alpha = 0.05). All the parameters analysed showed some significant difference (the t statistic > than the t critical value) between at least one combination of tissue types (normal/fibroadenoma, normal/cancer or cancer/fibroadenoma). Four of the nine parameters showed significant differences between two of the three tissue type combinations and only the relative intensity ratio showed a significant difference between all three tissue types. The P value shows the possibility of obtaining the t statistic value by chance alone, which for the parameters which show significant differences was <<0.001.

The t test assessed if the difference in the mean of one group was significantly different to the mean of another. The difference, even though significant, may not be caused by the presence of disease in these data but could be caused by experimental differences such as calibration (see Section 11.4.1). Even with a significant difference in the mean there may still be some overlap at the extremes of distribution which will limit the effectiveness of any given single parameter to be used in a diagnostic test. To asses the diagnostic potential of the two parameters they were plotted against each other to allow visualisation of the overlap of the data points from different tissue types and to determine values for the sensitivity and specificity.

		Variable 1	Normal	Cancer	Fibroadenoma
		Variable 2	Fibroadenoma	Normal	Cancer
		No. of samples variable 1	22	38	30
Radius of Gyration (Rg) (nm)	Variable 1	Mean	73.57319562	68.45210861	87.45468562
		Variance	149.5092299	57.96150198	70.57896989
	Difference between Variable 1 and 2	t Stat	4.589453627	1.739653827	9.247726231
		P(T<=t) two-tail	**5.50749E-05**	**0.091531606**	**5.18689E-13**
		t Critical two-tail	2.030110409	2.036931619	2.001715984
		t Stat > t Critical	Yes	No	Yes
Relative Intensity Ratio (RIR)	Variable 1	Mean	609.8874713	245.8287169	378.3340417
		Variance	30677.36282	9136.903852	15933.69329
	Difference between Variable 1 and 2	t Stat	5.276840475	8.857996753	4.610835243
		P(T<=t) two-tail	**6.43244E-06**	**7.12106E-10**	**2.49895E-05**
		t Critical two-tail	2.02809133	2.042270353	2.004881026
		t Stat > t Critical	Yes	Yes	Yes
Power law exponent	Variable 1	Mean	-2.922686933	-2.67678331	-2.720229097
		Variance	0.073341539	0.036480303	0.067675547
	Difference between Variable 1 and 2	t Stat	2.707982544	3.661449518	0.741538702
		P(T<=t) two-tail	**0.009604334**	**0.000820971**	**0.461640215**
		t Critical two-tail	2.0153675	2.030110409	2.005745046
		t Stat > t Critical	Yes	Yes	No
3rd order Bragg Peak Area (NPP nm^{-1})	Variable 1	Mean	0.000169031	8.88286E-05	0.000131429
		Variance	1.33716E-08	1.36466E-08	8.60799E-09
	Difference between Variable 1 and 2	t Stat	1.257080616	2.579237879	1.676020759
		P(T<=t) two-tail	**0.216200955**	**0.013321115**	**0.098465551**
		t Critical two-tail	2.022688932	2.0153675	1.996563697
		t Stat > t Critical	No	Yes	No
3rd order Bragg Peak Position (nm^{-1})	Variable 1	Mean	0.046496364	0.046266842	0.046281667
		Variance	1.64433E-08	5.50384E-08	3.91454E-08
	Difference between Variable 1 and 2	t Stat	4.739240741	4.898091608	0.282527634
		P(T<=t) two-tail	**1.88008E-05**	**8.11525E-06**	**0.778423112**
		t Critical two-tail	2.009574018	2.001715984	1.996563697
		t Stat > t Critical	Yes	Yes	No
3rd order Bragg Peak FWHM (nm^{-1})	Variable 1	Mean	0.001727318	0.002210684	0.0022949
		Variance	6.53622E-07	2.31658E-07	2.34057E-07
	Difference between Variable 1 and 2	t Stat	2.930510768	2.55444143	-0.714356005
		P(T<=t) two-tail	**0.006197667**	**0.015951877**	**0.477688061**
		t Critical two-tail	2.036931619	2.042270353	1.99896931
		t Stat > t Critical	Yes	Yes	No
2nd order Bessel Peak Area (NPP nm^{-1})	Variable 1	Mean	0.000779332	0.000527525	0.000563767
		Variance	6.31475E-08	5.93326E-07	7.86124E-08
	Difference between Variable 1 and 2	t Stat	2.909126186	1.852110848	0.268387058
		P(T<=t) two-tail	**0.005476981**	**0.07003923**	**0.789528115**
		t Critical two-tail	2.01063358	2.009574018	2.009574018
		t Stat > t Critical	Yes	No	No
2nd order Bessel Peak Position (nm^{-1})	Variable 1	Mean	0.025130909	0.023839474	0.029511
		Variance	4.68066E-06	1.9002E-05	2.59269E-06
	Difference between Variable 1 and 2	t Stat	-8.007867658	1.529628195	7.405851988
		P(T<=t) two-tail	**1.34703E-09**	**0.131639944**	**1.56359E-09**
		t Critical two-tail	2.026190487	2.002466317	2.009574018
		t Stat > t Critical	No	No	Yes
2nd order Bessel Peak FWHM (nm^{-1})	Variable 1	Mean	0.007073182	0.004805855	0.0094102
		Variance	2.45035E-05	0.00015237	1.38376E-05
	Difference between Variable 1 and 2	t Stat	-1.824038245	1.001680575	2.177538669
		P(T<=t) two-tail	**0.076017829**	**0.321049381**	**0.034723167**
		t Critical two-tail	2.024394234	2.005745046	2.014103302
		t Stat > t Critical	No	No	Yes

Table 10.3.2 Results of two tailed t test for X-ray scattering parameters

A value of t Stat > t Critical indicated that the difference between the groups was significant. Only the relative intensity ratio shows significant difference between all three tissue types. However, all parameters show significant difference between at least two separate tissue types.

10.3.3.2 Bragg and Bessel peaks

Separation of tissue types was previously reported using the peak position and area of the 3rd order axial (Bragg) peak (Lewis, 2000). The 1st order axial peal was superimposed on the Bessel peaks which were different between samples and resulted in lower confidence of fitting for the 1st order axial peak. Thus quantitative analysis of the breast tissue data used the third order axial peak, enabling direct comparison between our results and previous studies (Lewis, 2000; Fernandez, 2002). Significant difference between the normal and malignant tissue samples was observed (Table 10.3.2), However, when plotted (Figure 10.19) outliers were observed which reduced algorithmic separation of tissue types.

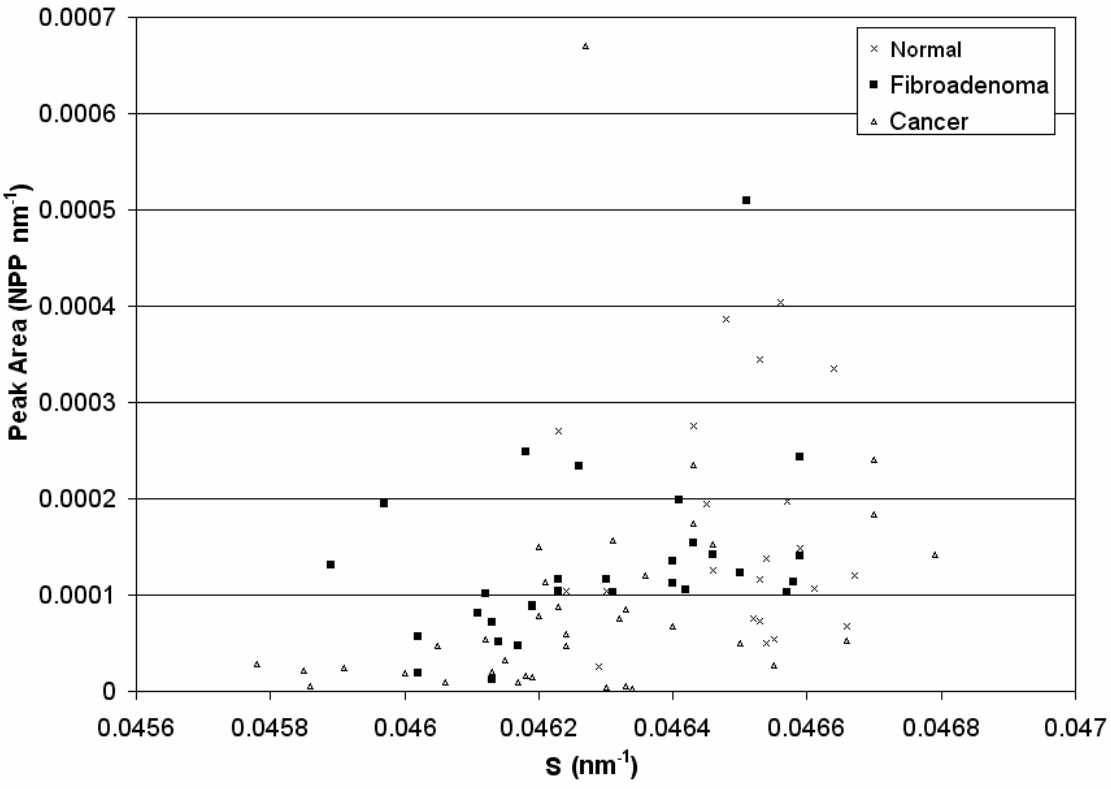

Figure 10.19 Plot of 3rd order Bragg peak spacing against area for all diagnostic data

Grouping of the different tissue types was evident. However, there are a number of outliers and which reduce the separation of diseased from normal tissues.

A group of four outlying samples from the cancer group were observed with an S position for the 3rd order peak above 0.0466 nm^{-1}, which is larger than the S position

for most of the normal samples. All four of these cancer outliers were from the same experimental data collection.

Grouping of outliers associated by data collection suggested a possible error in spacing calibration. This hypothesis was supported by plotting only the data collected from one experiment (Figure 10.20). Using only one data collection a large amount of data was excluded. No significant difference was seen between the tissue types using the peak area and the peak position, separation between normal and fibroadenoma samples was no longer significant (Table 10.3.3). However, the t stat value for the difference between normal and cancer tissues for peak position increased and the difference between cancer and fibroadenoma samples was significant when using only one data collection. The increase in significance of two of the three tissue type combinations by limiting the data to only one data collection showed that the differences in calibration between separate data collections (see Section 11.4.1.1) were significant.

		Variable 1	**Normal**	**Cancer**	**Fibroadenoma**
		Variable 2	Fibroadenoma	Normal	Cancer
		Number of samples variable 1	22	16	13
3rd order Bragg Peak Area (NPP nm^{-1})	Variable 1	Mean	0.000169031	0.000118289	0.000168985
		Variance	1.33716E-08	2.31436E-08	1.20499E-08
	Difference between Variable 1 and 2	t Stat	0.001181702	1.119540451	1.040610143
		P(T<=t) two-tail	**0.999066159**	**0.272770523**	**0.30728565**
		t Critical two-tail	2.055530786	2.051829142	2.051829142
		t Stat > t Critical	No	No	No
3rd order Bragg Peak Position (nm^{-1})	Variable 1	Mean	0.046496364	0.046285	0.046473846
		Variance	1.64433E-08	1.49867E-08	8.30897E-09
	Difference between Variable 1 and 2	t Stat	0.604711579	5.150480652	4.757239773
		P(T<=t) two-tail	**0.549634882**	**1.18367E-05**	**5.84862E-05**
		t Critical two-tail	2.036931619	2.03451691	2.051829142
		t Stat > t Critical	No	Yes	Yes

Table 10.3.3 Single data collection t test results on 3rd order axial peak position and area

No significant difference is observed in the peak area between any tissue types. Significant difference in peak position was observed between normal and cancer groups and cancer and fibroadenoma groups but no between normal and fibroadenoma.

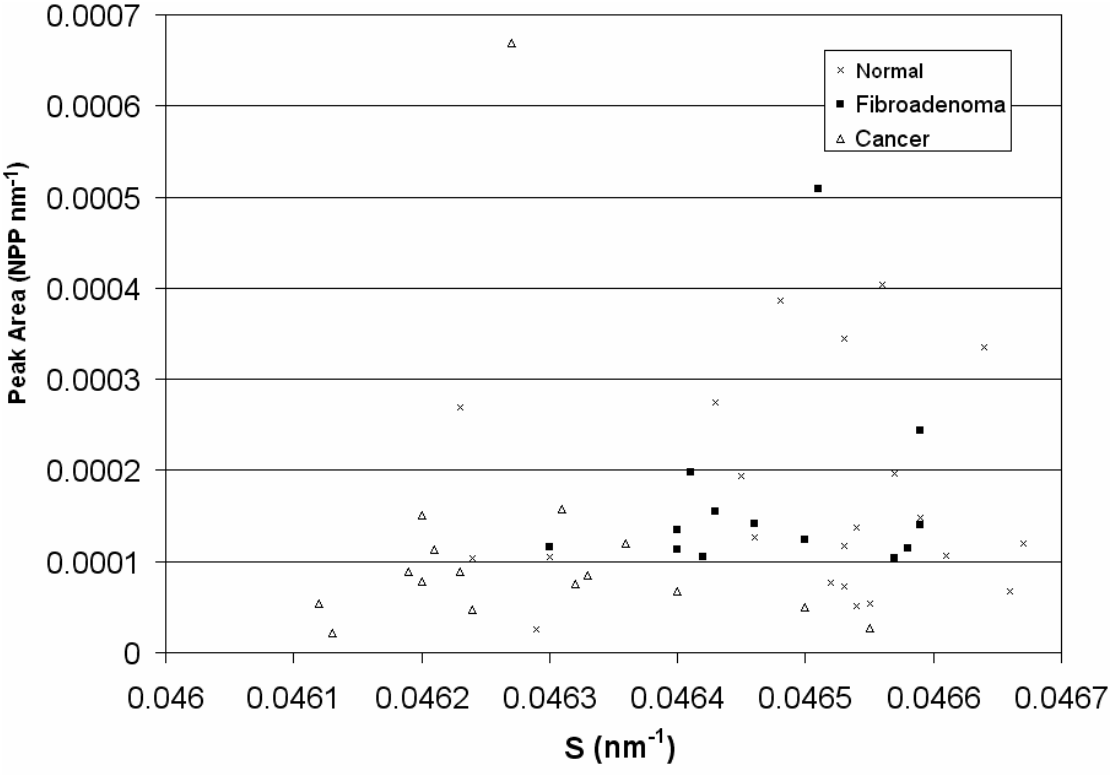

Figure 10.20 Plot of 3rd order Bragg peak spacing against area using data from a single experiment

Using only data from a single experiment shows relative differences between tissue types as all presented data was collected with identical geometry. The separation between cancer and normal samples is clearer suggesting some of the outliers may be caused my differences in the calibration between separate experiments though there are fewer data points on which to base a conclusion.

There were four outliers from the normal group observed with an S position for the 3rd order peak between 0.0462 nm^{-1} and 0.0464 nm^{-1}. These outlying normal samples were the only four samples from a tissue collection from 2004, while all other samples in were collected in 2005, meaning the four outlying normal samples were stored for significantly longer than the rest of the samples in the data collection. Thus their anomalous position may relate to a difference during their excision or storage and not the disease state of the tissue. The results of a student t test without the normal outliers further increases the significance of the separation between normal and cancer samples and shows the separation of normal and fibroadenoma samples as significant (see Table 10.3.4).

		Variable 1	Normal	Cancer	Fibroadenoma
		Variable 2	Fibroadenoma	Normal	Cancer
		Number of samples variable 1	18	16	13
3rd order Bragg Peak Position (nm^{-1})	Variable 1	Mean	0.046547778	0.046547778	0.046473846
		Variance	4.70065E-09	4.70065E-09	8.30897E-09
	Difference between Variable 1 and 2	t Stat	2.4639778	7.592659556	4.757239773
		P(T<=t) two-tail	**0.022455384**	**1.03892E-07**	**5.84862E-05**
		t Critical two-tail	2.079614205	2.068654794	2.051829142
		t Stat > t Critical	Yes	Yes	Yes

Table 10.3.4 Student t test results without normal outliers

To further investigate the possible differences in calibration the data from cancer samples containing greater than 80% tumour by volume as assessed by histopathology were plotted and ordered by data collection (Figure 10.21). The grouping of the data points with both parameters can be seen to correlate with data collection, which suggested the differences in the calibration and normalisation method (see Section 11.4.1) were affecting the diagnostic parameters. This observation shows that the absolute position and area of the peaks cannot be used to accurately determine disease state. However, within the same calibration the relative differences can be investigated with confidence for physiological effects of tumour invasion.

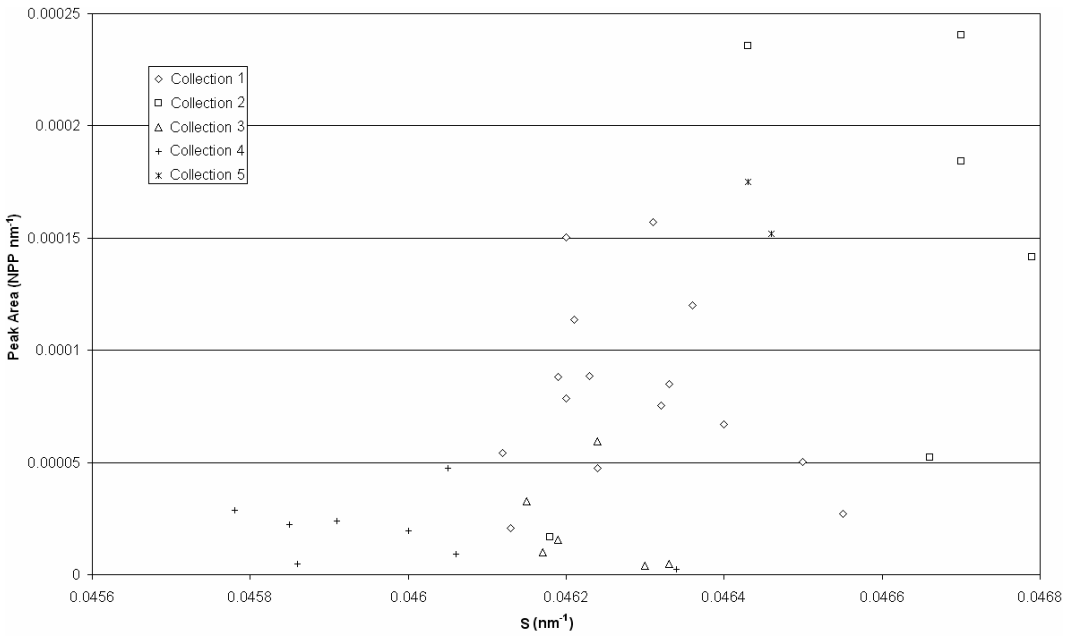

Figure 10.21 Bragg peak position versus area of samples with >80% tumour (by data collection)

Grouping of these samples correlates with the calibration suggesting that the differences in spacing related to disease cannot be accurately compared between separate data collections.

The plot of 3rd order peak position against intensity was partitioned into malignant, normal and benign areas (Figure 10.22) maximising the number of data points correctly corresponding to the chosen area. The sensitivity and specificity of partitioning was calculated using the number of data points which are within the bounds of the appropriate areas and are 100 % and 81.8 % respectively (see Section 11.6).

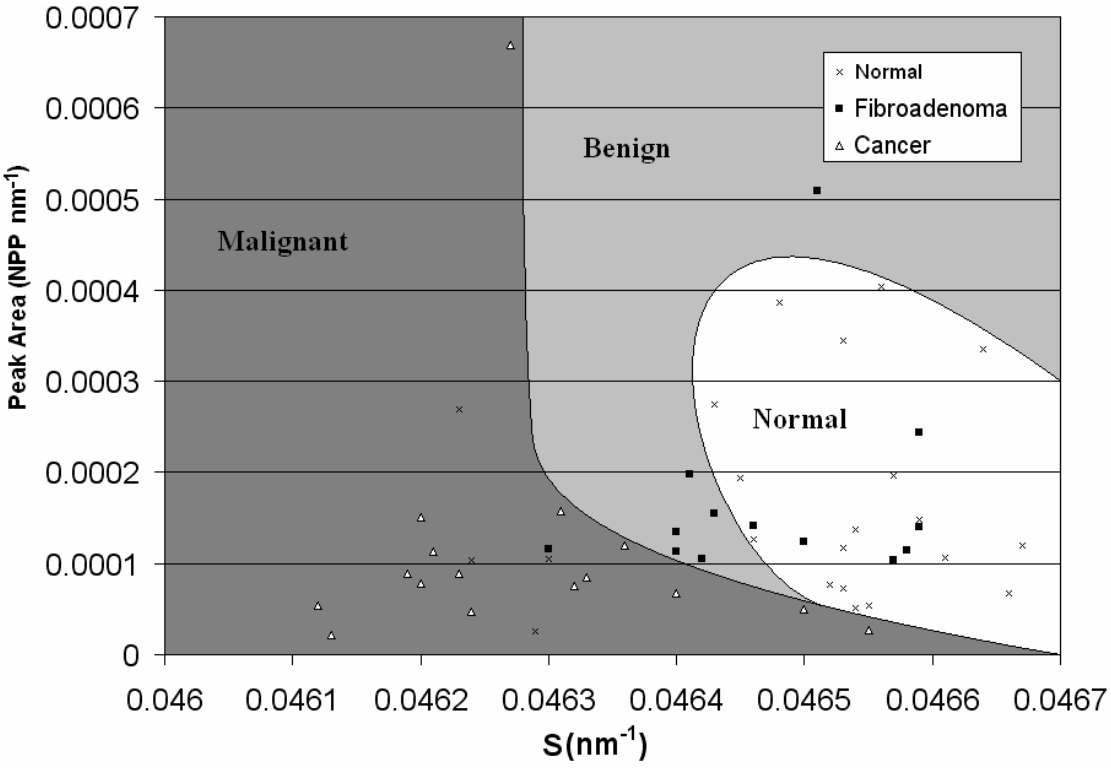

Figure 10.22 Plot of spacing versus 3rd order Bragg peak area (possible diagnostic areas annotated)

The majority of the data points fall within the appropriate annotated areas, However, there are some outliers which reduce the sensitivity and specificity.

The exploitation of a single peak in the scattering profile for categorisation disregards the other parameters which were observed. Parameters derived from the other observable Bragg peaks will yield similar information and be subject to the same experimental errors as the 3rd order peak. These parameters will show higher errors from the fitting process as the intensity of the other Bragg peaks will be lower.

The 1st order Bessel peak could not be used for analysis as over half of the peak was hidden behind the beam stop and could therefore not be fitted accurately. The second order Bessel peak was present and fitted in most data, while the third order present in many had a low intensity and therefore high fitting errors. Parameters derived from the 2nd order Bessel peak showed some separation using the same method as the 3rd order Bragg peak, plotting the peak area against position (Figure 10.23). The groups of different tissue types overlap to a greater degree than was observed from the Bragg peaks. No significant difference was observed between the normal and cancerous tissues (Table 10.3.2). However, there was significant difference between normal and fibroadenoma samples observed in peak area, while cancer and fibroadenoma groups showed significant separation with peak position.

One of the cancer samples has a peak area over double that of the next closest, this sample contained 95 % tumour tissue, 4 % fibrous and 1 % fat by volume assessed by histopathology. There were no anomalies noted during data collection or during fitting which would explain this result.

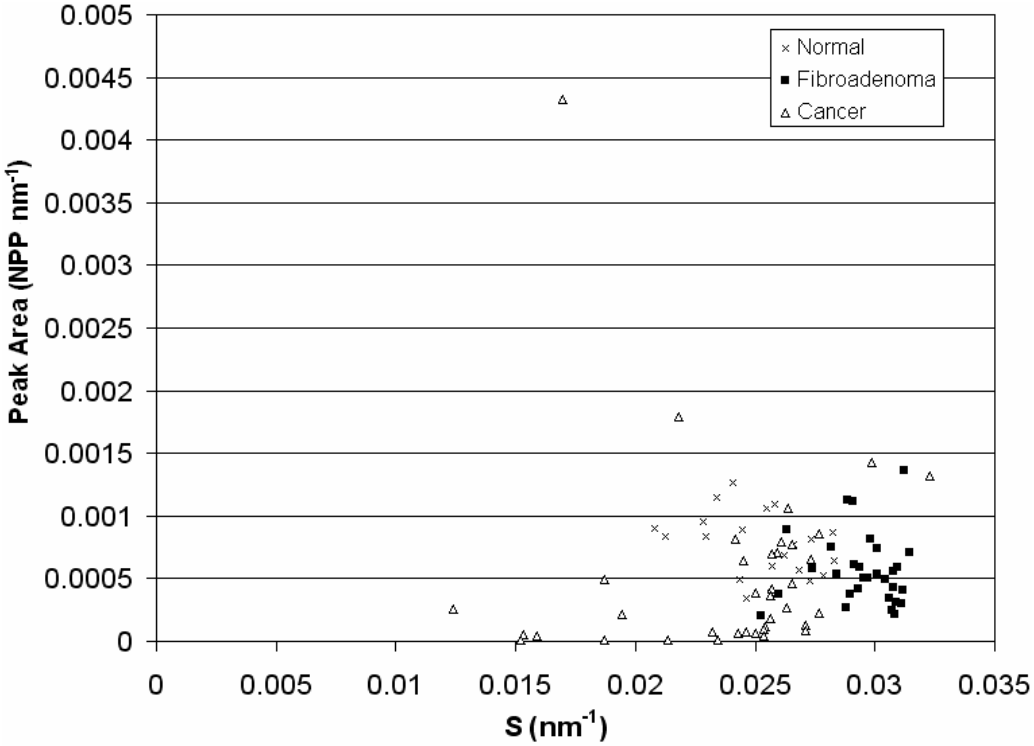

Figure 10.23 S spacing position against peak area for 2nd order Bessel peak

Normal and fibroadenoma samples appear to group with some overlap. The cancer samples show greater variation then the other tissue types with data points spread through the other groups.

10.3.3.3 Amorphous scatter

By virtue of being calculated from a linear region (see Section 10.3.3.1), Rg and the power law exponent were less sensitive to experimental errors such as spacing calibration and intensity normalisation. It was predicted that the intensity of the amorphous scatter would yield diagnostic information (see Section 10.3.2). As it was not possible to make an absolute calibration (see Section 11.4.1.2) the relative difference in the intensity of the amorphous scatter near the beam stop and between the 3rd and 5th axial collagen peaks was used.

The plot of Rg against RIR for normal, fibroadenoma and cancer data (Figure 10.24) showed significant separation of the three tissue groups (Table 10.3.2). The data from cancer tissue samples used in this plot all contained greater than 80 % tumour/tumour stroma by volume, the lower the amount of tumour tissue in the sample the greater the overlap with the normal group.

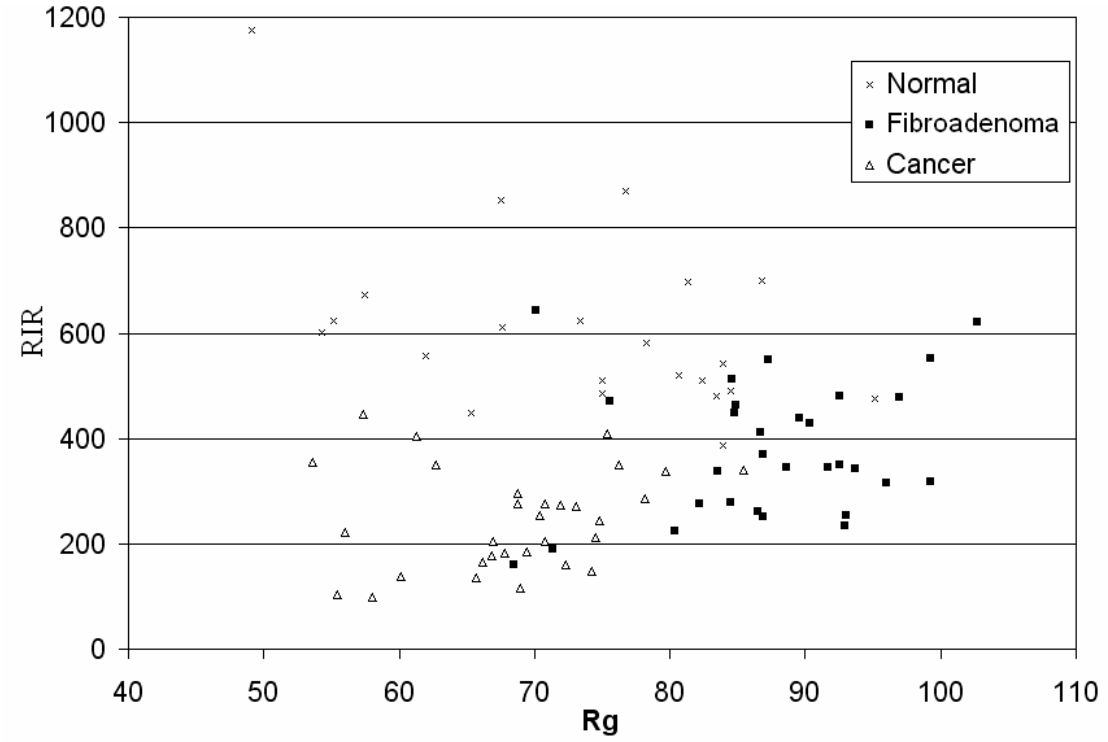

Figure 10.24 Radius of gyration against relative intensity ratio

Only tumour samples containing greater than 80 % tumour tissue by volume as observed by histopathology were included in this plot. The three tissue types form clear clusters. However, the separation between the normal and tumour samples becomes less clear with the inclusion of tumour samples with lower volumes of tumour tissue.

The RIR appeared to be correlated with the amount of tumour tissue present in the sample suggesting it to be a significant (Table 10.3.2) and reliable indicator of disease. As the percentage fat content and percentage fibrous content increase (Figure 10.25 and Figure 10.26 respectively) the RIR increased suggesting that the greater the volume of tumour in a sample the lower the intensity ratio.

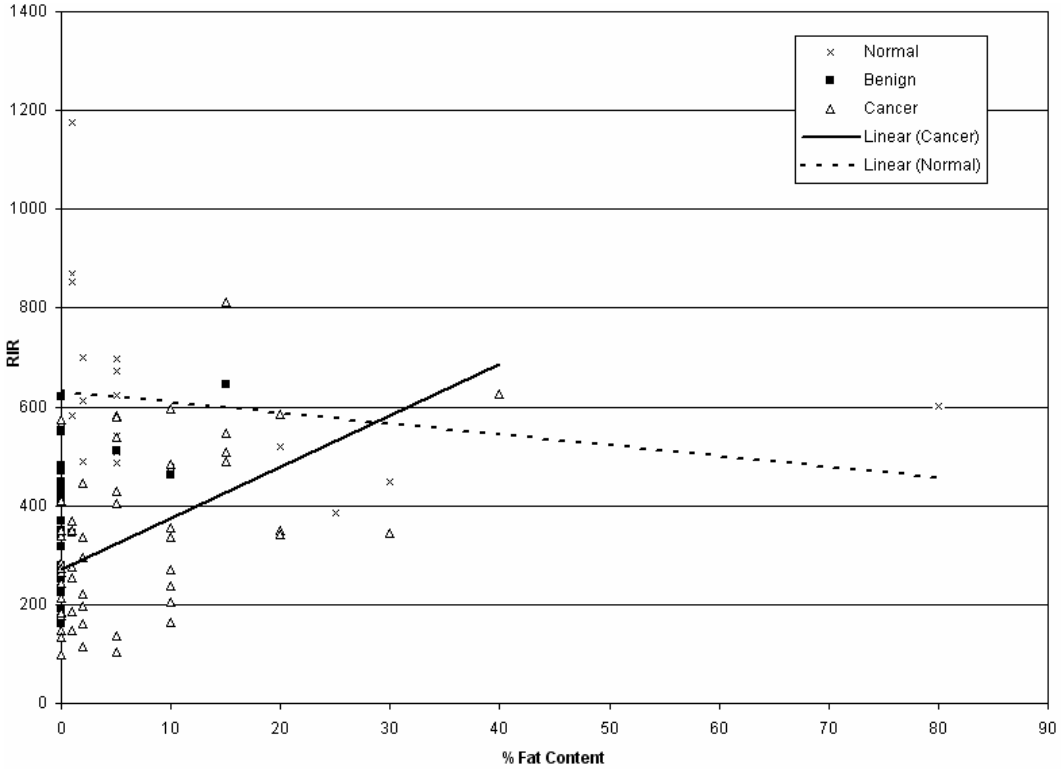

Figure 10.25 Relative intensity ratio versus the % fat content of the samples

As fat content increases the RIR of normal tissue decreases while the RIR of the cancer samples increases. The range of RIR values exhibited by the fibroadenoma values overlaps both the cancer and normal ranges, no trend can be observed with differing tissue content as all the fibroadenoma samples contained over 98% fibrous material.

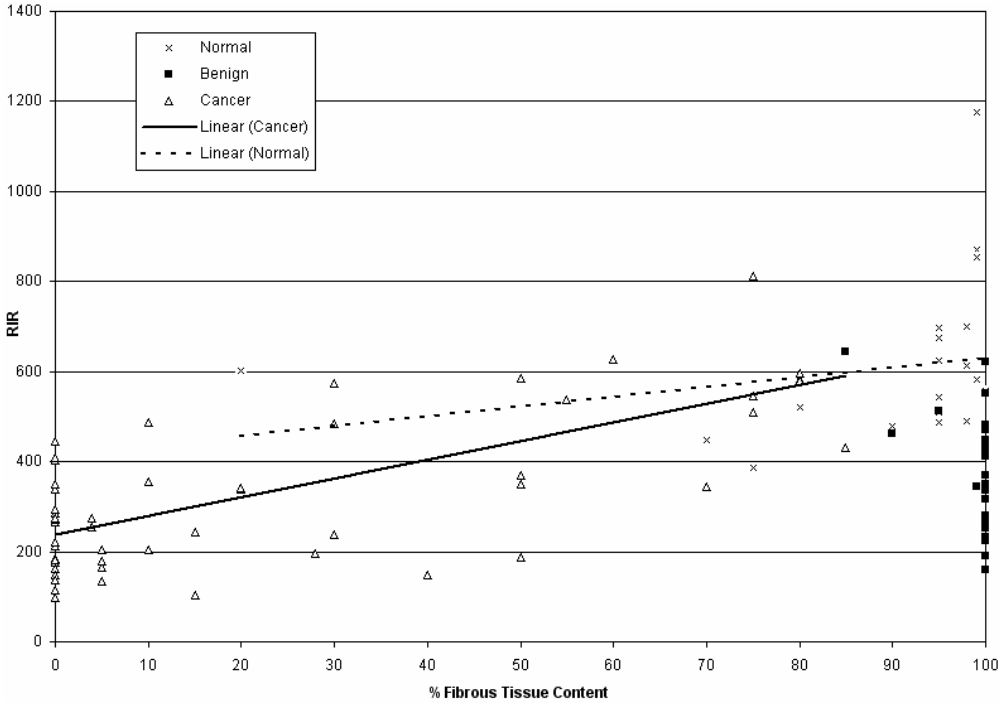

Figure 10.26 Relative intensity ratio versus the % fibrous content of the samples

The RIR of the cancer samples increases as fibrous content increases. The intensity ratio of normal tissue and the fibroadenoma samples appears as the opposite of the fat content, which is as expected as the tissue content of the normal and fibroadenoma samples was classified by just those two parameters, where as the cancer samples have a third component which is the volume of tumour in the sample.

Separating the samples using an intensity ratio below 500 to indicate disease yielded a specificity of 100% and a sensitivity of 90.9% (see Section 11.6). The fibroadenoma samples have an increased Rg compared to both normal and cancer samples which suggested that the average size of the scattering objects in the fibroadenoma samples was larger (see Section 11.10.1).

10.3.3.4 Comparison of oscillated and static data collection

The X-ray scattering data from breast tissue was collected while the sample was oscillated (see Section 8.1.2.3), irradiating as close to the full volume of tissue as possible. Investigating the average X-ray scattering pattern matched the histopathology which made an average assessment from the sections through the whole biopsy. It was not known what the variation within each sample would be. In order to investigate during one data collection session, static data points were also collected. The static data point parameters for the 3rd order Bragg peak area and position (Table 10.3.5 and Table 10.3.6 respectively), the amorphous scatter parameters Rg and RIR (Table 10.3.7 and Table 10.3.8 respectively) were compared to the parameters from the oscillated data. The calculated averages of the parameters from the static points were found to be comparable. The calculated average values were within 0.4 % of the oscillated values for the position of the 3rd order Bragg peak for all samples. Over 92 % of samples gave a calculated average value for the RIR within 20 % of the oscillated value and within 40 % for the calculated average values of Rg and the area of the 3rd order Bragg peak.

The samples which showed greater variation between the calculated average and the value obtained experimentally while the sample was oscillated, demonstrate the need for accurate sampling of all tissue present in the sample. The calculated average for the area of the 3rd order Bragg peak of sample 9 was almost half of the oscillated

value, looking at the static points for sample 9, 3 out of five points showed no collagen peaks. The sample contained 90 % fibrous material by volume which suggested that the highly fibrous region was missed in the static data collections explaining the lower average.

		Point 1 NPP nm^{-1}	Point 2 NPP nm^{-1}	Point 3 NPP nm^{-1}	Point 4 NPP nm^{-1}	Point 5 NPP nm^{-1}	Point 6 NPP nm^{-1}	Oscillation NPP nm^{-1}	Average NPP nm^{-1}
Normal	1	9.818E-05	7.035E-05	1.431E-04	1.276E-04	8.583E-05	1.206E-04	8.445E-05	1.076E-04
	2	9.547E-05	7.651E-05	1.209E-04	2.427E-04			1.516E-04	1.339E-04
	3	7.125E-05	8.724E-05	3.617E-05	1.827E-05	0.000E+00		4.820E-05	4.259E-05
	4	1.486E-04	1.010E-04	2.990E-04	2.145E-04	9.097E-05		1.103E-04	1.708E-04
Fibroadenoma	5	7.954E-05	3.591E-04	1.001E-04	9.112E-05	2.284E-04		1.942E-04	1.717E-04
	6	4.980E-05	2.561E-05	1.042E-04	1.211E-04	3.124E-05		8.567E-05	6.639E-05
	7	1.024E-04	1.572E-04	1.465E-04	1.622E-04	4.488E-05		1.273E-04	1.226E-04
	8	6.063E-05	8.014E-05	1.013E-04	3.176E-05	4.941E-05		1.058E-04	6.465E-05
	9	1.101E-04	8.440E-05	0.000E+00	0.000E+00	0.000E+00		7.315E-05	3.890E-05
	10	4.981E-05	9.080E-05	1.272E-04	9.092E-05			8.994E-05	8.968E-05
	11	5.466E-05	1.700E-04	1.984E-04	1.127E-04	2.029E-04		1.020E-04	1.477E-04
	12	7.696E-06	7.581E-05	2.969E-05	1.088E-04	4.802E-04	5.516E-05	1.639E-04	1.262E-04
	13	8.209E-05	6.407E-05	1.297E-05	1.305E-05	1.190E-05		4.692E-05	3.682E-05
	14	1.521E-04	9.041E-05	7.515E-05	2.764E-05			8.649E-05	8.633E-05
	15	5.122E-05	5.379E-05	7.747E-05				6.276E-05	6.083E-05
	16	1.535E-04	1.549E-04	1.298E-04	1.989E-04			1.539E-04	1.593E-04
	17	2.441E-05	8.200E-05	3.126E-05	0.000E+00	0.000E+00		1.316E-05	2.753E-05
	18	3.781E-05	2.585E-05	2.572E-04	1.124E-04	1.291E-04	5.705E-05	1.651E-04	1.032E-04
	19	2.712E-05	7.567E-05	4.847E-05	1.534E-04	7.143E-05	8.543E-05	6.686E-05	7.692E-05
	20	6.199E-05	1.784E-04	2.954E-05	5.856E-05	1.500E-04	1.816E-05	8.789E-05	8.278E-05
	21	2.340E-05	1.598E-05	5.901E-05				4.748E-05	3.280E-05
	22	1.056E-04	6.622E-05	7.548E-05	1.509E-04	1.321E-04		1.011E-04	1.061E-04
	23	0.000E+00	3.743E-04	4.028E-04	1.789E-04	4.101E-05		2.036E-04	1.994E-04
	24	7.761E-05	1.262E-04	8.441E-05				1.070E-04	9.607E-05
	25	1.334E-04	1.523E-04	1.447E-04	6.600E-05			1.199E-04	1.241E-04
	26	3.516E-04	1.195E-04	0.000E+00	3.114E-05	4.048E-05	8.835E-05	2.233E-04	1.052E-04
	27	1.109E-04	1.048E-04	1.526E-05	6.312E-04	7.385E-05		2.214E-04	1.872E-04
	28	2.383E-04	1.401E-04	1.675E-04				1.997E-04	1.820E-04
Cancer	29	2.524E-04	5.866E-04	7.510E-04	1.642E-04	1.517E-04		3.695E-04	3.812E-04
	30	1.679E-04	3.462E-05	3.548E-04	3.267E-04	1.312E-04	9.935E-05	2.697E-04	1.858E-04
	31	7.874E-05	5.263E-05	2.017E-04	1.099E-04	2.986E-05	3.724E-05	5.890E-05	8.501E-05
	32	1.166E-04	6.664E-05	5.585E-05	2.089E-05			4.406E-05	6.500E-05
	33	1.585E-04	2.015E-04	1.297E-04	3.322E-05	7.140E-05	1.912E-04	1.872E-04	1.309E-04
	34	0.000E+00	0.000E+00	8.626E-05	6.688E-05	3.079E-04	5.929E-05	1.184E-04	8.672E-05
	35	4.934E-05	2.210E-04	4.538E-05	1.382E-05			7.494E-05	8.239E-05
	36	2.160E-04	1.697E-04	2.447E-04	1.810E-04	0.000E+00		1.521E-04	1.623E-04
	37	1.491E-04	2.585E-04	1.743E-04	1.688E-04	6.863E-05		1.750E-04	1.639E-04
	38	1.032E-04	1.390E-04	2.102E-04	2.072E-04			2.523E-04	1.649E-04

Table 10.3.5 3rd order Bragg peak area comparison for static and oscillated data

The average peak positions match the values from the oscillated data (Table 10.3.6), which suggested there was minimal variation of the collagen spacing within the sample. The variation in the values was attributed to the error of fitting the low intensity peaks.

		Point 1 nm^{-1}	Point 2 nm^{-1}	Point 3 nm^{-1}	Point 4 nm^{-1}	Point 5 nm^{-1}	Point 6 nm^{-1}	Oscillation nm^{-1}	Average nm^{-1}
Normal	1	4.625E-02	4.614E-02	4.614E-02	4.620E-02	4.618E-02	4.614E-02	4.617E-02	4.618E-02
	2	4.606E-02	4.608E-02	4.610E-02	4.614E-02			4.614E-02	4.610E-02
	3	4.686E-02	4.684E-02	4.671E-02	4.673E-02			4.672E-02	4.679E-02
	4	4.716E-02	4.659E-02	4.694E-02	4.708E-02	4.697E-02		4.695E-02	4.695E-02
Fibroadenoma	5	4.608E-02	4.602E-02	4.597E-02	4.611E-02	4.607E-02		4.597E-02	4.605E-02
	6	4.609E-02	4.609E-02	4.616E-02	4.615E-02	4.612E-02		4.605E-02	4.612E-02
	7	4.603E-02	4.602E-02	4.566E-02	4.591E-02	4.592E-02		4.595E-02	4.591E-02
	8	4.633E-02	4.643E-02	4.630E-02	4.639E-02	4.629E-02		4.622E-02	4.635E-02
	9	4.639E-02	4.643E-02					4.649E-02	4.641E-02
	10	4.682E-02	4.692E-02	4.683E-02	4.685E-02			4.680E-02	4.686E-02
	11	4.664E-02	4.694E-02	4.691E-02	4.707E-02	4.661E-02		4.685E-02	4.683E-02
	12	4.690E-02	4.687E-02	4.708E-02	4.701E-02	4.688E-02	4.734E-02	4.687E-02	4.695E-02
	13	4.611E-02	4.627E-02	4.639E-02	4.648E-02	4.618E-02		4.621E-02	4.629E-02
	14	4.617E-02	4.618E-02	4.593E-02	4.613E-02			4.619E-02	4.610E-02
	15	4.632E-02	4.624E-02	4.619E-02				4.618E-02	4.625E-02
	16	4.625E-02	4.614E-02	4.620E-02	4.637E-02			4.629E-02	4.624E-02
	17	4.699E-02	4.686E-02	4.684E-02				4.701E-02	4.690E-02
	18	4.655E-02	4.690E-02	4.665E-02	4.677E-02	4.680E-02	4.662E-02	4.668E-02	4.673E-02
	19	4.703E-02	4.697E-02	4.683E-02	4.680E-02	4.691E-02	4.680E-02	4.681E-02	4.691E-02
	20	4.694E-02	4.688E-02	4.674E-02	4.689E-02	4.685E-02	5.129E-02	4.684E-02	4.686E-02
	21	4.635E-02	4.606E-02	4.635E-02				4.618E-02	4.625E-02
	22	4.655E-02	4.650E-02	4.646E-02	4.654E-02	4.645E-02		4.655E-02	4.650E-02
	23	4.694E-02	4.678E-02	4.687E-02	4.661E-02			4.685E-02	4.680E-02
	24	4.684E-02	4.678E-02	4.696E-02				4.683E-02	4.686E-02
	25	4.640E-02	4.634E-02	4.639E-02	4.623E-02			4.634E-02	4.634E-02
	26	4.618E-02	4.621E-02		4.613E-02	4.612E-02	4.620E-02	4.619E-02	4.616E-02
	27	4.674E-02	4.685E-02	4.666E-02	4.702E-02	4.688E-02		4.678E-02	4.683E-02
	28	4.695E-02	4.705E-02	4.688E-02				4.702E-02	4.696E-02
Cancer	29	4.677E-02	4.677E-02	4.674E-02	4.699E-02	4.668E-02		4.687E-02	4.679E-02
	30	4.693E-02	4.678E-02	4.675E-02	4.670E-02	4.663E-02	4.672E-02	4.670E-02	4.676E-02
	31	4.640E-02	4.620E-02	4.626E-02	4.621E-02	4.628E-02	4.613E-02	4.620E-02	4.627E-02
	32	4.677E-02	4.688E-02	4.698E-02	4.700E-02			4.674E-02	4.691E-02
	33	4.682E-02	4.688E-02	4.669E-02	4.681E-02	4.695E-02	4.684E-02	4.684E-02	4.683E-02
	34	4.672E-02	4.673E-02	4.692E-02	4.661E-02			4.668E-02	4.675E-02
	35	4.629E-02	4.645E-02	4.665E-02	4.646E-02			4.648E-02	4.646E-02
	36	4.659E-02	4.652E-02	4.636E-02	4.642E-02			4.646E-02	4.647E-02
	37	4.647E-02	4.658E-02	4.669E-02	4.649E-02	4.635E-02		4.643E-02	4.652E-02
	38	4.699E-02	4.693E-02	4.686E-02	4.679E-02			4.695E-02	4.689E-02

Table 10.3.6 3rd order Bragg peak position comparison for static and oscillated data

The average calculated Rg compared well with the value from the oscillated data (Table 10.3.7). One notable exception to this was sample 3 in which the static points showed a great deal of variation (75 %) which indicated that the static points may not have accurately sampled the full range of oscillation.

		Point 1 nm	Point 2 nm	Point 3 nm	Point 4 nm	Point 5 nm	Point 6 nm	Oscillation nm	Average nm
Normal	1	7.185E+01	7.083E+01	5.367E+01	6.685E+01	6.685E+01	7.712E+01	7.059E+01	6.786E+01
	2	9.891E+01	8.146E+01	8.241E+01	4.143E+01			6.766E+01	7.605E+01
	3	2.709E+01	7.583E+01	8.781E+01	9.768E+01	1.125E+02		4.941E+01	8.019E+01
	4	7.233E+01	7.069E+01	7.132E+01	7.202E+01	6.980E+01		7.216E+01	7.123E+01
Fibroadenoma	5	9.428E+01	6.974E+01	7.646E+01	3.608E+01	7.575E+01		8.489E+01	7.046E+01
	6	8.049E+01	9.978E+01	5.525E+01	7.306E+01	9.151E+01		7.330E+01	8.002E+01
	7	8.756E+01	6.779E+01	7.935E+01	6.363E+01	9.620E+01		6.954E+01	7.891E+01
	8	9.111E+01	9.610E+01	9.321E+01	9.982E+01	9.911E+01		6.288E+01	9.587E+01
	9	3.415E+01	1.535E+01	1.182E+02	1.186E+02	1.126E+02		6.456E+01	7.978E+01
	10	5.138E+01	9.340E+01	7.693E+01	3.370E+01			7.545E+01	6.385E+01
	11	7.735E+01	4.993E+01	5.996E+01	5.466E+01	6.200E+01		8.308E+01	6.078E+01
	12	1.086E+02	9.374E+01	1.011E+02	7.749E+01	7.502E+01	1.082E+02	6.860E+01	9.401E+01
	13	8.140E+01	6.374E+01	1.113E+02	1.100E+02	1.103E+02		6.488E+01	9.535E+01
	14	3.151E+01	6.469E+01	7.962E+01	8.602E+01			5.972E+01	6.546E+01
	15	7.268E+01	9.515E+01	9.921E+01				5.264E+01	8.901E+01
	16	5.982E+01	5.031E+01	7.205E+01	7.412E+01			7.060E+01	6.407E+01
	17	1.103E+02	1.117E+02	1.024E+02	1.105E+02	1.215E+02		6.598E+01	1.113E+02
	18	7.330E+01	8.615E+01	8.423E+01	6.614E+01	5.296E+01	8.219E+01	6.839E+01	7.416E+01
	19	9.957E+01	8.731E+01	9.891E+01	9.420E+01	1.062E+02	1.029E+02	6.739E+01	9.819E+01
	20	8.654E+01	9.617E+01	1.059E+02	1.009E+02	1.031E+02	1.109E+02	6.353E+01	1.006E+02
	21	8.815E+01	9.626E+01	1.173E+02	1.173E+02			6.471E+01	1.048E+02
	22	6.035E+01	7.359E+01	4.666E+01	4.360E+01	6.284E+01		7.690E+01	5.741E+01
	23	1.139E+02	7.687E+01	8.353E+01	8.655E+01	1.008E+02		8.037E+01	9.231E+01
	24	8.929E+01	3.583E+01	7.801E+01				7.968E+01	6.771E+01
	25	7.699E+01	3.979E+01	1.871E+01	1.036E+02			5.663E+01	5.979E+01
	26	2.870E+01	7.957E+01	1.143E+02	7.137E+01	7.552E+01	5.602E+01	8.229E+01	7.091E+01
	27	9.622E+01	7.210E+01	7.545E+01	9.307E+01	7.105E+01	7.942E+01	6.130E+01	8.122E+01
	28	3.047E+01	5.115E+01	6.672E+01				9.103E+01	4.945E+01
Cancer	29	6.525E+01	7.035E+01	5.916E+01	6.045E+01	5.932E+01		8.764E+01	6.291E+01
	30	7.213E+01	7.279E+01	1.374E+00	4.264E+01	7.554E+01	6.585E+01	7.130E+01	5.506E+01
	31	1.057E+02	1.117E+02	8.876E+01	8.681E+01	1.106E+02	1.068E+02	6.965E+01	1.017E+02
	32	7.484E+01	8.303E+01	9.004E+01	9.251E+01			6.421E+01	8.510E+01
	33	8.123E+01	6.409E+01	6.148E+01	8.435E+01	6.258E+01	7.677E+01	7.416E+01	7.175E+01
	34	1.110E+02	1.123E+02	7.709E+01	9.080E+01	7.603E+01	7.576E+01	7.060E+01	9.049E+01
	35	7.638E+01	6.359E+01	7.406E+01	9.288E+01			6.747E+01	7.673E+01
	36	1.008E+02	9.532E+01	8.880E+01	9.640E+01	9.754E+01		7.080E+01	9.577E+01
	37	8.324E+01	8.567E+01	8.676E+01	8.999E+01	8.196E+01		6.573E+01	8.552E+01
	38	6.715E+01	6.968E+01	7.615E+01	6.236E+01			7.929E+01	6.884E+01

Table 10.3.7 Rg comparison for static and oscillated data

The average RIR value calculated from the static data compares well with the oscillated value (Table 10.3.8). Sample 35 showed a high RIR for a cancer sample and showed the highest individual value among the cancer samples. Sample 35 contained only 10 % tumour tissue according to histopathology and thus the higher RIR indicates the sample contains less cancerous tissue than the other cancer samples. The next highest RIR of cancer samples was sample 29 and 31 which contained 30 % and 15 % tumour tissue respectively by volume from histopathological analysis. The lowest RIR was from sample 37 which showed 95 % tumour by volume. Indicating the RIR was inversely proportional to tumour volume.

		Point 1	Point 2	Point 3	Point 4	Point 5	Point 6	Oscillation	Average
Normal	1	640	798	556	628	628	451	629	617
	2	842	428	644	679			583	648
	3	547	487	809	829	312		641	597
	4	428	439	581	663	650		455	552
Fibroadenoma	5	552	542	427	503	605		462	526
	6	436	640	511	562	372		494	504
	7	669	403	732	589	942		590	667
	8	975	912	931	1051	975		831	969
	9	820	622	611	264	446		523	553
	10	514	613	778	495			565	600
	11	428	522	357	457	665		465	486
	12	649	794	1235	990	615	616	785	816
	13	447	453	493	857	754		552	601
	14	612	698	924	614			707	712
	15	479	562	602				535	548
	16	459	670	548	653			566	583
	17	344	447	476	318	741		355	465
	18	744	783	465	579	742	526	573	640
	19	637	657	1028	1321	1251	1238	1038	1022
	20	875	663	666	648	707	423	660	664
	21	407	394	758	330			543	472
	22	758	489	658	649	789		652	669
	23	170	414	381	383	372		395	344
	24	555	507	814				452	625
	25	448	626	516	607			546	549
	26	574	529	214	820	742	862	550	623
	27	70	468	464	159	200	208	281	262
	28	460	500	471				443	477
Cancer	29	566	614	541	628	505		580	571
	30	511	683	524	338	452	617	430	521
	31	671	625	992	704	482	487	586	660
	32	389	311	184	301			349	296
	33	126	211	386	293	392	263	187	279
	34	356	202	182	336	390	284	265	292
	35	480	725	975	761			596	735
	36	356	270	184	188	172		204	234
	37	160	113	132	157	162		135	145
	38	204	418	406	517			343	386

Table 10.3.8 Relative intensity ratio comparison of static and oscillated points

There was a large amount variance between of the static points (Table 10.3.9), averaging at approximately 50 % for Rg, RIR and peak area and reaching a maximum of 98 %. The average of the static points matched the oscillated data which suggested that oscillating the sample during data collection was an efficient way of examining the gross structure of the sample. This worked well for identifying samples which are predominantly tumour. However, in samples with only a small amount of diseased material the accuracy was reduced, suggesting that using the average was not an ideal method for building a model to define features associated with disease (see Section 11.3.3).

% variation in static data		Average	Max
Bragg 3 Area	Normal	62.963103	69.57525
	Fibroadenoma	69.551063	78.85219
	Cancer	79.867171	93.74661
Bragg 3 Centre	Normal	0.5399582	1.208651
	Fibroadenoma	0.9340739	0.803824
	Cancer	0.6061922	0.771704
Rg	Normal	41.986745	75.92819
	Fibroadenoma	42.523487	61.73129
	Cancer	28.56176	98.1817
RIR	Normal	47.619856	62.38079
	Fibroadenoma	44.366482	57.25643
	Cancer	48.882007	67.84191

Table 10.3.9 Percentage variation in static data

10.3.4 Principal component analysis

The output of the principal component analysis (PCA) consists of the principal components (or loadings), which describe the nature of the variance in the samples against spacing and coefficients which quantify the correlations of each file to calculated principle components (see Section 7.11.4). PCA was performed on data from synchrotron X-ray scattering experiments using both 1 m and 6.25 m cameras (see Section 8.3.3.1).

10.3.4.1 1 metre camera

Data from a small preliminary data set was collected using a 1m camera consisting of 8 malignant tissue samples and 4 samples from normal tissue. L1 and L2 (the primary and secondary loadings) (Figure 10.27) described roughly 96 % of the variance in the data analysed, the other 3 loadings (L3, L4 and L5) described the remaining 4 %. There were a number of significant features described by the loadings below 0.2 nm^{-1} S. Between 0.2 and 0.4 nm^{-1} S the scattering peak associated with fat (approximately 4.3 nm d spacing) can be observed, within this region the observed variance was related to the fat content of the samples. Fat content could not be directly related to disease and above 0.4 nm^{-1} S spacing there are only minimal differences between samples. Thus the spacing range <0.2 nm^{-1} showed the greatest variance with disease state.

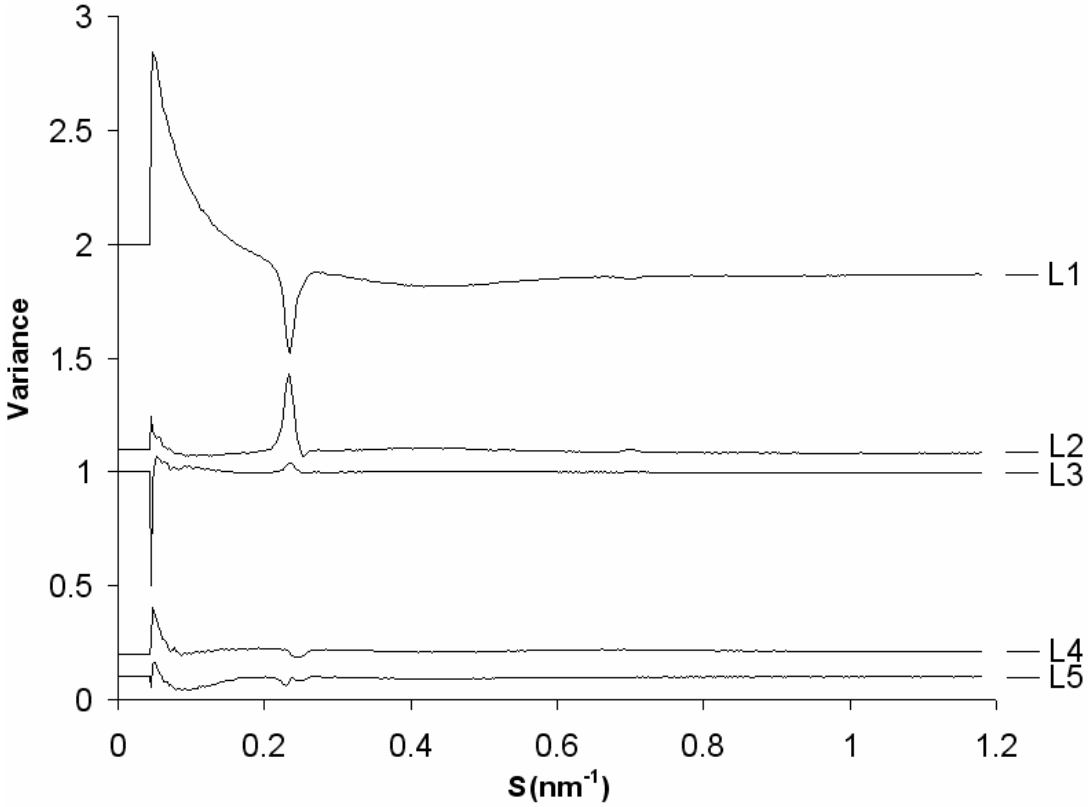

Figure 10.27 The principle components which describe the variance in the data set

The five loadings shown describe the variance between samples, 96 % of the variance is accounted for by L1 and L2. The remaining 3 loadings describe the remaining 4 %. The greatest variance exists in the data range below 0.2 nm^{-1}. Between 0.2 and 0.4 nm^{-1} the variance is dominated by the fat content of the sample which was not directly related to disease and above 0.4 nm^{-1} there are only minimal differences between samples.

Plotting C1 against C2 (Figure 10.28), the coefficients which describe the correlation with L1 and L2 respectively, suggested that there was a major variance in the data linked with the disease state of the tissue. All samples from malignant tissue show positive correlation with L1. All the normal samples showed a negative correlation with L1. Under histopathological analysis sample A16 showed no signs of malignancy, containing only stroma indicating that it was misclassified as a diseased sample and should have been classified as normal. The cause of the misclassification was not know but could have been caused either by mislabelling the tissue sample or sampling error during tissue collection. One of the tumour samples (A5) has a C1 value of 0.09 which is a weaker correlation with L1 that the other tumours which all exhibit C1 values above 0.2. Sample A5 contains only 10 % tumour tissue by volume assessed by histopathology which suggested C1 may not only be an indicator of

disease but also an indicator of the volume of diseased tissue a sample contains. Using C1 alone to classify the samples yields a sensitivity and specificity of 100 % (see Section 11.6).

There does not appear to be significant association of disease state with C2 as 4 out of 6 tumour samples have no significant correlation with C2, one tumour sample is positively correlated with C2, one tumour sample is negatively correlated with C2 and 3 out of 5 normal samples are positively correlated with C2 while the other 2, including sample A16 (the misclassified "tumour" sample) are negatively correlated with C2.

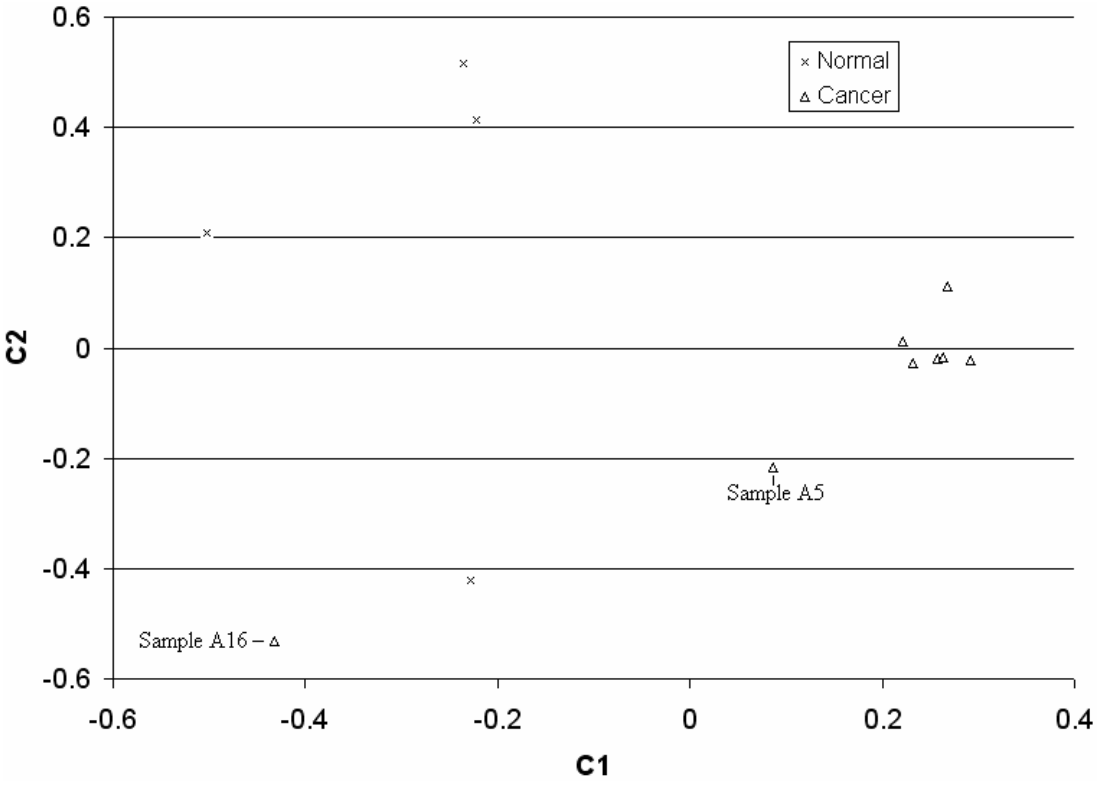

Figure 10.28 Coefficients showing agreement with principle components F1 and F2

The normal and tumour samples are well separated by the coefficient C1 which describes the agreement with L1. The only cancer sample to show a negative correlation with L1 (A16) was shown to contain only stroma and no sign of disease by histopathological analysis. The tumour sample with a C1 value of 0.09 (A5) contained only 10 % tumour tissue by histopathological analysis showing a possible trend with the amount of diseased tissue present in the sample. No difference can be observed between malignant and benign tumours using C1 or C2.

When plotted against S, it was possible to interpret the relationships in the data the loadings describe (the full spacing range Figure 10.27 and below 0.3 nm^{-1} Figure 10.29). L1 describes a high background at low S and a negative peak at S=0.233 nm^{-1} which indexes to the spacing of fat (d = 4.3 nm). This means the tumour samples which exhibit a positive C1 coefficient, display a weak peak associated with the presence of fat and high background levels, where as the normal peaks which have negative C1 coefficients exhibit low background scatter up to 0.2 nm^{-1} and a high intensity peak associated with fat. As a feature associated with the scattering peak from fat is present in L1 it is possible some of the separation was caused by fat content and not disease, with only 12 samples in this data set the diagnostic capabilities cannot be confirmed. To further establish the correlation with disease PCA needed to be performed on a larger data set and in a S spacing range below 0.2 nm^{-1} where the greatest variance is observed, but which excludes the scattering range which contains the scatter from the fat peak.

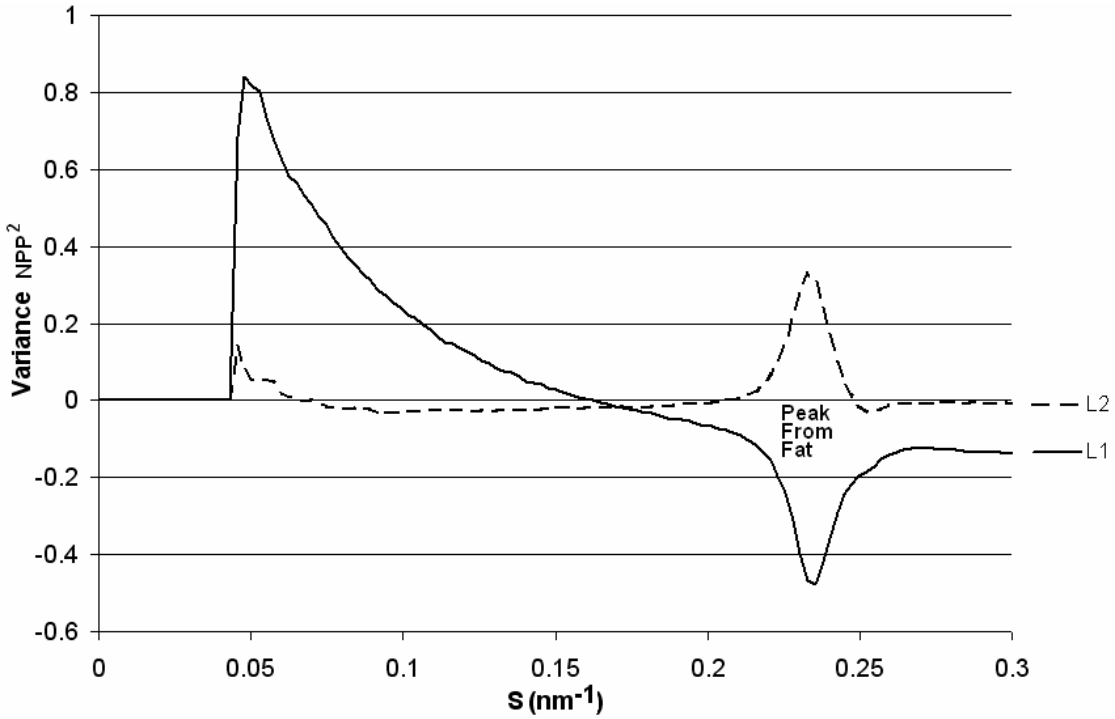

Figure 10.29 F1 and F2 from 0 to 1.6nm^{-1}

A positive correlation with L1 suggests amorphous scatter was increased below 0.2 nm^{-1} and decreased above 0.25 nm^{-1}. A lower amount of scattering from the fat peak (0.23 nm^{-1}) was also suggested by a positive correlation with L1.

10.3.4.2 6.25 metre camera

The PCA from the 1 m data suggested that the greatest variance associated with disease could be observed below S=0.2 nm^{-1}. The data collected using a 6.25 m camera provided data up to approximately S=0.1 nm^{-1} and was analysed using PCA with the aim of creating a model for classification (see Section 8.3.3.1.2).

The use of normalisation (scaling so the area under each X-ray scattering profile was equal) and scaling (Log_{10} or S^2 visualisation of data) did have an effect on the performance of the model (Table 10.3.10). The use of normalisation gave lower training performance (measure of the number of samples in the training data set correctly identified) which suggested that the method used to normalise intensity as part of the data processing (see Section 8.2.1.3 and Section 11.4.1.2) was adequate and that further normalisation as part of the PCA pre-processing was eliminating changes in intensity which carried diagnostic information. The use of scaling did improve the training performance of the model which indicated that differences in the scattering profiles at higher values of S were significant for diagnosis. Without scaling the difference in the low intensity areas was small and would have lower significance in the model.

Using no additional normalisation and intensity scaling by using Log_{10} gave the best performance and was investigated further. The plot of the 2 functions (LD1 and LD2) produced by linear discriminant analysis (see Section 8.3.3.1.2) showed clear separation of the tissue types with only a few outliers (Figure 10.30).

Intensity Normalisation	Yes			Yes			No			No		
Log_{10} Scaling	No			Yes			Yes			No		
S^2 Scaling	No			No			No			Yes		
Distance between Nor. and Fi.	9.5047			22.0738			21.9044			17.2841		
Distance between Nor. and Ca.	11.5158			12.1367			12.2519			10.8107		
Distance between Fi. and Ca.	17.7715			16.0818			16.5109			14.611		
Total Distance between all	38.7919			50.2924			50.6673			42.7058		
	PCA Classification			PCA Classification			PCA Classification			PCA Classification		
	Nor.	Fi.	Ca.	Nor.	Fi.	Ca.	Nor.	Fi.	Ca.	Nor.	Fi.	Ca.
Histopathology Nor. (No. of samples)	19	2	1	21	1	0	21	1	0	20	0	2
Histopathology Fi. (No. of samples)	1	27	2	1	27	2	1	27	2	1	26	3
Histopathology Ca. (No. of samples)	3	0	53	4	0	52	2	0	54	1	1	54
Nor. % Correct	86.3636			95.4545			95.4545			90.9091		
Fi. % Correct	90			90			90			86.6667		
Ca. % Correct	94.6429			92.8571			96.4286			96.4286		
Training Performance %	91.6667			92.5926			94.4444			92.5926		
Cross Validation	PCA Classification			PCA Classification			PCA Classification			PCA Classification		
	Nor.	Fi.	Ca.	Nor.	Fi.	Ca.	Nor.	Fi.	Ca.	Nor.	Fi.	Ca.
Histopathology Nor. (No. of samples)	16	4	2	18	2	2	18	2	2	18	1	3
Histopathology Fi. (No. of samples)	4	24	2	2	24	4	2	24	4	1	25	4
Histopathology Ca. (No. of samples)	8	2	46	6	2	48	6	1	49	2	5	49
Nor. % Correct	72.73			81.82			81.82			81.82		
Fi. % Correct	80.00			80.00			80.00			83.33		
Ca. % Correct	82.14			85.71			87.50			87.50		
Overall performance %	79.6296			83.3333			84.2593			85.1852		

Table 10.3.10 Output of principal component models using different scaling methods

Abbreviations for normal (Nor.), fibroadenoma (Fi.) and cancer (Ca.) were used in this table for clarity. All methods used yield training performances for the models of over 90 %. Although the performance is reduced when cross validation was used the reduction is not dramatic enough to suggest that random variation was overtly influencing the models. The use of scaling factors improves the performance of the models and the use of normalisation appears detrimental.

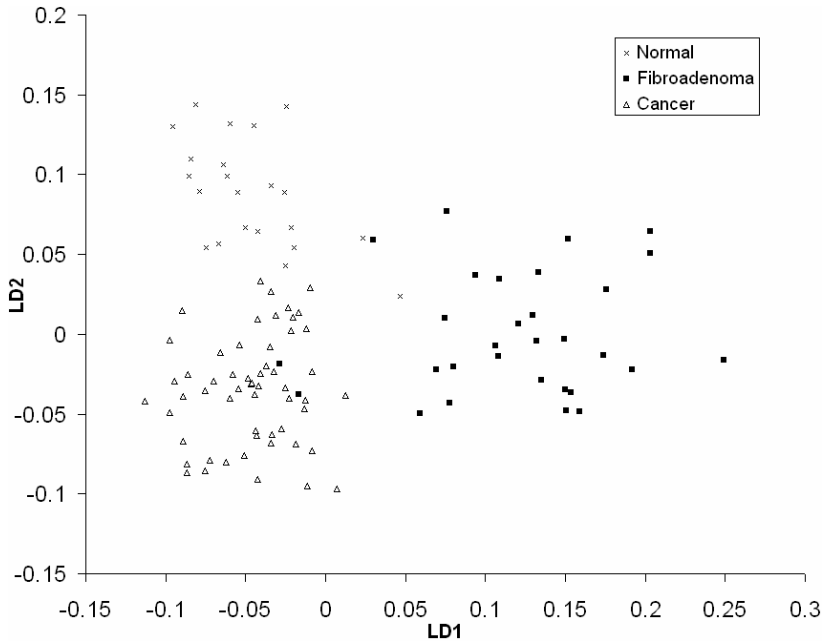

Figure 10.30 Separation of tissue types using linear discriminate analysis

Tissue types are clearly separated with only a few samples appearing in the wrong groups.

Not all loadings (L1 to L25) described variance in the data which was associated with the difference between tissue types. The loadings which were significant in building the model were identified by having an F value greater than the critical F value (F Crit = 2.3536) (Table 10.3.11).

Intensity Normalisation	Yes	Yes	No	No
Log_{10} Scaling	No	Yes	Yes	No
S^2 Scaling	No	No	No	Yes
F Value L1	**7.2147**	**22.156**	1.1033	0.6603
F Value L2	**16.129**	**13.686**	**17.792**	**16.93**
F Value L3	**4.4295**	**28.296**	**58.007**	**6.6138**
F Value L4	**5.1074**	**2.7638**	1.4308	**11.998**
F Value L5	**3.1073**	**3.6699**	**3.537**	1.4787
F Value L6	**4.4261**	1.5999	**5.3409**	**20.775**
F Value L7	**4.9091**	1.2716	1.084	1.1809
F Value L8	**10.751**	0.9341	2.0249	0.0592
F Value L9	**3.2121**	0.6039	0.2987	2.0851
F Value L10	2.1841	**7.2903**	0.9492	0.1571
F Value L11	0.8351	**3.8771**	**6.72**	1.9385
F Value L12	2.2125	0.5279	**3.7834**	**8.425**
F Value L13	0.044	1.4292	1.3827	0.6113
F Value L14	**2.7008**	0.9879	0.6561	1.3442
F Value L15	0.2401	0.2475	1.111	3.435
F Value L16	0.17	2.1516	0.4011	0.2201
F Value L17	2.1915	0.471	2.1726	2.1567
F Value L18	0.8908	0.1949	0.1314	0.4319
F Value L19	0.3011	0.0479	0.2074	0.4449
F Value L20	1.5992	1.216	0.8685	1.3416
F Value L21	0.8807	0.1353	1.4355	0.7322
F Value L22	1.0881	0.3382	0.0757	0.41
F Value L23	0.1061	0.3585	0.2313	1.1873
F Value L24	0.5767	0.3571	0.0465	0.674
F Value L25	0.0105	0.3173	0.3442	0.2951

Table 10.3.11 F values for loadings 1 through 25

The F values indicate the significance of the loading for separating the tissue types. An F value (shown in bold) over the critical F value (F crit = 2.3536) indicates the loading was significant.

L1 accounts for 93.89 % of the variance L2 3.57 % and L3 only 0.98 % the remaining loadings (up to L25) account for the remaining 1.66 %. Therefore the significant loadings which describe the greatest variance in the data (L2 and L3) contain the most relevant differences in the X-ray scattering profiles related to the changes in structure of the samples. The loadings which describe the least variance in the data describe noise (Figure 10.31). L2 shows Bessel peaks and all 5 Bragg orders (though the even orders are weak), while L12 shows some features in the region of the Bessel peaks and 3rd and 5th order Bragg features the profile was noisy.

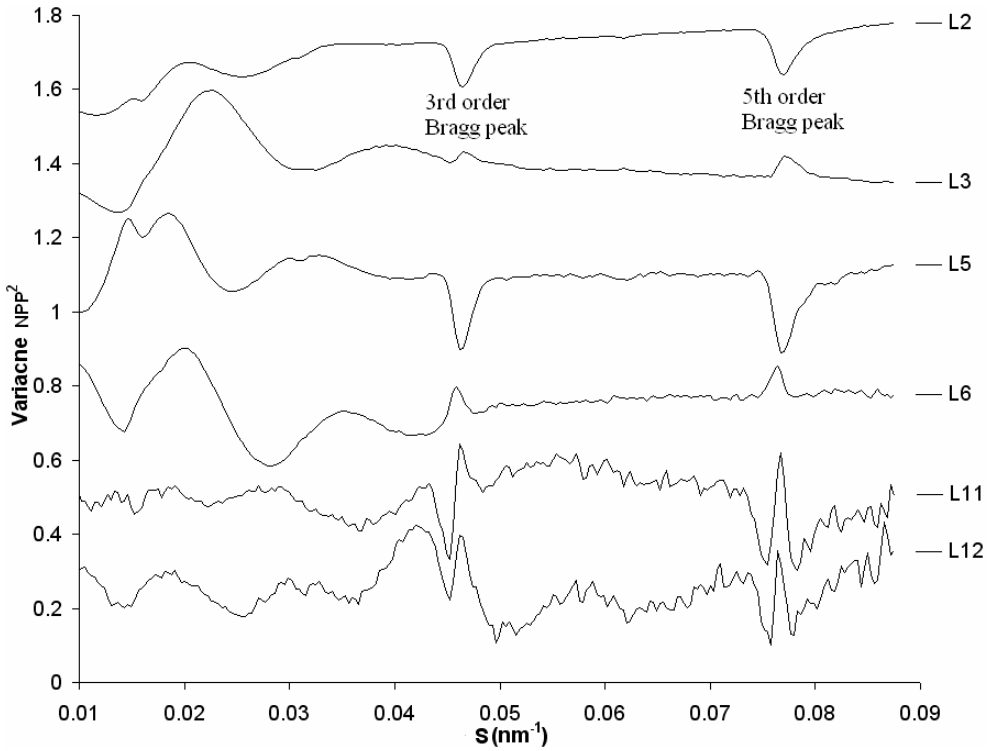

Figure 10.31 Significant loadings against S spacing

The lowest significant loading (L2) shows features associated with highly structured collagen, both Bessel peaks and Bragg (1st, 2nd, 3rd, 4th and 5th order) peaks are present. L3, L5 and L6 also some variation in the region of the Bessel peaks and the 3rd and 5th Bragg peaks. The higher significant loadings (L11 and L12) show features which account for only a small portion of the variance in the data and thus show noise.

The average scores for each tissue type (Table 10.3.12) combined with the loadings they are associated with represent the features associated with disease. L2 accounts for the greatest variance in the data of any of the significant loadings and thus was arguably the most important loading for determining the structural differences in between tissue types. S2 was negative for the normal average while positive for fibroadenoma and cancer, which suggested that normal samples have a greater amount of structural order in the collagen while both fibroadenoma and cancer tissues have a lower degree of ordering. The product of L2 and S2 also show that in normal samples the intensity near the beam stop ($S<0.15\ nm^{-1}$) would be higher in the normal samples than fibroadenoma and cancer samples. The intensity of the background between the 3rd and 5th axial orders would be higher in fibroadenoma and cancer samples.

The product of S3 and L3 shows a reduction in the axial peak intensity of normal and cancer samples and an increase in the peak intensity of fibroadenoma samples. While axial peak intensity increased for both normal and fibroadenoma samples and decreased for cancer samples with the product of S5 and L5.

The axial peak features of L6 appeared at slightly lower S spacing than in the other loadings. The score (S6) for the normal samples had a negative correlation suggested the peak intensity at the lower S position was reduced thereby appearing to increase S spacing. While the positive correlation of both fibroadenoma and cancer samples indicates a reduced S spacing in diseased tissues.

Loadings L11 and L12 accounted for the least variance in the data and as such are affected by noise. However, it is interesting to note that they do also show peaks corresponding to the 3^{rd} and 5^{th} axial orders of collagen. The effect of L11 and S11 was to increase axial peak intensity in all tissue types, with the greatest effect on normal samples and least in cancer samples as all show positive correlation with S11 the largest value for S11 being normal and the smallest being cancer. L12 and S12 would increase axial peak intensity in normal samples and decrease it in fibroadenoma and cancer samples.

The value of all the scores for the normal average were over 10 times the magnitude of both the fibroadenoma and the cancer samples which indicated that the average X-ray scattering profile of the normal samples varied greatly, while the fibroadenoma and cancer are close to the average. The reason for the fibroadenoma and cancer samples being close to the average was due to the fact that there were a disproportionate number of cancer samples (56, 30 and 22 samples for cancer fibroadenoma and normal respectively). Fibroadenoma was the second largest group

and exhibits similar features to cancer samples and thus was close to the average but showed greater difference than the cancer samples.

	Normal	Fibroadenoma	Cancer
S2	-0.159790909	0.015256667	0.000951786
S3	-0.54935	0.003913333	-0.001860714
S5	-0.446113636	-0.03397	0.003258929
S6	-0.563959091	0.027353333	0.000128571
S11	1.027231818	0.03951	0.00315
S12	0.367527273	-0.00689	-4.10714E-05

Table 10.3.12 Average scores for each significant loading for all 3 tissue types

The combined effects of all the significant scores and loadings was that normal samples show increased background scatter near the beam stop and reduced amorphous scatter intensity between the 3rd and 5th axial peaks compared to fibroadenoma and cancer samples. Axial peak intensity would be greatest in normal samples and lowest in tumour samples and the axial peak spacing for fibroadenoma samples would be lower in fibroadenoma and cancer samples compared to normal samples. The observations made from the PCA results matched the observations from manual analysis techniques (see Section 11.5.2.3).

10.4 Conventional X-ray source investigation of breast tissue

A small number of samples exhibited preferred orientation of the collagen fibres. In these samples weak peaks corresponding to the D spacing of collagen were seen. In samples with no preferred orientation the wide beam caused the rings to be superimposed and not easily visible. The only difference between tissue types that could be observed from the 2D X-ray scattering images was the high intensity region near the beam stop extended further in the data from tumour samples compared to the normal samples (Figure 10.32).

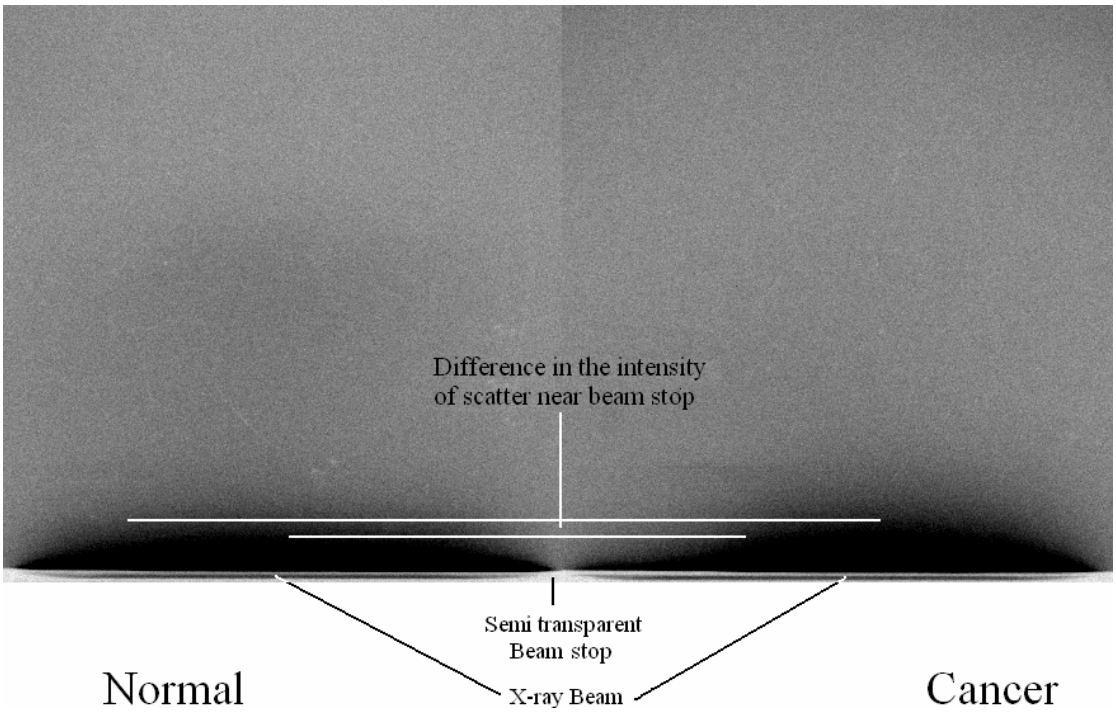

Figure 10.32 SAXSess X-ray scattering images of both normal and cancer samples

The wide X-ray beam can be observed through the semi transparent beam stop allowing for normalisation of spacing and intensity. The major difference in the two tissue types is that the area of high intensity close to the beam stop extends to higher S spacing in the data from the cancer samples compared to the normal samples.

The 2D images were integrated, combining all points of equal distance form the beam position to produce a 1 dimensional profile of intensity against scattering angle which enabled further investigation of the differences (see Section 8.2.2.1). Clear differences could be observed directly from the 1 dimensional plots of intensity against S (Figure 10.33). The samples excised from normal tissue produced a greater intensity of amorphous scatter close to the beam stop compared to the samples collected from tumour tissue. The average gradient of data close to the beam stop from normal tissue is approximately 6 % greater than that from tumour tissue for a range of S between 0.017 nm^{-1} and 0.047 nm^{-1}.

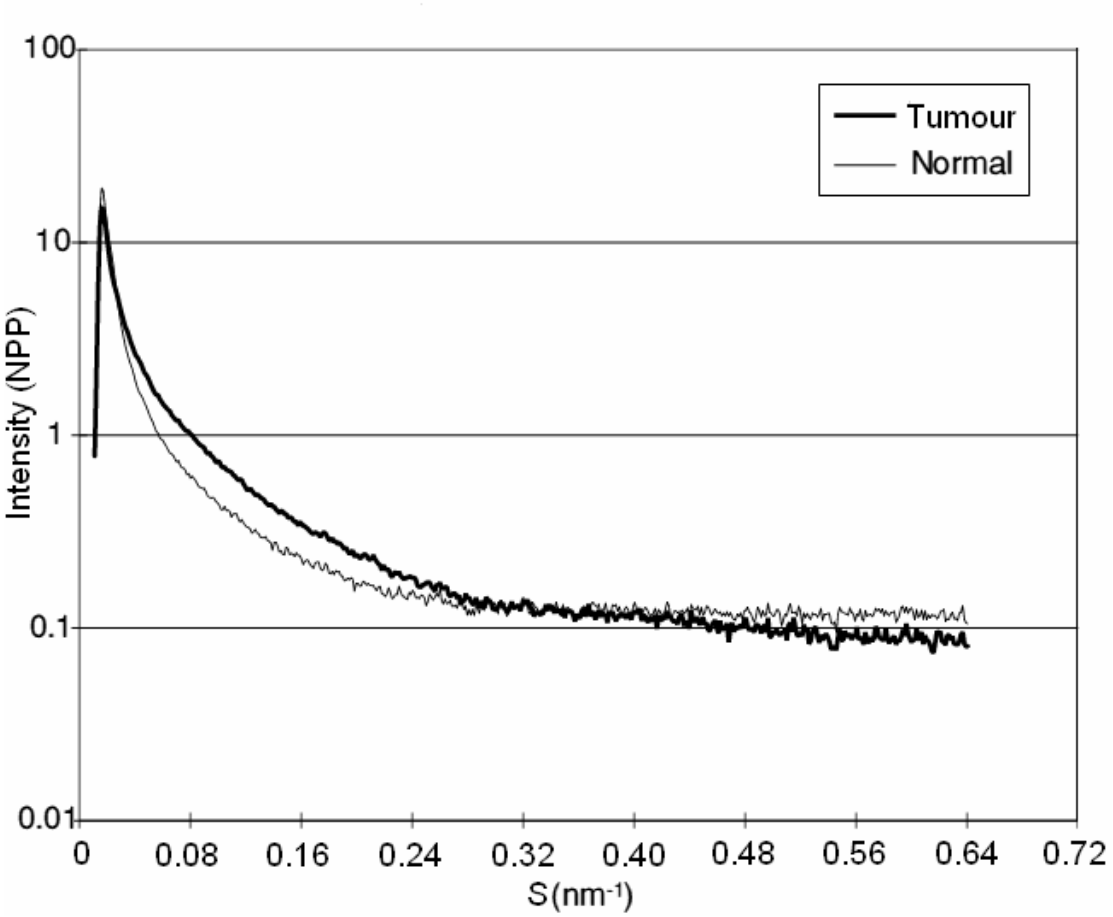

Figure 10.33 S against typical intensity plots for tumour and normal tissue

Differences in the intensity and gradients between the two tissue types can be observed. The normal data shows greater intensity near the beam stop but has a steeper gradient than the tumour data. The tumour showing greater intensity from S=0.04 $nm^{-1}$to S=0.24 nm^{-1}. The intensity of the tumour and normal data is approximately equal between S=0.24 nm^{-1} and S=0.40 nm^{-1} when the intensity of the normal data is once again higher than the tumour data.

PCA was applied to all 23 samples and analysed to determine whether any clustering associated with tissue type could be identified. Restricting the data used for the PCA analysis to exclude the area of the beam stop and the low intensity (noisy) regions at high S improved the clustering by excluding differences not related to the disease state of the samples. The range used for the PCA analysis was S=0.017 nm^{-1} to S=0.036 nm^{-1} for this data.

The first three loadings (L1, L2 and L3) provide the greatest variance, and showed normal and tumour tissue in distinct groupings (Figure 10.34).

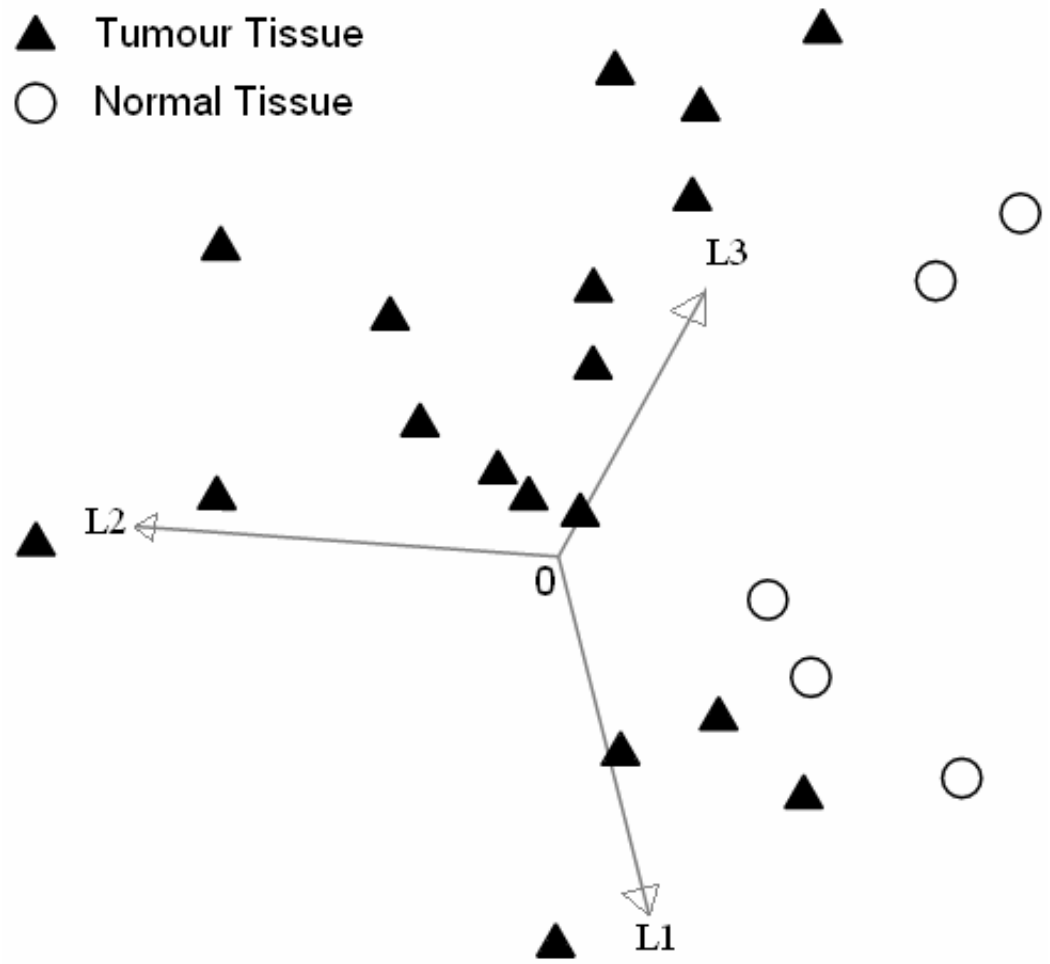

Figure 10.34 Results of PCA using Pirouette in the range S= 0.017nm^{-1} to 0.037 nm^{-1}.

Separation of tumour and normal samples using three principle components shows the 2 and 3 to be most significant.

Figure 10.34 suggests that the normal samples are negatively correlated with L2, positively correlated with L3, and also a small positive correlation with L1. Using the scores for each loading for all the samples, simple logic was used to show how well the correlations relate to the disease state of the tissue (Table 10.4.1).

	Factors			Indicators of Normal Tissue						
Sample Code	**L1**	**L2**	**L3**	**+L1**	**-L2**	**+L3**	**-L2 & +L3**	**+L1 & +L3**	**+L1 & -L2**	**+L1& -L2 & +L3**
UR4167048#TA-0	7.133395	0.841607	-0.351578	N	T	T	T	T	T	T
UR815397#TA-0	-7.405497	0.68646	0.106113	T	T	N	T	T	T	T
UR340090#TA-0	0.407523	5.673602	-0.058752	N	T	T	T	T	T	T
UR307936#TA-0	2.693728	1.754596	-0.781898	N	T	T	T	T	T	T
NA46630#0	7.664367	2.964785	0.165311	N	T	N	T	N	T	T
NA46546#0	9.681283	-1.565809	-0.958075	N	N	T	T	T	N	T
N700675#0	7.026618	6.079332	-0.663301	N	T	T	T	T	T	T
NA46628#T2	1.502628	1.326303	0.501008	N	T	N	T	N	T	T
NA46628#T1	-7.723698	1.955729	0.098687	T	T	N	T	T	T	T
NA44463#T1	-3.706326	1.535587	0.204385	T	T	N	T	T	T	T
NA44004#T1	3.925245	1.884472	0.381641	N	T	N	T	N	T	T
NA43035#T1	15.039019	1.638636	0.922232	N	T	N	T	N	T	T
NA42690#T1	17.176144	-0.995147	-1.069603	N	N	T	T	T	N	T
N948448#0	14.187178	-0.652772	-0.494224	N	N	T	T	T	N	T
N927396#T1	12.235553	-2.809982	-0.949205	N	N	T	T	T	N	T
N782288#T1	3.094351	1.380026	-0.157899	N	T	T	T	T	T	T
N780202#0	-5.285416	2.585394	0.129495	T	T	N	T	T	T	T
N339699#T1	4.175075	3.732681	0.180715	N	T	N	T	N	T	T
N70#A	-3.755688	-1.798374	-2.352582	T	N	T	T	T	T	T
N56#A	8.898535	-1.366473	1.21781	N	N	N	N	N	N	N
N56#1	5.907425	-1.895729	1.147455	N	N	N	N	N	N	N
N49#A	23.577097	-3.963522	0.852518	N	N	N	N	N	N	N
N49#1	15.614983	-2.116683	0.121061	N	N	N	N	N	N	N
			% Sensitivity	**22.222**	**77.778**	**50**	**100**	**72.222**	**77.778**	**100**
			% Specificity	**80**	**100**	**80**	**80**	**80**	**80**	**80**

Table 10.4.1 The scores for each of the three factors for the tissue samples used in the tumour normal comparison. As well as the indicators used in an attempt to correlate the scores for each factor with the disease state of the tissue (T = Tumour, N = Normal).

The corresponding sensitivities and specificities show F2 to be the most significant single factor to determine the disease state and a combination of F2and F3 provides a sensitivity of 100 %.

L1 is the factor which shows the greatest variance. However, the relationships it describes may not be due to changes caused by disease. The sensitivity and specificity using L1 as an indicator alone is only 22.2 % and 80 % respectively. The disease state of the tissue was better represented by using L2 as an indicator; yielding a sensitivity of 77.7 % and specificity 100 %. Using L3 as an indicator gives a sensitivity of 50 % and specificity 80 %. Classification was improved using a combination of the scores. The samples from tumour tissue that are negative in L2 are distinct from the normal samples in being also negative in L3. The samples from normal tissue are all positive in L3 with the exception of one. The “rogue” sample was distinct from all of the samples as its L2 score has a value of -2.35, more than twice the corresponding value of any of the other samples. Using a negative value for F2 and a positive value for L3

as a classifier it is possible to distinguish the 18 tumour tissue samples from 4 of the 5 normal tissue samples. With this classifier there is one false positive giving a sensitivity and specificity of 100 % and 80 % respectively. Using a positive L1 as well as the negative L2 and positive L3 yields no additional improvement in the sensitivity or specificity.

L2 and L3 are shown graphically in Figure 10.35. Negative correlation with L2 suggests a higher intensity below 0.020 nm^{-1} and lower intensity above this point. A positive correlation with F3 suggests increased intensity in the ranges below 0.0.019 nm^{-1} and above 0.020 nm^{-1} with a lower intensity in the range between these values. For all but one of the normal samples which show a negative correlation with F2 and a positive correlation with L3, the effect of these factors combined suggests a higher than average intensity below 0.019 nm^{-1} and lower than average intensity from 0.020 nm^{-1} to 0.026 mn^{-1}. Similar results for breast tissue using SAXS from a synchrotron source have been published previously (Fernandez, 2002).

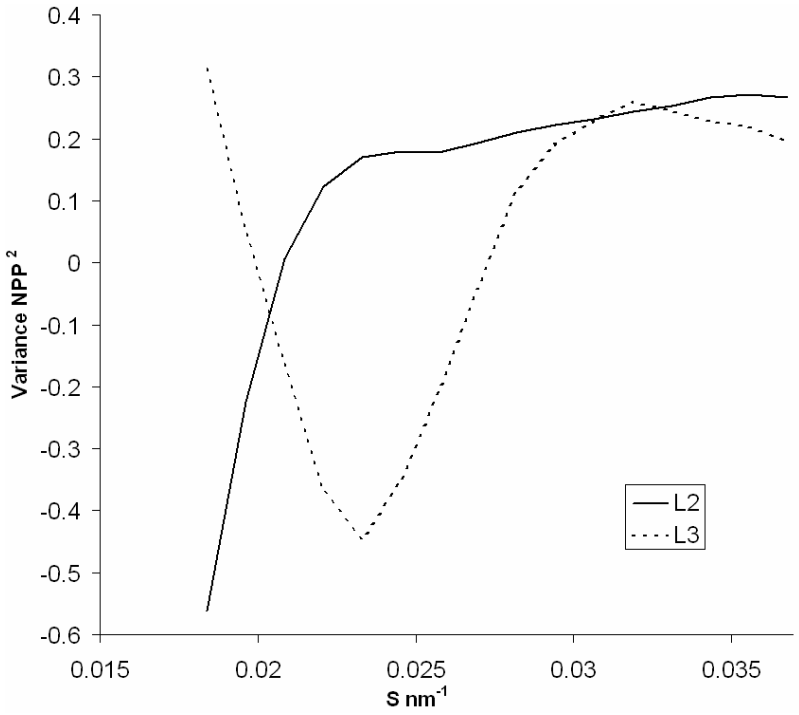

Figure 10.35 loadings 2 and 3 plotted against S

The relationships in the data L2 and L3 describe.

10.5 Investigation into diagnostic effects at distance

10.5.1 Summary

From previous research (Lewis, 2000) there was some suggestion that indicators of disease observed in the scattering profile could be detected in samples collected at some distance from the tumour site. Samples were taken from the same patient at increasing distances (1 cm, 2 cm, 4 cm and 6 cm) from the tumour site. SAXS data was collected from the distance samples and processed in the same way as all other data, using both synchrotron and conventional X-ray sources.

10.5.2 Conventional X-ray source

Results of PCA for the distance series were analysed to provide a classification. The scores for L2, which was shown to be an accurate indicator of disease (see Section 10.4) were plotted for the sample series against their distance from tumour centre (Figure 10.36). Tissue samples for series 1 were taken from the tumour site and on either side of the tumour at 1 cm and 2 cm. The sampling axis extended from the nipple through the tumour centre (the primary axis, PA) and along the axis at a radial distance equal to the tumour position around the nipple, termed the tumour axis (TA). Tissue samples forming the other distance series were taken at 0 cm, 2 cm, 4 cm and 6 cm from the tumour. Three out of the four series showed a positive value of the L2 score at the tumour site with decreasing values of the L2 score as distance increased. Series 4 was the exception and was also distinguished by having a negative value for the L2 score at the tumour site. The reason for series 4 not following the same trend as the other samples was an apparent mis-labelling to the samples in the series. 70 % of the 6 cm sample in series 4 was invasive ductal carcinoma determined by histopathological analysis. The 0 cm sample was normal stroma suggesting the series was labelled in reverse order. Accepting this series 4 would then conform to the

same trend as noted in all the other series i.e. the value of the L2 score would decrease with increasing distance from the tumour.

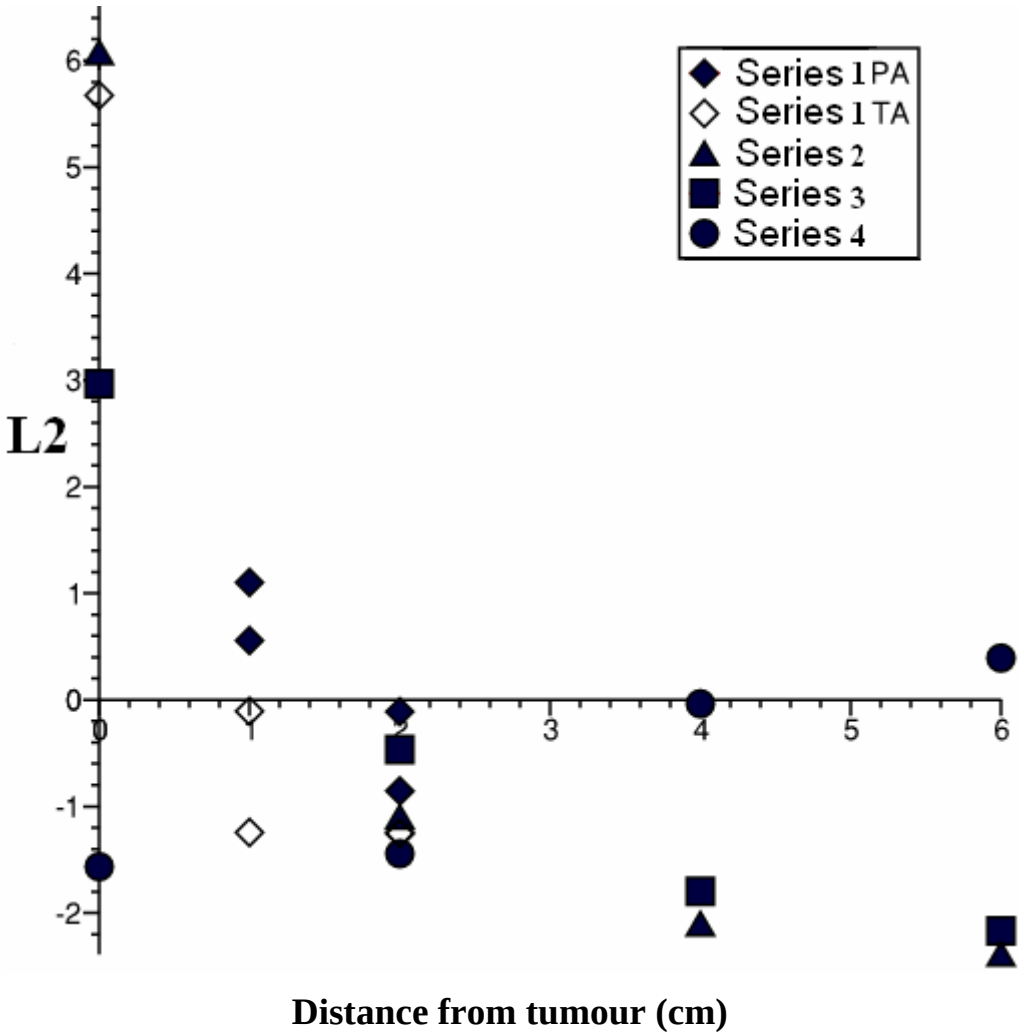

Figure 10.36 Plot of the L2 score for each sample against the distance from the tumour site.

Showed the general trend that as distance increases the value for the L2 score decreases**.**

Although using a negative value of L2 score alone would only have provided an indication of disease in one of the series (series 1 PA). The apparent dependence of the L2 score with distance indicates that the score for L2 may be used to highlight samples where further testing was needed.

10.5.3 Synchrotron radiation investigation

10.5.3.1 Peak fitting

The data was collected from the individual samples of the series over multiple calibrations. The errors in spacing calibration (see Section 11.4.1.1) were greater than the changes with disease and thus the changes in D spacing could not be accurately investigated for these samples. Parameters independent of the calibration were used to investigate the series data such as Bragg peak area and RIR.

The area of the 3rd order Bragg peak plotted against S provided diagnostic classification (see Section 10.3.3.2). However, when the area of the 3rd order Bragg peak is plotted against distance (Figure 10.37) no trends were observed, although the average area of the series data is lower than that of the normal samples. The difference in the peak area between the distance series and the normal does not appear to be related to the amount of fibrous tissue in the samples. Fibrous content changes (increased in most cases) with distance from the tumour site (Table 10.5.1) but peak area did not (Figure 10.37).

	Distance (cm)			
	0	2	4	6
S01	90	98	X	100
S02	0	60	95	50
S03	50	90	90	85
S04	10	70	80	X
S05	10	90	50	70
S06	10	85	70	X
S08	0	95	60	X
S09	70	5	90	60
S10	0	90	80	100
S11	90	80	75	50
S12	75	90	98	90
S13	0	90	60	90
S14	0	90	90	60

Table 10.5.1 Percentage fibrous non tumour tissue volume in series samples

(X = No tissue sample available from the patient at this distance)

The distance series 2 and 13 showed large fibrous content and low peak area in some of the samples distant from the tumour site. However, samples from series 3 and 6 exhibit peak areas similar to some of the normal samples. Diagnostic information from the area of the Bragg peaks was observed (Figure 10.22) though adequate separation was not observed using peak area alone. The low peak area of all points in series 2 and 13 suggests the possibility that diagnostic classification from the peak area was observed up to (and possibly over) 6 cm from the tumour site. However, the peak areas of the samples from series 3 and 6 showed a similar range as the normal samples, again suggesting that peak area alone was not an adequate indicator of disease state. A low peak area suggests the possibility of disease though it could simply be an indication of low levels of collagen in the sample.

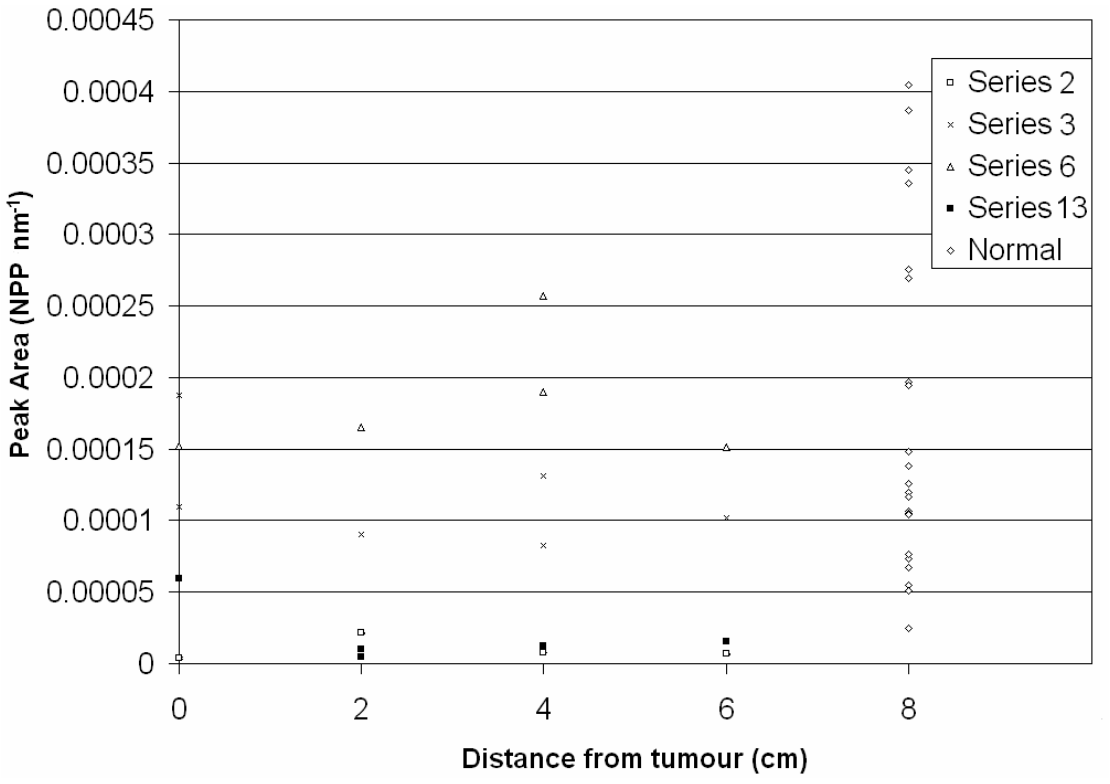

Figure 10.37 Area of the 3rd order Bragg peaks for samples increasing in distance from tumour site

Only series with >50 % tumour volume at distance 0 cm shown by histopathology were included in this plot. There was no correlation between peak area and distance. Series 2 and 13 exhibit low peak area at all distances below the values for peak area observed in the normal samples, series 3 and 6 yield peak areas within the range that the normal samples do.

The value of the RIR (see Section 10.3.3.3) showed that samples distant from the tumour exhibited similar values to that of normal tissue (Figure 10.38). There was a clear difference between the tumour and the normal samples but no conclusive evidence that the intensity ratio provided any diagnostic information away from the tumour site. The 2 cm sample of series 13 exhibits a reduced RIR value. However, this reduction was not an effect observed at distance, as the histopathological analysis of the 2 cm sample of series 13 showed it was invasive ductal carcinoma.

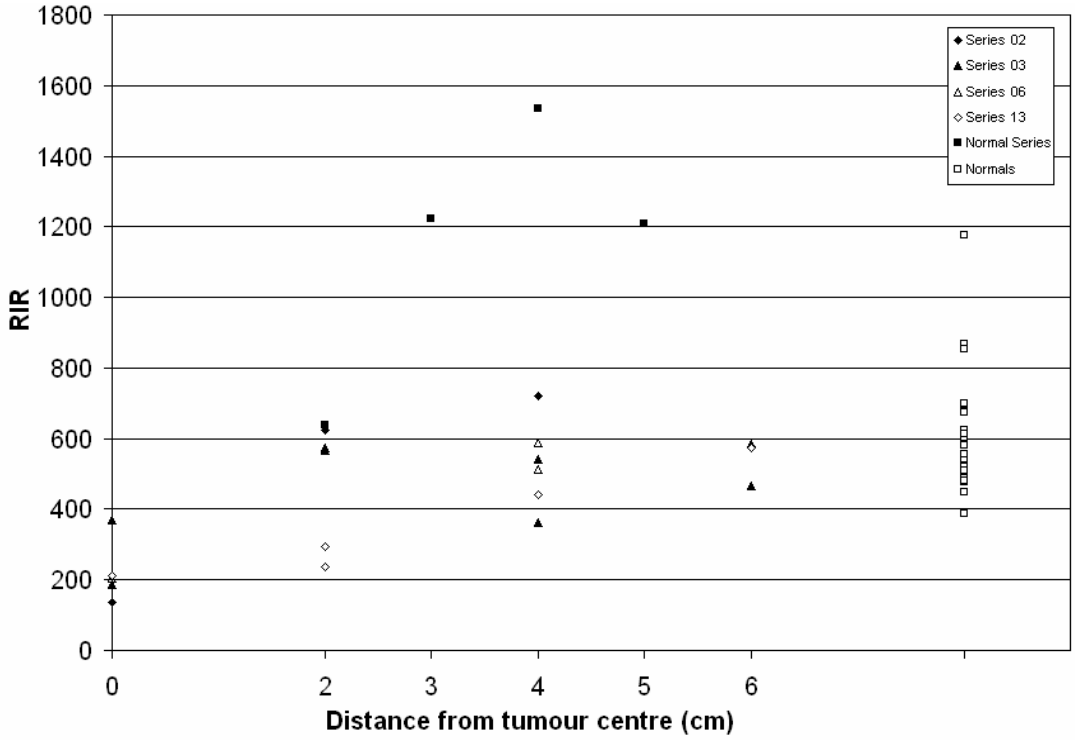

Figure 10.38 Relative intensity ratio of samples at increasing distance from tumour site

Only cancer series with tumour at distance 0 cm shown by histopathology were included in this plot. The normal series was obtained from a large mammoplasty to show the variation with position in a normal breast. There was noticeable variation but the average was well above that of the tumour tissues. The low intensity ratio of the 2 cm sample of series 13 suggested the presence of disease and was classified by histopathology as invasive carcinoma. None of the distance samples shown to be normal by histopathology exhibit the low intensity ratio associated with disease.

10.5.3.2 Principal component analysis

The linear discriminant model produced using PCA on the known malignant, normal and benign samples (see Section 10.3.4.2) was used to analyse the series samples. The series samples were compared to the model and an automated diagnosis produced.

The model compares all the features associated with disease, thus providing a more accurate diagnosis than investigating any one feature alone. The PCA diagnosis showed over 50 % of samples at all distances to be identified as cancerous (Table 10.5.2).

Distance (cm)	Number of Samples	% Samples classed as cancer
1	9	67
2	16	81
4	13	69
6	10	90

Table 10.5.2 Percentage of series samples classified as cancer using PCA model

Two of the series samples were identified as invasive ductal carcinoma, both of these samples were correctly identified as cancer by the PCA analysis (Table 10.5.3). The identification of samples as normal was not related to the amount of fibrous material they contain (Table 10.5.1) as samples such as series 3 (4 cm) contained 90 % fibrous material, series 6 (2 cm) contained 85 % but both were identified as cancer. Conversely series 11 (4 cm) contained 75 % and series 8 (4 cm) contained only 60 % fibrous material yet were classified as normal.

The classification of samples distant from tumours as cancerous by small angle X-ray scattering but which were classified as normal by histopathology suggested that cancer diagnosis using small angle X-ray scattering was less susceptible to biopsy sampling errors. Without cancerous cells in the sample the histopathologist cannot confirm a diagnosis. However, if the results of the PCA classification can be repeated in a double blind study (see Section 13.6) the ability to provide an indication of disease from up to (and possibly over) 6 cm would greatly reduce misdiagnosis.

Series	Distance from tumour site (cm)			
	1	2	4	6
01		Cancer	Normal	Cancer
02		Cancer	Cancer	Cancer
03			Cancer	Cancer
04		Cancer	Normal	
05		Cancer	Cancer	
06		Cancer	Cancer	Normal
07		Cancer		Cancer
08		Cancer	Normal	Cancer
09				Cancer
11		Cancer	Normal	Cancer
12			Cancer	
13		Cancer*	Cancer	Cancer
14			Cancer	Cancer*
15 PA	Cancer	Cancer		
15 TA	Cancer	Normal		
16 PA	Normal			
16 TA	Cancer	Cancer		
17 PA	Normal	Cancer		
17 TA	Cancer	Cancer		

Table 10.5.3 Classification of samples at distance from tumour by PCA

* denotes samples which were identified as invasive ductal carcinoma by histopathology

10.6 Degradation of tissue

10.6.1 Matrix metalloproteinase degradation

Initial experiments for matrix metalloproteinase degradation of breast tissue were undertaken at station 16.1 at Daresbury laboratories. Station 16.1 was selected due to its optimisation for time resolved SAXS. However, as the timescales for the degradation were found not to require short data collection times the subsequent experiments were undertaken on station 2.1. The normal breast tissue used in the initial experiments was collected during cosmetic reduction procedures. As such it was predominantly fatty and therefore not ideal for investigation of the effects of enzyme degradation on collagen. The experiments undertaken on station 2.1 used pure collagen from rat tail tendon and pork dermis to emulate a collagen/fat matrix.

In order to observe the effects of the MMP on collagen directly, rat tail tendon was selected since it is almost pure type I collagen. The samples of rat tail showed clear axial structure with the 1st to 9th order axial peaks visible (Figure 10.39) prior to the addition of collagenase. The intensity of the axial peaks decreases steadily with time until only the first order is visible in the final exposure. The Bessel peaks were not observed in any of the X-ray scattering profiles of rat tail tendon, but were present in pork dermis and breast tissue. Processing and analysis of MMP degradation of rat tail tendon, pork dermis and breast tissue was completed with the help of Dr K. Siu (Monash University). For visualisation the data was multiplied by S^2 allowing the peaks to be observed and each subsequent time frame was offset by a constant so as to prevent the profiles being superimposed.

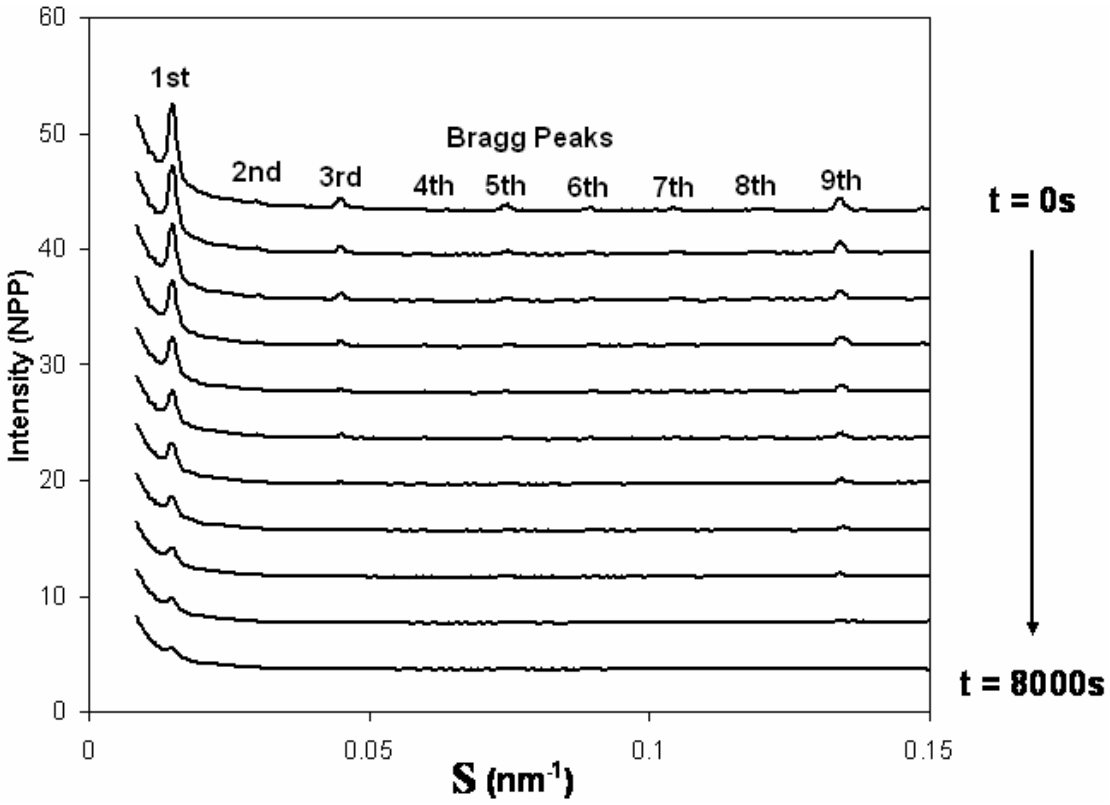

Figure 10.39 Degradation of rat tail tendon by matrix metalloproteinase

A series of 11 data points starting at 0 seconds and the final data collection taken 8000 seconds after the introduction of the collagenase with data collected at regular intervals. The intensity was scaled by multiplying it by S^2 and each separate exposure has been offset to allow visualisation. Degradation results in the 9 orders of the axial peaks clearly visible in the initial exposure reduced to only the 1st order being visible in the final exposure of the series.

Pork dermis was used as a model system to investigate MMP degradation of a matrix of collagen and fat. The 2nd and 3rd order Bessel peaks and the odd axial peaks (3rd, 5th, 7th and 9th) clearly visible in the initial exposure of the series (t = 0 seconds) reduce in area as the degradation continues (Figure 10.40). The final exposure (t = 8000 seconds) showed the presence of the 2nd and 3rd order Bessel peaks and the 3rd order axial peak, though the intensity was reduced. The other axial peaks cannot be distinguished in the final profile of the series suggesting disruption to the supra molecular structure of the collagen.

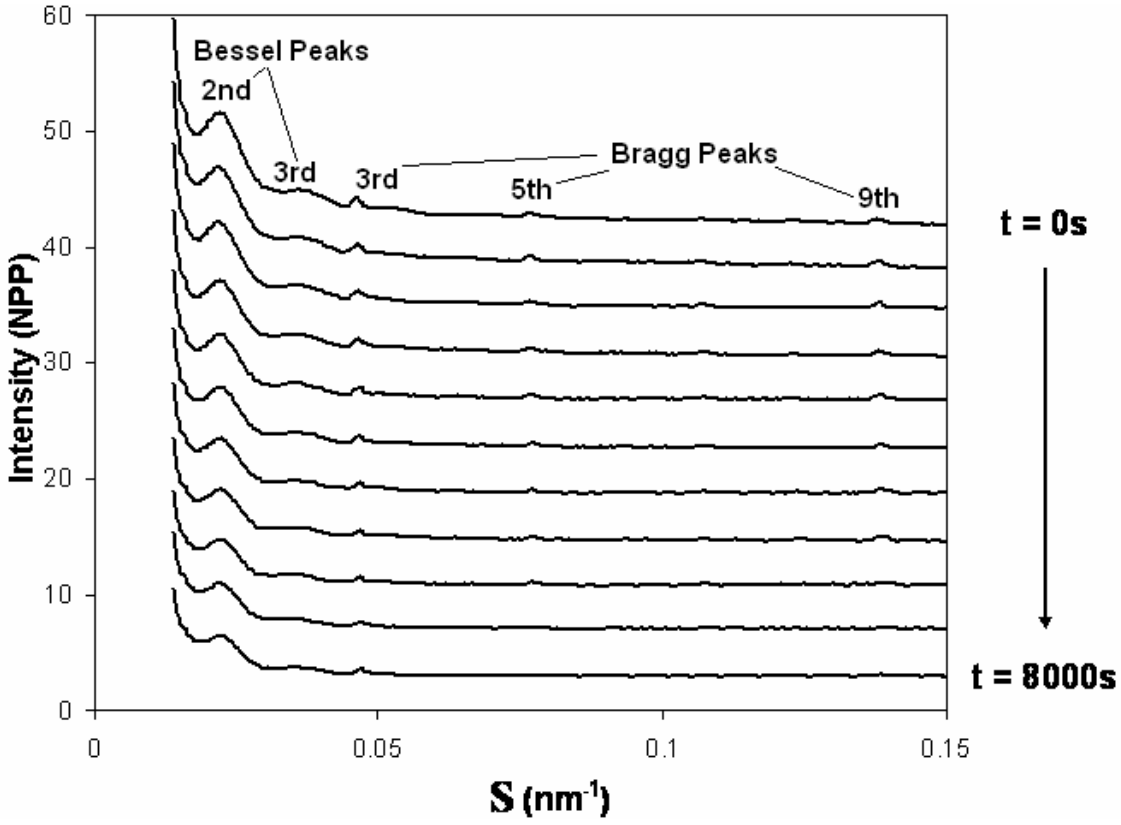

Figure 10.40 Degradation of pork dermis by matrix metalloproteinase

A series of 11 data points starting at 0 seconds and the final data collection taken 8000 seconds after the introduction of the collagenase with data collected at regular intervals. The intensity was scaled by multiplying it by S^2 and each separate exposure has been offset to allow visualisation. Degradation results in the 3rd, 5th, 7th and 9th orders of the axial peaks clearly visible in the initial exposure, reduced to only the 3rd order being visible in the final exposure of the series. Reduction in the area of the 1st and 2nd order Bessel peaks is observed as the degradation progresses with time.

The samples of rat tail tendon and pork dermis showed changes in the X-ray scattering profiles which initially appeared to be associated with MMP action (Figure 10.39 and Figure 10.40). However, the control samples also showed degradation which suggested that the X-ray radiation used to investigate the samples was damaging the collagen structure and contributing to the observed degradation. To assess the extent of the effect of MMP action quantitative analysis comparing the degradation with and without MMP present was required.

10.6.2 Effects on axial peak area

For quantitative analysis of the breast tissue degradation the 3rd order axial peak was used as it showed the highest intensity of any of the axial peaks and persisted through to the end of the series in both the MMP and control series. The peak area of both the MMP and control series reduce with time (Figure 10.41).

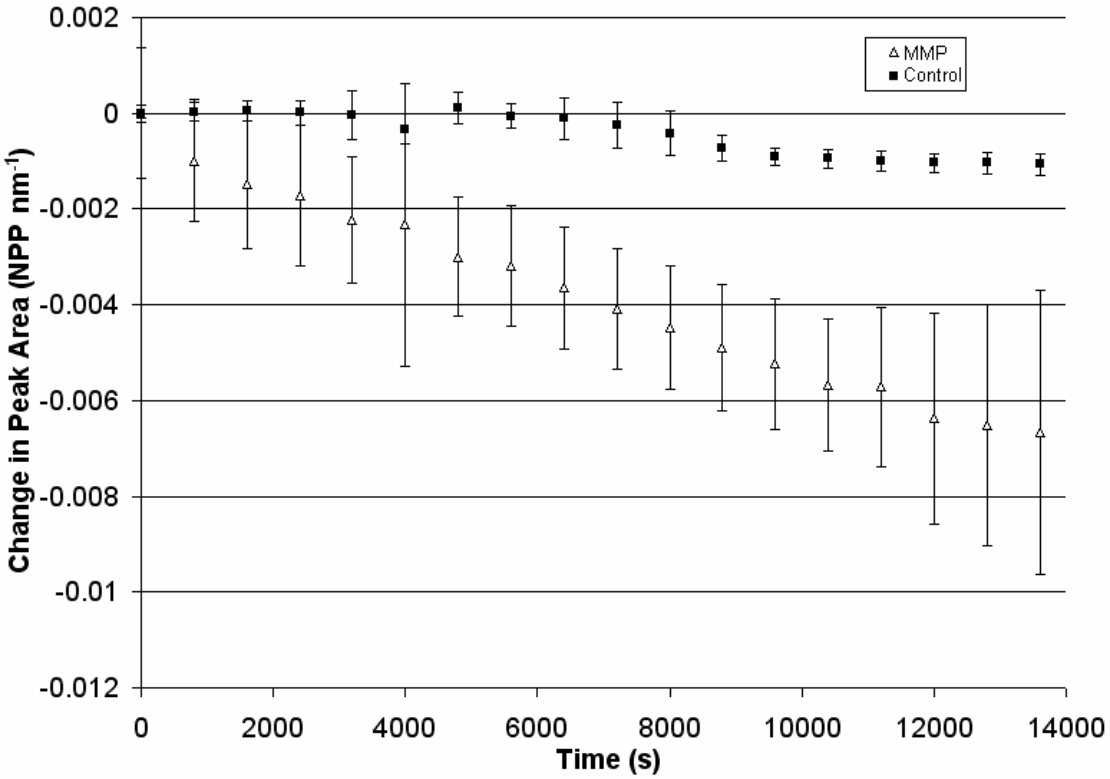

Figure 10.41 Axial peak area of breast tissue control and degradation series

Reduction of peak area is greater for the MMP series compared to the control. Errors shown were the standard errors calculated during the peak fitting process.

The degradation observed in the data was caused by the combination of radiation damage and MMP action. The peak area of the degradation series at 14000 s was reduced by 88.5 % of the peak area observed at the start of the series. Subtracting the degradation observed in the control series showed that 74.3 % of the total reduction was caused by MMP action and 14.2 % of the reduction was caused by radiation damage.

Analysis of the rat tail tendon degradation showed radiation damage caused a reduction in peak area (Figure 10.42). However, as with the breast tissue degradation presence of MMP resulted in a greater reduction of peak area than the control.

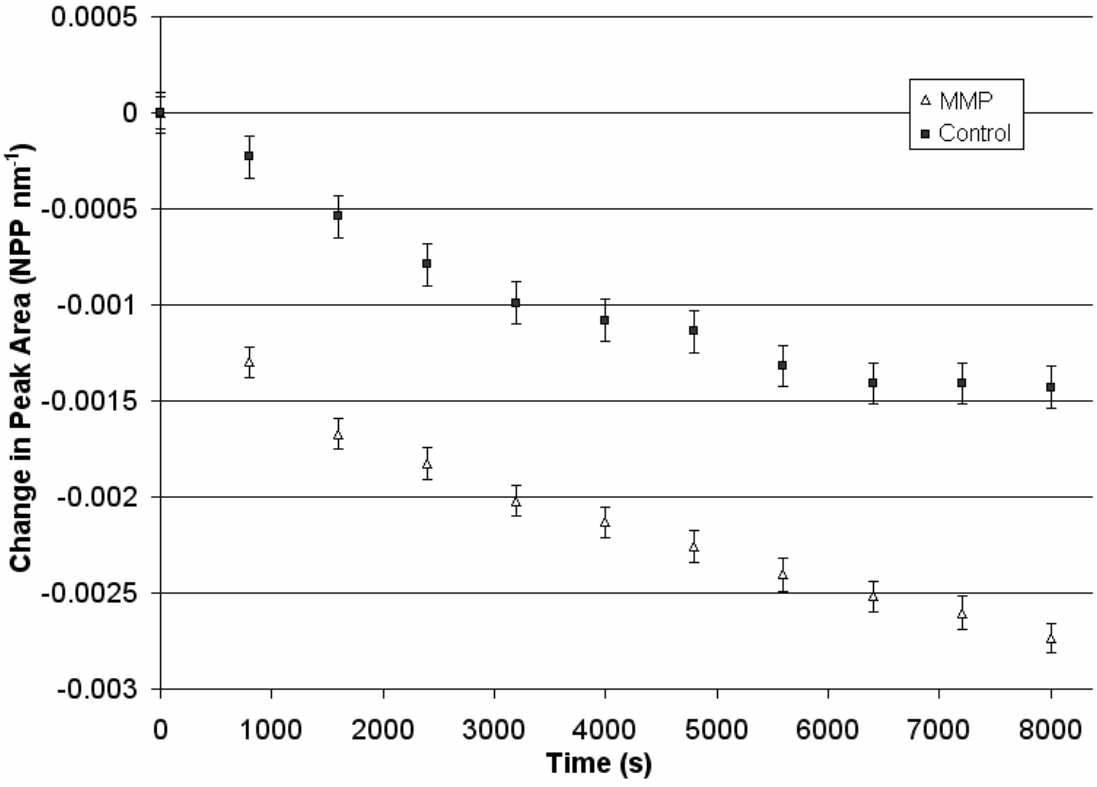

Figure 10.42 Change in Peak area of rat tail tendon by MMP and associated control

The control series shows a reduction in peak scatter due to the effects of radiation damage. The degradation series shows greater reduction in peak area beyond that which is shown in the control suggesting the MMP caused degradation of the collagen. Errors shown were the standard errors calculated during the fitting process.

A reduction in the scatter of both the Bessel and axial peaks was observed in the degradation of pork tissue (Figure 10.43). There appears to be little effect of radiation

damage on the Bessel peaks. Throughout the experiment the scatter from the peaks in the control sample appear constant. However, there is a difference between the first and second exposures in the control series. The cause of this reduction could be the sample slipping in the sample holder and therefore the second and subsequent exposures are from a different portion of the sample which contained less collagen. The Bessel peaks of the sample degraded by MMP showed significant reduction in scatter suggesting that the lateral as well as the axial structure of collagen was affected by the action of MMP (see Section 11.8.2.1).

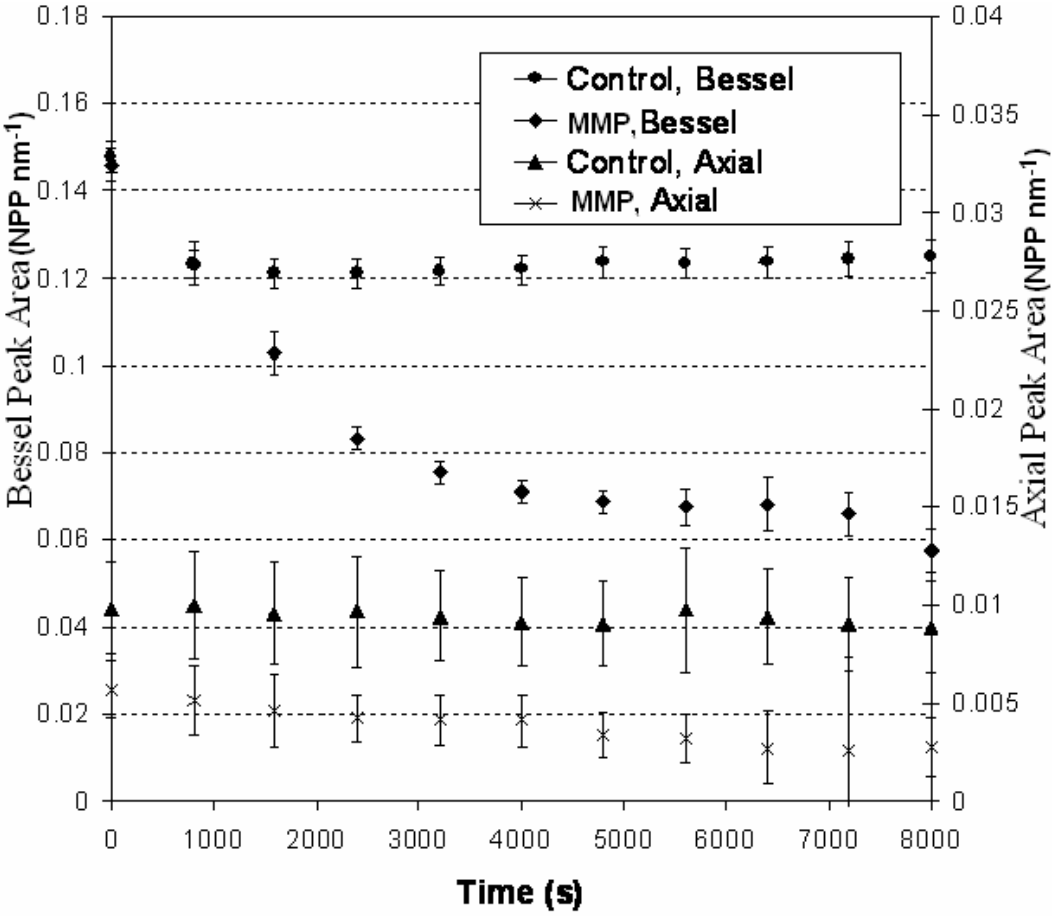

Figure 10.43 Area of Bessel and axial Bragg peaks for MMP and control series of pork tissue

Reduction in peak area can be observed in the Bessel peaks when collagenase is present but only minimal reduction in axial peaks. Errors shown were the standard errors calculated during the fitting process.

10.6.3 MMP effects on axial peak spacing

An increase in the S of the collagen peaks with time was observed in all tissues for both the control and the MMP series. The increase in S was attributed the dehydration caused by the high solute potential of the buffer solution used for the degradation series (see Section 11.8.2.1).

The S spacing of the 3rd axial order of collagen of breast tissue increased up to 4000 s after which time the change in S spacing was lower than the fitting errors (Figure 10.44). The MMP series shows a greater increase in S spacing However, the errors are much larger for the MMP series due to the lower peak intensity.

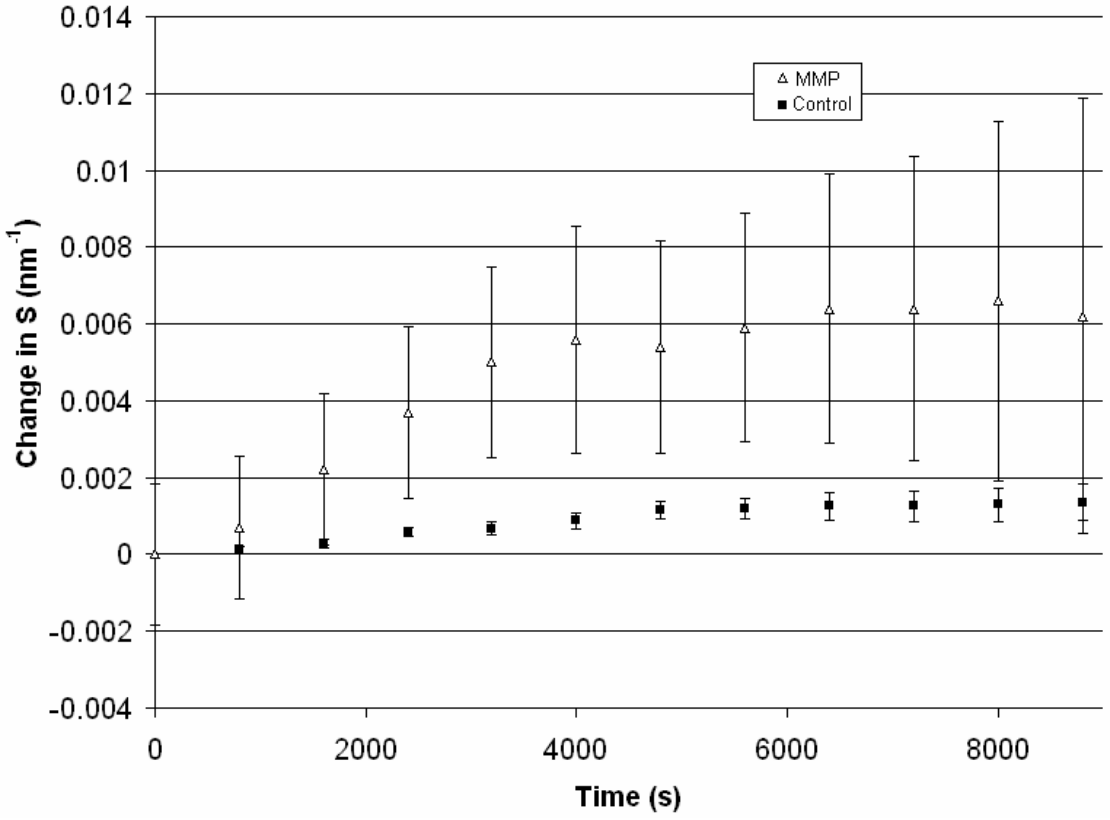

Figure 10.44 Change in S spacing of 3rd order axial peak for breast

The S spacing of the 3rd order axial peak increases with time up to 4000 s for the MMP series as does the control series but at a lower rate. Above 4000 s the changes to S spacing were within the errors. The errors shown were the standard errors calculated during the fitting process.

The S position of the 3rd order axial peak of collagen from pork dermis showed a small increase with time (Figure 10.45). Although the errors also increase with time, due to the peak intensity reducing, the increase in S position was greater than the error.

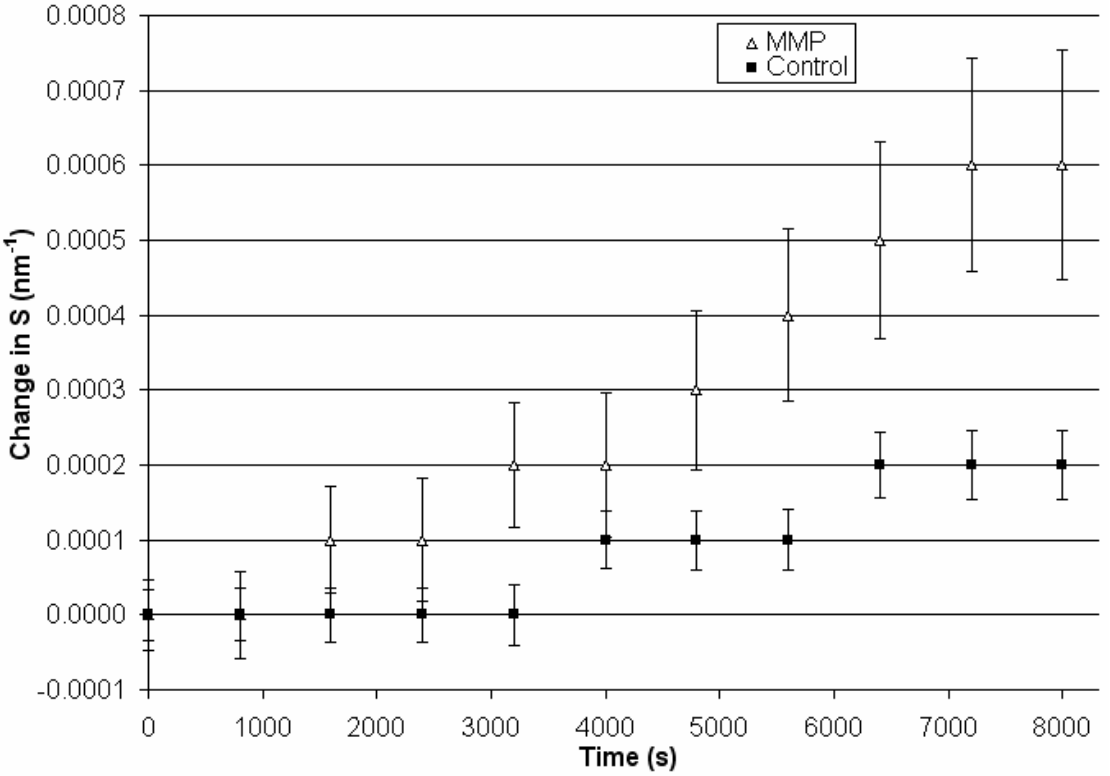

Figure 10.45 Change in 3rd order axial S position of the of pork dermis

There was an increase to the S spacing of the pork dermis with an error less than observed increase for both the control and MMP series suggesting a significant observable reduction of D spacing. The errors shown were the standard errors calculated during the fitting process.

The S position of the 3rd order axial peak of collagen from rat tail also showed a small increase with time (Figure 10.46). Rat tail tendon was the only tissue which showed less increase in S position for the MMP series than in the control. However, the errors for the degradation series were large making this result less significant.

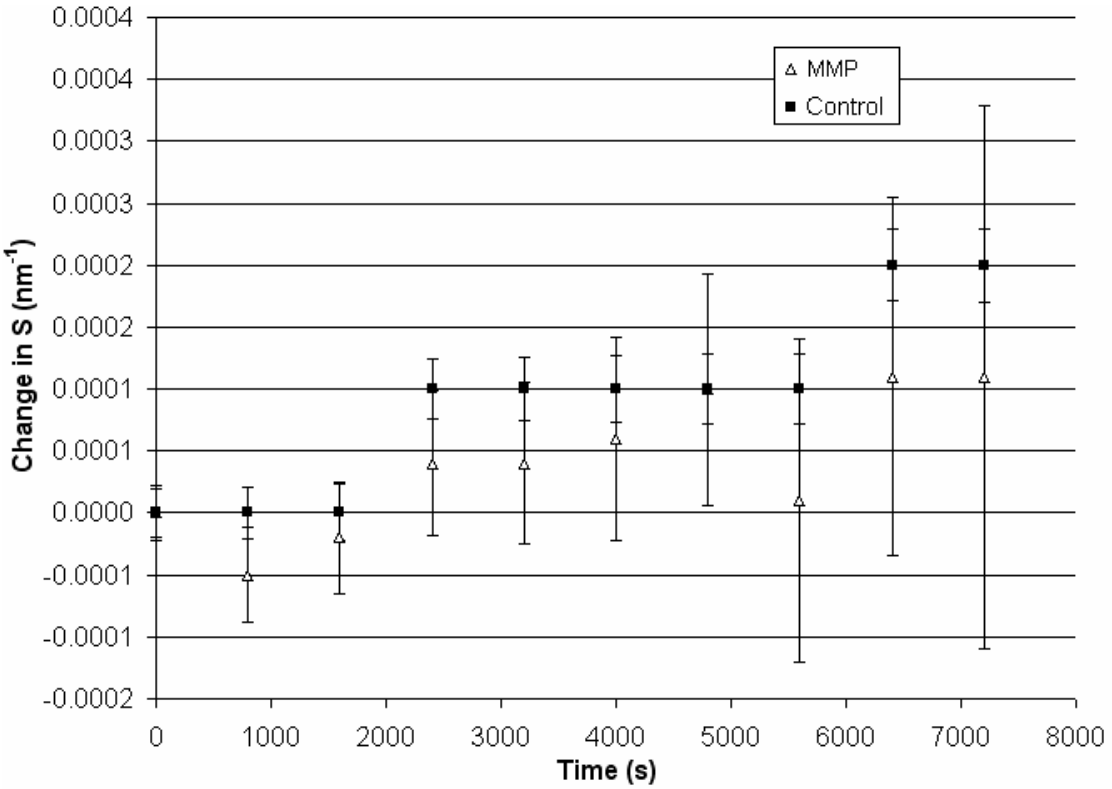

Figure 10.46 Change in 3rd order axial S position of rat tail tendon

Rat tail tendon exhibited a small increase in the S accompanied by an increase in the fitting error in the MMP series, associated with fitting low intensity peaks. The errors shown were the standard errors calculated during the fitting process.

10.6.4 MMP effects on the axial peak width

No obvious effect on peak width was observed in relation to the action of MMP (see Section 11.8.2.1). The fitted parameters for the peak widths do not alter noticeably during the MMP series. Any changes in peak width are much smaller than the errors (Figure 10.47).

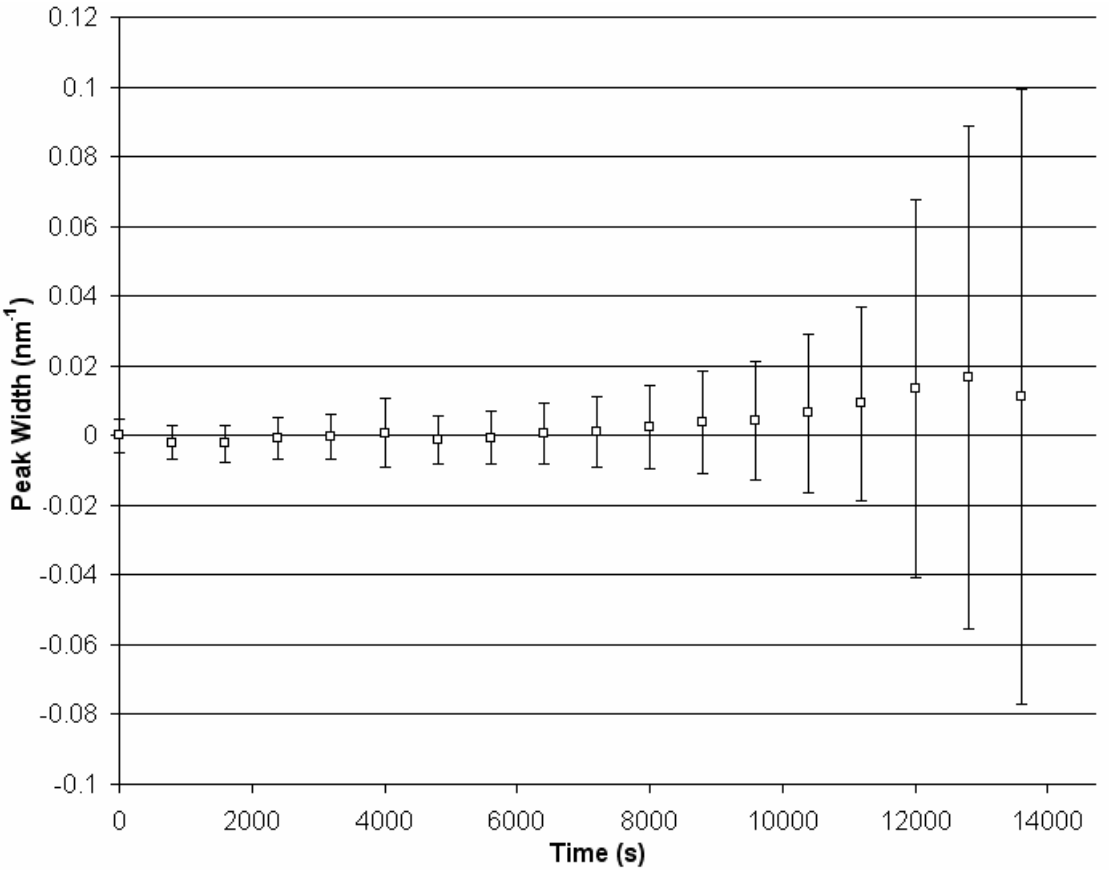

Figure 10.47 Change in 3rd order peak width of breast tissue collagen with MMP action

The change in peak width is smaller than the errors. The errors shown were the standard errors calculated during the fitting process the magnitude of which increase with time as the peak intensity decreases.

10.6.5 Effects of MMP action on amorphous scatter

No clear difference in Rg (see Section 7.7.5) was seen between the control and MMP series for rat tail tendon (Figure 10.48). In pork dermis the Rg for both the control and MMP series are comparable up to 2500 seconds, after which the Rg of the control series increases while with MMP Rg is constant (Figure 10.49). The values for Rg in rat tail tendon and pork dermis show no clear trend with the presence of MMP.

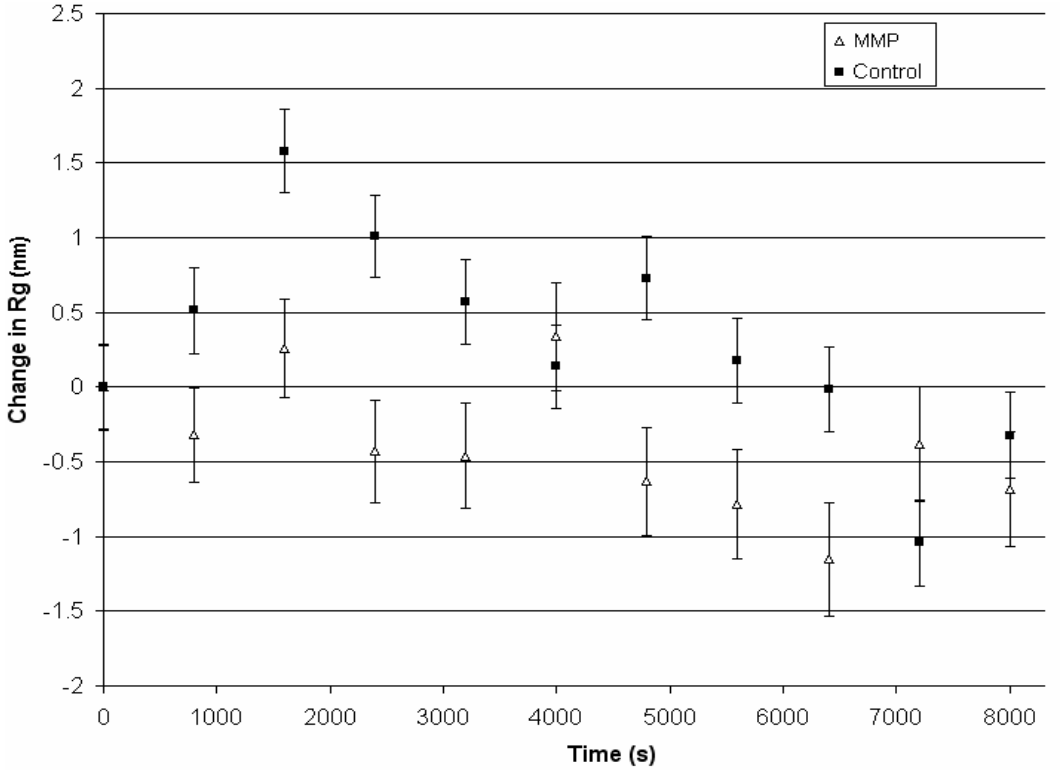

Figure 10.48 Change in Rg of rat tail tendon in the presence of MMP

Rg did appear to be marginally lower in the MMP series compared to the control. However, this was due to the apparent increase of the control series in the first two data points of the series. The change in the MMP series was only 0.66 % of the initial value and was not deemed significant. The errors shown were the calculated from the intensity errors (assuming Poisson statistics).

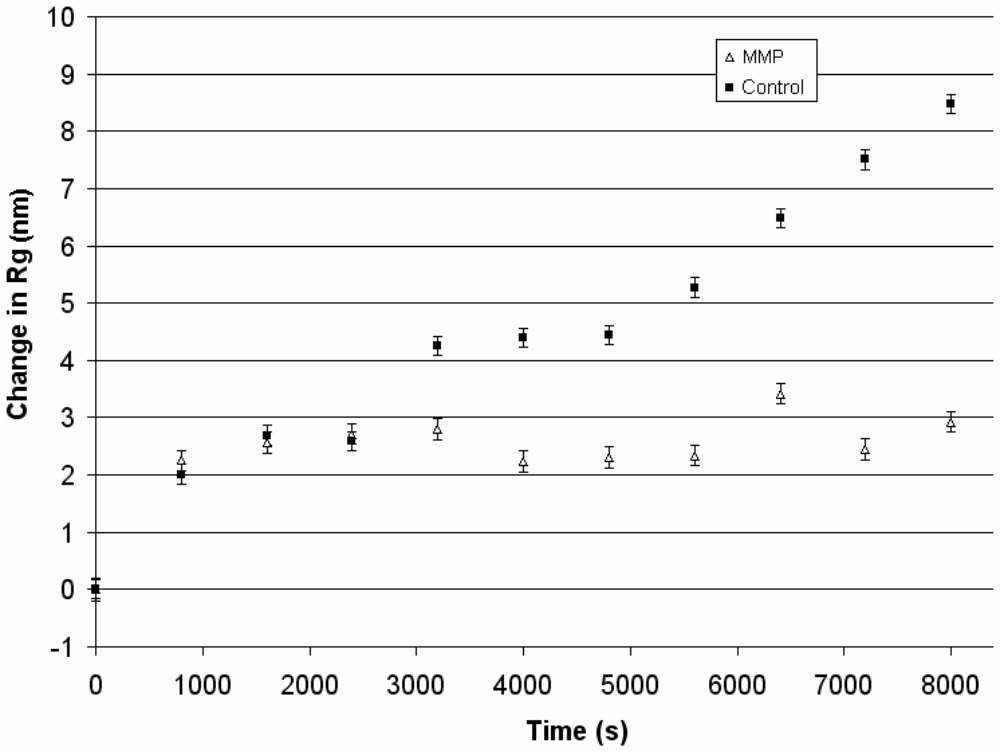

Figure 10.49 Change in Rg of pork dermis in the presence of MMP

The change in Rg for both the control and degradation series are comparable up to 2500 seconds, after which the Rg of the control series increases while the degradation stays constant. The errors shown were the calculated from the intensity errors (assuming Poisson statistics).

The average intensity of the region near the beam stop was greatly reduced in the presence of MMP in both rat tail tendon and pork dermis (Figure 10.50 and Figure 10.51 respectively). The pork dermis showed an approximately 5 times greater reduction in intensity than the rat tail tendon in the degradation series. The matrix forming collagen in the dermis was different to the tendon and so differences in the MMP degradation effects were expected between the samples. A reduction in the intensity of the control samples was observed in the pork dermis series, but in both the rat tail tendon and the pork dermis the reduction was greater in the presence of MMP. The reduction in intensity of the MMP degraded samples suggested that the MMP caused a reduction of the surface area of scattering objects with dimensions in the range of many tens of nanometres (see Section 11.8.2.1). The reduction of surface area was thought to be a function of MMP action reducing the size of scatterers and therefore the number of scatterers with dimensions of many tens of nanometres.

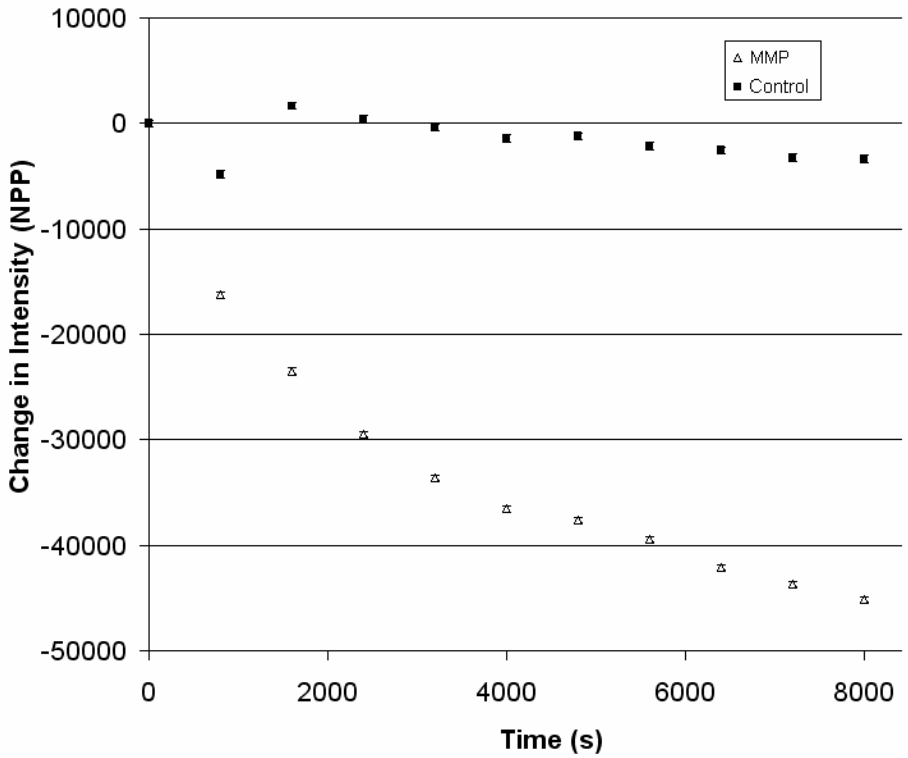

Figure 10.50 Average intensity change near beam stop, rat tail tendon in the presence of MMP

The MMP series showed a large reduction well above the control. The control does show a sudden increase which was thought likely to be that the sample moved at that time in the exposure. The errors shown were the calculated from the intensity errors (assuming Poisson statistics).

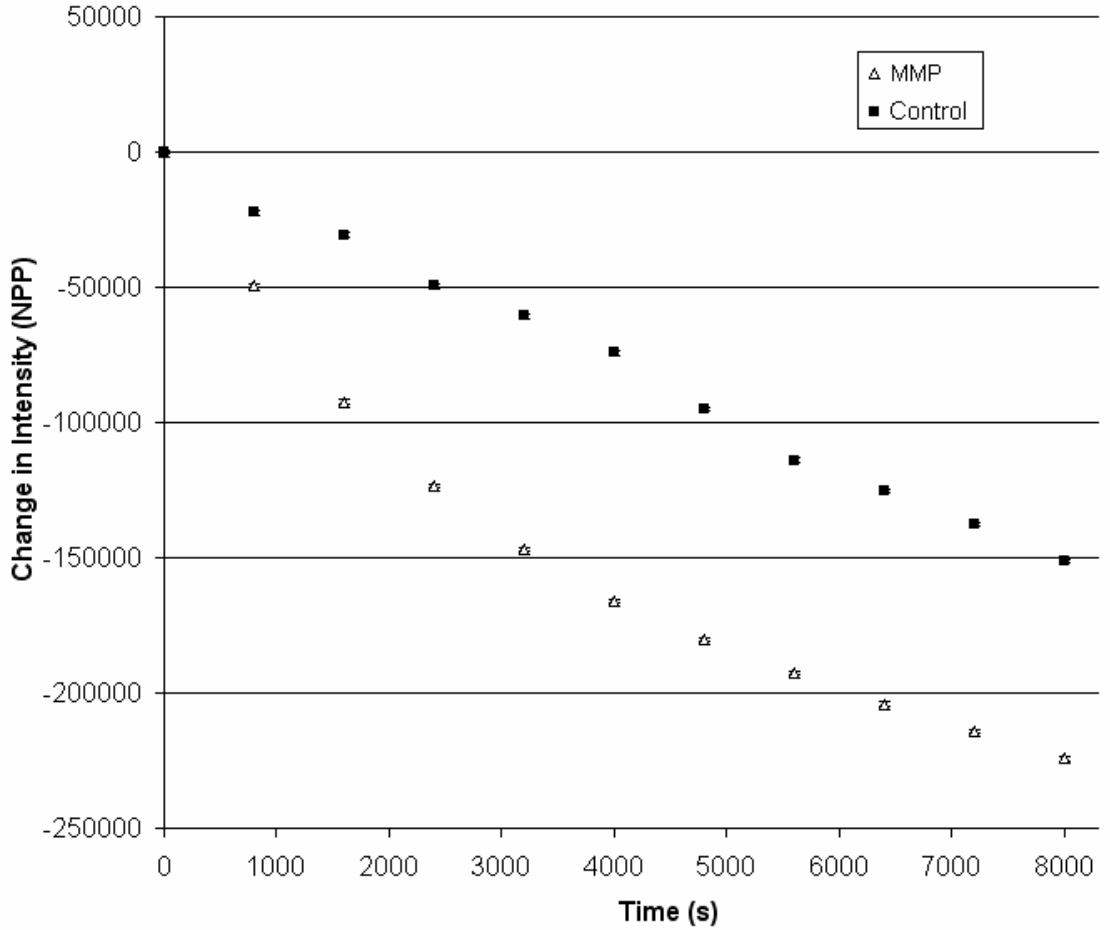

Figure 10.51 Average intensity change near beam stop, pork dermis in presence of MMP

Both the MMP and control series from pork dermis reduce in intensity. However, the reduction was much greater in the MMP series and the difference is considerably greater than the errors. The errors shown were the calculated from the intensity errors (assuming Poisson statistics).

The trends in the control series of the change in average intensity between the 3rd and 5th axial peaks was reversed in the different samples. The average intensity increased in rat tail tendon in both the MMP and control experiments (Figure 10.52) while with pork dermis the average intensity only increased in the presence of MMPs (Figure 10.53). The increase in intensity of the rat tail tendon with MMP was initially greater than the control but by the end of the series they were comparable (the difference between series was within the errors). However, the percentage increase in the MMP series was 75 % compared to only 45 % in the control.

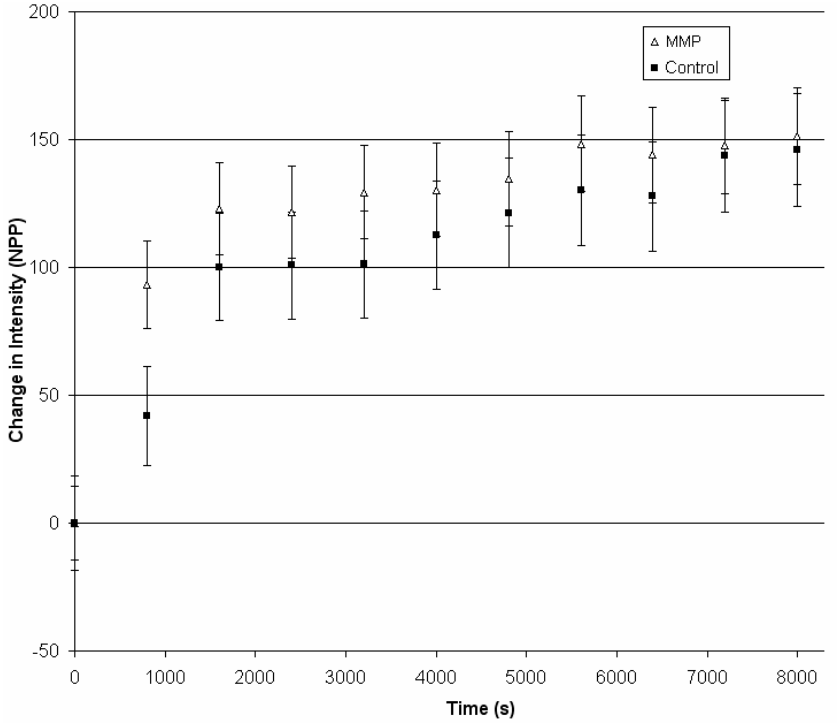

Figure 10.52 Change in average intensity between 3rd and 5th axial peaks of rat tail tendon

Average intensity increases for both the MMP series and the control. The increase is greater in the MMP series though the absolute change was comparable (within errors) the percentage change of the MMP series was a 75 % increase compared to a 45 % increase in the control series. The errors shown were the calculated from the intensity errors (assuming Poisson statistics).

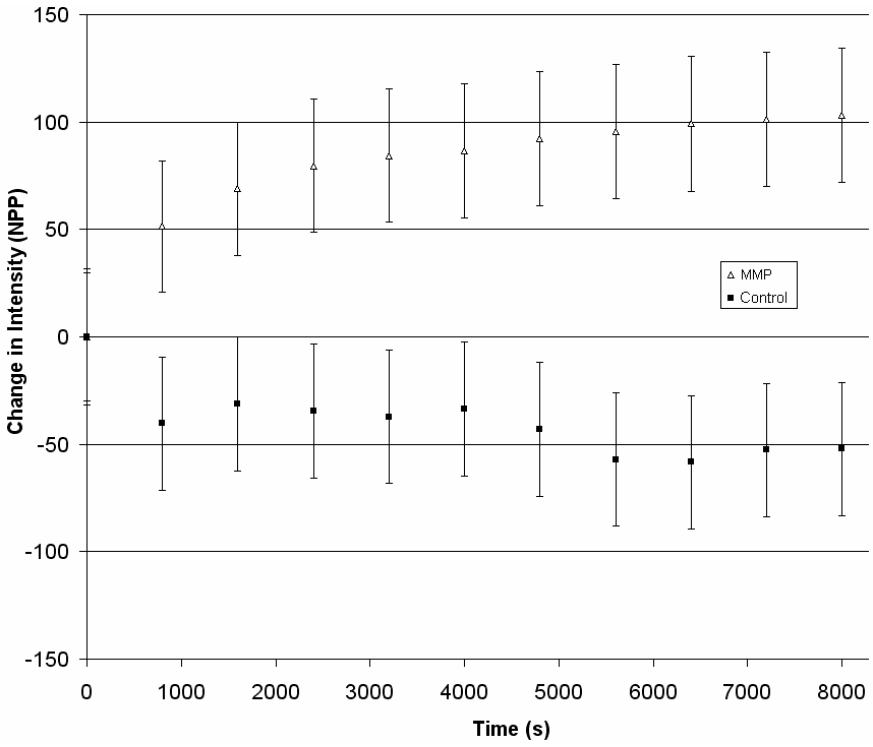

Figure 10.53 Change in average intensity between 3rd and 5th order axial peaks of pork dermis

The average intensity of the MMP series increases while the control decreases, which results in a clear difference associated with the action of MMP. The errors shown were the calculated from the intensity errors (assuming Poisson statistics).

The increase in the average intensity between the 3rd and 5th order peaks associated with the presence of MMP suggested an increase of the total surface area of scattering objects with dimensions in the range of a few tens of nanometres (see Section 11.8.2.1). The increase in surface area is thought to be an increase in the number of scatterers with dimensions of a few tens of nanometres not a modification to the surface area of the scatterers already present.

10.6.6 Thermal degradation

The 3rd and 5th axial orders were visible in the initial exposures of the temperature series (5 °C). However, the 5th order was not distinguishable in many of the exposures at higher temperatures. The average values of the 3rd order axial peak positions for 4 separate points in each sample were taken for each temperature to show the differences in the variation between normal and malignant breast tissue. Variations in S (Figure 10.54) can be observed, but the change in spacing was smaller then the errors.

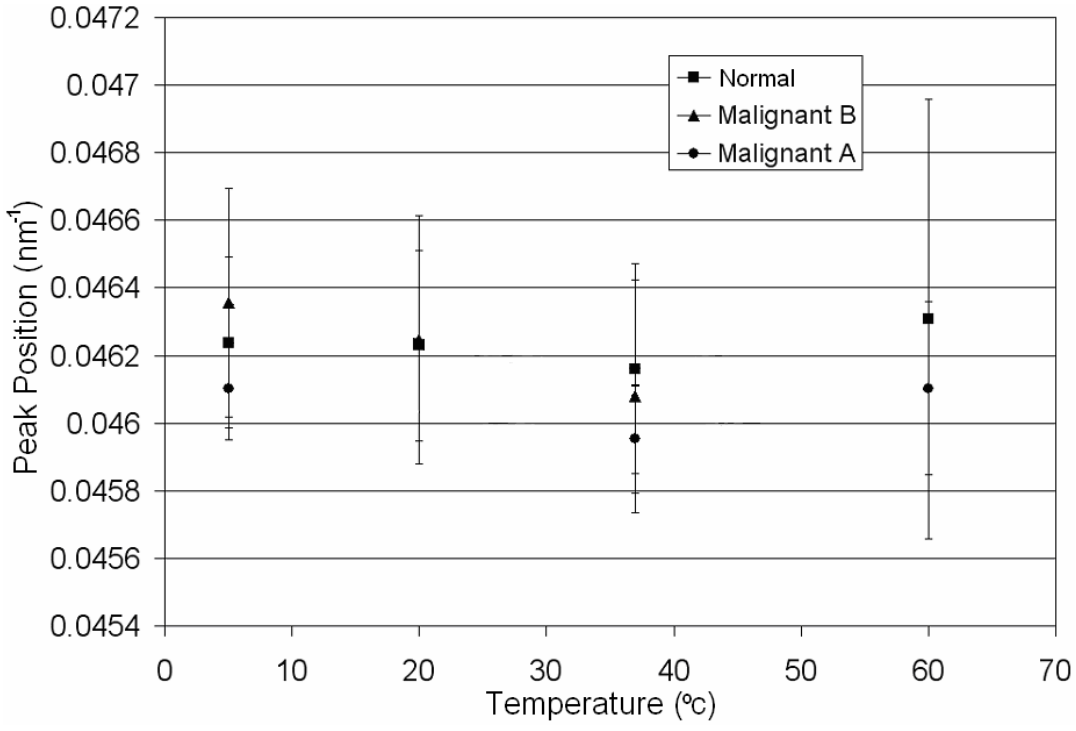

Figure 10.54 Variation in collagen D spacing with increasing temperature

Four different positions in the tissue were used to calculate the average D spacing at each temperature. Minimal variation (within errors) can be observed in D spacing with temperature.

The average peak area decreases with increasing temperature However, the errors in fitting were comparable with the observed variation (Figure 10.55). The reduction in peak area appears to follow a similar trend for both normal and malignant tissue. However, the percentage reduction in area between 5 °C and 60 °C is 49.5 % and 28.0% for normal and malignant tissues respectively, suggesting that the collagen from malignant tissues may be less susceptible to thermal damage than collagen in normal tissue.

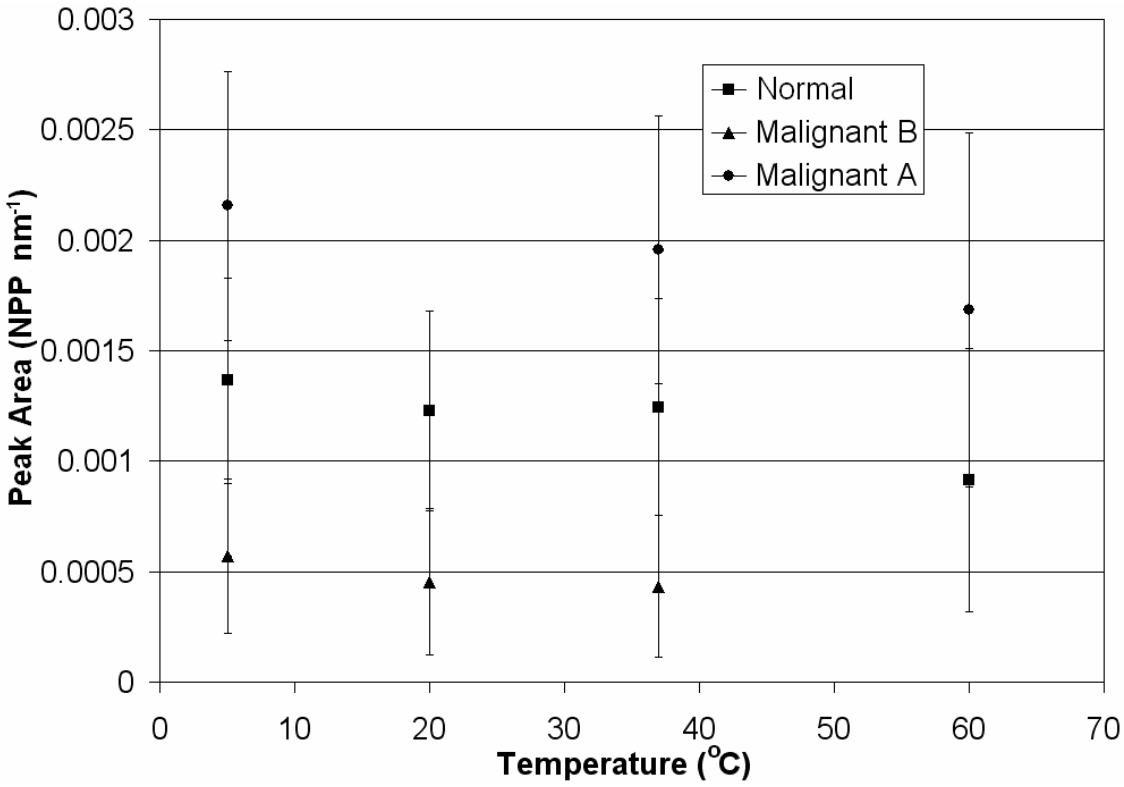

Figure 10.55 Variation in area of collagen 3rd order axial peak with increasing temperature

Four different positions in the tissue were used to calculate the average D spacing at each temperature. The peak area decreases with increasing temperature for both malignant and normal tissue.

10.7 Computer Simulation of X-ray Scattering

10.7.1 Shear of adjacent micro fibril units

Simulation of the small angle X-ray scattering of shearing micro fibrils was performed in collaboration with Professor T. Wess (Cardiff University). A model was constructed which fitted the first twelve orders from the amino acid sequence of collagen. The model was based on type I collagen (α1 and α2 chains) with 234 amino acids per D period and a 60 % contraction of N and C termini. The scattering pattern was calculated from the combination of 70 of the individual collagen models. Each of the 70 microfibrils was advanced by a fraction of the overall shear which is measured in amino acid lengths. The shear was calculated for 10 points between 0 and 50 amino acid lengths out of the 234 in a D period which gives a maximum shear of just over 21 % of a D period (Figure 10.56).

As the proportion of shear increases the intensity of the Bragg peaks reduces and the number of peaks visible reduces from all 12 orders with no shear to only the 1^{st}, 2^{nd} and 3^{rd} orders at 50 amino acid lengths of shear. The peak positions and the width of the peaks do not alter with increasing shear as the unit cell length remains constant. The results of increasing shear show that the peak intensity observed from a sample of collagen could be reduced without decreasing the amount of collagen present and without disrupting the D spacing of peak width. As the micro fibril units still exhibit a high degree of ordering the sample would still appear fibrous and tough as is observed in the collagen around tumors.

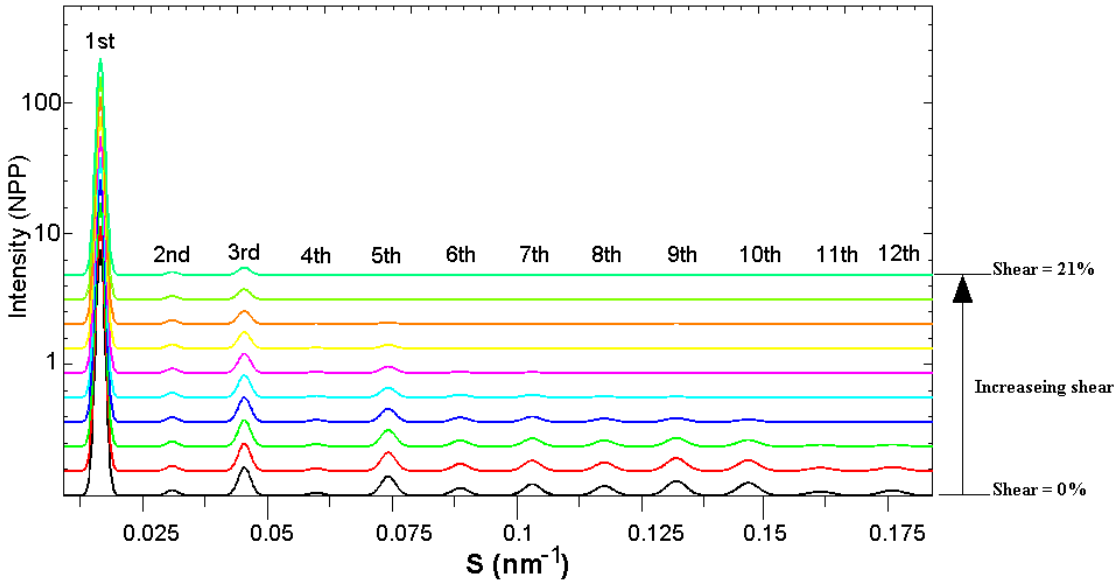

Figure 10.56 Calculated spacing versus intensity for increasing shear between micro fibril units

As the amount of shear in the system increased, the intensity of the Bragg peaks was reduced. There was no alteration in the width or spacing of the peaks as the lengths of the unit cells are identical and remain unaltered.

10.7.2 Change in the standard deviation of the collagen D spacing

The simulation of the small angle X-ray scattering patterns from collagen with an increasing standard deviation of the collagen D period was calculated using the SAXS simulation program (Suhonen, 2005). The simulations were performed in collaboration with Mr M. Ibison at the University of Liverpool. The program calculates small angle scattering from a set of cylinders that have axially periodic electron densities the input parameters are read from a text file, one for each scattering profile desired. The Scattering profile was calculated for standard deviations between 0.1 nm and 60 nm using 2.5 nm increments, all other parameters such as orientation, the number of cylinders and their width were kept constant.

No alteration in the positions of the peak maxima were observed in the output from the simulations (Figure 10.57). This was expected as the average D spacing remains unaltered. As the standard deviation in the collagen D period increased the peak width increased and the intensity of the Bragg peaks was reduced. With the higher the order of the Bragg peaks the more dramatic the effect. Changes to the D period cause

noticeable effects on the spacing of the Bragg peaks even if the average D period remains unaltered. This simulation shows that an increase in the standard deviation cannot be proposed as a model explaining the difference in intensity observed between diseased and normal tissues. Furthermore this simulation shows that the change in D spacing observed between the tissue types must be consistent throughout the tissues as only minimal differences to the peak width have been observed.

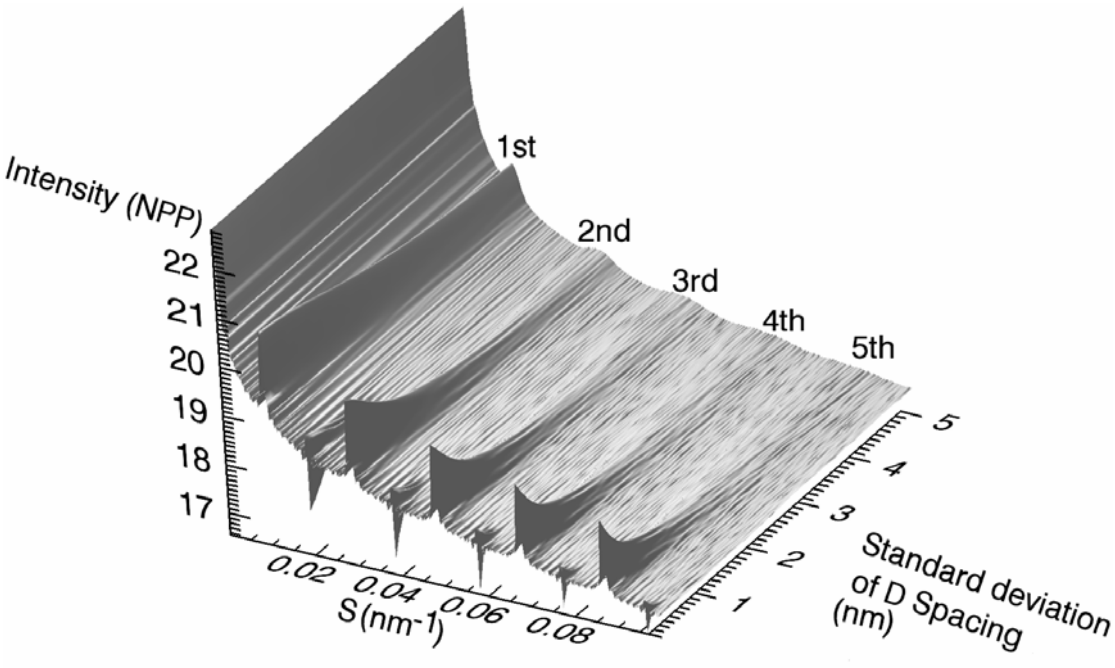

Figure 10.57 Calculated spacing versus intensity for increasing standard deviation of the D period

The first five axial orders of collagen are visible up to a standard deviation of 2 nm. With a standard deviation of less then 0.3 nm artefacts were observed between the collagen peaks giving a localised reduction in intensity. As the standard deviation in the collagen D period increases the intensity of the Bragg peaks is reduced. There is no alteration in the position of the peak maxima as the average unit cell length remains unaltered. However, the peak width increases as there is a greater variation in the unit cell lengths of individual fibrils.

11 Discussion

11.1 Summary

The discussion section of this thesis has been organised so that parameters which may cause errors in the interpretation of subsequent data, were addressed prior to the data the parameters might affect. For instance the possible implications of parameters such as dehydration and tension on the structure of collagen and the small angle X-ray scattering pattern were discussed prior to the interpretation breast tissue data. Within each section the associated experimental and data processing errors were discussed, such as the effect of sample handling on tissue samples as well as calibration of spacing and intensity on the interpretation of the scattering data from breast tissue. For the synchrotron radiation and conventional X-ray source investigations, each parameter measured was discussed taking account of the implications of the preliminary studies as well as the experimental and processing errors. The results of small angle X-ray scattering for disease diagnosis, MMP degradation and computer simulation studies were discussed, which allowed differences between tissue types observed with small angle X-ray scattering to be discussed with regard to the proposed biological causes for the structural changes with disease. Thus the interdependent though separate experiments were brought together showing the relationship between each individual part of the research.

11.2 Parameters affecting X-ray scattering from collagen

11.2.1 1st order axial peak for quantitative analysis

The peak fitting process used to parameterise the X-ray scattering data provided values for the peak intensity, position and width as well as the associated standard

errors for each parameter. The highest axial peak orders visible showed greater absolute changes to peak position with changes of the D spacing of samples. However, due to the short data collection times the peak intensity of the higher visible orders was insufficient to provide fitted parameters with changes greater than the standard errors. The 1st order peak was used to plot the relationships with force and dehydration as it was the peak with the greatest intensity and therefore the lowest errors thereby increasing the confidence in the observed changes.

11.2.2 Effects of dehydration

The differences between the X-ray scattering patterns of hydrated and dehydrated rat tail tendon (type I collagen) are known (see Section 7.8.2). However, it was not clear at what time these changes were observable in the tension studies and how quickly the breast tissue samples needed to be mounted before dehydration affected the data.

11.2.2.1 Effects on axial peak intensity

The intensity of the axial peaks of the X-ray scattering pattern of collagen show clear changes when dehydrated (see Section 7.8.2). However, the peak intensities did not change linearly from the ratios observed in the hydrated state to the dehydrated state. There were different changes at different times i.e. the 1st, 3rd and 5th order initially decreasing as unbound water was lost. After 10 minutes the intensity of the peaks increased as continued water loss will remove water used in hydrogen bonding (Figure 10.14 and Table 10.2.6). Though all the changes were the result of dehydration the results observed showed different effects on the collagen structure depending whether the water lost was bound or unbound.

11.2.2.2 Effects on axial peak D spacing

Dehydration results in the contraction of bonds in the collagen structure, reducing the size of the collagen molecules and the D spacing (see Section 7.8.2). The dehydration of rat tail tendon (Figure 10.15), showed that there was a slow rate of reduction in D spacing in the first few minutes of the data collection (-0.0065 nm min^{-1}) giving approximately a 0.04 nm reduction in D spacing 6 minutes after the start of the data collection. The rate of reduction then increased to almost 4 times the rate observed before 6 minutes (-0.0254 nm min^{-1}) which resulted in a total reduction of 0.4nm after 24 minutes. The D spacing expected from dry collagen is 64.7 nm (see Section 7.8.2), a reduction of 2.5 nm from the 67.2 nm quoted from when the sample was fully hydrated (Wess, 2000). The observed reduction from the literature (Wess, 2000) was greater than the change observed in the results presented here. However, the rate of reduction that was observed was constant which indicated that the process of dehydration was not completed when the experiment was stopped after 24 minutes.

11.2.2.3 Effects on axial peak width

The observed changes in peak width caused by dehydration were negligible compared to the associated standard errors. For the 1st order peak the smallest standard error was three times larger than the largest change in the axial peak width (Table 10.2.8). For the higher order peaks although absolute increases in peak width would be greater the associated errors were also larger due to the lower peak intensity. Minimal (within errors) change in peak width indicated that in subsequent experiments increased intensity was required to reduce the associated errors in order to measure changes in peak width.

11.2.2.4 Implications for tension experiments

The 1st order axial peak was used for quantitative analysis of the tension experiments. The peak intensity shows the effects of dehydration earlier than its position. A 2.9 % reduction in peak intensity after only 1.5 minutes compared to a 0.0065 % increase in D spacing after 4.5 minutes. The peak intensity was affected before the position as peak intensity was affected by the loss of unbound water which occurs first while the change to peak position was caused by the loss of bound water (see Section 7.8.2). The effects of dehydration on D spacing of the sample of rat tail tendon under tension should have been minimal as the sample snapped after 4.5 minutes. However, the peak intensity of the rat tail tendon with 1.02 N would show the effects of force on intensity but with a 20 % reduction in intensity caused by dehydration. With regard to the chicken dermis and chicken tendon tension experiments the effects of dehydration should be apparent later as the volume to surface area ratio of those samples was much greater than the rat tail.

11.2.2.5 Implications for breast tissue diagnosis data collections

The 3rd order axial peak was quantitatively analysed to determine structural changes caused by the presence of disease in breast tissue, as the 1st order axial peak was superimposed over the Bessel peaks. This also allowed comparison with previous studies which used the 3rd order axial peak (Lewis, 2000) (see Section 10.3.3.2). The change in axial peak intensity was affected more rapidly than the position, a 1% change in intensity occurring after only 1.5 minutes compared to no reduction in the D spacing of the collagen after 9 minutes. The conditions for the dehydration experiment left a large surface area of rat tail tendon exposed with less than 1/3 of the length of the tendon touching the wetted cotton wool. Whereas during the mounting procedure for the breast tissue samples the whole of the sample was covered in phosphate buffered saline at all times. As the effect of dehydration would affect the diagnostic

results the time for mounting was kept below 1.5 minutes from thawing to sealing the capillary tube thus minimising dehydration effects. Exceptions to the 1.5 minute mounting were noted in the experimental log book for future reference, most being caused by the capillary tube breaking.

11.2.3 Effects of tension

11.2.3.1 Rat tail tendon

The application of 0.48 N tension increased the axial peak intensity of the 1st order by 2.24x10^5 Normalised photons per pixel (NPP) resulting in an observed intensity 13.5 times greater than the initial value at 0 N. When the force was increased further to 1.02 N the intensity reduced to only 1.9x10^5 NPP above the value at 0 N. However, after the same time the rat tail tendon dehydrating under similar conditions showed a 20 % reduction in intensity. The observed intensity change was a combination of both effects (see Section 11.2.2.4). Scaling of the observed intensity at 1.20 N to remove the 20 % reduction caused by dehydration thus showing the effect of tension only resulted in an increase in intensity of 2.28x10^5 NPP. The scaled intensity with 1.02 N applied load was therefore approximately 13.7 times the intensity with 0 N. Thus after the initial application of force to align the sample increasing the degree of order, further increase of force results in only a small increase to axial peak intensity. The application of force would appear greatly beneficial by improving the signal to noise ratio. However, the axial D spacing increased by 0.59 nm and 0.82 nm with the application of 0.48 N and 1.02 N respectively which could confound the results of the breast tissue diagnosis data.

11.2.3.2 Chicken tendon

The chicken tendon was larger than the rat tail tendon; approximately 8.7 mm wide by 2.3 mm deep compared to less than 0.2 mm width and depth for the rat tail tendon.

The increased size allowed the investigation of the effects of greater force than was possible on the rat tail tendon. The results observed from the tendon samples show the effects of force on almost pure collagen which was not directly comparable to the breast tissue as the breast tissue samples were a mix of collagen fat and cellular material.

The maximum intensity and D spacing were both measured at a force of approximately 10 N. The 1st order peak intensity increased to over 8 times the intensity observed at 0 N due to the increase in alignment of collagen fibres and the D spacing was increased by 1.1 nm, the force causing an extension of the collagen molecules. During the application of force the intensity and D spacing reached a threshold but due to dehydration the intensity and D spacing decrease. The effects of dehydration were expected to appear later than in the hydrated rat tail tendon (see Section 11.2.2.4). The variation in the spacing of the 3rd order peak (Figure 10.8) showed time dependant, rather than force dependant properties i.e. the plot that follows the time of exposure was linear whereas when plotted with respect to force the relationship was not linear. The separation in force/time dependence was observed as the increase in force was not applied progressively. Interpretation of Figure 10.8 with respect to force would indicate that there are forces at which the S position of peaks increased and at other forces the peak position decreased. The interpretation that these changes are a result of force alone was not realistic. When plotted with respect to time, the change in S spacing appears linear with a steady increase in S after 10 minutes attributed to dehydration. The 5 points where the S position of the peaks decreases corresponded to the times an increase in force was applied to the sample. Thus change in peak position was concluded to be time/dehydration dependant after 10 minutes with a decrease in S position of the peaks still apparent with the application of force.

11.2.3.3 Chicken dermis

The chicken dermis was selected to be a closer approximation to tissue than the almost pure collagen in the tendon samples. The axial peak intensities were much lower in the dermis than in the tendon: 4 NPP for dermis compared to 60 NPP and 80 NPP for rat tail and chicken tendon respectively. The odd orders 1^{st}, 3^{rd}, 5^{th} and 9^{th} were clearly visible, the even orders were present but very weak (Figure 10.11), which was also the case for the X-ray scattering pattern of breast tissue. The difference in intensity of the odd and even orders is related to the ratio of the overlap to the D spacing (O/D) (Bigi, 1987). The peak intensity ratios were similar to tendon but the intensity of all the peaks were lower in the chicken dermis. The even order peaks were not much greater than the background. The intensity ratios being the same suggests that the difference in intensity was not due to a difference in order but a consequence of the chicken dermis containing less collagen with a greater range of orientations.

The maximum increase in intensity observed is approximately 74 % at a force of 3.2 N. However, the time the data for this point was collected was after 12 minutes so there could be an effect of dehydration affecting this as the chicken tendon showed dehydration effects after 10 minutes. The dehydration effects were not evident before 4.5 minutes in the rat tail tendon so only examining the data before 4.5 minutes will yield effects of tension without dehydration affects. The application of 0.61 N tension gives a 36 % increase in axial peak intensity with a 0.08 nm increase in D spacing. This suggests that in tissues a significant increase in peak intensity can be observed with only a small increase in D spacing.

11.2.3.4 Implications for breast tissue diagnosis data collection

The increase in peak intensity caused by the application of force was attributed to an increase in the alignment of fibrils and fibres and thus the degree of order in the direction of the force. Alignment of fibrils and an increase in peak intensity are beneficial in data collection as the signal to noise ratio would be increased. However, the application of force causes an increase to the D spacing of the sample which may confound small diagnostic changes in the breast tissue data. By mounting the samples in capillary tubes under light vacuum the samples were subjected to force during the mounting process which was only maintained by friction between the sample and the walls of the capillary tube. Thus the force on the samples when mounted was expected to be minimal, increasing peak intensity with only a small increase to the D spacing. There was no direct method to determine the force that any of the samples were subjected to, so the extent of the effect on the D spacing of the sample was not determined.

11.3 Experimental errors in breast tissue diagnosis data collections

In order to determine the presence and nature of possible structural differences between normal, malignant and benign tissues, samples of breast tissue for each type were required. As the procurement of tissues was dependant on willing patients undergoing treatment consenting to tissue being used for this study, sample procurement was an ongoing process throughout the term of the project. As samples were collected at different times and from different patients undergoing slightly different procedures there was the possibility of the introduction of errors in sample selection and sample handling which needed to be addressed.

11.3.1 Sample selection

Normal tissues used for this investigation were collected from two sources the first being cosmetic reduction procedures. The second being tissue taken from the opposite quadrant of the diseased breast or the opposite breast from patients undergoing prophylactic bilateral mastectomy procedures.

Cosmetic reductions procedures are carried out to ease discomfort in women with large breasts and as such the tissue tends to be highly fatty. Without careful attention to the constituents on the samples difference in the scattering pattern of the tissues caused by differing amounts of collagen may be attributed to disease.

Prophylactic bilateral mastectomies are carried out on women with a high risk of the recurrence of breast cancer and to reduce the risk of women developing cancer if they have either a family history of breast cancer and/or have tested positive for the BRCA1 or 2 mutations. The normal tissue collected in these cases is from the opposite breast to that one in which the cancer has been diagnosed but it does not rule out the possibility that the cancer may be present in more than one location. The sample believed to be normal from this source may contain tumours. As well as misclassification there may be systemic effects that could be affecting the tissue in other areas of the breast that may result in differences in the scattering pattern. Differences in the scattering pattern of tissues at up to 6cm from the site of tumours were noted in previous studies (Lewis, 2000).

11.3.2 Sample handling

Tissue samples for the breast cancer diagnosis study were collected with consent of the patients donating the tissues by the tissue bank at Nottingham City Hospital. The

date the samples were collected was recorded. However, there were no details of how long there was between excision and snap freezing for each sample. It was reasonable to assume that there was not enough time between excision and freezing for dehydration to occur as the staff are aware of the detrimental effects of dehydration and followed procedures to ensure that the samples were stored in the best possible condition.

The samples were wrapped in aluminium foil and sealed in plastic bags before immersion in liquid nitrogen. The bags become brittle and can rupture in a minority of cases allowing the liquid nitrogen to come in to direct contact with the samples. Prolonged direct contact between the samples and the liquid nitrogen resulted in the samples being freeze dried or dissociating. Fortunately the rupture of a bag was a rare occurrence, fewer than ten samples throughout all the data collections have been unusable for this reason.

The effects of freezing and thawing were investigated and only minimal differences could be noted in the scattering patterns from test samples of rat tail tendon and chicken dermis. Though the scattering pattern was not detrimentally affected by a number of freeze thaw cycles the cellular structure used by the histopathologists to confirm diagnosis was compromised by repeated freezing. If a sample was frozen too slowly then large ice crystals form and rupture the cell membrane. To ensure that an accurate diagnosis can be obtained for each sample the samples were snap frozen and the number freeze thaw cycles kept to a minimum. Some damage was observed by the histopathologists due to freezing but only 1 sample could not be diagnosed due to excessive cellular damage.

During the sample mounting procedure the samples were kept hydrated at all times. Once sealed, the phosphate buffered saline in the capillary tubes ensured that the samples would not dehydrate. The fragile nature of the capillary tubes results in the occasional breakage. The samples from tubes that have broken are likely to dehydrate during remounting. Any sample that had to be remounted was recorded in the logbook in case the dehydration caused any effects on the scattering pattern. Capillary tubes were damaged in the freezer, when only one sample was damaged it could be remounted. If more than one was damaged then the sample codes could not be matched to the samples. If the samples were remounted before X-ray data collection a new code was assigned to the remounted samples allowing the histopathology to be matched with the X-ray scattering data.

Three different methods of sealing the capillary tubes were tested:

(i) Melting the glass

(ii) Plasticine

(iii) Paraffin wax.

Melting the glass required high temperatures which caused visible damage to the rat tail tendon held inside, although an adequate seal was made. The plasticine did not provide an adequate seal and the phosphate buffered saline leaked out when the samples were held vertically. Also a number of tubes were broken during the attempt to seal them with plasticine. Sealing the capillary tubes with candle wax provided a simple and effective method of sealing. The candle wax melted using a soldering iron was drawn into the tubes by capillary action where it then solidified, sealing the tube. Fewer tubes were broken using this method compared to using plasticine. The wax sealed tubes held the saline without leaking when held vertically and saline was still present in the wax sealed tubes some weeks after sealing. This method of sealing the

samples does require the close proximity of a hot soldering iron to the sample and it was feared that this may have caused thermal damage to the samples. Tests with two samples of rat tail tendon showed that no visible damage to the D spacing of the collagen was caused by proximity to the soldering iron at the distances used in wax sealing, even at extended periods of exposure. However, with closer proximity damage was not only observed in the scattering pattern but visible by eye as well. The heat damage observed in the rat tail test showed that care was needed when sealing the tissue samples for data collection. As an extra precaution the edges of the sample were not exposed during data collections.

A number of tissue samples dissociated during formalin fixation leaving too little tissue to embed in paraffin wax for sectioning and staining in order to provide histopathological analysis. The diagnosis from a number of tissue samples was compromised by dehydration and physical damage to the cellular structure preventing classification. In the cases where standard histopathological processing and analysis was not available, the initial diagnosis given to the patient at the time the tissue was excised was used. However, the information obtained from patient records only provides a general disease classification for tissues from a source not the sample itself. Overall 225 average X-ray scattering profiles were collected from 225 samples taken from 82 individual patients. Only 180 X-ray scattering profiles have corresponding histopathological diagnosis. The disease states of the remaining 45 samples were inferred from the tissues origins i.e. normal from mammoplasty and diseased from mastectomy. The amounts of the different tissue constituents will not be known without histopathological confirmation, also no guarantee of the true nature of a tissue sample can be made due to possible sampling errors. Therefore only X-ray scattering data from samples where the disease state was confirmed using

histopathological analysis were used to determine structural changes associated with disease.

11.3.3 Sample homogeneity

The cross sectional area of tissue investigated was defined by the diameter of the capillary tube and so was constant for all samples. The oscillation of the samples in the beam was set so that only areas of the capillary tube filled by tissue were exposed (i.e. no air gaps). Although the cross sectional area of tissue was constant for all samples, each was not purely of one tissue type. The scatter image collected for each sample shows the combination of all scattering from the structures within the tissue sample. The amounts of each tissue type such as tumour stroma, fibrous content and fat were estimated by the histopathologist during microscopic investigation. The values given are an indication and are not assumed to be precise. In order to determine the features associated with disease only samples that were predominantly normal, benign and tumour were used to extract scattering features associated with disease. Remaining samples were then examined for their correlation with the possible diagnostic features.

Investigation of individual points from within a single tissue sample (see Section 10.3.3.4) showed a large variation in axial peak intensity caused by the varying amounts of collagen and fat. The average was comparable with the oscillated data, which showed that the method of oscillating the sample provides a reasonable average of the X-ray scattering pattern of the sample. Acquiring the average pattern for diagnosis was acceptable as further tests would be done for verification in samples where diagnosis wasn't clear. However, for determining features associated with disease the inclusion of different tissue types reduces diagnostic precision.

To minimise the effects of non diseased tissue influencing the choice of parameters that were associated with disease and thus used for diagnosis, only cancer samples with greater than 80 % tumour by volume were used. For more precise association of features in the X-ray scattering pattern and the true disease state of the area investigated, precise SAXS to histopathological comparisons are required (see Section 13.3).

11.4 Errors in breast tissue diagnosis data analysis

11.4.1 Calibration

11.4.1.1 Peak position

The axial peak position and area appeared to yield diagnostic information (Figure 10.19). However, the average D spacing difference between normal and malignant tissue types of 0.3±0.034 nm (relative difference observed from a single data collection) may be confounded by the 1nm error in calibration between data collected during different experiments during the 2.5 year duration of this study. By plotting only data from one data collection period (Figure 10.20) separation of tissues types using the spacing and peak area of the 3rd order Bragg peak was improved but the numbers of samples was dramatically reduced. The difference in the spacing between data collections can be observed by the grouping of tissue samples with the data collection the data was obtained (Figure 10.21). Figure 10.21 showed tumour samples all with greater than 80 % tumour volume a maximum difference from the mean of ±0.2 nm can be observed between samples from a single data collection. However, the mean spacing varies by almost 1 nm between the outlying groups. Although the observed differences in spacing between data collections could be explained as random variations in small groups it is more likely that the error was in the calibration process. Without an accurate absolute calibration for each data set this

could not be verified. Each dataset was calibrated to a high degree of precision (centre of diffraction to 5 decimal places and camera length to within 1 mm) based on the scattering from rat tail tendon. However, during the calibration process the rat tail tendon is assumed to have a D spacing of 67 nm. The actual spacing observed from an individual specimen of collagen depends upon the hydration and tension the sample was subjected to as well as a number of other factors. The data collections for this investigation into the possible diagnosis of breast cancer was undertaken during a number of data collections over a two and a half year period separated roughly into six month periods during which time samples were collected. Rat tail tendon degrades with time and so the calibration standard used at experimental facilities is changed frequently and as such no two data collections will have had the same piece of rat tail tendon for calibration. The D spacing used for calibration that is assumed to be 67 nm is going to be marginally different in each case introducing an unknown error. For shorter camera lengths silver behenate was used as the standard and as a non biological sample was more stable (though does degrade in light). Silver behanate cannot be used effectively to calibrate the 6.25 m camera used for the breast tissue as only 1 diffraction peak was observed on the detector (Figure 8.1). Until another standard can be found to provide absolute calibration, rat tail samples used to calibrate the 6.25 m camera should be compared to a shorter camera calibrated using silver behenate to ascertain the actual spacing of the rat tail tendon instead of assuming the D spacing to be 67 nm. The calibration of a long camera can also be checked by accurately measuring the sample to detector geometry. In hindsight the D spacing of the rat tail calibration sample should have been checked against another reference standard (such as silver behenate) and accurate camera geometry should have been incorporated into the experimental procedure. However, it was not realised to what precision the calibration would deviate between experiments and this variation was only noticed when all data was compared for the first time. Relative differences can

still be observed between tissue types in single data collections but due to the variations a precise value for the D spacing of collagen from malignant, normal and fibroadenoma cannot be given.

11.4.1.2 Intensity

The normalisation of intensity (see Section 8.2.1.3) corrects the X-ray scattering images collected for differences in attenuation of the sample and the storage ring current to allow direct comparison of intensity between samples. Differences in the attenuation of the semi-transparent beam stop used in different data collection periods resulted in differences in intensity that could not be accounted for. Thus relative differences in Bragg and Bessel peak intensity between tissue types were obtained from individual data collections but direct comparison between all data collections could not be made with confidence. For future studies the incorporation of a sample with a known scattering profile such as glassy carbon has been proposed. The intensity of the scattering profile from a known sample in all experiments could then be used to normalise any differences in intensity between data collections.

11.4.2 Manual analysis methods

11.4.2.1 Peak fitting

The areas, FWHM and spacing of the Bragg peaks were fitted simultaneously using Gaussian approximations on a quadratic background to describe the amorphous scatter (see Section 8.3.1.3.2). This allowed the peak parameters to be found without offsets caused by other scattering and thus exclude systematic errors. The quadratic equation was chosen as an empirical descriptor which used the minimum number of parameters to describe the amorphous scatter.

The error in the calibration of the spacing prevents an accurate absolute value for the D spacing of normal and diseased collagen to be given. However, relative differences can be found between tissue types.

All output profiles were checked to ensure the output represented a physical model i.e. that the fitted peaks represented scattering peaks not noise in the amorphous scatter. The high R^2 values obtained from the fitting process indicated that the output parameters of the fitting program (PAN), described the peaks and amorphous scatter within the uncertainty given. It was noted that the uncertainty of the fit of scattering peaks is related to the intensity of the peak. Reduced peak intensity of a given peak yields a lower signal to noise ratio. Low signal to noise ratios give a greater likelihood that the fitted parameters will be affected by the noise in the scattering profile rather than describing the scatter from the sample. Therefore care must be taken with the interpretation of low intensity peaks.

11.4.2.2 Amorphous scatter

The calculated value of the radius of gyration (Rg) (see Section 7.7.5) was not precise as the scattering from the sample holder was not accurately subtracted from the scattering profile of the sample and the sample under investigation was not a mono-disperse solution extrapolated to infinite dilution. This is the ideal case when measuring Rg. However, the effect of the sample holder was the same for all samples investigated. Thus the obtained value of Rg yields the average size of scattering objects in the sample and was used to investigate the relative differences between the size of scattering objects in normal, malignant and benign tissues. The samples investigated in the breast cancer diagnosis study were predominantly collagen for normal and fibroadenoma samples over 90 % contained greater then 95 % fibrous

tissue. The fibrous tissue content in tumour samples was lower, many containing no normal fibrous material. However, the tumour stroma which was the main component of the tumour tissues contained collagen, thus the value obtained for Rg was believed to be related to the size of features in the collagen.

The power law decay in the Porod regime yields information regarding the surface and dimensionality of the scattering objects. As with the calculation of Rg the values obtained for the power law decays will be the average of all the scattering objects in the sample.

The calculated values for the power law exponents and Rg can be used to observe relative differences in the scattering profiles as all the data was processed using the same method. Also as the power law exponent and Rg were calculated from the gradient of linear regions in the scattering profile the errors in the calibration and normalisation between data collections will not affect results.

The Relative Intensity Ratio (RIR) (see Section 8.3.2) was calculated from intensities over a limited linear range, thus the sensitivity to errors in the spacing calibration was reduced. The two areas used for the calculation of the RIR were scaled by the same factor in the normalisation procedure. Thus the relative difference between the two ranges would have remained the same and so the RIR was not thought to be affected by the errors in the normalisation between data collections.

11.5 Diagnostic X-ray scattering

11.5.1 Conventional X-ray source

Significant differences in the small angle X-ray scatter patterns were evident between malignant tumour and normal specimens when measured using a conventional X-ray

source. Though only a small number of samples were compared in this preliminary investigation (18 and 5 samples for tumour and normal respectively), the differences in the amorphous scatter between tumour and normal tissue samples observed using SAXSess allowed them to be separated with high accuracy. The observed differences were in accordance with the results from previous observations using synchrotron radiation (Fernandez, 2002).

To determine the significance of the separation of the tissue types using the scores of the principle components (loadings, L2 and L3) a Student t-test was used. The variance of the scores in each group was checked and found to be significantly different using a two tailed t-test for unequal variance. L2 was determined to have a statistically significant difference ($P<<0.01$). No significant difference between tumour and normal samples could be determined from L3 alone ($P>0.05$) However, if the single normal sample with $F3<0$ is excluded from the normal set then the difference does become significant ($P<0.02$) indicating a considerable bias introduced by this single sample. This may indicate the presence of a 3rd grouping. However, with only one sample in this group further tests are required to investigate the difference between this and the other normal samples.

Distance from the tumour site has been shown to affect the value of L2. Three of the 4 samples from tumour tissue which have a negative value of L2 were dissected from larger samples of tissue and therefore could have been from up to 2 cm away from the site of the tumour and therefore not actually tumour tissue. Sampling error could therefore be the cause of the apparent miss-classification. Histopathological diagnosis on these tissues may help to resolve these observations. The series which showed the opposite trend to the others is an outlier as the 6 cm sample is actually tumour tissue and it is correct that it should appear to have the PCA factors associated with disease.

11.5.2 Synchrotron radiation

11.5.2.1 Manual analysis of axial collagen peaks

11.5.2.1.1 Axial spacing

On average the D spacing of malignant tissues was 0.3 nm larger than the average of normal tissues. The absolute D spacing values observed in this study were not identical to the published results of 65.3 nm and 65.0 nm for malignant and normal tissues respectively (Fernandez, 2002). However, the relative increase of 0.3 nm in malignant tissues compared to normal tissues reported (Fernandez, 2002) was verified by our results. The published study (Fernandez, 2002) was undertaken at the ESRF hence different experimental parameters and a different calibration standard, therefore a minor difference in the absolute values is to be expected. The corroboration of the relative increase in the D spacing in the collagen of malignant tissues would confirm that the axial packing arrangement of collagen from malignant tissue was on average larger.

An observed increase in axial D spacing supported the hypothesis that OF/LB collagen was present in diseased tissues, as the axial periodicity of OF/LB collagen was reported to be larger than normal collagen (see Section 7.10.2.1). The difference in the axial spacing between malignant and benign disease suggested that the malignant disease contained a greater amount of the OF/LB collagen than the fibroadenoma. The collagen in diseased tissues was thought to be a combination of OF/LB collagen and normal collagen (see Section 11.10).

Previous research showed possible diagnostic differences in the D spacing of collagen. However, the major difference was a lower D spacing for benign samples compared to normal and malignant tissues (Lewis, 2000). The D spacing of the

malignant samples was reported to be extended to higher D spacing than the normal samples and the average D spacing of the malignant samples was increased though not significantly. The cause for the difference in the D spacing of the benign samples was not known in the published study (Lewis, 2000). The data presented in this thesis showed significant differences in D spacing between all three tissue types (Table 10.3.4). However, the average D spacing for the fibroadenoma samples presented in this thesis was between the malignant and normal samples, a different result than the published study (Lewis, 2000).

All the tissues examined have a range of values and with low sample numbers there will be a possibility for the trends to be affected by these variations. The difference in the change in axial D spacing of the fibroadenoma samples between the observed result and published literature (Lewis, 2000) may have been a function of variation and small sample numbers with only 7 benign samples in the published study. The observation of the change in the axial spacing of malignant tissues was corroborated by the published literature (Fernandez, 2002). It is unlikely to be merely coincidence that two separate studies with reasonable sample numbers replicated the average increase in the D spacing of malignant tissues.

11.5.2.1.2 Axial peak intensity

The reduction in peak intensity of the axial collagen peaks has been suggested as an indicator of disease (Lewis, 2000 and Fernandez, 2002). The results from this study show that the average of the sum of the area of the 3rd and 5th axial peaks of collagen is 1.49x10^{-4} NPP nm^{-1}, 2.01x10^{-4} NPP nm^{-1} and 2.74x10^{-4} NPP nm^{-1} for malignant, fibroadenoma and normal tissue samples respectively. The difference between the average of the 3rd order Bragg peak area for malignant and normal tissues was shown

to be significant $P<0.015$ but there was no significant difference between the other combination of tissue types (Table 10.3.2).

The area of the Bragg peaks was dependant on not only the supra-molecular order of the collagen within the tissue sample but also the amount of collagen in the tissues and its preferred orientation. Without prior knowledge regarding the amount of collagen in the tissue an accurate diagnosis cannot be made using this value alone. High peak intensity suggests normal collagen while a lack of intensity could be due to either poorly ordered collagen from malignant tissues or simply low collagen content from normal tissues. The intensity of the fat peak may aid classification when used in conjunction with the intensity of the axial peaks of collagen. Low intensity from collagen peaks in fatty samples would suggest disease, but if the intensity of the fat peak (which would be high in such tissues) was measured, correct classification may be achieved.

11.5.2.2 Manual analysis of amorphous scatter

11.5.2.2.1 Radius of gyration

The plot of ln I(s) against S^2 showed a linear section close to the beam stop. The gradient of this linear section gave the value for Rg (see Section 8.3.2). As discussed previously the value of Rg obtained will not be accurate but will be an average from the tissue (see Section 11.4.2.2), which may be diagnostic. The average values of Rg calculated from the region near the beam stop were 69.45±0.14 nm, 87.45±0.12 nm, and 73.57±0.15 nm for malignant, fibroadenoma and normal tissue samples respectively. The changes in Rg close to the beam stop suggest an average reduction in size of the scattering objects of 5.6 % for malignant tissues and an increase of 18.8 % for fibroadenomas compared to normal tissues. The increase in the average

size of scattering objects in tissue samples from fibroadenomas is thought to be caused by the increase in collagen in these tissues. The reduction in the average size of scattering objects in malignant tissues is thought to be the result of MMP action degrading the collagen.

11.5.2.2.2 Relative intensity ratio

The average values calculated for the RIR (see Section 8.3.2) were 334.6±0.5, 378.3±0.6 and 609.8±1.2 for malignant, fibroadenoma and normal tissue samples respectively. The RIR shows a considerable difference between normal samples and the diseased tissues. There appears to be only a small difference between the malignant and benign values for the RIR. The high intensity ratio of normal tissues indicates a high intensity near the beam stop with a lower intensity between the Bragg peaks; as opposed to the diseased tissues which have a lower intensity near the beam stop and a higher intensity between the Bragg peaks. The ranges investigated correspond to scattering objects with spacings of approximately 50 nm to 60 nm and 15 nm to 20 nm for the area near the beam stop and between the 3^{rd} and 5^{th} axial peaks. The dimensions of the scattering objects are not confined to within the calculated ranges but their contributions outside the observed areas cannot be directly observed due to the presence of Bragg or Bessel peaks causing local increases in the scattering profile. The difference in the RIR therefore suggests normal tissues have a high surface area of scattering objects with dimensions in the range of many tens of nanometres and lower surface area of scattering objects with dimensions of a few tens of nanometres which caused the high intensity near the beam stop and rapid decay of the amorphous scatter. The diseased tissue appears to have a lower surface area of scattering objects with dimensions in the range of many tens of nanometres and an increase of the surface area of scattering objects per unit volume with dimensions in

the range of a few tens of nanometres, causing the increased contribution to the amorphous scatter. The increase in surface area for smaller scattering objects compares with published literature which presented results suggesting that the surface area of scattering objects with dimensions of a few tens of nanometres is very much larger in diseased tissues (Fernandez, 2002). The change in the surface area of scattering objects would suggest that the average size of the scattering objects in diseased tissues was lower compared to normal tissues. The cause of the reduction in the surface area of large scattering objects and increase in the surface area of smaller scattering objects is believed to be caused by diseased tissues not possessing large amounts of highly ordered fibrillar collagen. The highly ordered collagen fibril bundles have a diameter of 70 nm (Fernandez, 2002). However, the collagen fibrils from malignant tissues appear smaller, exhibiting a range of diameters down to individual micro fibrils with a diameter of approximately 4 nm (Orgel, 2001). The cause of the reduction in diseased tissues could be either the OF/LB collagen not forming ordered structures, the action of MMP degrading the collagen structure reducing its size or a combination of both mechanisms (see Section 11.10).

11.5.2.2.3 Power law exponent

The average values for the power law exponents calculated from the linear region between the 3rd and 5th axial peaks (see Section 8.3.2) were -2.71±0.008, -2.72±0.008 and -2.9±0.1 for malignant, fibroadenoma and normal tissue samples respectively. The quoted values in the literature (Fernandez, 2002) for the power law exponent were -2.5 in the axial direction and -3 in the equatorial direction. This published study used a very small beam size and was able to separate the equatorial from the axial scattering. The results shown here are from an average of a large volume of tissue with multiple orientations summed together. As such the observed scatter is a

combination of both axial and equatorial scattering which may account for the values for the power law exponent being between the two values from the literature. The shape of the scatterers would appear to match the published results of being coils which are locally rod like.

11.5.2.3 Principle component analysis

The overlap of values for individual parameters makes definitive diagnosis difficult when only using single parameters. However, when used in combination the different parameters produced allow separation. This can be seen in the plots of axial spacing against peak area (Figure 10.19, Figure 10.20 and Figure 10.22) or Rg against the intensity ratio (Figure 10.24). The scattering profiles contain a large amount of information and it would be difficult and time consuming to attempt to maximise the diagnostic potential manually. Using PCA techniques and linear discriminate analysis, the known diagnosis of the samples can be used to build a model which maximises the separation of the groups using all the information present in the scattering profiles.

PCA of the data collected with a camera length of 1m showed the greatest variation in data close to the beam stop. The region near the beam stop corresponds to the region that can be measured with increased resolution using a 6.25 m camera. From the small number of samples 100 % specificity and sensitivity was achieved using the 1 m camera, once one outlier from the tumour group was shown to be normal under histopathological analysis (see Section 10.3.4.1).

The PCA of 6.25 m data which was within the range of greatest variance from the 1 m study showed 95 %, 90 % and 96 % of the normal, fibroadenoma and malignant samples respectively were correctly identified. The interpretation of the significant

scores and loadings of the model showed increased background scatter near the beam stop and reduced background intensity between the 3rd and 5th axial peaks for the normal samples compared to fibroadenoma and cancer samples. Axial peak intensity would be greatest in normal samples and lowest in tumour samples and the axial peak spacing for fibroadenoma samples would be lower in fibroadenoma and cancer samples compared to normal samples.

The observations made from the PCA results matched the observations from manual analysis techniques. i.e. malignant samples showing reduce ordered collagen (reduced peak area), reduced amorphous intensity at low S and increased between the 3rd and 5th order Bragg peaks (RIR). The matching features observed with manual and automated techniques indicated that the features observed manually were reliable markers of disease when used in combination.

11.6 Sensitivity and specificity of SAXS as a diagnostic test

For any diagnostic test to be implemented clinically there has to be a motivating factor. The most important being the improvement of diagnostic capabilities measured by an improvement in the sensitivity and specificity over the current method. If there is no improvement in diagnostic capabilities but the proposed method has a lower cost, either for associated consumables or a reduction in required man-hours through automation then there is also benefit in pursuing clinical implementation. The sensitivity and specificity of classification of various SAXS parameters compared well histopathological techniques (Table 11.6.1).

Sensitivity is the more important of the two parameters as the higher the sensitivity, the fewer false negatives there are, meaning cases where disease was present were not missed. With low specificity there will be a higher number of false positives. However, as all positive results will be referred for further tests in order assess the extent of disease the cases that were false positives will be found. Although it is not ideal to subject patients free from disease to further testing, the consequences of missing cases of disease are too great and therefore clinical diagnostic tests will accept lower specificity to ensure the highest possible sensitivity.

	Diagnostic test	Sensitivity %	Specificity %
Histopathology	Biopsy cut 18G	93-96	100
	Biopsy cut 14G	88-98	100
Mammography	Overall	63-95	14-90
	Palpable	95	90
	Impalpable	50	
	Women over 50	83-92	
	Dense Breasts	35	
SAXS	RIR	90.9	100
	3rd Order Bragg Peak	100	81.8
	1m PCA correlation with C1	100	100
	6.25m PCA Model	**96.4**	**95.4**
	SAXSess PCA	100	80

Table 11.6.1 Sensitivity and specificity for various diagnostic techniques

Calculated values for sensitivity and specificity for SAXS techniques in comparison with known values for histopathology and mammography (Singhal, 2006).

The calculated values presented were based on chosen parameters to maximise classification. The 6.25 m PCA model used linear discriminant analysis upon which to base the model rather then manual decisions and was subsequently tested using cross validation techniques (see Section 8.3.3.1.2). The PCA model provided automated classification with comparable sensitivity and specificity to current clinical techniques, an encouraging result which requires further investigation (see Section 13.6).

11.7 Effect at distance

The X-ray scattering data showed differences in parameters such as the 3rd order Bragg peak area that did not appear to be related to the amount of fibrous material in the sample, but which still showed differences from normal samples up to 6 cm away from the tumour site (see Section 10.5.3.1). Trends dependant on distance were also noted in the principal components that showed diagnostic potential in the conventional X-ray source study (see Section 10.5.2). Using a model created from the samples with known disease state, the series samples (1 cm, 2 cm, 4 cm and 6 cm) were compared and an automated classification obtained (see Section 10.5.3.2), which in most cases identified the samples as cancer.

The classification obtained from X-ray scattering was not based on the amount of tumour present in the tissues at distance as the histopathological classification for most of the series samples was normal, i.e. they did not contain any cancerous cells. Misclassification of samples shown to be normal by histopathology could be used as evidence to show the model was not accurate. However, the samples in question were not "normal" they were samples from an area near tumours, thus the collagen in these samples was affected by the remodelling processes present in diseased tissues. Features in these samples had been observed to reflect those observed in diseased tissues. The classification of cancer in samples up to 6 cm from the known tumour site suggests that the remodelling processes are not just local to the tumour site but effect surrounding tissues as well.

The PCA model was tested using cross validation techniques (see Section 8.3.3.1.2) which indicated that the model was not influenced by random variation and was based on systematic difference between the three tissue types. If there was any misclassification some of the samples would be expected to appear as fibroadenoma,

none did but this is not enough evidence to validate the model. To validate the model a double blind study would be required which is beyond the scope of this study but, in order to show clinical relevance, will need to be undertaken in the future (see Section 13.5).

11.8 Degradation of tissues

11.8.1 Errors

The errors associated with the fitting increase as the peak area decreases. However, it was still possible to observe trends. In the case of most of the degradation series errors associated with the peak areas were smaller than the changes observed and the differences between the degradation and controls was clear. The errors observed associated with the D spacing changes from the degradation series were comparable to the changes. The controls show as much if not more reduction in the D spacing than the degradation series.

11.8.2 Changes in collagen structure by different types of degradation

11.8.2.1 Matrix metalloproteinase

The area of the Bragg peaks is reduced by the action of MMP (see Section 10.6.2), which was consistent with the expected effects from the known model of MMP action (see Section 7.10.3.2). The tropocollagen molecules cleaved by the MMP action into ¾ and ¼ length molecule fragments being unstable at physiological temperatures degrade further. As more molecules are removed from the structure there will be less ordered collagen to contribute to the Bragg scatter. The reduction appears to be linear with the time of exposure and the reaction will continue until there is no collagen left. Complete disruption of the collagen was observed in many of the MMP degradation studies.

No change in axial peak width was observed in relation to MMP action as no change to the range of D spacings in the degraded collagen was expected (see Section 7.10.3.2). However, there was an observed increase in peak position (see Section 10.6.3), which was not expected from the known model of MMP action (see Section 7.10.3.2), nor was it thought to be an effect of radiation damage. The decrease in D spacing of the axial collagen peaks was observed in both the control and degradation series which suggested that the MMP was not the cause of the decrease. However, the decrease was greater in the degradation series for breast tissue and pork dermis which suggested the MMP was contributing to the effect in some way. The decrease was attributed to dehydration of the collagen in the tissue even though the sample was fully immersed in buffered saline for the duration of the experiment which initially was thought would prevent dehydration. The buffer solution used for the degradation experiments was made to ensure the MMP would be in an active state, this required a buffer solution of specific pH. The addition of hydrochloric acid and hydrogen peroxide was used to achieve the required pH of 7.5, resulting in the presence of salt in the solution. Calcium chloride was added as part of the recipe to ensure the adequate presence of calcium ions required for the activation of the MMP. The resulting solution therefore had a high salt content and thus a high solute potential which would tend to draw water out of the sample resulting in similar effects on the collagen in the sample as dehydration. The degradation series showed a greater change in D spacing beyond the control as the degradation products from the action of the MMP would further increase the solute potential which would exacerbate the dehydration effects of the sample.

The intensity of the amorphous scatter near the beam stop reduces, while between the 3rd and 5th order axial peaks intensity increases in the experiments performed (see Section 10.6.5). The observed changes in intensity suggested that the surface area of

scattering objects with dimensions in the range of many tens of nanometres was reducing while the surface area of scattering objects with dimensions in the range of only a few tens of nanometres was increasing. The conclusion was that change in the surface areas of scatterers in both dimension ranges was linked. Which would be consistent with the known mechanism of MMP action, reducing the large collagen molecules (280 nm long, see Section 7.3.4) to fragments which then degrade further to smaller sizes, being unstable at physiological temperatures (see Section 7.10.3.2).

The observation of the changes in intensity (both of the peaks and amorphous scatter) were consistent with the model of MMP action (see Section 7.10.3.2). The changes caused by MMP action were consistent with the observations of diseased breast tissue (see Section 11.5), which suggested that MMP action may be at least partly responsible for the structural changes in breast tissue associated with the progression of disease (see Section 11.10).

11.8.2.2 Thermal

No significant difference between the D spacing of normal and malignant tissues used in the thermal degradation series was observed. However, the reduction in peak area between the two extremes of temperature tested showed a 49 % reduction for malignant tissues yet only 28 % in normal tissues. A difference in the thermal properties would suggest a possible difference in the amount of hydroxyproline in the collagen samples (see Section 7.8.4). To test the thermal properties to confirm a difference in the amount of hydroxyproline the T_{melt} temperature needs to be determined which requires a test with gradually increasing temperature. The thermal degradation test undertaken here only had a limited number of tissue samples and therefore the differences observed could be inter-sample variation. Therefore although

the results observed indicate a difference in the amount of hydroxyproline suggesting a different type of collagen, further testing would be needed for confirmation.

11.9 Computer simulation

11.9.1 Micro fibrillar shear

A simulation showing varying degrees of shear between adjacent micro fibrils showed a reduction in peak intensity with no alteration to the spacing. This model was thought to be a realistic representation of the way in which the apparent disorder in diseased collagen surrounding tumours manifests. The collagen known to be present (determined by histopathology) exhibiting reduced axial peak intensity, indicated a lower degree of structural order. However, this model is not the only explanation and cannot be the only mechanism acting as it did not account for the change to the D spacing of the collagen.

11.9.2 Increase in the variation of collagen D spacing

Increase in the variation of D spacing in the modelled collagen was achieved by increasing the standard deviation of the D spacing variable in the modelling programme (Suhonen, 2005). Increasing the standard deviation of the D spacing distribution causes a reduction in peak intensity. However, the higher order peaks alter more dramatically than the lower orders. The increase in the standard deviation was accompanied by an increase in peak width reflecting the range of scattering objects around the mean increasing. The relative intensities of the peaks appear the same in diseased and normal tissues. Also the increase in the peak width was not as large compared to the reduction in peak intensity in diseased tissues. Therefore the reduction in axial peak intensity observed in diseased tissues was not the result of a decrease in the degree of order of the axial collagen repeat.

11.10 Cause of structural differences in diseased tissues

11.10.1 Does any one system account for all observed changes?

MMP action can account for the reduction in peak intensity of the collagen around tumours but cannot be the cause of the increased levels of collagen present in and around tumours. The increase in the observed D spacing from malignant and benign tissues also cannot be a result of MMP action as the degradation studies (see Section 10.6.3) showed no discernable change in the D spacing other than a decrease which was attributed to dehydration (see Section 11.8.2.1). The changes to the amorphous scatter observed in diseased tissues (reduction in intensity near the beam stop and increase between the 3rd and 5th order axial peaks) were also observed with the action of MMP under control conditions (see Section 10.6.5). The action of MMP has been associated with metastasis (McCawley, 2000) and the presence of MMP has been confirmed in malignant tissues (Duffy, 2000). MMP action on collagen does not account for all the changes in the collagen of diseased tissue, therefore MMP action cannot be the sole cause of the differences between malignant and normal tissues.

The presence of large amounts of collagen even in tissues from post menopausal women where the tissues are expected to be highly fatty suggests the production of new collagen around tumours. The increase in Bragg peak intensity from invaded fatty tissues (Fernandez, 2002) also suggests the production of collagen associated with disease. The D spacing of the collagen around diseased tissues was increased compared to normal tissues, a result corroborated for malignant disease by published research (Fernandez, 2002). The increase in the D spacing was consistent with the hypothesis that the collagen around the tumours was onco-foetal laminin binding (OF/LB) collagen (Pucci-Minafra, 1993). The collagen around tumours being OF/LB collagen would also account for the possible differences in the thermal properties. The

lower Bragg peak intensity observed from the OF/LB may be attributed to lack of order in the fibrils as demonstrated by the modelling of adjacent fibril shear. The Bragg peak intensity was reduced by increasing the shear but the D spacing and peak width remained unchanged in the model. However, the collagen from breast cancer tissues was not pure OF/LB as α_2(I) chains, which form normal collagen were present but at reduced levels (Pucci-Minafra, 1993). The combination of normal collagen and OF/LB collagen would be expected to show a lower degree of order within the collagen and increase variation in D spacings, which would result in lower axial peak intensity and increase axial peak width. SAXS from samples of pure OF/LB collagen could not be measured as manufactured OF/LB collagen was not commercially available. The purification or production of OF/LB collagen under controlled conditions would yield samples in a non physiological state which would therefore not provide comparable results.

11.10.2 Is a combination of the proposed mechanisms possible?

The production of OF/LB collagen around tumours can account for the majority of changes but the degree of order within the native OF/LB collagen cannot be determined. The effects of MMP on collagen have been shown to affect the Bragg peak intensity and to have a limited effect on the D spacing. The action of MMP may account for the reduction of peak intensity from diseased tissue but may be reducing the D spacing of the affected collagen increasing the variation in observed D spacing from different samples. Although the action of MMP is likely to be restricted to the exposed surfaces of collagen its effects account for the reduction in the average size of the scattering objects and change in the surface area of different sized scattering objects. It would appear that both mechanisms are occurring within the tissues and it is a combination of these processes that is required to account for all the observed

changes in the examined tissues, OF/LB collagen causing the increased D spacing in both malignant and benign disease. The action of MMP then degrades the OF/LB collagen around malignant tumours causing the reduction of the degree of ordering of the OF/LB collagen.

12 Conclusion

12.1 Structural differences between tissue types

There was a 0.3±0.034 nm increase in the collagen D spacing of malignant tissue compared with normal tissues. There was significant increase in the axial peak width between normal and diseased tissues which suggested a small increase in the variation of D spacing about the mean in diseased tissues.

The reduction in peak intensity of the axial collagen peaks indicated a reduction to the degree of order within the collagen structure of diseased tissues. The average of the sum of the intensity from the 3rd and 5th axial peaks showed a 45 % decrease for malignant tissues and a 26 % decrease for fibroadenomas compared to normal samples.

The shape of the scatters would appear to match the previously published results for collagen, being coils which are locally rod like (Fernandez, 2002). The shape of the scattering objects did not appear to be significantly different between tissue types. However, the dimensions of the scattering objects did appear to exhibit differences between tissue types.

The changes in Rg suggest an average reduction in size of the scattering objects of approximately 6 % from malignant tissues and an increase of approximately 19 % from fibroadenoma compared to normal tissues.

The intensity ratio shows a considerable difference between normal samples and the diseased tissues. The average intensity ratio for malignant tissues was observed to be 45 % lower and the average for fibroadenoma samples was 38 % lower compared to

normal tissues. The reduction in the intensity ratio indicates a reduction in the surface area of scattering objects with dimensions in the range of many tens of nanometres and an increase in the surface area of scattering objects with dimensions in the range of a few tens of nanometres. The change in the surface area of scattering objects was attributed to diseased tissues not possessing large amounts of highly ordered fibrillar collagen. The highly ordered collagen fibril bundles have a diameter of 70 nm (Fernandez, 2002). However, in diseased tissues the amount of collagen with this highly ordered structure appears greatly reduced and the scattering profile suggests a range of diameters present down to individual micro fibrils with a diameter of approximately 4 nm (Orgel, 2001).

12.2 Proposed cause of structural differences

The proposed mechanism behind the observed changes is a combination of the production of OF/LB collagen around tumours and the degradation of the OF/LB collagen and native collagen by matrix metalloproteinases. The production of OF/LB collagen around tumours can account for the changes observed by X-ray scattering, such as the increase in the D spacing and the reduced order within the collagen structure with regard to both the variation in fibril diameter and the reduction of axial order. The action of MMP has been shown to be unable to account for the increase in D spacing. Therefore MMP action cannot be the major cause of the observations but MMP action can cause reduction of axial peak intensity and reduction in fibril diameter and the presence of MMP in and around malignant tissues has been documented.

It was concluded that the presence of OF/LB collagen was the major cause of differences observed in malignant and fibroadenoma tissues compared to normal tissues. The differences which separate the malignant from fibroadenoma samples was

attributed to the action of MMP on the OF/LB collagen surrounding the tumour, further disrupting the order of the collagen structure, which would then allow further invasion and metastasis.

12.3 Diagnosis using a conventional X-ray source

Clear differences between normal and diseased tissues from both the tumour site and at up to 1 cm from the tumour can be seen using the SAXSess system and PCA, which showed that automated diagnosis using a conventional X-ray source may be possible. The observed differences in amorphous scatter using SAXSess were also observed using synchrotron radiation. The differences were attributed to changes in the surface area of scattering objects at different length scales, decreasing in the range of many tens of nanometres and an increasing in the range a few tens of nanometres in diseased tissues compared to normal tissues. This preliminary study of using conventional X-ray production to allow diagnostic data to be collected in a clinical setting suggests that optimised dedicated machines could be implemented in hospitals to aid pathological diagnosis and to guide surgeons during lumpectomies.

12.4 Automated diagnosis

Preliminary use of PCA indicates that a reliable model can be built using maximum variations in the samples. The scatter profile of future samples can then be compared to the model to provide an automated diagnostic test for breast cancer and possibly other tissues. The initial results show accurate diagnostic data can be collected by investigating the average scatter pattern from a core cut biopsy and that diagnosis of disease may be possible in tissue samples up to (and possibly over) 6 cm from the tumour site.

13 Further Work

13.1 Absolute calibration

13.1.1 Spacing

Knowing the absolute D spacing related to diseased tissues and OF/LB (onco foetal laminin binding) collagen would enable more precise interpretation of the structure of the collagen from diseased tissues. Absolute calibration would also allow direct comparison of data collected using different experimental systems.

Some preliminary work has begun to find a calibration standard suitable for calibration of appropriate spacing ranges with limited success. One proposed technique was to use glass nano-spheres with a diameter of 100 nm. However, in preliminary tests the concentration of scattering objects was too low to observe a significant signal. Until an alternate standard can be tested and verified, accurate measurement of the sample to detector distance as well as the calibration of the rat tail standard to silver behenate is proposed to reduce the calibration error in further data collections.

13.1.2 Intensity

Following the difficulty in normalisation it is proposed to find a standard with a known scatter profile of set thickness to expose during all data collections. A feature in the scatter from this sample would then be used to normalise the intensity of all data sets in order to ensure that the observed intensity from different data collections would be identical.

13.2 New sample holder

The mounting of the samples in glass capillary tubes has been the cause of the loss of some of the samples through damage to the fragile tubes at cryogenic temperatures. The mounting procedure is also time-consuming and in some cases takes long enough for possible dehydration effects to become apparent. A new sample holder (see Appendix I) has been designed to make the mounting procedure quicker and thereby reduce the possibility of dehydration effects and the damage to samples. The new sample holder has been built and can now be tested and commissioned.

13.3 Micro-focused investigation of individual points in tissue

The investigation of a possible diagnostic tool was effectively accomplished by investigating the average scatter pattern form a volume of tissue. However, variations in the amount of the different tissue constituents caused some difficulties with the interpretation of the underlying cause of the changes. To accurately determine the nature of scatter from diseased tissues and more specifically the scatter from different tissue constituents in the diseased and normal states, the use of a micro focused beam was proposed to look at points across a slice of tissue mounted on a mica slide. The slide can then be stained using standard histopathological techniques so that direct comparison of the scatter and the histopathological diagnosis can be made.

13.4 Optimisation of a conventional X-ray source to maximise diagnostic information

The SAXSess system employed a wide beam in order to minimise exposure time but when collecting data using this method the axial peaks were not clearly visible. The axial peaks have been shown to contain diagnostically relevant information and therefore if the peaks are not visible information required for accurate diagnosis may

be missed. Thus the use of a conventional X-ray source with a wide beam may not be adequate for clinical diagnosis. Further studies are required to optimise a conventional X-ray system to ensure the maximum diagnostic information is collected in the minimum of time.

13.5 Automated diagnosis

The processing method in this study used a radial integration to convert a 2 dimensional image to a 1 dimensional scattering profile of spacing against intensity. Using just the 1 dimensional profile automated diagnosis has been shown to be effective. However, as computers can handle large amounts of information more accurate diagnosis might be achieved if the PCA was performed on the whole of the scatter image which may allow the separation of the equatorial features from the axial features and allow the effects of preferred orientation to be visualised so as to not affect the diagnostic information. Studies analysing the benefits of using PCA, wavelet analysis and/or curvelet analysis have been undertaken in collaboration with the University of New England in Armadale, Australia.

13.6 Double blind study

All of the diagnostic methods, either manual or automated 1D and 2D PCA, will require thorough testing using double blind methods comparing new samples (i.e. samples not used to build the diagnostic model) with the model. Until the accuracy of diagnosis has been replicated using double blind methods the reliability of X-ray scattering as a diagnostic technique will remain in question.

13.7 Use of alternate techniques to investigate collagen structure

X-ray scattering is a useful technique and does show a difference between tissue types but only provides limited information. Combining what is known from the SAXS data with other investigative techniques might provide a more detailed picture of the fundamental biochemical processes involved in tumour invasion and metastasis. Collagen exhibits a strong signal in a number of investigative techniques such as second harmonic generation microscopy, infra-red spectroscopy and circular dichroism. It has been proposed to investigate the tissue slices mounted on mica using all appropriate techniques to match the observed signals with the SAXS and histopathological analysis in order to obtain the maximum amount of data regarding the differences in the collagen between tissue types.

14 References

Bigi A., Fichera A.M., Roveri N., Koch M.H.J. 1987.
Structural modifications of air dried tendon collagen on heating.
Int. J. Biol. Macromol., **Vol. 9,** pp. 176–180

Bigi A. 1996.
Small-angle X-ray diffraction studies of collagen.
Biomedical Applications of Synchrotron Radiation Int., pp 251-68

Bigi A. and Roveri N. 1991.
Fibre diffraction: collagen.
In S. Ebashi, M. Koch. and E. Rubenstein, eds.
Handbook of Synchrotron Radiation, **Vol 4**, pp 199-239

Brinckerhoff C.E. and Matrisian L.M. 2002.
Matrix metalloproteinases: a tail of a frog that became a prince.
Nature Reviews, Molecular Cell Biology, **Vol. 3**, pp 207-214

Butler S.M., Webb G.I., Lewis R.A. 2003.
A Case Study in Feature Invention for Breast Cancer Diagnosis Using X-Ray Scatter Images.
Proceedings of the 16th Australian Joint Conference on Artificial Intelligence (as 'Lecture Notes in Artificial Intelligence').

Carney P.A., Miglioretti D.L., Yankaskas B.C., Kerlikowske K., Rosenberg R., Rutter C.M., Geller B.M., Abraham L.A., Taplin S.H., Dignan M., Cutter G., Ballard-Barbash R. 2003.
Individual and combined effects of age, breast density, and hormone replacement therapy use on the accuracy of screening mammography.
Ann. Intern. Med., **Vol.138** (3), pp 168-75

Duffy M.J., Maguire T.M., Hill A., McDermott E., O'Higgins N. 2000.
Metalloproteinases: role in breast carcinogenesis, invasion and metastasis.
Breast Cancer Res., Vol. 2, pp 252-257

Eikenberry E.F., Brodsky B., Parry D.A.D., 1982.
Collagen fibril morphology in developing chick metatarsal tendoms: 1. X-ray diffraction studies.
Int. J. Biol. Macromol., **Vol. 4**, pp 322-328

Evans S.H., Bradley D.A, Dance D.R., Bateman J.E., Jones C.H. 1991.
Measurement of small angle photon scattering for some breast tissues and tissue substitute materials.
Phys. Med. Biol., **Vol. 36** (1), pp 7-18

Feigin L.A., Svergun D.I. 1987.
Structure Analysis by Small-Angle X-ray and Neutron Scattering.
New York
Plenum Press

Ferguson J.E., Schor A.M., Howell A, Ferguson M.W. 1992.
Changes in the extracellular matrix of the normal human breast during the menstrual cycle.
Cell Tissue Res., **Vol. 268** (1), pp 167-77

Fernandez A., Scheraga H.A. 2003.
Insufficiently dehydrated hydrogen bonds as determinants of protein interactions.
Proc. Natl. Acad. Sci., **Vol. 100**, (1), pp 113-118

Fernandez M., Keyrilainen J., Serimaa R., Torkkeli M., Karjalainen-Lindsberg M.L., Tenhunen M., Thomlinson W., Urban V., Suortti P. 2002.
Small-angle X-ray scattering studies of human breast tissue samples.
Phys. Med. Biol., **Vol. 47**, pp 577-592

Fenandez M., Keyrilainen J., Karjalainen-Lindsberg M.L., Leidenius M., von Smitten K., Fiedler S., Suortti P. 2002.
Human breast tissue characterisation with small-angle X-ray scattering.
Spectroscopy, **Vol. 18** (2) pp 167-176

Fernandez M., Keyrilainen J., Serimaa R., Torkkeli M., Karjalainen-Lindsberg M.L., Leidenius M., von Smitten K., Tenhunen M., Fiedler S., Bravin A., Weiss T.M., Suortti P. 2005.
Human breast cancer in vitro: matching histo-pathology with small-angle X-ray scattering and diffraction enhanced X-ray imaging.
Phys. Med. Biol., **Vol. 50**, pp 2991-3006

Fessler L.I., Duncan K.G., Fessler J.H., Salo T., Tryggvason K. 1984.
Characterization of the procollagen IV cleavage products produced by a specific tumor collagenase.
J. Biol. Chem., **Vol. 259** (15), pp 9783-9789,

Fratzl P., Misof K., Zizak I., Rapp G., Amenitsch H., Bernstorff S. 1997.
Fibular structure and mechanical properties of collagen.
Journal of Structural Biology, **Vol. 122**, pp 119-122,

Fullwood N.J., Meek K.M. 1993.
A synchrotron X-ray study of the changes occurring in the corneal stroma during processing for electron microscopy.
Journal of Microscopy, **Vol. 169** (1), pp 53-60

Gross J., Nagai Y. 1965.
Specific degradation of the collagen molecule by tadpole collagenolytic enzyme.
Proc. Natl. Acad. Sci., **Vol. 54**, pp 1197-1204

Harkness R.D. 1961.
Biological Functions of Collagen.
Biol. Rev., **Vol. 36**, pp. 399-463

Heppner K.J., Matrisan L.M., Jensen R.A., Rogers W.H. 1996.
Expression of most matrix mettalloprotinase family members in breast cacner represents a tumour induced host response.
American Journal of Pathology, **Vol. 149** (1), pp 273-282

Kufe D., Pollock R., Weichselbaum R., Bast R., Gansler T., Holland J., Frei E. 2003.
Cancer Medicine 6
Hamilton, Ontario
BC Decker Inc. (An approved publication of the American Cancer Society)

Hukins D.W.L. 1981.
X-ray Diffraction by disordered and ordered systems.
Oxford
Pergamon Press

James V.J., McConnell J.F., Amemiya Y. 1993.
Two very long periodicities in collagen.
Biochim. Biophys. Acta, **Vol. 1202** (2), pp 305-308

James V.J., Wilk K.E., McConnell J.F., Baranov E.P. 1995.
Intermediate filament structure of α-keratin in baboon hair.
Int. J. Biol. Macromol., **Vol. 17** (2), pp 99-104

James V.J., McConnell J.F., Amemiya Y. 1998.
Molecular structural changes in human foetal tissue during the early stages of embryogenesis.
Biochimica et Biophysica Acta, **Vol. 1379** (2), pp 282-288

James V. 2003.
Response to P. Suortti et al.'s and K. D. Rogers et al.'s Comments on Synchrotron fibre diffraction identifies and locates foetal collagenous breast tissue associated with breast carcinoma.
letters to the editor *J. Synchrotron Rad.,* **Vol. 10**, pp 200-201

James V.J. 2002.
Synchrotron Fibre diffraction identifies and locates foetal collagenous breast tissue associated with breast carcinoma.
J. Synchrotron Rad. **Vol.9**, pp 71-76

Keilty C.M., Hopkinson I., Grant M.E. 1993.
Collagen: The collagen family: Structure, Assembly, and organisation in the Extracellular Matrix.
pp. 103-147
In Royce M., Steinmann B. eds. 1993.
Connective Tissues and its Heritable Disorders.
New York
Wiley-Liss

Kidane G., Speller R.D., Royle G.J., Hanby A.M. 1999.
X-ray scatter signatures for normal and neoplastic breast tissues.
Phys. Med. Biol., **Vol. 44**, pp 1791-1802

Khun K. 1987
The classical Collagens: Types I, II and III
pp 1-42, In Mayne R., Bergson R.E. Mecham R.P. eds.
Structure and Function of collagen types
New York
Academic Press Inc.

Leikina E., Mertts M.V., Kuznetsova N., Leikin S. 2002.
Type I collagen is thermally unstable at body temperature.
PNAS, **vol. 99** (3), pp 1314-1318

Lazarev P., Paukshto M., Pelt N., Sakharovaiv A. 2000.
Human Tissue X-ray Diffraction: Breast, Brain, and Prostate
Proceedings of the 22nd Annual EMBS International Conference, July 23-28, 2000, Chicago IL.

Lewis R.A. 1997.
Medical applications of synchrotron radiation X-rays.
Phys. Med. Biol., **Vol. 42**, pp 1213-1243

Lewis R.A., Rogers K.D., Hall C.J., Towns-Andrews E., Slawson S., Evans A., Pinder S.E., Ellis I.O., Boggis C.R., Hufton A., Dance D.R. 1999.
Preliminary observations of breast tumour collagen using synchrotron radiation.
Proc. SPIE, Medical Applications of Penetrating Radiation, **Vol. 3770**, pp 32-37

Lewis R.A., Rogers K.D., Hall C.J., Towns-Andrews E., Slawson S., Evans A., Pinder S.E., Ellis I.O., Boggis C.R., Hufton A., Dance D.R. 2000.
Breast cancer diagnosis using scattered X-rays.
J. Synchrotron Rad., **Vol. 7**, pp 348-352

Luparello C., Pucci-Minafra I. 1986.
Different behavior of type I and type I-trimer collagen in neutral sodium chloride solutions.
Anal. Biochem., **Vol. 155** (2), pp 352-357

MacDougall J.R., Matrisan L.M. 1995.
Contributons of stromal matrix metalloprtinases to tumor progression, invasion and metastasis.
Cancer Metastasis Review, **Vol. 14**, pp 351-362

McCawley L.J., Matrisan L.M. 2000.
Metalloprtinases: multifunctional contributors to tumour progression.
Molecular Medicine Today, **Vol. 6** (4), pp 149-156

Minafra S., Luparello C., Rallo F., Pucci-Minafra I. 1988.
Collagen biosynthesis by a breast carcinoma cell strain and biopsy fragments of the primary tumour.
Cell Biol. In.t Rep., **Vol. 12** (10), pp 895-905

Minafra S., Pucci-Minafra I., Tomasino R.M., Sciarrino S. 1984.
Collagen Composition in the ductal infiltrating carcinoma of human breast.
Cell Biology International Reports, **Vol. 8** (1), pp 79-85

Montes G.S. 1996
Structural Biology of the Fibres of the Collagenous and Elastic Systems.
Cell Biology International, **Vol. 20**, 15-27

Nagase H., Woessner J.F. Jr 1999.
Matrix Metalloproteinases
J. Biol. Chem., **Vol. 274** (31), pp 21491-21494

Nie L., Wu S., Lin X., Zheng L., Rui L. 2002.
Approximate Derivative Calculated by Using Continuous Wavelet Transform
J. Chem. Inf. Comput. Sci., **Vol. 42** (2), pp 274-283

Orgel J.P.R.O., Miller A., Irving T.C., Fischetti R.F., Hammersley A.P., Wess T.J. 2001.
The In Situ Supermolecular Structure of Type I Collagen.
Structure, **Vol. 9**, pp 1061-1069

Perslow P.P., Wess T.J., Hukins D.W.L. 1998.
Collagen orientation and molecular spacing during creep and stress relaxation in soft connective tissues.
The Journal of Experimental Biology, **Vol. 201**, pp 135-142,

Poletti M.E., Goncalves O.D., Mazzaro I. 2002.
X-ray scattering from human breast tissues and breast-equivalent materials.
Phys. Med. Biol., **Vol. 47**, pp 47–63

Porod G. 1951.
Die Röntgenkleinwinkelstreuung von dichtgepackten kolloiden Systemen.
Colloid & Polymer Science, **Vol. 124** (2), pp 83-114

Privalov P.L. 1982.
Stability of Proteins; Proteins which do not present a single cooperative system.
Advances in Protein Chemistry, **Vol. 35**, pp 1-104.

Pucci-Minafra I., Luparello C., Sciarrino S., Tomasino R.M., Minafra S. 1985.
Quantitative determination of collagen types present in the ductal infiltrating carcinoma of human mammary gland.
Cell Biol. Int. Rep., **Vol. 9** (3), pp 291-6

Pucci-Minafra I., Minafra S., Tomasino R.M., Sciarrino S., Tinervia R. 1986.
Collagen changes in the ductal infiltrating (scirrhous) carcinoma of the human breast. A possible role played by type I trimer collagen on the invasive growth.
J. Submicrosc. Cytol., **Vol. 18** (4), pp 795-805

Pucci-Minafra I, Luparello C, Schillaci R, Sciarrino S. 1987.
Ultrastructural evidence of collagenolytic activity in ductal infiltrating carcinoma of the human breast.
In. J. Cancer., **Vol. 39** (5), pp 599-603

Pucci-Minafra I., Luparello C., Andriolo M., Basirico L., Aquino A., Minafra S. 1993.
A New Form of Tumor and Fetal Collagen That Binds Laminin.
Biochemistry, **Vol. 32**, pp 7421-7427

Quantock A.J., Meek K.M., Chakravarti S. 2001.
An X-ray Diffraction Investigation of Corneal Structure in Lumican-Deficient Mice
Investigative Ophthalmology and Visual Science, **Vol. 42**, pp 1750-1756

Rogers K.D., Hall C.J., Hufton A., Pinder S.E. 2003.
Comments on Synchrotron fibre diffraction identifies and locates foetal collagenous breast tissue associated with breast carcinoma by V. J. James 2002.
Letters to the editor *J. Synchrotron Rad.*, **Vol. 10**, pp 199

Ryan E.A., Farquharson M.J., Flinton D.M. 2005.
The use of Compton scattering to differentiate between classifications of normal and diseased breast tissue.
Phys. Med. Biol., **Vol. 50**, pp 3337–3348

Sasaki N., Odajima S. 1996(a).
Stress-Strain curve and Young's Modulus of a collagen Molecule as determined by the X-ray diffraction technique
J. Biomechanics, **Vol. 29** (5), pp 655-658

Sasaki N., Odajima S. 1996(b).
Elongation mechanism of collagen fibrils and force strain relations of tendon at each level of structural hierarchy.
J. Biomechanics, **Vol. 29** (9), pp 1131-1136

Sasaki N., Shukunami N., Matsushima N., Izumi Y. 1999.
Time resolved X-ray diffraction from tendon collagen during creep using synchrotron radiation.
J. Biomechanics, **Vol. 32** (3), pp 285-292

Schor S.L., Schor A.M. and Rushton G. 1998.
Fibroblasts from cancer patients display a mixture of both foetal and adult-like phenotypic characteristics.
Journal of Cell Science, **Vol. 90** (3), pp 401-407

Seibert J.A. 2004.
X-Ray Imaging Physics for Nuclear Medicine Technologists.
Part 1: Basic Principles of X-Ray Production
Journal of Nuclear Medicine Technology, **Vol. 32** (3), pp 139-147

Shah N., Cerussi A., Eker C., Espinoza J., Butler J., Fishkin J., Hornung R., Tromberg B. 2001.
Non-invasive functional optical spectroscopy of human breast tissue.
PNAS, **Vol. 98** (8), pp 4420-4425

Stedman T. 2000.
Stedman's Medical Dictionary, 27th Edition
Baltimore
Lippincott, Williams & Wilkins

Suortti P., Fernandez M., Urban V.
Comments on Synchrotron fibre diffraction identifies and locates foetal collagenous breast tissue associated with breast carcinoma by V. J. James 2002.
letters to the editor *J. Synchrotron Rad*. **Vol. 10**, pp 198

Suhonen H., Fernandez M., Serimaa R., Suortti P. 2005.
Simulation of small-angle X-ray scattering from collagen fibrils and comparison with experimental patterns.
Phys. Med. Biol., **Vol. 50** (22), pp 5401-5416

Taylor C.A. 2001.
A Non-Mathematical Introduction to X-ray Crystallography.
Cardiff
University College Cardiff Press for IUCr.

Thompson A.C., Vaughan D. eds.
X-ray data booklet, Second edition, 2001
Berkeley, California
Lawrence Berkeley National Laboratory
Thompson E.W., Yu M., Bueno J., Jin L., Maiti S.N., Palao-Marco F.L., Pulyaeva H., Tamborlane J.W., Tirgari R., Wapnir I., Azzam H. 1994.
Collagen induced MMP-2 activation in Human breast cancer.
Breast cancer research and treatment, **Vol. 31**, (2-3), pp 357-370

Tryggvason K., Hoyhtya M., Salo T. 1987.
Proteolytic degradation of Extracellular matrix in tumour invasion.
Biochemica et biophysica acta, **Vol. 907**, pp 191-217

Wess T.J., Orgal J.P. 2000.
Changes in collagen structure: Drying, de-hydrothermal treatment and relation to long term deterioration.
Thermochemica Acta, **Vol. 365**, pp 119-128

Wess T.J. 2005.
Collagen fibril form and function.
in Parry D. eds
Fibrous Proteins: Coiled-Coils, Collagen and Elastomers.
Advances in Protein Chemistry, **Vol. 70,** pp 341-74

14.1 Web Based References

Beaucage G. 1999.
lectures, Analysis, Chapter 8.
University of Cincinnati
http://www.eng.uc.edu/~gbeaucag/Classes/Analysis/Chapter8.html
[Cited 6/8/2004]

breastcancercare 2005.
Breast development and ageing
http://www.breastcancercare.org.uk/Breasthealth/Breastawareness/Breastdevelopmentandageing
[Cited 14/2/2005]

Cancer research UK 2002.
Stages of breast cancer
http://www.cancerhelp.org.uk/help/default.asp?page=3315
[Cited 12/2/2005]

Cancer research UK 2002
Incidence, survival and mortality
http://www.cancerhelp.org.uk/help/default.asp?page=154
[Cited 12/2/2005]
Fiber diffraction and Bessel functions 1998.

Max Plank institute in Heidelberg
http://www.mpimf-heidelberg.mpg.de/~holmes/fibre/branden.html
[Cited 7/8/2004]

Infometrix 2006.
Products, Software.
http://www.infometrix.com/software/softdesc.html
[Cited 04/04/2006]

Mathworks 2006.
http://www.mathworks.com/
[Cited 04/04/2006]

Imaginis 2005.
Milestones in medical diagnosis and diagnostic imaging
http://imaginis.com/faq/milestones.asp
[Cited 25/04/05]

More.com 2005.
Hormones and Breast Cancer
http://www.more.com/more/story.jhtml?storyid=/templatedata/lhj/story/data/MP_Breastcancer_04092003.xml&catref=cat2440122
[Cited 20/03/05]

National statistics 2002.
Series MB1 no. 33
Cancer statistics
Registrations
Registrations of cancer diagnosed in 2002, England
http://www.statistics.gov.uk
[Cited 14/10/2005]

National statistics 2001.
Series MB1 no. 32
Cancer statistics
Registrations
Registrations of cancer diagnosed in 2001, England
http://www.statistics.gov.uk
[Cited 14/10/2005]

National statistics 2003.
Breast cancer incidence
http://www.statistics.gov.uk/cci/nugget.asp?id=575
[Cited 14/10/2005]

National statistics 1999.
Breast cancer mortality
http://www.statistics.gov.uk/statbase/expodata/files/10391440192.csv
[Cited 14/10/2005]

Physics of X-ray production 2004.
http://www.fnrf.science.cmu.ac.th/theory/radiation/Physics%20of%20X-RAY%20Production.html
[Cited 25/04/05]

Research Systems Inc. 2006.
http://www.rsinc.com/
[Cited 04/04/2006]

Roentgen and the discovery of X-rays 2005.
http://www.xray.hmc.psu.edu/rci/ss1/ss1_2.html
[Cited 25/04/05]

Seljee F.R. 2005.
ALL YOU WANTED TO KNOW ABOUT COLLAGEN . . .
http://www.science.uva.nl/research/crystallography/franks/collageen/
Alternate http://www.seljee.nl/collagen/
[Cited 10/10/2005]

Singhal H., Kaur K., Thomson S. 2006.
Breast Cancer Evaluation.
http://www.emedicine.com/med/topic3287.htm
[Cited 15/2/2005]

Stanford synchrotron radiation Laboratory (SSRL) 2000.
Graph of emission spectra for mending magnets and wigglers.
http://www-project.slac.stanford.edu/ssrltxrf/bending_magnet.htm
[Cited 26/04/05]

Systat Software 2006.
http://www.systat.com/
[Cited 04/04/2006]

Appendix I

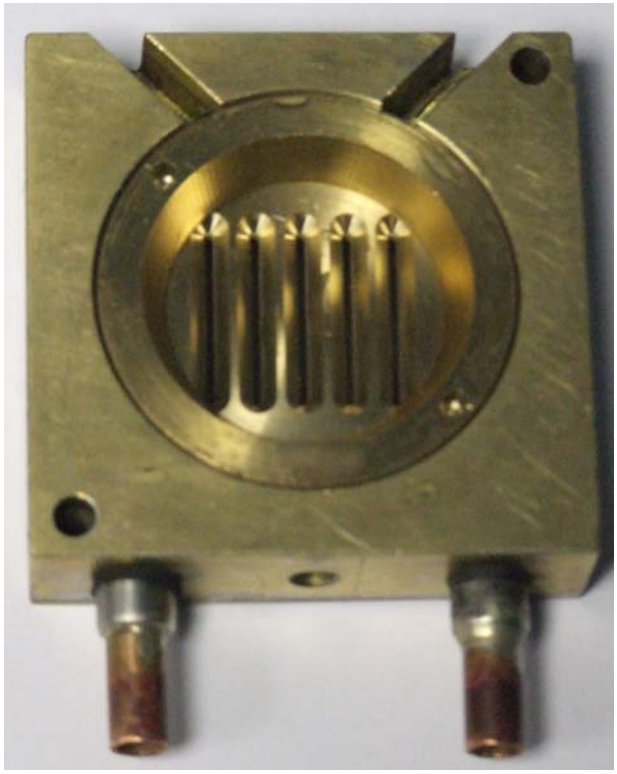

Figure I.1 New sample holder fully assembled

Figure I.2 Sample holder base unit designed by Dr S. Wilkinson

Figure I.3 Sample securing discs, sample holder disc (top) and sample clamp disc (bottom)

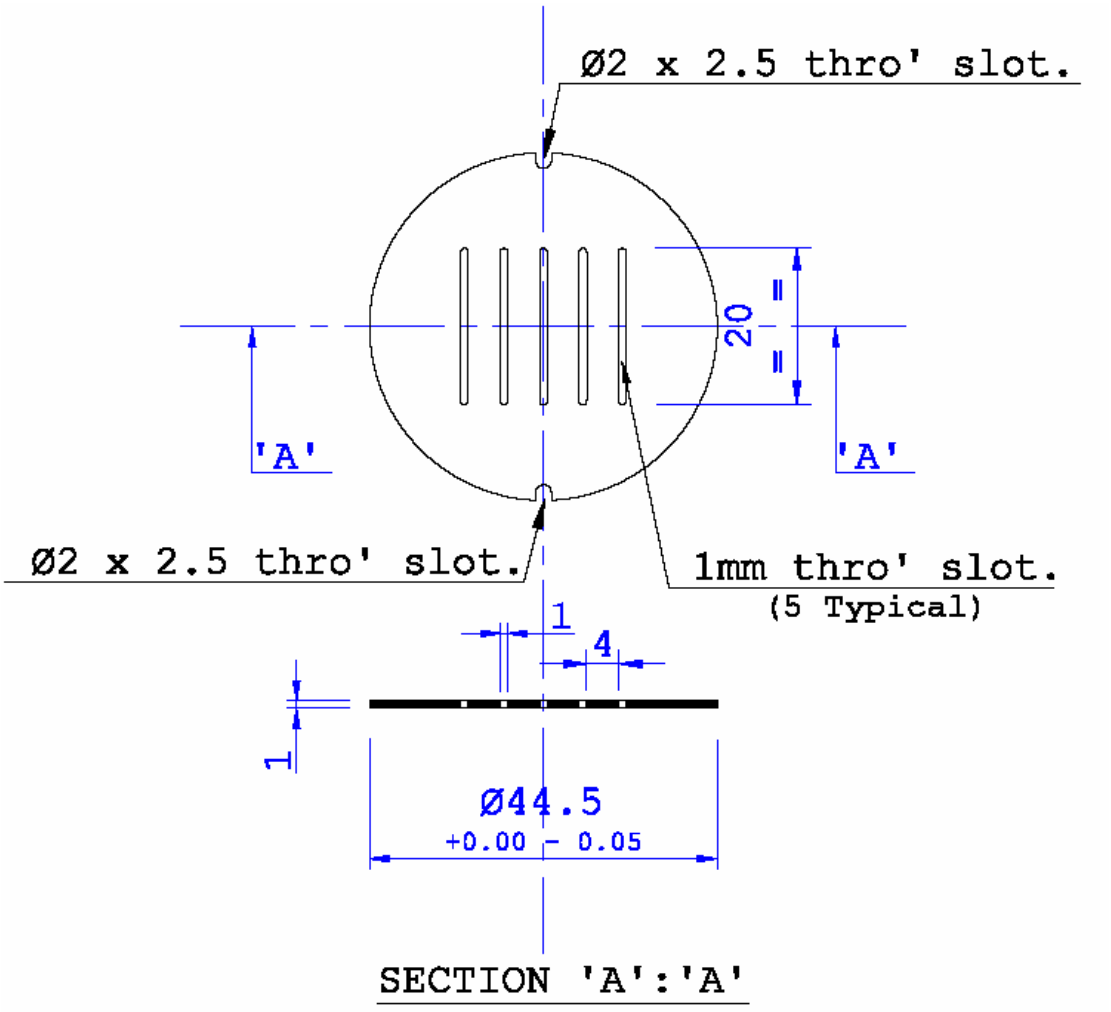

TITLE. BIOMED SAMPLE HOLDER DISC	
DRAWING No:- MW0161	QUANTITY 2 off
SCALE 0 50 All Dimensions in mm's Unless Otherwise Stated.	
MATERIAL. BRASS	SPEC,
TOLERANCES ± 0.2 Unless Otherwise Stated.	
Drawn by - Mike Wardell	Date - 10/01/06

Figure I.4 Sample holder disc

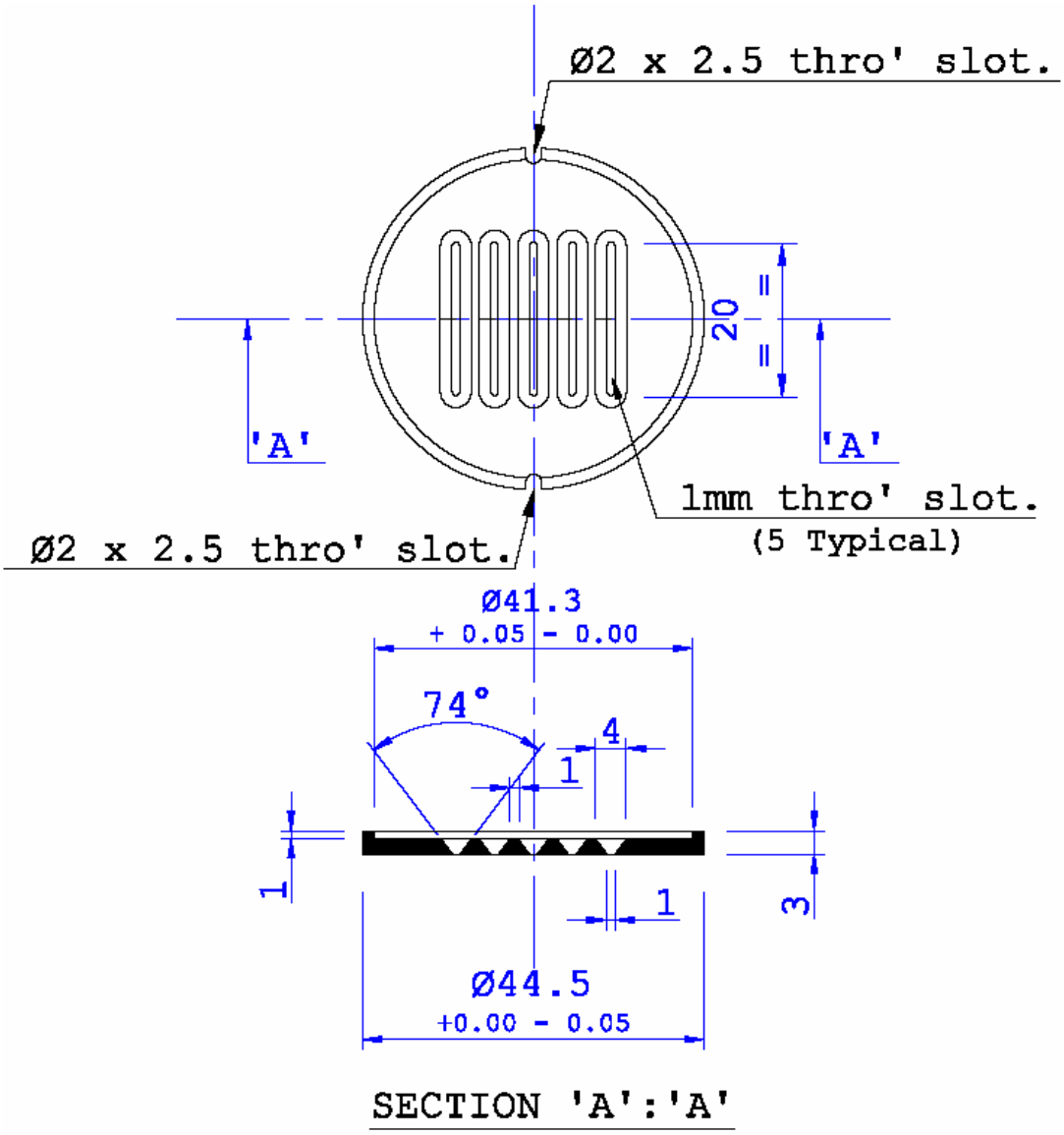

TITLE. BIOMED SAMPLE CLAMP DISC	
DRAWING No:- MW0160	QUANTITY 4 off
SCALE 0 50 All Dimensions in mm's Unless Otherwise Stated.	
MATERIAL. BRASS	SPEC,
TOLERANCES ± 0.2 Unless Otherwise Stated.	
Drawn by - Mike Wardell	Date - 10/01/06

Figure I.5 Sample clamp disc

Appendix II